ADVANCEMENTS OF PHASE BEHAVIOR AND FLUID TRANSPORT IN PETROLEUM RESERVOIRS

EDITED BY: Xiaohu Dong, Jing Wang, Zhehui Jin, Feng Yang and Yulong Zhao

PUBLISHED IN: Frontiers in Earth Science

frontiers Research Topics

ISSN 1664-8714
ISBN 978-2-88976-460-0
DOI 10.3389/978-2-88976-460-0

About Frontiers

Frontiers is more than just an open-access publisher of scholarly articles: it is a pioneering approach to the world of academia, radically improving the way scholarly research is managed. The grand vision of Frontiers is a world where all people have an equal opportunity to seek, share and generate knowledge. Frontiers provides immediate and permanent online open access to all its publications, but this alone is not enough to realize our grand goals.

Frontiers Journal Series

The Frontiers Journal Series is a multi-tier and interdisciplinary set of open-access, online journals, promising a paradigm shift from the current review, selection and dissemination processes in academic publishing. All Frontiers journals are driven by researchers for researchers; therefore, they constitute a service to the scholarly community. At the same time, the Frontiers Journal Series operates on a revolutionary invention, the tiered publishing system, initially addressing specific communities of scholars, and gradually climbing up to broader public understanding, thus serving the interests of the lay society, too.

Dedication to Quality

Each Frontiers article is a landmark of the highest quality, thanks to genuinely collaborative interactions between authors and review editors, who include some of the world's best academicians. Research must be certified by peers before entering a stream of knowledge that may eventually reach the public - and shape society; therefore, Frontiers only applies the most rigorous and unbiased reviews.
Frontiers revolutionizes research publishing by freely delivering the most outstanding research, evaluated with no bias from both the academic and social point of view. By applying the most advanced information technologies, Frontiers is catapulting scholarly publishing into a new generation.

What are Frontiers Research Topics?

Frontiers Research Topics are very popular trademarks of the Frontiers Journals Series: they are collections of at least ten articles, all centered on a particular subject. With their unique mix of varied contributions from Original Research to Review Articles, Frontiers Research Topics unify the most influential researchers, the latest key findings and historical advances in a hot research area! Find out more on how to host your own Frontiers Research Topic or contribute to one as an author by contacting the Frontiers Editorial Office: frontiersin.org/about/contact

ADVANCEMENTS OF PHASE BEHAVIOR AND FLUID TRANSPORT IN PETROLEUM RESERVOIRS

Topic Editors:
Xiaohu Dong, China University of Petroleum, Beijing, China
Jing Wang, China University of Petroleum, Beijing, China
Zhehui Jin, University of Alberta, Canada
Feng Yang, China University of Geosciences Wuhan, China
Yulong Zhao, Southwest Petroleum University, China

Citation: Dong, X., Wang, J., Jin, Z., Yang, F., Zhao, Y., eds. (2022). Advancements of Phase Behavior and Fluid Transport in Petroleum Reservoirs. Lausanne: Frontiers Media SA. doi: 10.3389/978-2-88976-460-0

Table of Contents

frontiers | Frontiers in Earth Science

EDITORIAL
published: 06 June 2022
doi: 10.3389/feart.2022.913751

Editorial: Advancements of Phase Behavior and Fluid Transport in Petroleum Reservoirs

Xiaohu Dong[1], Jing Wang[1], Zhehui Jin[2], Feng Yang[3] and Yulong Zhao[4]*

[1]State Key Laboratory of Petroleum Resources and Prospecting, China University of Petroleum, Beijing, China, [2]Department of Civil and Environmental Engineering, University of Alberta, Edmonton, AB, Canada, [3]College of Natural Resources, China University of Geosciences, Wuhan, China, [4]College of Petroleum and Natural Gas Engineering, Southwest Petroleum University, Chengdu, China

Keywords: phase behavior, fluid transport, advancement, petroleum reservoir, shale

Editorial on the Research Topic

Advancements of Phase Behavior and Fluid Transport in Petroleum Reservoirs

MOTIVATION AND BACKGROUND

Petroleum reservoirs are one of the most important energy resources in the world. In such a difficult time, its efficient development plays an important role for the security of world energy supply. Specifically, during the recovery process of petroleum reservoirs, fluid phase behavior and transportation in porous media are always the two most important issues. The former can determine the fluid state in reservoirs, and the latter controls the fluid flowability. Thus, an accurate description of the two issues usually guarantees the development efficiency of a petroleum reservoir. Especially, in recent decades, with the successful development of various unconventional petroleum resources, the Research Topic of phase behavior and fluid transport in such unconventional reservoirs have also attracted significant attention.

Firstly, for conventional petroleum reservoirs, during the recovery process, with the reduction of reservoir pressure and the injection of different additives (e.g., N_2, CO_2, solvent, and chemical additives, etc.), the original fluid phase state in the reservoir will change, simultaneously, the fluid transportation characteristics also vary because of the continuous change of reservoir conditions. Then, for unconventional reservoirs, because of the complicated porous medium condition, an accurate description of the fluid phase behavior and transportation is a challenge. Therefore, the focus of this Research Topic is therefore placed on an improved understanding of the phase behavior and fluid transport mechanisms in different types of petroleum reservoirs. It addresses the most recent advances in experimental and numerical simulation methods to study the fluid phase behavior and transportation process in different petroleum reservoirs.

CONTENTS OF THE RESEARCH TOPIC

Fluid Phase Behavior and Transportation in Unconventional Reservoirs

By considering the various fluid flow mechanisms in shale, Guo et al. propose an apparent permeability model for shale gas reservoirs. They comparatively analyze the contribution of viscous slippage flow, Knudsen diffusion, and surface diffusion to the apparent permeability of

OPEN ACCESS

Edited and reviewed by:
David R. Lentz,
University of New Brunswick
Fredericton, Canada

****Correspondence:***
Xiaohu Dong
donghu820@163.com

Specialty section:
This article was submitted to Economic Geology, a section of the journal Frontiers in Earth Science

Received: *06 April 2022*
Accepted: *02 May 2022*
Published: *06 June 2022*

Citation:
Dong X, Wang J, Jin Z, Yang F and Zhao Y (2022) Editorial: Advancements of Phase Behavior and Fluid Transport in Petroleum Reservoirs. Front. Earth Sci. 10:913751. doi: 10.3389/feart.2022.913751

shale. This work provides a good basis for an accurate measurement on the permeability of shale rocks.

Wang et al. develop a water–oil flow model for the behavior of water imbibition and the oil drainage process in hydraulically fractured shales. Based on their model, the main characteristics of post-fracturing soaking are simulated. Simultaneously, the oil–water exchange efficiency and exchange volume are also evaluated. This work provides some new insights to understanding the oil–water exchanging behavior in shale oil reservoirs.

Jia et al. investigate the mechanisms of the shut-in process in shale reservoirs after fracturing and summarize the EOR mechanisms of the well shut-in process. Then, a single well shut-in numerical simulation model is established and the oil-water distribution and change laws of shut-in shale reservoirs after fracturing are analyzed. This work provides a deep understanding of the EOR mechanisms of shut-in wells in shale reservoirs.

Qiao et al. experimentally and numerically discuss the CO_2 mass transfer behavior and oil replacement capacity in fractured shale oil reservoirs. It is found that CO_2 can gradually exchange the oil in a matrix into fractures and improve oil fluidity in a matrix until an equilibrium state is achieved. This work provides a good reference for the evaluation of well shut-in time and production management after CO_2 fracturing in shale oil reservoirs.

Based on a series of tests on the physical properties of shale in Sichuan Basin, Wu et al. numerically evaluate the post-fracturing flowback behavior of shale gas wells. Some sensitive factors and their mechanisms are analyzed. This work provides a good basis to understanding the shale gas drainage–production system after hydraulic fracturing.

Fluid Phase Behavior and Transportation in Conventional Reservoirs

Zheng et al. develop a visual fluid flow experimental device to investigate the flow behavior of N_2 water in porous media. Then, by using a field scale reservoir simulation model, the water-coning behavior of edge water is systematically studied through two novel indicators. This work further clarifies the mechanisms of the N_2 injection process to control water coning in heavy oil reservoirs and provides a useful reference for the EOR process of heavy oil reservoirs with edge water.

Kang et al. simulate the unsteady flow behavior of gas and water in dual-medium gas reservoirs from a proposed two-phase flow model. They fully consider the effect of stress sensitivity and non-Darcy flow. Then, by introducing the perturbation theory, a productivity evaluation model is developed for the dual-medium gas reservoir. This work provides a good reference to understanding the recovery performance of dual-medium gas reservoirs.

Aiming at the productivity of gas wells, Er-hu et al. establish a single-point deliverability formula from the binomial productivity equation and modified isochronous well test method. Based on their proposed method, the productivity of the Jingbian sector in Yan'an gas field is evaluated. It is found that the one-point productivity formula has high precision and is suitable for the productivity analysis of gas wells.

Aiming at a sour gas reservoir in Sichuan Basin, Zhang et al. experimentally discuss elemental sulfur solubility by using a static method. The effect of pressure and H_2S content is experimentally discussed. Furthermore, some published models are also used to history match the experimental data. Considering the important role of elemental sulfur solubility, this work provides some important basic data for the development process of a sour gas reservoir.

AUTHOR CONTRIBUTIONS

XD-Draft manuscript; JW, ZJ, FY, and YZ-Review and revision.

ACKNOWLEDGMENTS

We are grateful to all the authors for their great contributions to this Research Topic. We also thank the reviewers who helped us to evaluate and contribute to these papers.

Conflict of Interest: The authors declare that the research was conducted in the absence of any commercial or financial relationships that could be construed as a potential conflict of interest.

Publisher's Note: All claims expressed in this article are solely those of the authors and do not necessarily represent those of their affiliated organizations, or those of the publisher, the editors and the reviewers. Any product that may be evaluated in this article, or claim that may be made by its manufacturer, is not guaranteed or endorsed by the publisher.

frontiers in Earth Science

BRIEF RESEARCH REPORT
published: 07 October 2021
doi: 10.3389/feart.2021.767015

Experimental Study on the Elemental Sulfur Solubility in Sour Gas Mixtures

Rui Zhang[1,2], *Shaohua Gu*[1,2], *Liang Huang*[1,3]*, *Daqian Zeng*[1,2], *Tong Li*[2,4] *and Guangdong Zhang*[5]

[1]State Key Laboratory of Shale Oil and Gas Enrichment Mechanisms and Effective Development, Beijing, China, [2]SINOPEC Petroleum Exploration and Production Research Institute, Beijing, China, [3]College of Energy, Chengdu University of Technology, Chengdu, China, [4]School of Earth and Space Science, Peking University, Beijing, China, [5]Department of Petroleum Engineering, Southwest Petroleum University, Chengdu, China

The investigation of elemental sulfur solubility plays critical roles on sour gas reservoir development. In this paper, the solubility of elemental sulfur was directly measured by static method with gas samples from well M1 of a sour gas reservoir in Sichuan Basin. The results show that the solubility of elemental sulfur ranges from 0.001 g/cm^3 to 0.968 g/cm^3 at 40–98.9 MPa and 15–49.8 MPa. The elemental sulfur solubility increases with increasing temperature and pressure, especially when the pressure is greater than 30 MPa. Moreover, the H_2S content in sour gas mixtures is also an important factor affecting elemental sulfur solubility. The elemental sulfur solubility increases with increasing H_2S content of the sour gas mixtures. The experimental data in this paper display a consistent trend with the reported experimental data. Based on the experimental results, the chrastil-type model, Robert's model and Hu's model were investigated and compared. The results show that the chrastil-type model by fitting experimental data in this paper has less error and higher accuracy in calculating elemental sulfur solubility in M gas reservoir. The chrastil-type models proposed in the literature, meanwhile, are only based on the regression of specific gas components and experimental conditions, which lead to a large error in the calculation of elemental sulfur solubility of sour gas samples in this research. The research results provide important basic data and technical support for the development of M gas reservoir.

Keywords: elemental sulfur, solubility, sour gas, H_2S content, chrastil model

OPEN ACCESS

Edited by:
Xiaohu Dong,
China University of Petroleum, China

Reviewed by:
Weiqi Fu,
China University of Mining and Technology, China
Jinghong Hu,
China University of Geosciences, China
Lie Kong,
Monash University, Australia

***Correspondence:**
Liang Huang
huangliang@cdut.edu.cn

Specialty section:
This article was submitted to Economic Geology, a section of the journal Frontiers in Earth Science

Received: *30 August 2021*
Accepted: *23 September 2021*
Published: *07 October 2021*

Citation:
Zhang R, Gu S, Huang L, Zeng D, Li T and Zhang G (2021) Experimental Study on the Elemental Sulfur Solubility in Sour Gas Mixtures. Front. Earth Sci. 9:767015. doi: 10.3389/feart.2021.767015

INTRODUCTION

Natural gas reservoirs with high sulfur content have huge resource prospects all over the world. Meanwhile, the development of high-sulfur gas reservoirs is also facing great challenges. In these different challenges, elemental sulfur deposition in formation is one of the main problems in gas development process (Kuo, 1972; Chesnoy and Pack, 1997; Roberts, 1997; Roberts, 2017). As the concentration of elemental sulfur in the sour gas exceeds the critical dissolved concentration during the development of sour gas reservoirs, sulfur deposition may occur in the formation. The characteristics of sulfur dissolution, like hydrocarbon dissolution in organic matter (Huang et al., 2020; Huang et al., 2021), are crucial in the analysis of elemental sulfur deposition limit and deposition amount (Smith et al., 1970; Brunner and Woll, 1980; Brunner et al., 1988). Thus, many researchers have been devoted to the study on the elemental sulfur solubility in sour gas from experiment (Kennedy and Wieland, 1960; Roof, 1971; Swift and Manning, 1976; Brunner and Woll,

1980; Brunner et al., 1988; Davis et al., 1993; Gu et al., 1993; Sun and Chen, 2003; Zeng et al., 2005; Yang et al., 2009; Bian et al., 2010; Serin et al., 2010; Cloarec et al., 2012), thermodynamic model (Karan et al., 1998; Heidemann et al., 2001; Cézac et al., 2007; Cézac et al., 2008), semi empirical model (Chrastil, 1982; Eslamimanesh et al., 2011a; Hu et al., 2014; Guo and Wang, 2016), artificial intelligence algorithm (Mohammadi and Richon, 2008; Mehrpooya et al., 2010; Aminian, 2011; Bian et al., 2018; Fu et al., 2019; Bemani et al., 2020; Chen et al., 2020) and molecular simulation (Kadoura et al., 2013; Chen et al., 2019).

Kennedy and Wieland (Kennedy and Wieland, 1960) first measured the elemental sulfur solubility in pure CH_4, CO_2, H_2S and sour gas mixtures. Their results showed that the solubility of sulfur increased with increasing temperature and pressure. The H_2S solution presented the largest elemental sulfur solubility, while the CH_4 solution showed the smallest solubility. However, their experimental method was questioned by roof (Roof, 1971). Subsequently, Roof (Roof, 1971) also measured the elemental sulfur solubility in H_2S, and found that with the increase of temperature, the elemental sulfur solubility initially increased and then presented a decreasing trend as the solubility reached a critical point. However, the sulfur solubility experiment was limited to low temperature and low pressure conditions. Since then, Swift (Swift and Manning, 1976) and Brunner (Brunner and Woll, 1980; Brunner et al., 1988) have reported the measurement of sulfur solubility in pure H_2S under extended temperature and pressure conditions. Davis (Davis et al., 1993) extended the dissolution of sulfur in typical components to complex multi-component sour gas, and broadened the temperature and pressure range of the experiment. Gu (Gu et al., 1993) used a set of static method equipment to determine the solubility data of sulfur in CH_4, CO_2, H_2S and their mixtures. Sun (Sun and Chen, 2003), Zeng (Zeng et al., 2005), Yang (Yang et al., 2009) and Bian (Bian et al., 2010) also expanded the range of the solutions and the limits of experimental conditions. Serin (Serin et al., 2010) measured the elemental sulfur solubility in pure CO_2 under lower temperature and pressure conditions. Cloarec (Cloarec et al., 2012) measured the elemental sulfur solubility in pure CH_4 by improving the capture device and gas expansion device, and their results were slightly different from those of Kennedy and Wieland.

The published experiments on the elemental sulfur solubility are summarized in **Appendix A**. With the advancement of experimental methods, the experimental pressure and temperature ranges have been extended to 0.5–138 MPa and 303.2–563 K, and the solutions have been extended from single-component H_2S, CO_2, CH_4 to multi-component wellhead gas sample of the gas fields. These experimental results provide crucial data for the solubility model. However, due to the huge experimental costs, as well as the potential experimental risks from toxic gas, the experimental data of elemental sulfur solubility are far from sufficient. Especially, the experimental data of elemental sulfur solubility in sour gas mixtures from high-containing sulfur gas well in China remain limited. Also, owing to the small solubility value, the sulfur solubility is susceptible to various interferences, such as temperature, pressure, and H_2S content (Eslamimanesh et al., 2011b; Luo et al., 2012; Eslamimanesh et al., 2013). Some documented experimental work has reported inconsistent results, the elemental sulfur solubility urgently needs further verification and supplementation. The theoretic model of sulfur solubility can overcome the experimental demerits like huge cost, long period, and high risk, and thus predict the sulfur solubility conveniently. Nevertheless, the accuracy of reported theoretic models of sulfur solubility in sour gas samples from Chinese high-sulfur gas wells remains to be verified. Accordingly, this wok is aimed to supplement key sulfur solubility data in sour gas samples from Chinese high-sulfur gas well. The effects of temperature, pressure, and H_2S content are analyzed. Combined with the measured data, the accuracy of the common chrastil-type model and its extended models are further explored.

EXPERIMENTAL METHODOLOGY

Principles and Apparatus

Based on the principle of solvent dissolution, the sour gas sample is pressed into the sample reaction vessel by the piston pump, the sample reaction vessel can simulate the high temperature and high pressure of the formation. Subsequently, fully reacted and mixed sour gas sample is passed through the CS_2 solution, CS_2 solvent is a commonly used elemental sulfur solvent, the elemental sulfur in the sour gas sample is dissolved in CS_2 solution and the content of elemental sulfur in the CS_2 solution is measured with a gas chromatograph to calculate the sulfur content in the original gas sample. After that, the H_2S in the mixed gas is absorbed by the NaOH solution from a security perspective, and the gas flow meter can measure the volume of gas mixtures without H_2S at room temperature and pressure. The experimental apparatus is shown in **Figure 1**. The key parts of the apparatus are: 1) gas mixing system; 2) high temperature and high pressure resistant experimental reaction vessel; 3) gas absorption device; 4) gas chromatograph. Finally, the sulfur solubility of gas mixtures can be calculated by the following formula:

$$c = \frac{mS}{100V} \tag{1}$$

Where c is sulfur solubility, g/m^3; m is CS_2 solvent quality, g; S is elemental sulfur content in CS_2 solvent, %; V is volume of gas mixtures, m^3.

Gas Sample and Determination of Elemental Sulfur Content

The gas sample is taken from a downhole gas sample from well M1 in a sour gas field in the Sichuan Basin. The sampling depth is 3800 m, the sampling pressure is 35 MPa, and the temperature is 98.1°C. The temperature and pressure are restored indoors, and the opening pressure is checked. The H_2S content is determined by titration for three times. The molar contents of the three titrations are 17.982%, 17.891 % and 17.668%. Take the middle value of three titration, the H_2S content of the downhole sample

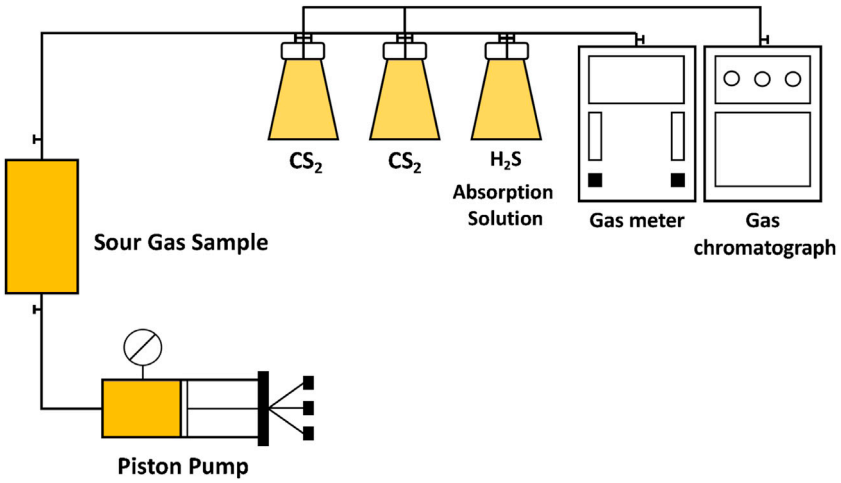

FIGURE 1 | The experimental apparatus for measuring elemental sulfur content

TABLE 1 | Solubility of elemental sulfur in well M1 by experiments and predictions.

Pressure (MPa)	Elemental sulfur solubility (g/m^3)						
	Measured data				Predicted data		
	98.9°C	80°C	60°C	40°C	Hu's model[a]	Roberts's model[b]	This paper[c]
49.8	0.968	0.429	0.175	0.076	0.0012	369.7	0.829
40	0.550	0.225	0.095	0.040	0.00083	227.4	0.523
30	0.220	0.104	0.039	0.015	0.00043	101.7	0.243
15	0.031	0.008	0.002	0.001	0.00017	7.2	0.019

[a]*Model coefficients (see **Eq. 2**): k = 1.592, a = –2737, b = –8.89768 (ρ < 200); k = 3.288, a = –4880, b = –12.4969 (ρ > 200).*
[b]*Model coefficients: k = 4, a = –4666, b = –4.5711.*
[c]*Model coefficients: k = 3.8, a = –6648, b = –4.7293.*

of well M1 is 17.891%, which is a high-sulfur content gas reservoir. The composition of the natural gas in well M1 can be obtained by gas chromatograph. The CH_4 content in the gas sample is 73.418%, the CO_2 content is 8.66%, the C_2H_6 content is 0.032%, and the contents of other components are negligible.

To determine the sulfur content of a gas sample, a group of solutions with known sulfur content are used for calibration. In order to cover the measured range of elemental sulfur solubility, high-concentration standard samples were prepared. The sulfur contents are 0.005%, 0.01%, 0.03% and 0.05% respectively. The standard peak areas of different sulfur contents are used as the reference values. Then the differences between the measured peak area and the standard peak areas are used to obtain the sulfur content of the gas sample.

The elemental sulfur contents of the gas in well M1 are determined by experiments. The original elemental sulfur content of the gas sample in downhole under formation condition is 0.091 g/m^3, the elemental sulfur content under sampling conditions (35 MPa, 98.1°C) is 0.357 g/m^3, and the saturated sulfur content under formation conditions is 0.968 g/m^3. Thus, the elemental sulfur in the gas sample has not reached saturation under the formation conditions and the sampling conditions.

RESULTS AND DISCUSSION

Solubility of Elemental Sulfur in Well M1

The elemental sulfur solubility experiment was carried out using gas samples from well M1, the solubility of elemental sulfur was measured among 40–98.9°C and 15–49.8 MPa. The elemental sulfur solubility was determined by taking the average of three tests for each pressure point. The errors among different measurements were checked to be smaller than 2%. The experimental results are shown in **Table 1** and **Figure 2A**. It can be seen from **Figure 2A** and **Table 1** that at the same temperature, the solubility of sulfur increases with increasing pressure; and at the same pressure, the solubility of elemental sulfur increases as the temperature increases. At the formation temperature (98.9°C), the solubility of elemental sulfur reaches 0.968 g/m^3 at 49.8 MPa and then drops to 0.031 g/m^3 as the pressure decreases to 15 MPa. At the

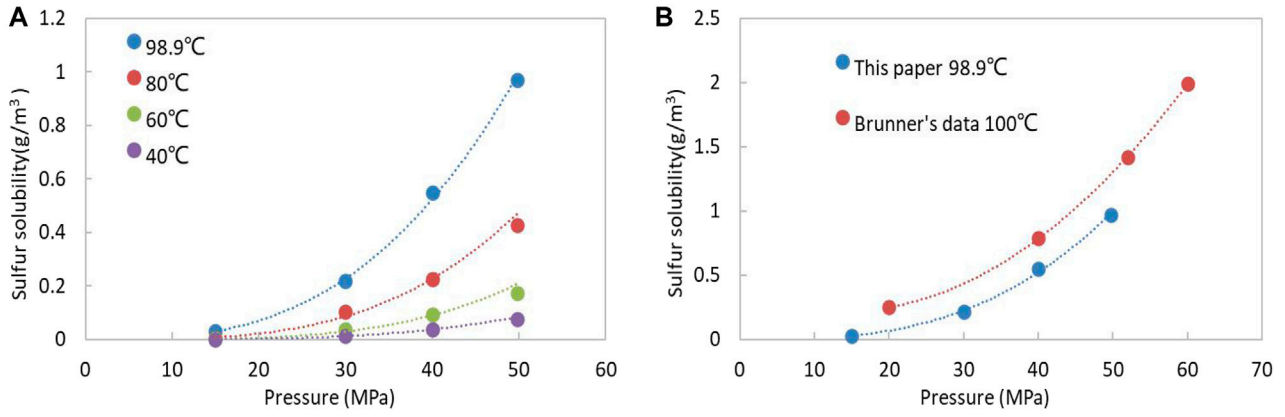

FIGURE 2 | Sulfur solubility in well M1 gas sample. **(A)** experimental results in this work; **(B)** comparison with Brunner's data at similar gas compositions. The sour gas in Brunner's data contains 20 % H_2S, 66 % CH_4, 10 % CO_2, and 4 % N_2.

formation pressure (49.8 MPa), the solubility of elemental sulfur drops to 0.076 g/m^3 with the temperature decreasing to 40°C. The elemental sulfur solubility is sensitive to variations of temperature and pressure. The experimental results of sulfur solubility at 98.9°C are compared with Brunner's data at 100°C in **Figure 2B** (Brunner and Woll, 1980). The sour gas mixtures in Brunner's data possess similar gas compositions (20% H_2S, 66% CH_4) with the gas samples from well M1. As seen from **Figure 2B**, the experimental data in this paper are basically consistent with the Brunner's data. The sulfur solubility in the literature is slightly higher than the measured results in this work, the deviations can be well attributed to the slightly higher H_2S content and temperature in Brunner's gas sample than that in this paper.

Chrastil Model Fitting

Chrastil derived solubility correlation of solids and liquids in supercritical gases base on the law of mass action (Chrastil, 1982). Chrastil model was used to study the solubility of various food additives in supercritical CO_2 fluids in the early days. Subsequently, Roberts (Roberts, 1997) used the Chrastil solubility prediction model for the first time to study the solubility of elemental sulfur in sour gases containing H_2S. By fitting the experimental data in the literature, the Chrastil prediction model for the solubility of elemental sulfur in sour gases was obtained. Since then, the Chrastil solubility prediction model has been widely used in the fitting of existing sulfur solubility experimental data, and the elemental sulfur solubility prediction model suitable for different temperatures and pressures and different gas components has been obtained (Eslamimanesh et al., 2011a; Hu et al., 2014; Guo and Wang, 2016). The expressions of this correlation are as follows, the detailed derivation process of this correlation and coefficients can be found in the Chrastil's paper (Chrastil, 1982):

$$c = \rho^k e^{(a/T+b)} \tag{2}$$

$$a = \frac{\Delta H}{R} \tag{3}$$

$$b = \ln(M_A + kM_B) + q - k\ln M_B \tag{4}$$

Where ρ is gas density, kg/m^3; T is temperature, K; k is an association number, which denotes a solute A associates with k molecules of a gas B to form one molecule of a solvato complex AB_k in equilibrium with the system (Chrastil, 1982); a and b are constant coefficients; ΔH is the total reaction heat, kJ/mol; R is gas constant, 8.314 J·mol^{-1}·K^{-1}; M_A、M_B are the molecular weights of the solute and of the gas, correspondingly; q is a constant. Subsequently, Roberts obtained the constant coefficients of the expression by fitting experimental data (Roberts, 1997):

$$c = \rho^4 e^{(-4666/T-4.5711)} \tag{5}$$

However, Roberts's model has a limited applicability due to the temperature and pressure range and gas composition. Consequently, Hu proposed a segmentation fitting method according to different gas density ranges by using published data (Hu et al., 2014). Meanwhile, the three coefficients in **Eq. 1** are obtained according to the above fitting method using this experiment data, The fitting process and method are detailed in Hu's article (Hu et al., 2014), the results are compared and shown in **Figure 3A,B** and **Table 1**. As seen from **Figure 3A,B** and **Table 1**, the chrastil-type model fitted in this paper has a comparatively well prediction effect, while the predicted results of the Roberts's and Hu's models deviate seriously from the experiment data, which indicates the values of coefficients a and b have a great influence on the predicted solubility results due to the temperature and pressure conditions and different components of the sour gas mixtures.

The association number k will change with the system temperature and pressure. As the temperature increases at a constant pressure, the molecular thermal motion becomes more violent, and the association number k decreases; when the temperature is a constant and the pressure increases, the molecular distance is shortened, the chance of intermolecular

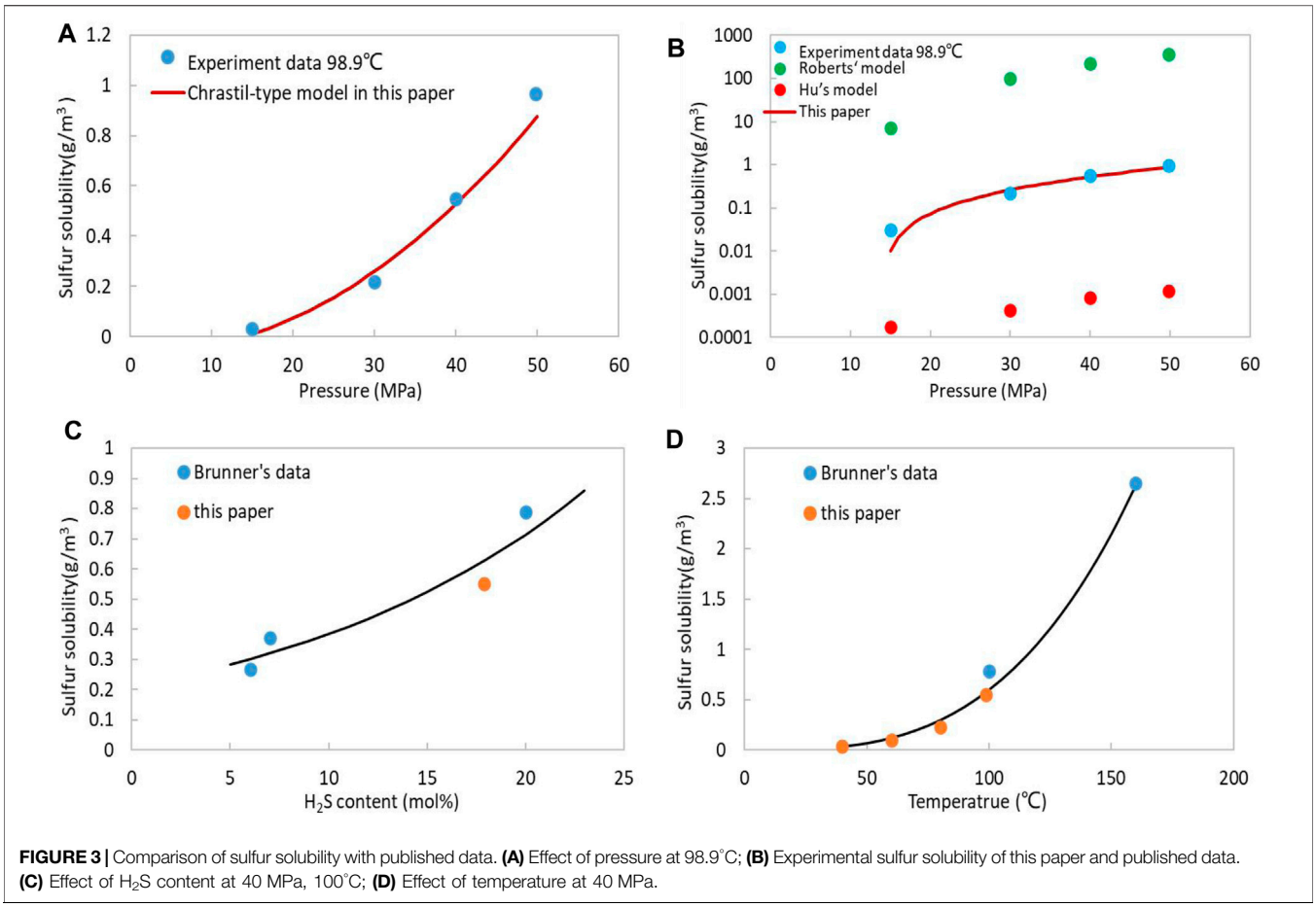

FIGURE 3 | Comparison of sulfur solubility with published data. **(A)** Effect of pressure at 98.9°C; **(B)** Experimental sulfur solubility of this paper and published data. **(C)** Effect of H_2S content at 40 MPa, 100°C; **(D)** Effect of temperature at 40 MPa.

collisions increases, and the association number k increases. ΔH will change accordingly with the association number k. Therefore, the practice of treating k, a, and b as constants will inevitably lead to larger deviations. In order to improve the accuracy of the model, it is necessary to obtain the values of k, a, and b within a specific range of temperature, pressure, and gas composition.

H_2S Content and Temperature

In order to investigate the influence of H_2S content on the solubility of elemental sulfur, the sulfur solubility data at 40 MPa and 100°C in the published literature (Brunner and Woll, 1980) were compared with the measured results of sour gas mixtures from M1 well at 40 MPa and 98.9°C, as shown in **Figure 3B**. The results show that under the same pressure and temperature conditions, as the molar content of H_2S increases, the dissolved elemental sulfur content in the sour gas mixtures increases. The experimental results in this paper are in good agreement with the published experimental data.

Similarly, the influence of temperature on the solubility of elemental sulfur is also investigated. The sulfur solubility data of the sour gas mixtures at 40 MPa and 100–160°C in the published literature (Brunner and Woll, 1980) were compared with the measured results of sour gas mixtures from M1 well at 40 MPa and 40–98.9°C, as shown in **Figure 3C**. The H_2S molar content of the sour gas mixtures in Brunner's work is 20%, which is close to the H_2S content of the sour gas mixtures in this work. The results show that under the same pressure, as the temperature increases, the dissolved elemental sulfur content in the sour gas mixtures increases. The experimental results also show good consistency with Brunner's data.

CONCLUSION

In this study, the elemental sulfur solubility was measured by the static method within sour gas mixtures samples from M1 well in Sichuan Basin. The results show that the experimental data in this work show good agreement with the published results. The sulfur solubility increases with increasing pressure and temperature. At the same pressure and temperature conditions, the sulfur solubility increases as the H_2S molar content increases. The reported chrastil-type model with coefficients fitted by the measured results can well predict the sulfur solubility of gas sample from M1 well, while the presented chrastil-type formulas with documented coefficients fail to obtain reasonable prediction results. Owing to the great influence of temperature on sulfur solubility, wellbore electric heating can be utilized to prevent sulfur deposition and plugging in the wellbore, and improve sulfur recovery in the middle-late stage of sour gas reservoir development.

DATA AVAILABILITY STATEMENT

The original contributions presented in the study are included in the article/Supplementary Material, further inquiries can be directed to the corresponding author.

AUTHOR CONTRIBUTIONS

RZ: Data creation, Formal analysis, Writing-original draft, Writing-review and editing, Funding acquisition. SG: Data creation, Visualization, Writing-review and editing. LH: Conceptualization, Project administration, Supervision, Writing-review and editing. DZ: Conceptualization, Funding acquisition, Project administration. TL: Investigation, Methodology, Writing-original draft. GZ: Formal analysis, Validation.

ACKNOWLEDGMENTS

The financial supports of National Natural Science Foundation of China (U19B6003) are acknowledged. The helpful comments and suggestions by the reviewers are greatly appreciated.

REFERENCES

Aminian, Z. N. (2011). Predicting the Sulfur Precipitation Phenomena during the Production of Sour Natural Gas by Using an Artificial Neural Network. *Petrol. Sci. Technol.* 29, 401. doi:10.1080/10916460903394052

Bemani, A., Baghban, A., and Mohammadi, A. H. (2020). An Insight into the Modeling of Sulfur Content of Sour Gases in Supercritical Region. *J. Pet. Sci. Eng.* 184, 106459. doi:10.1016/j.petrol.2019.106459

Bian, X. Q., Du, Z. M., Guo, X., Tang, Y., and Yang, X. F. (2010). Measurement of the Solubility of Sulfur in Natural Gas with High H_2S Content. *Nat. Gas Ind.* 30, 57–58. doi:10.3787/j.issn.1000-0976.2010.12.014

Bian, X. Q., Zhang, L., Du, Z. M., Chen, J., and Zhang, J. Y. (2018). Prediction of Sulfur Solubility in Supercritical Sour Gases Using Grey Wolf Optimizer-Based Support Vector Machine. *J. Mol. Liq.* 261, 431. doi:10.1016/j.molliq.2018.04.070

Brunner, E., Place, M. C., Jr., and Woll, W. H. (1988). Sulfur Solubility in Sour Gas. *J. Pet. Technol.* 40 (12), 1587–1592. doi:10.2118/14264-pa

Brunner, E., and Woll, W. (1980). Solubility of Sulfur in Hydrogen Sulfide and Sour Gases. *SPE J.* 20 (5), 377–384. doi:10.2118/8778-pa

Cézac, P., Serin, J.-P., Reneaume, J.-M., Mercadier, J., and Mouton, G. (2008). Elemental sulphur Deposition in Natural Gas Transmission and Distribution Networks. *J. Supercrit. Fluids* 44, 115–122. doi:10.1016/j.supflu.2007.11.005

Cézac, P., Serin, J. P., Mercadier, J., and Mouton, G. (2007). Modelling Solubility of Solid sulphur in Natural Gas. *Chem. Eng. J.* 133 (1-3), 283–291. doi:10.1016/j.cej.2007.02.014

Chen, H., Liu, C., and Xu, X. (2019). Molecular Dynamic Simulation of Sulfur Solubility in H2S System. *Int. J. Mod. Phys. B* 33, 1950052. doi:10.1142/s0217979219500528

Chen, H., Liu, C., Xu, X., and Zhang, L. (2020). A New Model for Predicting Sulfur Solubility in Sour Gases Based on Hybrid Intelligent Algorithm. *Fuel* 262, 116550. doi:10.1016/j.fuel.2019.116550

Chesnoy, A. B., and Pack, D. J. (1997). S8 Threatens Natural Gas Operations. *Oil Gas J.* 95 (17), 74–78.

Chrastil, J. (1982). Solubility of Solids and Liquids in Supercritical Gases. *J. Phys. Chem.* 86, 3016–3021. doi:10.1021/j100212a041

Cloarec, E., Serin, J.-P., Cézac, P., Contamine, F., Mercadier, J., Louvat, A., et al. (2012). Experimental Studies of Solubility of Elemental Sulfur in Methane at 363.15 K for Pressure Ranging from (4 to 25) MPa. *J. Chem. Eng. Data* 57, 1222–1225. doi:10.1021/je201091g

Davis, P. M., Lau, C. S., and Hyne, J. B. (1993). Data on the Solubility of Sulfur in Sour Gases. *ASRL* 2, 3–4.

Eslamimanesh, A., Gharagheizi, F., Mohammadi, A. H., and Richon, D. (2013). Assessment Test of Sulfur Content of Gases. *Fuel Process. Techn.* 110, 133–140. doi:10.1016/j.fuproc.2012.12.005

Eslamimanesh, A., Mohammadi, A. H., and Richon, D. (2011). Determination of Sulfur Content of Various Gases Using Chrastil-type Equations. *Ind. Eng. Chem. Res.* 50 (12), 7682–7687. doi:10.1021/ie200187v

Eslamimanesh, A., Mohammadi, A. H., and Richon, D. (2011). Thermodynamic Consistency Test for Experimental Data of Sulfur Content of Hydrogen Sulfide. *Ind. Eng. Chem. Res.* 50, 3555–3563. doi:10.1021/ie1017332

Fu, L., Hu, J., Zhang, Y., and Li, Q. (2019). Investigation on Sulfur Solubility in Sour Gas at Elevated Temperatures and Pressures with an Artificial Neural Network Algorithm. *Fuel* 262, 116541. doi:10.1016/j.fuel.2019.116541

Gu, M. X., Li, Q., Zhou, X. Y., Chen, Y. D., and Guo, T. M. (1993). Solubility of Solid Sulfur in Super/near-Critical H_2S-Containing Sour Fluid Mixtures (I) Experimental Investigation. *J. Chem. Ind. Eng. (China)* 44 (3), 315–320.

Guo, X., and Wang, Q. (2016). A New Prediction Model of Elemental Sulfur Solubility in Sour Gas Mixtures. *J. Nat. Gas Sci. Eng.* 31, 98–107. doi:10.1016/j.jngse.2016.02.059

Heidemann, R. A., Phoenix, A. V., Karan, K., and Behie, L. A. (2001). A Chemical Equilibrium Equation of State Model for Elemental Sulfur and Sulfur-Containing Fluids. *Ind. Eng. Chem. Res.* 40 (9), 2160–2167. doi:10.1021/ie000828u

Hu, J.-H., Zhao, J.-Z., Wang, L., Meng, L.-Y., and Li, Y.-M. (2014). Prediction Model of Elemental Sulfur Solubility in Sour Gas Mixtures. *J. Nat. Gas Sci. Eng.* 18, 31–38. doi:10.1016/j.jngse.2014.01.011

Huang, L., Khoshnood, A., and Firoozabadi, A. (2020). Swelling of Kimmeridge Kerogen by normal-alkanes, Naphthenes and Aromatics. *Fuel* 267, 117155. doi:10.1016/j.fuel.2020.117155

Huang, L., Zhou, W., Xu, H., Wang, L., Zou, J., and Zhou, Q. (2021). Dynamic Fluid States in Organic-Inorganic Nanocomposite: Implications for Shale Gas Recovery and CO2 Sequestration. *Chem. Eng. J.* 411, 128423. doi:10.1016/j.cej.2021.128423

Kadoura, A., Salama, A., Sun, S., and Sherik, A. (2013). An NPT Monte Carlo Molecular Simulation-Based Approach to Investigate Solid-Vapor Equilibrium: Application to Elemental Sulfur-H2s System. *Proced. Comput. Sci.* 18, 2109–2116. doi:10.1016/j.procs.2013.05.381

Karan, K., Heidemann, R. A., and Behie, L. A. (1998). Sulfur Solubility in Sour Gas: Predictions with an Equation of State Model. *Ind. Eng. Chem. Res.* 37 (5), 1679–1684. doi:10.1021/ie970650k

Kennedy, H. T., and Wieland, D. R. (1960). Equilibrium in the Methane-Carbon Dioxide-Hydrogen Sulfide-Sulfur System. *AIME* 219, 166–169. doi:10.2118/1351-g

Kuo, C. H. (1972). On the Production of Hydrogen Sulfide-Sulfur Mixtures from Deep Formations. *J. Pet. Technol.* 24 (09), 1142–1146. doi:10.2118/3838-pa

Luo, Q., Tu, Z. Q., and Ji, Z. L. (2012). Influencing Factors of the Sulfur Content Measurement in High-Sulfur Natural Gas (In Chinese). *Nat. Gas Ind.* 32, 95–98. doi:10.3787/j.issn.1000-0976.2012.11.022

Mehrpooya, M., Mohammadi, A. H., and Richon, D. (2010). Extension of an Artificial Neural Network Algorithm for Estimating Sulfur Content of Sour Gases at Elevated Temperatures and Pressures. *Ind. Eng. Chem. Res.* 49 (1), 439–442. doi:10.1021/ie900399b

Mohammadi, A. H., and Richon, D. (2008). Estimating Sulfur Content of Hydrogen Sulfide at Elevated Temperatures and Pressures Using an Artificial Neural Network Algorithm. *Ind. Eng. Chem. Res.* 47 (21), 8499–8504. doi:10.1021/ie8004463

Roberts, B. E. (2017). Flow Impairment by Deposited Sulfur - A Review of 50 Years of Research. *J. Nat. Gas Eng.* 2 (1), 84–105. doi:10.7569/jnge.2017.692504

Roberts, B. E. (1997). The Effect of Sulfur Deposition on Gas Well Inflow Performance. *SPE Reserv. Eng.* 12 (2), 118–123. doi:10.2118/36707-pa

Roof, J. G. (1971). Solubility of Sulfur in Hydrogen Sulfide and in Carbon Disulfide at Elevated Temperature and Pressure. *SPE J. Pet. Technol.* 11 (3), 272–276. doi:10.2118/3264-pa

Serin, J. P., Jay, S., Cezac, P., Contamine, F., Mercadier, J., Arrabie, C., et al. (2010). Experimental Studies of Solubility of Elemental sulphur in Supercritical Carbon Dioxide. *J. Supercrit. Fluid* 53 (1), 12–16. doi:10.1016/j.supflu.2010.02.010

Smith, J. J., Jensen, D., and Meyer, B. (1970). Liquid Hydrogen Sulfide in Contact with Sulfur. *J. Chem. Eng. Data* 15 (1), 144–146. doi:10.1021/je60044a022

Sun, C.-Y., and Chen, G.-J. (2003). Experimental and Modeling Studies on Sulfur Solubility in Sour Gas. *Fluid Phase Equilibria* 214, 187–195. doi:10.1016/s0378-3812(03)00351-0

Swift, S. C., and Manning, F. S. (1976). Sulfur-bearing Capacity of Hydrogen Sulfide Gas. *SPE J. Pet. Technol.* 16 (2), 57–64. doi:10.2118/5669-pa

Yang, X. F., Huang, X. P., and Zhong, B. (2009). Experimental Test and Calculation Methods of Elemental Sulfur Solubility in High Sulfur Content Gas. *Nat. Gas Geosci.* 20 (3), 416–419.

Zeng, P., Zhao, J. Z., and Li, Z. P. (2005). Study on the Mechanism of Sulfur Solubility in Natural Gas. *J. Southwest. Pet. Inst.* 27 (4), 67–69. doi:10.3863/j.issn.1674-5086.2005.01.018

Conflict of Interest: Author RZ, SG, DZ, and TL were employed by SINOPEC. The remaining author declares that the research was conducted in the absence of any commercial or financial relationships that could be construed as a potential conflict of interest.

Publisher's Note: All claims expressed in this article are solely those of the authors and do not necessarily represent those of their affiliated organizations, or those of the publisher, the editors and the reviewers. Any product that may be evaluated in this article, or claim that may be made by its manufacturer, is not guaranteed or endorsed by the publisher.

APPENDIX A THE EXPERIMENTAL SUMMARY FOR DETERMINATION OF SULFUR SOLUBILITY.

Researcher	Time	Temperature (K)	Pressure (MPa)	Gas components
Kennedy and Wieland, (1960)	1960	338.71–394.26	6.89–41.35	Pure CH_4, CO_2, H_2S and sour gas mixtures with different proportions
Roof, (1971)	1971	316.46–383.15	7–31.15	H_2S
Swift and Manning, (1976)	1976	394–450	34.5–138	H_2S
Brunner and Woll, (1980)	1980	373.15–433.15	10–60	H_2S and H_2S-CO_2-CH_4-N_2 mixtures
Brunner et al. (1988)	1988	398–486	6.7–155	H_2S-CO_2-CH_4-N_2-C_2H_6-C_4H_{10} mixtures
Davis et al. (1993)	1992	333–425	5–55	Sour gas mixtures with different proportions
Gu et al. (1993)	1993	353.2–383.3	20.52–50.17	Pure CH_4、CO_2、H_2S and mixtures
Sun and Chen, (2003)	2003	303.2–363.2	20–45	Pure CH_4、CO_2、H_2S and mixtures
Zeng et al. (2005)	2005	353.15–433.15	10–60	H_2S-CO_2-CH_4-N_2-C_2H_6-C_4H_{10}-C_6H_{14} mixtures
Yang et al. (2009)	2009	373.15	16–36	Wellhead gas sample of a gas well (mixtures)
Bian et al. (2010)	2010	336.2–396.6	10–55.2	Wellhead gas sample of a gas well (mixtures)
Serin et al. (2010)	2010	333.15/393.15	0.93–29.45	CO_2
Cloarec et al. (2012)	2012	363.15	4–25	CH_4

frontiers in Earth Science

ORIGINAL RESEARCH
published: 14 October 2021
doi: 10.3389/feart.2021.735972

Numerical Investigation of Oil–Water Exchange Behaviors in Shale During Post-Fracturing Soaking Periods

Fei Wang, Qiaoyun Chen, Jingchen Zhang, Yingqi Ruan, Ye Zhuang, Jian Zhu and Shicheng Zhang*

State Key Laboratory of Petroleum Resources and Prospecting, China University of Petroleum, Beijing, China

Fracturing fluid imbibition and retention are treated as a main mechanism for oil production from shale reservoirs. However, the oil–water exchange phenomenon during post-fracturing soaking periods has not been thoroughly studied. In this study, a water–oil flow model is built to investigate the water imbibition and oil drainage phenomenon in hydraulically fractured shale. With the developed numerical simulator, the main characteristics of post-fracturing soaking, that is, pressure diffusion, water imbibition, and especially, the oil–water exchange behavior are simulated. Three key time points, that is, oil–water exchange equilibrium, steady exchange efficiency, and oil breakthrough in fracture are found. The oil–water exchange efficiency and exchange volume are also calculated. Moreover, the proposed model is validated by field wellhead pressure dynamics, indicating a relevance of time between the oil–water exchange efficiency and the wellhead pressure falloff derivatives. Finally, the influences of shale permeability, wettability, fracture complexity, and oil viscosity on the oil–water exchange behavior are investigated. Results indicate that the matrix of oil-wet shale almost does not suck water and discharge oil, and only the oil in natural fractures exchanges with the water in hydraulic fractures. The water-wet shale with low permeability, high oil viscosity, and few natural fractures needs extra soaking time to achieve good oil–water exchange performance. The suitable soaking period for the water-wet base case in this study is from 17.25 to 169 days, among which 64 days is the optimal soaking time.

Keywords: shale oil, post-fracturing soaking, oil–water exchange, soaking time, modeling and simulation

OPEN ACCESS

Edited by:
Zhehui Jin,
University of Alberta, Canada

Reviewed by:
Sen Wang,
China University of Petroleum (Huadong), China
Yuliang Su,
China University of Petroleum (Huadong), China

****Correspondence:***
Fei Wang
wangfei@cup.edu.cn

Specialty section:
This article was submitted to Economic Geology, a section of the journal Frontiers in Earth Science

Received: *04 July 2021*
Accepted: *13 August 2021*
Published: *14 October 2021*

Citation:
Wang F, Chen Q, Zhang J, Ruan Y, Zhuang Y, Zhu J and Zhang S (2021) Numerical Investigation of Oil–Water Exchange Behaviors in Shale During Post-Fracturing Soaking Periods. Front. Earth Sci. 9:735972. doi: 10.3389/feart.2021.735972

INTRODUCTION

Compared with conventional oil reservoirs, shale has relatively high clay content and covers a wide range from 16.8 to 70.1% (Yang et al., 2013). The development of shale oil reservoirs heavily relies on multistage hydraulic fracturing technology (Zhou et al., 2019). After the hydraulic fracturing, the initial production of fractured shale oil wells is good, but the stable production period is quite short (Zou et al., 2020). For pursuing a high oil production rate, a long-term well shut-in has gradually been adopted as an effective mode for field practice, instead of flowing back immediately after hydraulic fracturing because it is believed that fracturing fluid imbibition may strengthen and oil–water exchange may happen during the soaking period. Although extended well soaking may intensify fracturing fluid retention, which is proved by field practice and laboratory experiments. After all, sacrificing water recovery for more oil is acceptable.

The investigation of imbibition behavior is mainly based on laboratory experiments and a pore/core scale analysis. In general, fracturing fluid imbibition behavior can be related to many factors, including rock type (Xiong et al., 2013a; Xiong et al., 2013b; Ren et al., 2015), mineral composition (Akin and Kovscek, 1999; Ali Habibi et al., 2015; Ge et al., 2015), pore structure (Liu and Dai, 2008), formation wettability (ZhuJu et al., 2002; Wang et al., 2012), formation temperature (Li et al., 2011; Zhou et al., 2014), the bedding structure (Ren et al., 2015), connate water saturation (Gao and Hu, 2016), formation fluid (Wang, 2000; Wang and Zhang, 2000), and fracturing fluid type (Paktinat et al., 2005; Penny et al., 2005; Li, 2006; Roychaudhuri et al., 2013). Based on the results of experiments, formation wettability is the most important factor for fluid imbibition since it determines the direction of imbibition, and the extent of wettability determines the oil recovery. The contact area affects the imbibition speed, that is, the larger the contact area is, the faster the imbibition speed is (ZhuJu et al., 2002). Moreover, fluid properties are critical to the imbibition behavior. The content of polar substance in oil may alter the formation wettability and further change the imbibition behavior (Wang, 2000; Wang and Zhang, 2000). In practice, surfactants are added into the fracturing fluid. The existence of surfactant can reduce the interfacial tension (Li, 2006; Roychaudhuri et al., 2013), making the rock more hydrophilic to enhance the capacity of water suction, while microemulsion as a cleanup additive can make the rock wettability to water from strong to weak and then inhibit the capacity of water suction (Paktinat et al., 2005; Penny et al., 2005). Besides, the porosity and permeability of formation are very important to fluid imbibition. It shows that the capillary pressure increases with the decrease of porosity and permeability, which makes the driving force of imbibition to increase (Liu and Dai, 2008).

Besides the experiment-based pore/core scale analysis, the well/reservoir scale imbibition, and the well shut-in simulation mainly focuses on shale gas reservoirs. Wang et al. (2017a) studied the phenomenon of fluid imbibition under the driving forces of osmosis and capillarity and investigated the influence of imbibition on the microfractures induced by hydraulic fracturing in shale gas reservoirs. Their research result shows that clay minerals have the function of a semipermeable membrane and the capacity of water suction is stronger than organic matter and other minerals. Fakcharoenphal et al. (2013) shows that fracturing fluid imbibition in shale can generate microfractures, and it is related with the physical characteristics of reservoir itself and the composition of fracturing fluids. Roychaudhuri et al. (2013) shows that shale reservoir has the characteristics of mixed wetting, which has an important impact on the fracturing fluid imbibition. Odumabo et al. (2014) shows the relation between imbibition volume and soaking time. It shows that the change of permeability in the invasion area of the fracture surface and the distribution of water saturation near the fracture surface are two important factors affecting the post-fracturing shale gas production. Fakcharoenphol et al. (2014) studied the effect of salinity on the fluid imbibition. It shows that osmotic pressure is an important driving force for fluid imbibition. Wang and Leung (2015) established a triple-porosity two-phase flowback model to study the control mechanism of fracturing fluid retention. Their simulation results show that the initial production rate can be increased by extension of soaking time, but for a long-term production rate, soaking is not helpful. Zhang et al. (2017) established a triple-porosity numerical model for hydraulically fractured shale gas wells, which considers the effects of imbibition, stress sensitivity, and gravity differentiation. Their simulation results show that the spontaneous imbibition rate of fracturing fluids in a tight matrix is very low during the well-soaking process. Although shale reservoir has high capillary force, the fracturing fluid still mainly remains in the fracture and near the fracture area after 100 days of soaking. Their simulation results show that although the long-term soaking increases the initial gas production, the long-term cumulative gas production decreases with the extension of soaking time.

From the perspective of modeling and simulation, water imbibition and oil drainage has not been systematically coupled with different driving mechanisms, such as hydraulic pressure difference, wettability-dominated capillarity, and chemical osmosis. To investigate the oil–water exchange behavior in a well/reservoir scale, we build a fracture-matrix water–oil flow model to simulate the fracturing fluid imbibition and the oil drainage process during the post-fracturing soaking periods. We try to use the numerical simulation results to investigate the efficiency and equilibrium time of oil–water exchange under different shale permeability, wettability, fracture complexity, and oil viscosity conditions, which help to optimize the well-soaking time for hydraulically fractured shale oil wells.

OIL–WATER EXCHANGE MECHANISM MODEL

Mechanism Description

The water–oil exchange phenomenon in hydraulically fractured shale reservoirs involves two-phase fluids, that is, oil and water, and multiple interconnected media, that is, main hydraulic fractures, induced natural fractures, and matrix pores. In the treatment of hydraulic fracturing, a large amount of water is injected into the wellbore, through the perforating hole into the reservoir to open fractures. When the well is shut-in after fracturing, the wellhead will not be injected anymore and the bottom-hole pressure will diffuse in the reservoir. At the same time, 100% water-saturated hydraulic fractures with high-pressure discharge water into the matrix through induced natural fractures and almost oil-statured shale matrix pores suck water, that is, the water imbibition under the potential difference, which includes hydraulic, capillary, and osmotic pressures (Wang et al., 2017b). Simultaneously, the oil in matrix pores is replaced to hydraulic fractures as compensation. **Figure 1** shows a sketch of the oil–water exchange process.

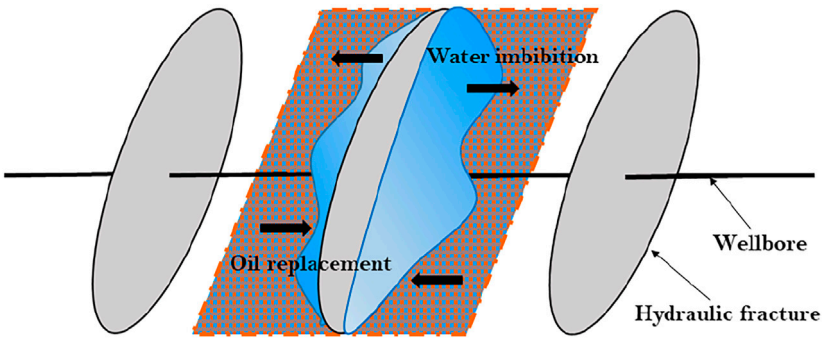

FIGURE 1 | Sketch of oil–water exchange process.

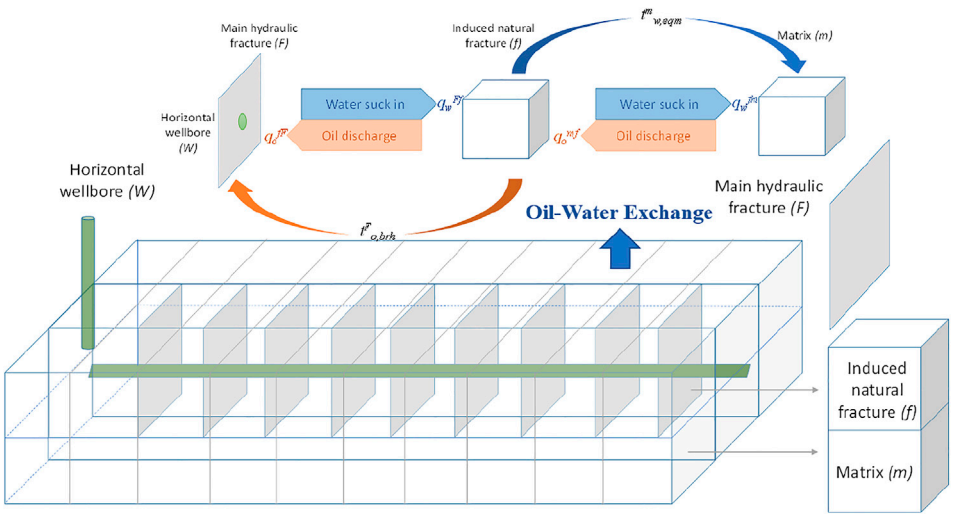

FIGURE 2 | Grid representation and mass transfer of the oil–water exchange model.

Mechanism Model Development

A multi-pore medium comprising of main hydraulic fractures (*F*), induced natural fractures (*f*), and matrix pores (*m*) is proposed for characterizing hydraulically fractured shale reservoirs. The grid representation is exhibited in **Figure 2**. As shown in the figure, the whole medium is separated into two layers, with the lower one representing *m* and the upper one representing *f*. A shape factor (Kazemi et al., 1992) is used to quantify the complexity of *f*. The refined grids with high conductivity in the upper layer are used to characterize *F*, which is an identical transverse fracture with height, width, and length. *F* directly connects to the wellbore (*W*). In the soaking process, water suck in and oil discharge occurs between two adjacent porous media, as shown in **Figure 2**. q_w^{Ff} and q_w^{fm} represent the water exchange between *F* and *f* and between *f* and *m*, respectively, while q_o^{fF} and q_o^{mf} represent the oil exchange between *F* and *f* and between *f* and *m*, respectively. The water–oil exchange in this triple-porosity system is a hydrodynamic equilibrium process. It takes time for oil breakthrough in hydraulic fractures ($t_{o,brh}^F$) and water sucking termination in the matrix ($t_{w,eqm}^m$).

MATHEMATICAL SOLUTION

Assumptions made for this study are as follows. 1) Sodium chloride is the only solute and totally dissolves in either formation brine or fracturing fluid; 2) gravity is not considered; 3) mass transfer occurs inside *F*, *f*, *m*, and between the adjacent media; and 4) the system is isothermal. According to the aforementioned physical model and assumptions, a mathematical model is developed as follows.

Oil–Water Flow Model

Following equations describe fluid mass transfer in *F*, *f*, and *m*, respectively. The subscript *j* represents water (*w*) and oil (*o*). *F*

$$\frac{\partial\left(\rho_j\phi^F S_j^F\right)}{\partial t} = -\nabla\left(\rho_j v_j^F\right) + q_j^{WF} - q_j^{F-f}, \tag{1}$$

where ρ_j is density [kg/m^3]; ϕ^F is the porosity of *F* [-]; S_j^F is the fluid saturation in *F* [-]; v_j^F is the velocity in *F* [m/s]; q_j^{WF} is the fluid source sink term [kg/m^2/s]; and q_j^{F-f} is the fluid transfer term

linking F and f, and the flow direction is different between w and o [kg/m^2/s].

$$v_j^F = -\frac{k^F k_{rj}^F}{\eta_j}\nabla p_j^F, \tag{2}$$

where $k^F$is absolute permeability of F [m^2]; $k_{rj}^F$is fluid relative permeability of F [-];$p_j^F$is hydraulic pressure in F [Pa]; and $\eta_j$is viscosity [Pa·s].

$$q_j^{F-f} = \frac{\alpha_1 \rho_w k^F k_{rj}^F h}{\eta_j}\left(p_j^F - p_j^f\right), \tag{3}$$

where $\alpha_1$is the shape factor between F and f, and the expression and derivation of $\alpha_1$is presented in **Supplementary Appendix SA** [m^{-2}] and $p_j^f$is hydraulic pressure in f, and when $j = w$, capillary pressure is considered [Pa].

$$q_j^{WF} = \frac{\alpha_3 \rho_w k^F k_{rj}^F h}{\eta_j B_j}\left(p_{wf} - p_j^F\right), \tag{4}$$

where $\alpha_3$is the shape factor which links F and W, and the expression and derivation of $\alpha_3$is presented in **Supplementary Appendix SA** [m^{-2}] and$B_j$is the fluid formation volume factor [-]; and $p_{wf}$is the following pressure of bottom-hole [Pa].

$$h\frac{\partial\left(\rho_j \phi^f S_j^f\right)}{\partial t} = -\nabla\left(h\rho_j v_j^f\right) + q_j^{F-f} - q_j^{f-m}, \tag{5}$$

where $\phi^f$is the porosity of f [-];$S_j^f$is the fluid saturation in f [-];v_j^f is the velocity in f [m/s]; and $q_j^{f-m}$is the fluid transfer term linking f and m, and the flow direction is different between w and o [kg/m^2/s].

$$v_j^f = -\frac{k^f k_{rj}^f}{\eta_j}\nabla p_j^f, \tag{6}$$

where k^f is the absolute permeability of f [m^2] and $k_{rj}^f$is the fluid relative permeability of f [-].

$$q_j^{f-m} = \frac{\alpha_2 \rho_j k^f k_{rj}^f h}{\eta_j}\left(p_j^f - p_j^m + p_\pi\right), \tag{7}$$

where$\alpha_2$is the shape factor linking f and m, and the expression of $\alpha_2$is presented in **Supplementary Appendix SA** [m^{-2}]; $p_j^m$is the hydraulic pressure in m, and when $j = w$, capillary pressure is considered [Pa]; and $p_\pi$is the osmotic pressure only for w [Pa].

$$p_\pi = \lambda\frac{RT}{V_W}\ln\frac{x_f}{x_m}, \tag{8}$$

where $V_w$is the molar volume of water [m^3/mol]; $T$is temperature [K]; $R$is ideal gas constant [J/(mol·K)]; $\lambda$is membrane efficiency [-]; $x_f$is the water activity of f [-]; and $x_m$is the water activity of m [-] m

$$h\frac{\partial\left(\rho_j \phi^m S_j^m\right)}{\partial t} = -\nabla\left(h\rho_j v_j^m\right) + q_j^{f-m}, \tag{9}$$

where $\phi^m$is the porosity of m [-]; $S_j^m$is the fluid saturation in m [-]; and $v_j^m$is the velocity in m [m/s].

$$v_j^m = -\frac{k^m k_{rj}^m}{\eta_j}\nabla\left(p_j^m - p_\pi^m\right), \tag{10}$$

where $k^m$is the absolute permeability of m [m^2] and $k_{rj}^m$is the fluid relative permeability of m [-].

Model Coupling and Variables Solution

Closed boundary is designed for outer boundary, while initial condition is set according to the end of injection process. The mathematical model is solved with the use of the finite difference method with the detailed algorithm presented in **Supplementary Appendix SB**. After the model solution, four key variables are obtained, that is, q_w^{Ff}, q_w^{fm}, q_o^{mf}, and q_o^{fF}, after which oil–water exchange efficiency and volume dynamics with soaking time can be calculated.

The oil–water exchange efficiency, which is the water imbibition flux divided by the oil drainage flux, can be calculated below.

Oil drainage efficiency of the fracture is as follows:

$$E_{ts}^F = q_o^{fF}/q_w^{Ff}, \tag{11}$$

where q_o^{fF} is the oil exchange between F and f and q_w^{Ff} is the water exchange between F and f.

Oil drainage efficiency of the matrix is as follows:

$$E_{ts}^m = q_o^{mf}/q_w^{fm}, \tag{12}$$

where q_o^{mf} is the oil exchange between f and m and q_w^{fm} is the water exchange between f and m.

The oil–water exchange volume, which is the cumulative flux rate in the soaking period, can be calculated below:

Water sucking volume into the matrix is as follows:

$$Q_w^m = \sum q_w^{fm}\cdot t_s, \tag{13}$$

where t_s is time.

Oil drainage volume into hydraulic fractures is as follows:

$$Q_o^F = \sum q_o^{fF}\cdot t_s, \tag{14}$$

Oil drainage volume into natural fractures is as follows:

$$Q_o^f = \sum q_o^{mf}\cdot t_s - \sum q_o^{fF}\cdot t_s. \tag{15}$$

Three key time points are also determined. The oil–water exchange equilibrium time ($t_{w,eqm}^m$) is the time when $q_w^{fm} = 0$. The steady exchange efficiency time ($t_{ow,std}^F$) is the time when $E_{ts}^F = 1$. The time of oil breakthrough in fracture ($t_{o,brh}^F$) is the time when $q_o^{fF} > 0$.

OIL–WATER EXCHANGE SIMULATION

Simulation Model Description

Numerical simulation of the oil–water exchange is conducted with the use of this model. The length of the horizontal well is 1200 m, the total fracture stages are 15, and

TABLE 1 | The simulation parameters (Fritz and Marine, 1983; Cheng et al., 2009; Fakcharoenphol et al., 2014; Wang et al., 2020).

Variable	Value	Variable	Value
Initial reservoir pressure, MPa	38	Initial water saturation	0.48
Reservoir temperature, K	388	Matrix porosity	0.078
Hydraulic fracture porosity	0.3	Matrix permeability, md	0.001
Hydraulic fracture conductivity, md·m	20	Oil density, kg/m^3	777
Water density, kg/m^3	1000	Oil viscosity, cp	0.36
Water viscosity, cp	0.81	Oil compressibility, MPa^{-1}	8.46 × 10^{-4}
Water compressibility, MPa^{-1}	4.6 × 10^{-4}	Natural fracture porosity	0.1
Membrane efficiency	0.3	Natural fracture permeability, md	0.01
Molar volume of water, m^3/mol	18.02 × 10^{-6}	Shape factor α_2, m^{-2}	3

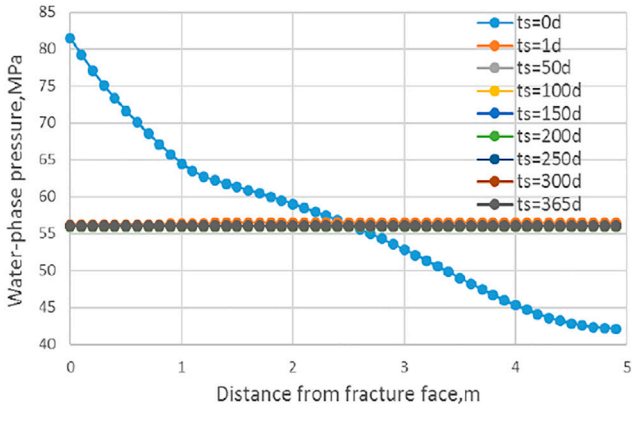

FIGURE 3 | Fracture pressure profile during soaking periods.

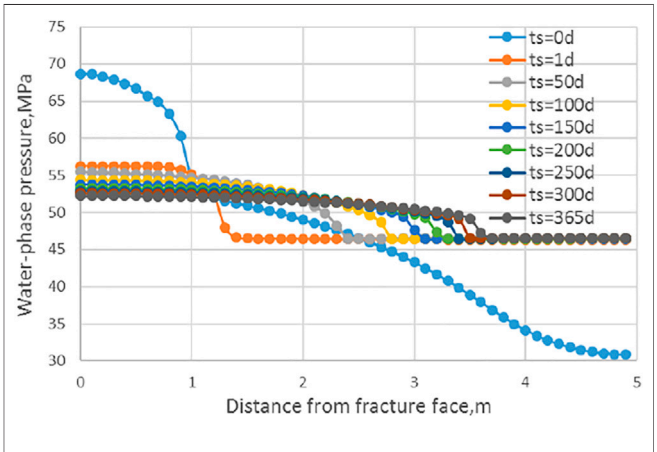

FIGURE 4 | Matrix pressure profile during soaking periods.

the well lies in the reservoir center (1500 m × 560 m×40 m). In every stage, there are four identical transverse hydraulic fractures with a fracture half-length of 140 m and a fracture spacing of 20 m along the horizontal wellbore.

The relative permeability and capillary force (Brooks and Corey, 1964) are used to represent the formation wettability, so the curves of each domain are set on the basis of the typical water-wet formation in the Bakken shale oil basin (Fakcharoenphol et al., 2014). The porosity and permeability of the fracture system are assigned according to Aguilera chart of compressibility coefficients (Aguilera, 1999). Other parameters input are detailed in **Table 1**. The fracturing fluid pumping scheme is simulated as the injection of water with pressure-dependent fracture porosity curve increases. The results of saturation as well as fluid pressure are input as initial conditions for the following 1 year soaking simulation.

Simulation Results of Pressure and Saturation Fields

Figures 3, **4** display the evolution of pressure profiles during the soaking periods in the fracture and the matrix, respectively. Results shows that during the well soaking, the water phase pressure inside and near the hydraulic fracture declines, while the distant pressure in the natural fracture and the matrix increases. That is a typical bottom-hole pressure diffusion and reservoir energy storage phenomena in soaking periods.

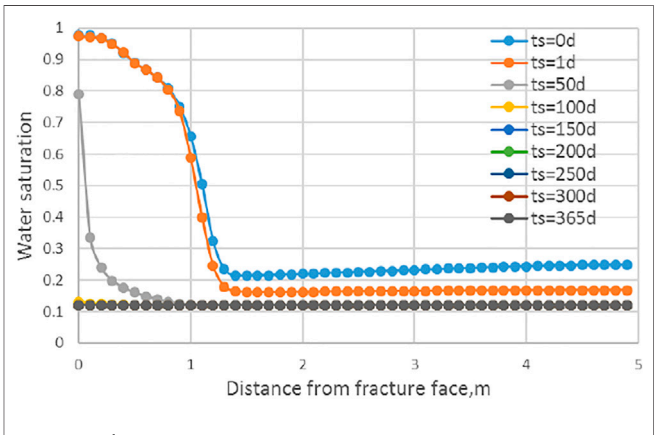

FIGURE 5 | Fracture saturation profile during soaking periods.

Figures 5, **6** display the evolution of saturation profiles during the soaking periods in the fracture and the matrix, respectively. It shows that during the well-soaking process, the water saturation in the fracture decreases, while the distant water saturation in the matrix increases continually. That is a typical water imbibition phenomenon in soaking periods.

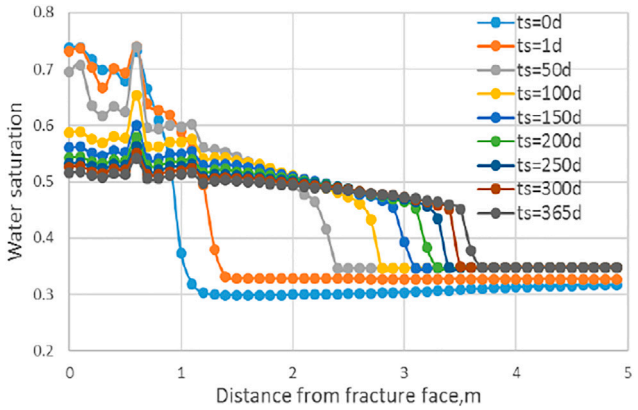

FIGURE 6 | Matrix saturation profile during soaking periods.

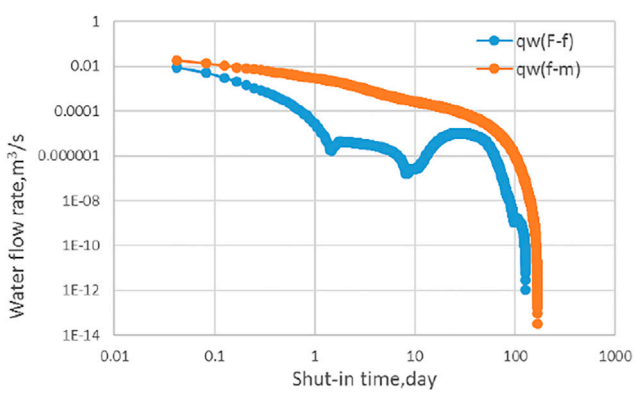

FIGURE 7 | Water fluxes with soaking time.

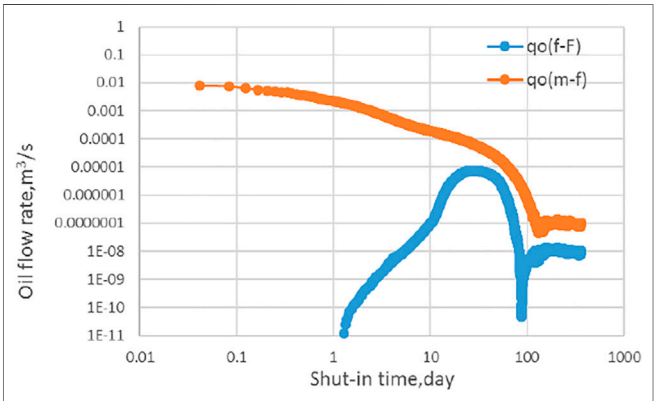

FIGURE 8 | Oil fluxes with soaking time.

Simulation Results of Oil–Water Fluxes

Figures 7, **8** display the water and oil fluxes among *F*, *f*, and *m*, respectively, during soaking periods. It indicates that *F* discharges water to *f*, while *m* sucks water from *f* and discharges oil into the fracture system. The end time of *F* discharging water is about the 110th day and the imbibition equilibrium time of *m* is about 169 days. The oil breakthrough time is about 1.29 days.

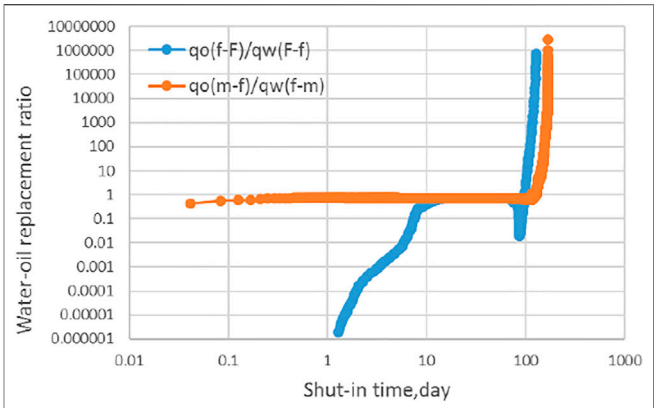

FIGURE 9 | Water–oil exchange efficiency with soaking time.

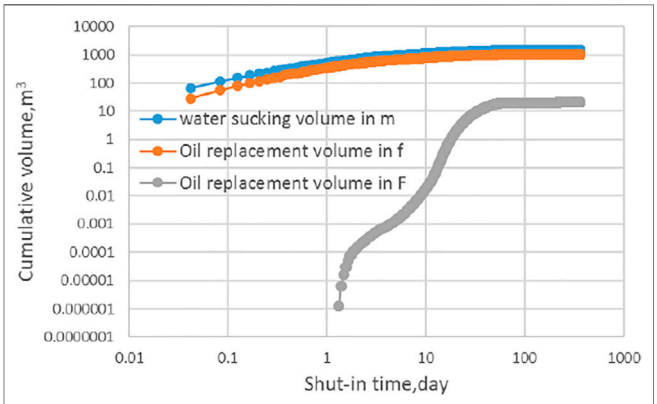

FIGURE 10 | Water–oil exchange volume with soaking time.

As shown in **Figure 9**, the simulated oil drainage efficiency of the fracture system shows a hump trend in the first several weeks, while the exchange efficiency of the matrix system shows a slightly downward trend. The maximum values of exchange efficiency occur at the end time of *F* discharging water and *m* sucking water, respectively. The steady exchange efficiency of *F* occurs at the soaking time of 17.25 days and lasts to 64 days, during which the value of exchange efficiency is 0.805. **Figure 10** shows the evolution of water–oil exchange volumes with soaking time. It indicates that the three volumes of water sucking into *m*, oil drainage into *F*, and *f* all increase with soaking time, but the increment tends to slow down from the 64th day on. At the end of 1 year soaking, there are 1486 m^3 of water sucking into the matrix and 1056 m^3 of oil being replaced into the fracture system (21 m^3 in *F* and 1035 m^3 in *f*).

Simulation Results of Bottom-Hole Flowing Pressure Dynamics

Figure 11A displays the simulated bottom-hole flowing pressure dynamics of the base case during 1 year soaking. To describe the

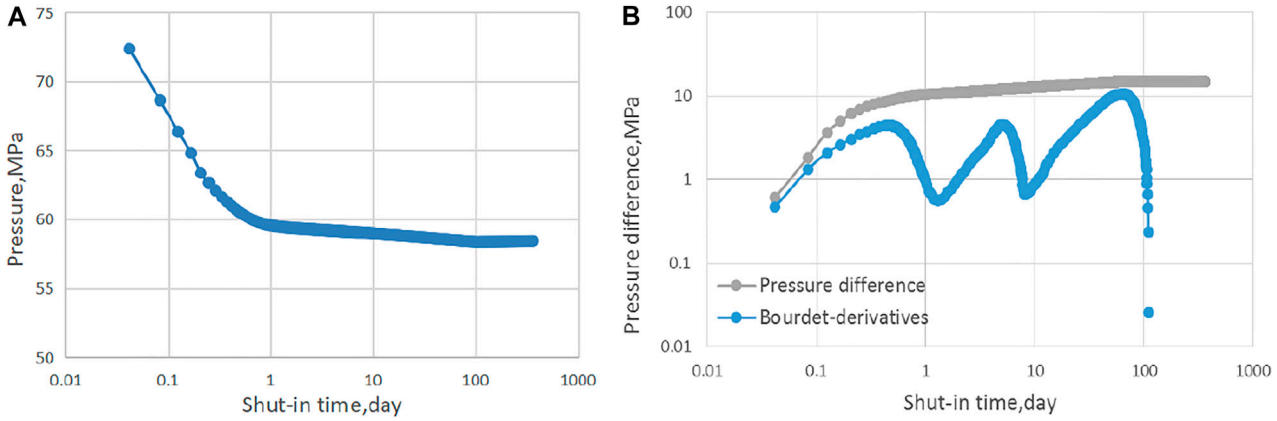

FIGURE 11 | The simulated pressure falloff dynamics: **(A)** bottom-hole flowing pressure and **(B)** pressure falloff and derivatives.

water–oil flow dynamics, pressure falloff analysis theory is applied. **Figure 11B** displays the calculated pressure falloff and Bourdet derivatives. The Bourdet derivatives show a W-shaped curve. The first derivative rising stage in W-shaped derivative curve starts from 1.29 days, corresponding to the simulated oil breakthrough time $t^F_{o,brh.}$ In the later stage, the fluctuations of the derivative curve, like the inflection points at 5.6 and 8.7 days, are consistent with the trend change points on the oil drainage efficiency curve of the hydraulic fracture, that is, the blue curve shown in **Figure 9**. The steady exchange efficiency of F, which occurs from 17.25 to 64 days, is reflected by a constant slope of the second derivative rising stage in the W-shaped derivative curve. After soaking for 64 days, the pressure drop is very small, which exhibits the derivative curve falling. Until soaking 110 days, there is no pressure drop, and the derivative curve drops to zero.

Model Validation

The fluid mass transfer between different media and the pressure of these media are difficult to monitor, because monitoring techniques in the soaking period are limited. Therefore, the wellhead or bottom-hole pressure falloff is the only index that can be used to validate the model.

Shale formation C is characterized by the following reservoir properties: initial pressure = 38 MPa; effective thickness = 10~40 m; permeability = 0.001~0.01 md; porosity = 0.07~0.11; and induced natural fracture density = 0.16~0.25 m^{-2}. The induced natural fracture density is obtained from the field report. It is converted to the α_2 in the model (α_2 = 2.5~5 m^{-2}) based on previous studies (Kazemi et al., 1992; Yan and Mi, 2017). This formation is stimulated by hydraulic fracturing treatment for commercial oil production. The volume of fracturing fluid injected to each well ranges from 7,920 to 6,3589 m^3; the volume of proppant added to each well ranges from 440 to 4,550 m^3; the fracture stages for each well range from 5 to 36. The wells in this formation are shut-in from 19 to 61 days after stimulation. During the well soaking period, the wellhead pressure is monitored continuously. The wellhead pressure records of 10 wells during post-fracturing soaking periods are shown in **Figure 12A**. The Bourdet derivatives of recorded wellhead pressure falloff, shown in **Figure 12B**, exhibit the typical W-shaped curves, which are consistent with our simulated results in **Figure 11B**. Based on the simulated relevance of time between the oil–water exchange and the pressure falloff derivatives above, it can be inferred that oil breakthrough already happens for most of wells since the first derivative rising stage in their W-shaped derivative curves exists from the initial 3 days recorded pressure data. However, the derivative falling after the second rising stage in their W-shaped derivative curves is not prevalent, indicating that water–oil exchange efficiency of well is still in a rising stage and it is still early to open the well for production.

SENSITIVITY ANALYSIS

The influences of shale permeability (k_m), wettability, fracture complexity (α_2), and oil viscosity (μ_o) on the oil–water exchange behavior are investigated. The evaluation indicators include oil breakthrough time ($t^F_{o,brh}$), steady exchange efficiency time ($t^F_{ow,std}$), exchange equilibrium time ($t^m_{w,eqm}$), and water–oil exchange efficiency volumes (Q^F_o, Q^f_o, and Q^m_w). The oil–water relative permeability and capillary pressure curves for the sensitivity analysis of oil-wet shale formation are assigned below (Wang, 2000; Li, 2006).

Figure 13 shows the times of imbibition equilibrium, oil breakthrough, and steady exchange efficiency with different shale prosperities during well soaking. It indicates that μ_o increasing from 0.36 to 1.62 causes $t^F_{o,brh}$, $t^F_{ow,std}$, and $t^m_{w,eqm}$ to increase, while both α_2 increasing from 0.03 to 10 and k_m increasing from 0.001 to 0.01 cause $t^F_{o,brh}$, $t^F_{ow,std}$, and $t^m_{w,eqm}$ to decrease. By contrast to the water-wet base case, the oil-wet case shows a shorter imbibition equilibrium time ($t^m_{w,eqm}$ = 0.25 days) and a longer oil breakthrough time ($t^F_{o,brh}$ = 1.75 days). The steady exchange efficiency for the oil-wet case is about 0.01, which is far below that of the water-wet base case.

Figure 14 shows the 1-year oil–water exchange volumes with different shale prosperities. The simulation results indicate that μ_o

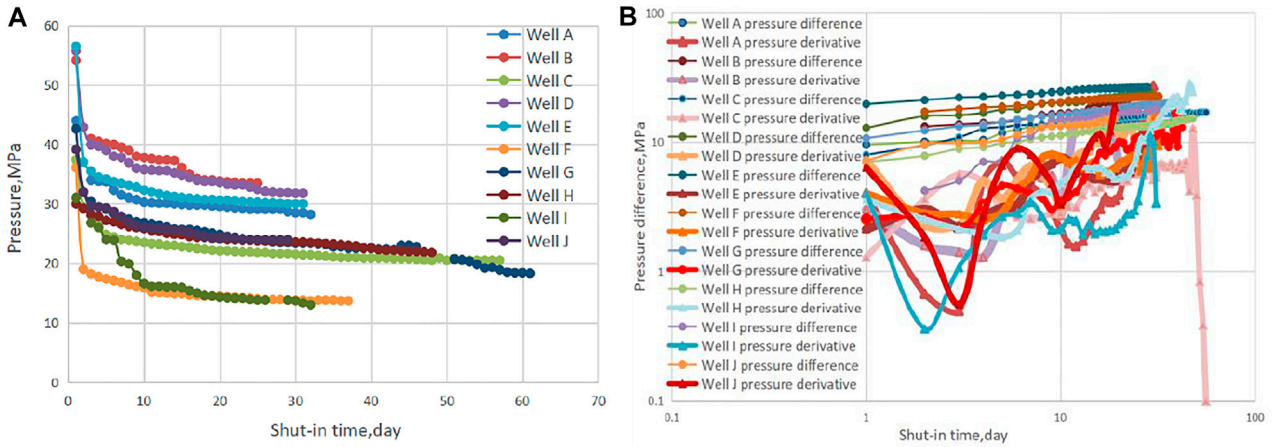

FIGURE 12 | The field recorded pressure falloff dynamics of 10 wells in shale formation C: **(A)** wellhead pressure and **(B)** pressure falloff and derivatives.

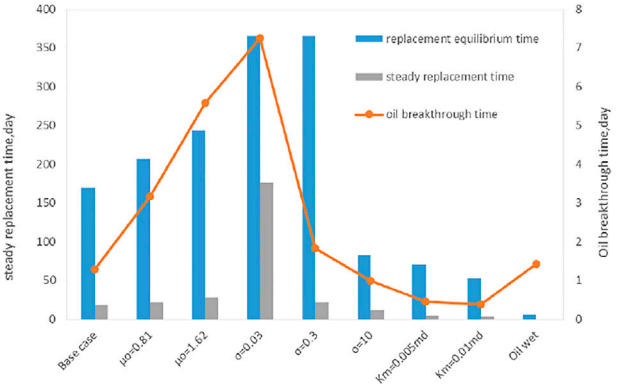

FIGURE 13 | Times of imbibition-replacement equilibrium, oil breakthrough, and steady exchange efficiency with different shale prosperities.

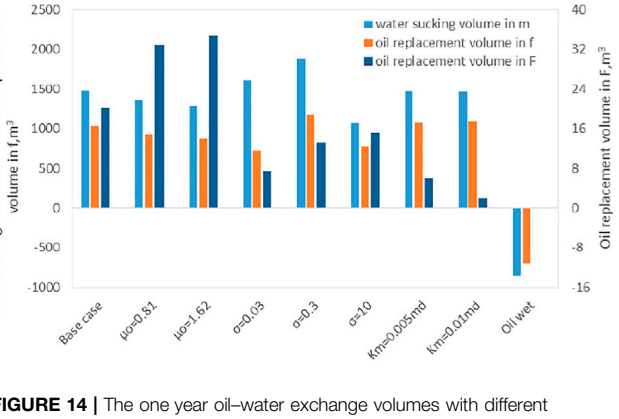

FIGURE 14 | The one year oil–water exchange volumes with different shale prosperities.

increasing from 0.36 to 1.62 causes the $Q_w{}^m$ and $Q_o{}^f$ to decrease, but it causes $Q_o{}^F$ to increase slightly from 21 m^3 to 35 m^3 and k_m increasing from 0.001 to 0.01 causes both the $Q_w{}^m$ and $Q_o{}^F$ to decrease, but it causes $Q_o{}^f$ to increase from 1035 m^3 to 1093 m^3. The α_2 increasing from 0.03 to 10 causes the $Q_w{}^m$, $Q_o{}^f$ and $Q_o{}^F$ to increase first and then decrease, which indicates a complicated imbibition-replacement behavior in the fracture-matrix system. By contrast to the water-wet base case, the oil-wet case shows that the matrix sucks water 36.72 m^3 within the first 0.25 days and then discharges water for 1 year, which leads to a negative water-sucking volume ($Q_w{}^m$ = −851 m^3) and a negative oil discharge volume ($Q_o{}^f$ = −697 m^3). The oil drainage volume in the hydraulic fracture is very small: $Q_o{}^F$ = 0.003 m^3.

Based on our simulation results above, the oil–water exchange behavior during soaking periods can be summarized and used to direct the engineering practice for determination of optimal well-soaking time. For the water-wet base case, the water imbibition and oil drainage occur in the matrix at the beginning of the soaking periods, which exhibits that the water in *F* enters *m* through *f*, but the oil breakthrough in *F* will be delayed to 1.29 days. The water sucking equilibrium of the matrix occurs on the 169th day, which means that the oil–water displacement driven by hydraulic pressure difference ends, after which the water flow into the matrix is driven by spontaneous imbibition. The imbibition equilibrium time of the matrix, that is, 169 days, can be the upper limit soaking time. Before that, the water–oil exchange efficiency shows a hump trend. The imbibition efficiency tends to be stable from 17.25 to 64 days, and the stable value is 0.805. The volume of water–oil exchange from 64 to 169 days is very small, which is mainly the amount that the oil already discharged from *f* and enters *F*. So the suitable soaking period for the water-wet base case is from 17.25 to 169 days, among them 64 days are the optimal soaking time.

From the sensitivity simulation, it can be inferred that the water-wet shale reservoir with low permeability, high oil viscosity, and few natural fractures needs extra soaking time to achieve good oil–water exchange performance. However, for the oil-wet shale reservoir, the matrix almost does not suck water and

discharge oil, but only the oil in natural fractures exchanges with the water in hydraulic fractures. So the water–oil exchange efficiency is very low, and extending the soaking time cannot achieve good oil–water exchange performance.

CONCLUSION

In this study, a water–oil flow mechanism model is built to investigate the water–oil exchange behaviors in hydraulically fractured shale during soaking periods. Some understandings of the key points are summarized below.

1) The simulation results prove the occurrence conditions for water–oil exchange, that is, water-wet rock can make the oil in the matrix replaced by the water in fractures, while for oil-wet rock, the oil in the matrix cannot be replaced out by well soaking and the oil in natural fractures will be further squeezed into matrix pores with the extension of soaking time, resulting in production difficulty.
2) The simulation results reflect the water–oil exchange behavior in water-wet shale, that is, the water imbibition and oil drainage occur in the matrix at the beginning of the soaking periods, but the oil breakthrough will be delayed to 1.29 days. The water-sucking equilibrium in the matrix occurs on the 169th day, which means that the oil–water exchange driven by hydraulic pressure difference ends, after which the water flow into the matrix is driven by spontaneous imbibition.
3) The simulation results indicate that low matrix permeability and high oil viscosity are detrimental to oil–water exchange, which exhibits low exchange efficiency, late oil breakthrough, and longer equilibrium time. On the contrary, the existence of natural fractures is advantageous to oil–water exchange, which is characterized by short imbibition equilibrium time, fast oil breakthrough, and high oil exchange efficiency.
4) Simulation results guide the determination of optimal soaking time. The steady exchange efficiency time ($t^F_{ow,std}$) and imbibition equilibrium time ($t^m_{w,eqm}$) can be the lower and upper limit soaking time, respectively. Among this period, the optimal soaking time can be further determined according to the expected oil discharge rate of the matrix and oil drainage rate of hydraulic fractures.
5) The model simulation results also indicate a relevance of time between the oil–water exchange efficiency of hydraulic fractures and the pressure falloff derivatives. This indication can be used for determining oil–water exchange efficiency of actual wells.

DATA AVAILABILITY STATEMENT

The original contributions presented in the study are included in the article/**Supplementary Material**; further inquiries can be directed to the corresponding author.

AUTHOR CONTRIBUTIONS

Methodology, FW; software, QC; formal analysis, JZ and YR.; data curation, YZ, JZ, and YR; writing—original draft preparation, FW, QC, and YR; writing—review and editing, FW, QC, and YR; and supervision, SZ.

FUNDING

The authors would like to acknowledge the National Natural Science Foundation of China (No. 51974332 and No. U1762210) and Xinjiang TianshanYouth Program (No. 2018Q030) for their financial support.

SUPPLEMENTARY MATERIAL

The Supplementary Material for this article can be found online at: https://www.frontiersin.org/articles/10.3389/feart.2021.735972/full#supplementary-material.

REFERENCES

Aguilera, R. (1999). Recovery factors and reserves in naturally fractured reservoirs. *J. Can. Pet. Technol.* 38, 4. doi:10.2118/99-07-da

Akin, S., and Kovscek, A. R. (1999). *Imbibition studies of low-permeability porous media*. Calgary: Society of Petroleum Engineers. SPE-54590-MS.

Ali Habibi, A., Xu, M., Dehghanpour, H., and Bryan, D. (2015). *Unconventional Resources Conference in the Montney Tight Oil Play*. Calgary: Society of Petroleum Engineers. doi:10.2118/175924-MS

Brooks, R., and Corey, A. (1964). Hydraulic Properties of Porous Media, Hydrol. Pap. No. 3. *Hydrol. Pap.* 3, 892–898.

Cheng, Y., Lee, W. J., and MacVay, D. A. (2009). A New Approach for Reliable Estimation of Hydraulic Fracture Properties Using Elliptical Flow Data in Tight Gas Wells. *SPE Reservoir Eval. Eng.* 12 (2), 254–262. doi:10.2118/105767-pa

Fakcharoenphol, P., Kurtoglu, B., Kazemi, H., Charoenwongsa, S., and Wu, Y.-S. (2014). *The Effect of Osmotic Pressure on Improve Oil Recovery from Fractured Shale Formations*. Calgary: Society of Petroleum Engineers. doi:10.2118/168998-MS

Fakcharoenphol, P., Torcuk, M., Bertoncello, A., Kazemi, H., Wu, Y.-S., Wallace, J., et al. (2013). *Managing Shut-In Time to Enhance Gas Flow Rate in Hydraulic Fractured Shale Reservoirs: A Simulation Study*. Calgary: Society of Petroleum Engineers. doi:10.2118/166098-MS

Fritz, S. J., and Marine, I. W. (1983). Experimental support for a predictive osmotic model of clay membranes. *Geochimica et Cosmochimica Acta* 47 (8), 1515–1522. doi:10.1016/0016-7037(83)90310-1

Gao, Z., and Hu, Q. (2016). Initial Water Saturation and Imbibition Fluid Affect Spontaneous Imbibition into Barnett Shale samples. *J. Nat. Gas Sci. Eng.* 34, 541~551. doi:10.1016/j.jngse.2016.07.038

Ge, H. I., Liu, Y., and Shen, Y. H. (2015). Experimental Investigation of Shale Imbibition Capacity and the Factors Influencing Loss of Hydraulic Fracturing Fluids. *Pet. Sci.* 12, 636–650. doi:10.1007/s12182-015-0049-2

Kazemi, H., Gilman, J. R., and Elsharkawy, A. M. (1992). Analytical and numerical solution of oil recovery from fractured reservoirs with empirical transfer functions (includes associated papers 25528 and 25818). *SPE Reservoir Eng.* 7 (2), 219–227. doi:10.2118/19849-pa

Li, A., Fan, T., and Zhao, L. (2011). Experimental Research on Spontaneous Imbibition of Low Permeability Core in Fractured Reservoir. *Pet. Geology. Recovery Efficiency* 18 (5), 67–69.

Li, J. S. (2006). The Effect of Surfactant System on Imbibition Behavior. 2006. PhD thesis, Chinese Academy of Sciences, 2006.

Liu, X., and Dai, Q. (2008). Experimental Study of Imbibition Law in Low Permeability Sandstone Oilfield. *Drilling Prod. Tech.* 31 (6), 110–112.

Odumabo, S. M., Karpyn, Z. T., and Ayala H., L. F. (2014). Investigation of gas flow hindrance due to fracturing fluid leakoff in low permeability sandstones. *J. Nat. Gas Sci. Eng.* 171-12, 1–12. doi:10.1016/j.jngse.2013.12.002

Paktinat, J., Pinkhouse, J., and Williams, C. (2005). Penny Microemulsion Reduces Adsorption and Emulsion Tendencies in Bradford and Speechley Sandstone Formations. *SPE*, 93270. doi:10.2118/93270-MS

Penny, G., Pursley, J. T., and Holcomb, D. (2005). The Application of Microemulsion Additives in Drilling and Stimulation Results in Enhanced Gas Production. *SPE*, 94274. doi:10.2118/94274-MS

Ren, K., Ge, H., and Yang, L. (2015). Experimental Spontaneous Imbibition in Shale and its Application of Flowback Analysis. *Reservoir Sci. Tech. Eng.* 30 (15), 106–109.

Roychaudhuri, B., Tsotsis, T. T., and Jessen, K. (2013). An Experimental Investigation of Spontaneous Imbibition in Gas Shales. *J. Pet. Sci. Eng.* 111, 87–97. doi:10.1016/j.petrol.2013.10.002

Wang, F., Chen, Q., and Ruan, Y. (2020). Hydrodynamic Equilibrium Simulation and Shut-in Time Optimization for Hydraulically Fractured Shale Gas Wells. *Energies* 13, 961. doi:10.3390/en13040961

Wang, F., Pan, Z., and Zhang, S. (2017). Impact of chemical osmosis on water leakoff and flowback behavior from hydraulically fractured gas shale. *J. Pet. Sci. Eng.* 151, 264–274. doi:10.1016/j.petrol.2017.01.018

Wang, F., Pan, Z., and Zhang, S. (2017). Modeling Water Leak-off Behavior in Hydraulically Fractured Gas Shale under Multi-mechanism Dominated Conditions. *Transp Porous Med.* 118, 177–200. doi:10.1007/s11242-017-0853-9

Wang, M., and Leung, J. Y. (2015). Numerical investigation of fluid-loss mechanisms during hydraulic fracturing flow-back operations in tight reservoirsfluid-loss mechanisms during hydraulic fracturing flow-back operations in tight reservoirs. *J. Pet. Sci. Eng.* 133, 85–102. doi:10.1016/j.petrol.2015.05.013

Wang, Q., Guo, B., and Gao, D. (2012). Is Formation Damage an Issue in Shale Gas Development? *Soc. Pet. Eng.* doi:10.2118/149623-MS

Wang, W. (2000). The Effect of Oil Composition and Pore Structure on Absorption. *Pet. Geology. Oilfield Dev. Daqing.* 1 (6), 7~9. doi:10.2118/149623-MS

Wang, W., and Zhang, G. (2000). The Effect of Irreducible Water Saturation and Rock Properties on Imbibition. *Acta Petrolei Sinica* 21 (3), 69.

Xiong, W., Cheng, X., and Liu, H. (2013). Experimental Research of Spontaneous Imbibition in Low-permeabilityGlutenite. *Reservoir. Sci. Tech. Eng.* (26), 7793–7797.

Xiong, W., Cheng, X. Q., and Liu, H. X. (2013). Experimental study on spontaneous imbibition of low permeability glutenite reservoirs in Xinjiang. *Sci. Tech. Eng.* (26), 7793–7797.

Yan, B., and Mi, L. (2017). Mechanistic Simulation Workflow in Shale Gas Reservoirs. Presented at the SPE Reservoir Simulation Conference Held in Montgomery. TX, USA. SPE-182623-MS, 20–22. doi:10.2118/182623-MS

Yang, F., Ning, Z. F., and Hu, P. C. (2013). Characterization of microscopic pore structures in shale reservoirs. *Acta Pet. Sin.* 34 (2), 301–310.

Zhang, T., Li, X., Li, J., Feng, D., Li, P., Zhang, Z., et al. (2017). Numerical investigation of the well shut-in and fracture uncertainty on fluid-loss and production performance in gas-shale reservoirsfluid-loss and production performance in gas-shale reservoirs. *J. Nat. Gas Sci. Eng.* 46, 421–435. doi:10.1016/j.jngse.2017.08.024

Zhou, Q., Jin, Z., Yang, G., Dong, N., and Shang, Z. (2019). Shale oil exploration and production in the U.S.: Status and outlook. *Oil Gas Geology.* 40 (3), 469–477.

Zhou, Z., Hoffman, B., and Bearinger, D. (2014). Experimental and Numerical Study on Spontaneous Imbibition of Fracturing Fluids in Shale Gas Formation. *SPE*, 171600. doi:10.2118/171600-ms

ZhuJu, W. Y., Zhao, M., Chen, Q., and Yang, Z. (2002). Spontaneous Imbibition Mechanism of Low through Porous Media and Waterflooding in Low-Permeability Fractured Sandstone Reservoir. *Acta Petrolei Sinica* 2002 (06), 56–59+3.

Zou, C., Pan, S., Jin, Z., Gao, J., Yang, Z., Wu, S., et al. (2020). Shale Oil and Gas Revolution and its Impact. *Acta Petrolei Sinica* 41 (1), 1–12.

Conflict of Interest: The authors declare that the research was conducted in the absence of any commercial or financial relationships that could be construed as a potential conflict of interest.

Publisher's Note: All claims expressed in this article are solely those of the authors and do not necessarily represent those of their affiliated organizations, or those of the publisher, the editors, and the reviewers. Any product that may be evaluated in this article, or claim that may be made by its manufacturer, is not guaranteed or endorsed by the publisher.

frontiers in Earth Science

ORIGINAL RESEARCH
published: 23 December 2021
doi: 10.3389/feart.2021.793293

On the One-Point Model for the Productivity Evaluation in Jingbian Sector of Yan'an Gas Field

Liu Er-hu[1], Liu Yang-yang[1], Gao Li-jun[1], Zhou De-sheng[2], Liu Xiong[2] and Xu Jin-ze[3]*

[1]Gas Production Plant 2 of Yanchang Gasfield, Shanxi Yanchang Petroleum(Group)Co., Ltd., Jingbian, China, [2]School of Petroleum Engineering, Xi'an Shiyou University, Xi'an, China, [3]Department of Chemical and Petroleum Engineering, University of Calgary, Calgary, AB, Canada

The productivity equation of a gas well is, in the final analysis, an expression that describes the relationship between the production of a gas well and its bottom-hole flowing pressure. There are two kinds of productivity equations in common use at present: binomial productivity equation and exponential productivity equation. Combined with the modified isochronal well test, the test data are interpreted, and it is found that the open flow rates calculated by the two productivity equations are basically the same when the pressure difference at the test point is large, and the deviation of the exponential productivity equation is large when the pressure difference at the test point is small. Using binomial productivity equation and modifying isochronous well test, we established the single-point deliverability formula for the Jingbian sector of the Yan'an gas field. The field experience formula and production data are used to verify it. Their average errors are 2.59% and 7.12%, respectively; and the coincidence rate of productivity evaluation is 90%. The one-point productivity formula established has high precision and is suitable for productivity analysis of gas wells in paleozoic reservoirs in the Jingbian sector of the Yan'an gas field. This paper provides insights into the one-point productivity evaluation and its future application in the gas field.

Keywords: productivity equation, gas field, modified isochronal test, one-point deliverability formula, open flow

OPEN ACCESS

Edited by:
Jing Wang,
China University of Petroleum, China

Reviewed by:
Jinghong Hu,
China University of Geosciences, China
Jing Li,
China University of Petroleum, China

****Correspondence:***
Zhou De-sheng
dzhou@xsyu.edu.cn

Specialty section:
This article was submitted to Economic Geology, a section of the journal Frontiers in Earth Science

Received: *11 October 2021*
Accepted: *26 November 2021*
Published: *23 December 2021*

Citation:
Er-hu L, Yang-yang L, Li-jun G, De-sheng Z, Xiong L and Jin-ze X (2021) On the One-Point Model for the Productivity Evaluation in Jingbian Sector of Yan'an Gas Field. Front. Earth Sci. 9:793293. doi: 10.3389/feart.2021.793293

INTRODUCTION

The productivity of a gas well is mainly controlled by reservoir geological conditions (Li et al., 2001; Tang et al., 2004; Fu et al., 2021). During the development of gas field, it is of great significance to predict the productivity and analyze the performance dynamics, which is the basis of developing fields efficiently. During the development of gas field, productivity analysis is the most important method to predict the productivity, study the performance dynamics, and understand the characteristics of gas zones (Nowrouzi et al., 2020). The key gas production zone in the Jingbian sector of the Yan'an gas field is the Xiagumawu formation, which shows the features of low porosity, low permeability, and high heterogeneity. With the time being of production, wells with low productivity continue to appear (Yan et al., 2021), which leads to the slow recovery of shut-in pressure of gas wells; this further brings difficulty to the evaluation of single-well productivity. The one-point well test method only requires stable production and flowing pressure under one single-well constraint (Wakabayashi and McGouldrick, 2020), which is applied in China widely. The one-point method can significantly reduce the workload of well tests, reduce the burden of production, and provide theoretical evidence for the production allocation based on the gas productivity equations.

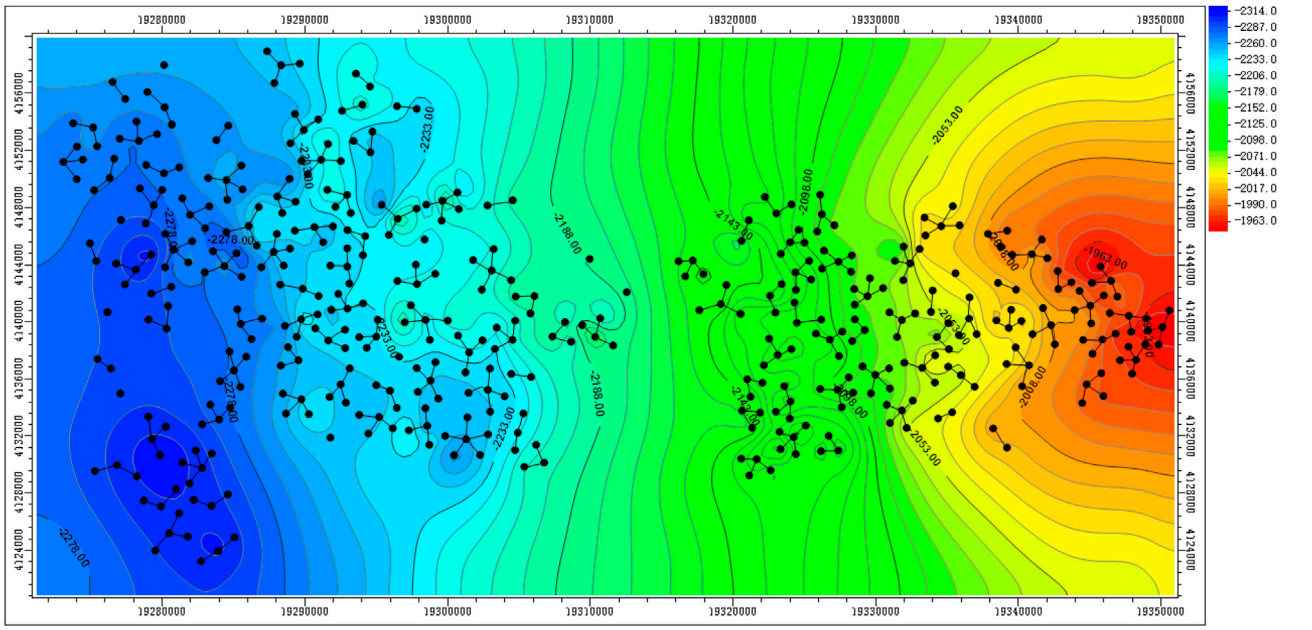

FIGURE 1 | Tectonic map of the top surface of reservoir formation.

Based on the stable condition proposed by O'Dell and Mill (O'dell, 1967) in 1965, a simplified method to calculate the gas productivity was proposed. Until 1995, Xiong (Yu et al., 1996) introduced the concept of unstable seepage and proposed the modification on the gas well analysis. In 1987, Chen et al. (2017) presented a simple method to determine the absolute open flow of gas wells. In 1992, Chen (1990) further proposed a series of one-point productivity formulas based on 16 gas wells in China. In 2004, Qin and Li (Bin et al., 2005) studied the gas production dynamics and built the oil–gas two-phase flow model and distribution of reservoir parameters. At the same time, Tang et al. proposed the back-pressure isochronal well test methodology to better evaluate the productivity of low-permeability gas wells. In 2005, Huang et al. (2005) studied the reservoir stratigraphy and seepage characteristics and established the productivity calculation model for gas wells in dual porous media. In 2011, Zhang et al. (2011) applied Saphir well test software to perform the analysis for well test data in seven wells in the Chuanxi area and corrected the coefficients of the one-point empirical formula. In 2013, Zhong et al. (2013) employed reservoir simulation to derive the "one-point" productivity formula for the Sulige gas field and correct the coefficients. In 2015, Zhao et al. (2015a) utilized the well test data in the Daniudi gas field to perform the revision for coefficients in one-point formula and established models for different formations. In 2018, Liang et al. (2018) applied the one-point production method into low-perm and low-porosity gas wells in Donghai and shrunk the well test time.

The Jingbian sector of Yan'an field is located in the middle of the Yishan slope in Ordos Basin. The main oil formation is $Mawu_{1+2}$. The reservoir exhibits the characteristics of low

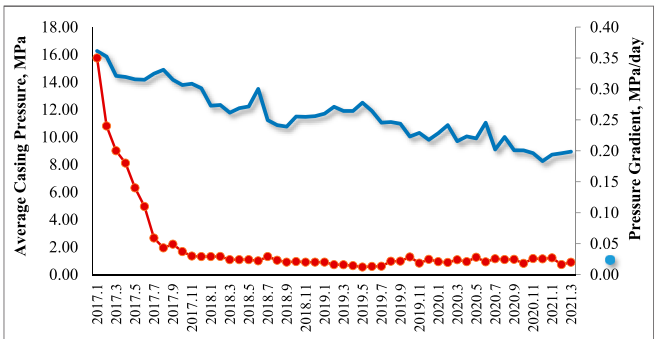

FIGURE 2 | Pressure profile of gas wells in the Jingbian sector (blue, average casing pressure; red, pressure gradient).

porosity, low permeability, and high heterogeneity with developed valleys. The development of grooves is closely related to the paleogeomorphology, paleocurrent, and paleokarst of carbonates. The phenomenon indicates a west-height and east-low trend in paleogeomorphology with toppling toward the southeast (**Figure 1**). The relative height difference is less than 70 m, and the average gradient of the slope is not greater than 0.001. The west is a coast during the sedimentation, and the surface water flows from the west to the east. The groove is mainly affected by the erosion of linear water and the gap of formations. As the main channel for the depletion of groundwater, the west of the groove is the water source, and the east is the water sink. It exhibits a "V" shape and follows the principle of erosion into the source. The direction of extension of the groove is in agreement with the direction of the paleocurrent. Many grooves are developed in the internal gas

reservoirs, which exhibits the parallel distribution. The study area started production in December 2016. Until now, 300 gas wells have been in production, and the cumulative gas production is 3.65 billion cubic meters. With the continuation of production, some wells show the trend of low production and low efficiency (**Figure 2**), which leads to a slow recovery of pressure after shut-in. These bring many challenges to production evaluations.

The key objective of the one-point well test method is to apply the appropriate productivity equation (Sun et al., 2020) to provide the reference for evaluating early-stage gas well production, which further satisfies the management requirement of fields (Zhao et al., 2017). The key workflow in this study is to compare different one-point methods and summarize their advantages and disadvantages. After that, the most appropriate one-point method is selected, and its usability is validated. The key innovation of this study is to evaluate different one-point methodologies based on physics and mathematics, and their applications are also discussed in depth.

COMPARISON OF ONE-POINT PRODUCTIVITY MODELS

The binomial productivity model and the exponential productivity model are the most popular types to apply one-point methods into the evaluation of productivity. The binomial one-point productivity model is derived based on the flow equation, phase behavior equation, and mass balance equation under a certain boundary condition, which has higher accuracy and a wider application range. The exponential productivity model is dependent on an empirical formula for certain fields and formations, which has relatively low applicability.

Binomial Productivity Model

The binomial productivity equation is based on the high-velocity Darcy's flow around gas wells (Du et al., 2022). It assumes the laminar flow in pores far away from the wells. However, when the gas flows into the bottom of wells, the seepage velocity significantly increases with a smaller flow radius. In this case, the turbulent flow exists, and the non-Darcy equation is applied to describe the flow mechanism. In the practice of gas field, it is difficult to find the pure laminar flow, and the non-Darcy is essential to be applied into gas-well evaluation. In the following paragraphs, the binomial productivity models under steady, pseudo-steady, and non-steady states will be introduced and discussed. The main difference between stead and non-steady is whether the pressure and flow rate are time dependent. The choice of different states should be dependent on the field observation of the relationship between time, pressure, and flow rate.

Binomial Productivity Model Under Steady State

Considering Darcy's flow and non-Darcy's flow (Al Rbeawi, 2020; Li and Chen, 2020), the one-point model is established based on mass balance equation and equation and state, and the boundary condition is defined as $\partial p/\partial t = 0$. In this way, the gas productivity model is obtained as follows:

$$P_e^2 - P_{wf}{}^2 = \frac{1.291 \times 10^{-3} T\bar{\mu}\bar{Z}}{Kh}\left(\ln\frac{r_e}{r_w} + S\right)Q_{SC} + \frac{1.291 \times 10^{-3} T\bar{\mu}\bar{Z}}{Kh} DQ_{SC}{}^2 \quad (1)$$

Eq. 1 can be further simplified as follows:

$$P_e^2 - P_{wf}{}^2 = A_1 Q_{SC} + B_1 Q_{SC}{}^2 \quad (2)$$

where P_e is the boundary pressure, MPa; P_{wf} is the bottom-hole flowing pressure, MPa; T is the temperature, K; $\bar{\mu}$ is the average viscosity, mPa·s; $\bar{z}$ is the deviation factor, dimensionless; K is the permeability, mD; h is the reservoir thickness, m; r_e is the effective radius, m; r_w is the well radius, m; S is the skin factor, dimensionless; Q_{SC} is the gas production at standard condition, 10^4 m^3/day; A_1 is the coefficient, $= \frac{1.291\times10^{-3}T\bar{\mu}\bar{Z}}{Kh}(\ln\frac{r_e}{r_w} + S)$; and B_1 is the coefficient, $= \frac{1.291\times10^{-3}T\bar{\mu}\bar{Z}}{Kh} D$.

In the formula above, the average properties of the gas are determined based on average pressure and temperature. In **Eq. 2**, the first item A_1 stands for the consumed energy by Darcy's flow and the second item B_1 indicates the consumed energy by non-Darcy's flow. If B_1 equals zero, the expression obeys Darcy's flow mechanism.

Binomial Productivity Model Under Pseudo-Steady State

The boundary condition is set up as $\partial p/\partial t = C$ (Li and Chen, 2020; Ying et al., 2021), and the productivity equation can be further derived as

$$P_R^2 - P_{wf}{}^2 = \frac{1.291 \times 10^{-3} T\bar{\mu}\bar{Z}Q_{SC}}{Kh}\left(\ln\frac{0.472r_e}{r_w} + S\right) + \frac{2.828 \times 10^{-3}\beta\gamma_g\bar{Z}TQ_{SC}{}^2}{r_w h^2} \quad (3)$$

Eq. 3 can be further simplified as follows:

$$P_R^2 - P_{wf}{}^2 = A_2 Q_{SC} + B_2 Q_{SC}{}^2 \quad (4)$$

where P_R is the reservoir pressure, MPa; β is the coefficient for turbulent flow, m^{-1}; γ_g is the relative density of natural gas, dimensionless; A_2 is the coefficient, $= \frac{1.291\times10^{-3}T\bar{\mu}\bar{Z}}{Kh}(\ln\frac{0.472r_e}{r_w} + S)$; and B_2 is the coefficient, $= \frac{2.828\times10^{-3}\beta\gamma_g\bar{Z}T}{r_w h^2}$.

In **Eq. 4**, A_2 indicates the pressure loss due to the viscous resistance, and B_2 indicates the pressure loss due to inertial resistance. The total loss presents the total pressure decline during the gas inflow procedure.

Binomial Productivity Model Under Non-Steady State

The gas flow state is unsteady when the pressure wave does not arrive at the boundary during the early stage of production (Zhao et al., 2015b), which can be regarded as the seepage characteristics in infinite formation. The productivity equation is shown as follows:

TABLE 1 | Correction of isochronal well test data table of well J53-1.

Work mode	Reservoir pressure, MPa	Bottom-hole flowing pressure, MPa	Gas production, 10^4 m^3/day
Initial shut-in	31.872	-	-
First mode	-	30.277	1.2460
Second mode	-	28.351	1.9847
Third mode	-	26.405	2.6542
Fourth mode	-	24.014	3.5041

$$P_e^2 - P_{wf}{}^2 = \frac{42.42\bar{\mu}\bar{Z}p_{SC}Q_{SC}}{KhT_{SC}}\left(\lg\frac{8.085Kt}{\varphi\mu C_t r_w} + 0.87S + 0.87DQ_{SC}\right) \tag{5}$$

Equation can be further simplified as follows:

$$P_e^2 - P_{wf}{}^2 = A_3Q_{SC} + B_3Q_{SC}{}^2 \tag{6}$$

where p_{SC} is the pressure at the standard condition, = 0.101325 MPa; T_{SC} is the temperature at the standard condition, = 293.16 K; φ is the porosity, dimensionless; C_t is the compressibility factor, MPa^{-1}; D is the non-Darcy flow coefficient, $(10^4\ m^3/day)^{-1}$; m is the coefficient, = $\frac{42.42\bar{\mu}\bar{Z}p_{SC}}{KhT_{SC}}$; A_3 is the coefficient, = $m\left(\lg\frac{8.085Kt}{\varphi\mu C_t r_w} + 0.87S\right)$; and B_3 is the coefficient, = $0.87mD$.

In **Eq. 6**, A_3 is a function of time for single wells, and its change with time fulfills the semi-log relationship.

Based on the derivation above, it can be seen that the productivity of gas wells satisfies the binomial format under unstable, pseudo-state, and state states. However, the coefficients have different definitions.

Exponential Productivity Model

An exponential productivity model is proposed based on the relationship between production and pressure difference, which is based on massive practice in the specified field as follows:

$$q_g = C\left(P_R^2 - P_{wf}{}^2\right)^n \tag{7}$$

where C is the coefficient, $(10^4\ m^3/day)/(MPa^2)^n$ and n is the coefficient between 0.5 and 1.

The exponent n shows the degree of non-Darcy flow. If n equals 1, it indicates the complete Darcy's flow. If n equals 0.5, it is a complete turbulent flow.

APPLICATION IN JINGBIAN SECTOR OF YAN'AN FIELD

Comparison Between Binomial Model and Exponential Model

Case Study with Big Pressure Difference in Different Work Modes

The gas well of J53-1 is taken as an example for the application of the one-point method. **Table 1** shows the well test data, and four well modes are applied to correct the isochronal well test, which are located at 30.3, 28.4, 26.4, and 24.0 MPa.

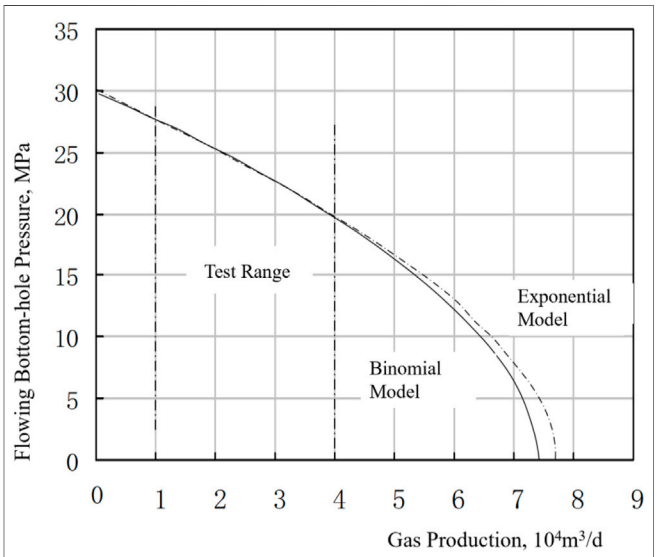

FIGURE 3 | Comparison of inflow performance relationship curves produced by different productivity equations.

Based on the data in **Table 1**, the exponential and binomial productivity equations can be obtained as follows:

$$P_R^2 - P_{wf}{}^2 = 255.79492Q_{SC} + 2.0756Q_{SC}{}^2 \tag{8}$$

$$Q_{SC} = 0.007741\left(P_R^2 - P_{wf}{}^2\right)^{0.89087} \tag{9}$$

Figure 3 shows the inflow performance relationship curves based on the models. In the range of well tests, the difference between binomial and exponential curves is small. Out of the range of well tests, there are some deviations between the two inflow performance relationship curves, but the difference is pretty small.

Based on the equations, the absolute open flow can be obtained as follows.

$$q_{AOF-Binomial} = 3.8101 \times 10^4 m^3/d \tag{10}$$

$$q_{AOF-Exponential} = 3.9165 \times 10^4 m^3/d \tag{11}$$

Based on **Eqs 10**, **11**, it is shown that the absolute open flow rate is pretty similar based on exponential and binomial equations, and the relative difference is only 2.8%. The square pressure difference for J53-1 is 439.15 MPa^2, which achieves 43% of the square pressure difference of the formation. The maximum

TABLE 2 | Correction of isochronal well test data table of well Jing 32-1.

Work mode	Reservoir pressure, MPa	Bottom-hole flowing pressure, MPa	Gas production, 10^4 m^3/day
Initial shut-in	33.38	-	-
First mode	-	32.743	3.2051
Second mode	-	32.313	5.3239
Third mode	-	31.997	7.1535
Fourth mode	-	31.616	9.1910

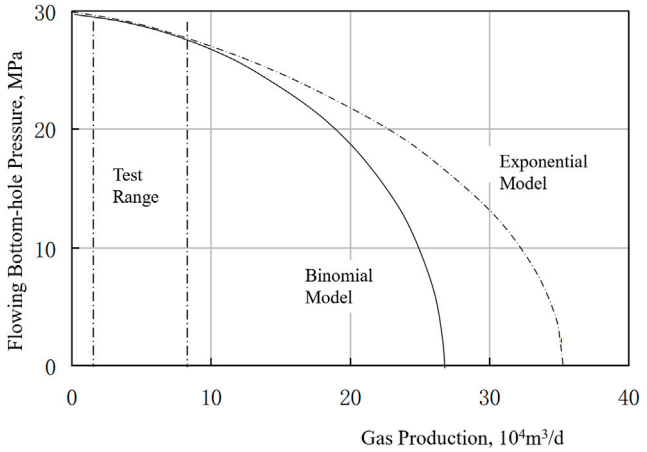

FIGURE 4 | Comparison of inflow performance relationship curves produced by different productivity equations.

production of 3.5041×10^4 m^3/day exceeds the half rate of absolute open flow. This indicates that if the pressure difference in different work modes is large, the difference of productivity between binomial and exponential models is small.

Case Study With Small Pressure Difference in Different Work Modes

The gas well of J32-1 is taken as an example in this case. **Table 2** shows the well test data, and four well modes are applied to correct the isochronal well test, which are located at 3.2, 5.3, 7.2, and 9.2 MPa. The square pressure difference for J53-1 is 114.65 MPa^2, which is only 10% of the square pressure difference of the formation.

Based on **Table 2**, the binomial and exponential productivity equations are obtained as follows.

$$P_R^2 - {P_{wf}}^2 = 35.8768 Q_{SC} + 0.1333 {Q_{SC}}^2 \quad (12)$$

$$Q_{SC} = 0.075\left(P_R^2 - {P_{wf}}^2\right)^{0.8629} \quad (13)$$

The absolute open flow is thus calculated as follows.

$$q_{AOF-Binomial} = 3.8101 \times 10^4 \ \ m^3/day \quad (14)$$

$$q_{AOF-Exponential} = 3.9165 \times 10^4 \ \ m^3/day \quad (15)$$

The equations above indicate that the relative difference of absolute open flow is 14.8%, which has a big difference. **Figure 4** shows the difference of inflow performance relationship curves, which indicates that the difference is small within the well test range but big outside of the well test range. While using this chart in the field, the maximum value by the exponential model and the minimum model is able to generate a range to determine the bottom-hole pressure.

One-Point Productivity Model

Based on the study, this paper establishes the one-point productivity model based on the binomial productivity equation, which has wider applicability for different states (steady, pseudo-steady, and non-steady). The production of gas wells in the Jingbian sector is under the pseudo-steady state. Thus, the proposed model is based on the pseudo-steady binomial productivity equation.

Eq. 4 can be further established to the one-point model to calculate the absolute open flow, as follows:

$$Q_{AOF} = \frac{2(1-\alpha)Q_g}{\alpha\left[\sqrt{1+4\left(\frac{1-\alpha}{\alpha^2}\right)p_D} - 1\right]} \quad (16)$$

where α is the one-point coefficient = $\frac{A}{A+BQ_{AOF}}$; and p_D is the dimensionless pressure = $\frac{p_R^2 - p_{wf}^2}{p_R^2}$.

Four work modes are taken based on a corrected isochronal well test, and the time periods are as 4, 8, 12, 16, 20, and 24 h. Thus, the one-point characteristic parameters are obtained as **Table 3**.

The average value of α is obtained as 0.9037 from **Table 3**. Thus, the one-point productivity model in the Jingbian sector of the Yan'an gas field is as follows:

$$q_{AOF} = \frac{0.2130 q_g}{\sqrt{1 + 0.4714 P_D} - 1} \quad (17)$$

Regarding the established one-point productivity model, only a stable production and a related pressure are needed to obtain the absolute open flow.

Case Study 1: Comparison With Empirical Formula

Case study 1 is based on seven early-stage wells from the Jingbian sector as shown in **Table 4**. The established one-point model is compared with an empirical formula for the Xiagu formation in the Jingbian sector. The empirical formula to calculate the absolute open flow based on correlation is as follows (Shah et al., 2020):

$$q_{AOF} = \frac{0.7189 q_g}{\sqrt{1 + 1.9545 P_D} - 1} \quad (18)$$

TABLE 3 | Calculation result of productivity characteristic parameter of single-well and single-point deliverability formula.

Well name	B	A	ΔP^2/MPa^2	q_{AOF}/10^4 m^3/day	α
J32-1	0.1619	34.4174	1,114.2141	28.5416	0.8816
J44	1.7577	184.0653	952.2059	4.9401	0.9549
J53-1	1.5880	273.1753	1,015.8141	3.6415	0.9793
Y924	0.7448	52.0380	1,099.5090	16.9950	0.8043
Y942-3	0.4263	87.4788	1,060.4038	11.4796	0.9470
Y865	0.4088	46.9808	1,101.1676	19.9688	0.8520
Y313-1	0.4913	64.7204	963.4093	13.5019	0.9070

TABLE 4 | Data of stability test point of paleozoic gas reservoir in Jingbian sector of Yan'an gas field.

Well name	FBHP, MPa	Reservoir pressure, MPa	Production, 10^4 m^3/day
J32-1	29.407	33.380	6.2109
J44	8.831	30.858	3.8570
J53-1	13.296	31.972	2.3937
Y924	30.103	33.159	3.2295
Y942-3	26.438	32.564	3.7263
Y865	24.315	33.184	9.0216
Y313-1	24.550	31.039	4.5254

TABLE 5 | Comparison of two single-point deliverability formulas.

Well name	Corrected absolute open flow	One-point model		Empirical formula	
		Absolute open flow, 10^4 m^3/day	Relative difference, %	Absolute open flow, 10^4 m^3/day	Relative difference, %
J32-1	25.2655	25.7157	1.78	22.4375	11.19
J44	4.1862	4.1706	0.37	4.1281	1.38
J53-1	2.8878	2.8531	1.20	2.7894	3.40
Y924	15.5213	16.9357	9.11	16.9357	9.11
Y942-3	10.5575	10.2618	2.80	9.2111	12.75
Y865	18.0391	18.5187	2.65	17.0547	5.45
Y313-1	11.4087	11.3853	0.20	10.2956	9.75

TABLE 6 | Comparison of productivity calculated by production data and productivity calculated by single-point method.

Well name	FBHP, MPa	Reservoir pressure, MPa	Production, 10^4 m^3/day	Absolute open flow, 10^4 m^3/day		Relative difference, %
				One-point model	Field data	
J5-1	27.433	31.027	5.968	25.3326	24.1940	4.71
J5-2	28.775	32.027	3.1234	14.9687	16.1851	7.52
J12	8.746	18.531	1.9794	2.4959	2.7415	8.96
J12-1	12.117	18.531	1.0417	1.7489	2.0974	16.62
Y910-1	11.203	12.087	5.0058	32.6268	31.3741	3.99
Y910-2	11.554	12.087	2.5386	26.8679	27.5783	2.58
Y976-2	9.991	21.249	3.8631	4.8615	5.1680	5.93
Y976-3	14.468	21.249	1.9473	3.4766	3.7751	7.91
J44	13.688	17.469	2.4793	6.0573	6.2579	3.21
J44-1	14.904	17.469	1.3333	4.5661	5.0672	9.89

Table 5 indicates that the average relative difference based on the one-point model is only 2.59%, which is much lower than the value of 7.58% from the empirical formula.

More production data can be obtained after the gas wells are in production. In this case, 10 late-stage wells after pressure build-up test in the Xiagu formation are selected to perform the analysis as shown in **Table 6**.

Table 6 indicates that the average relative difference is about 7.12% for late-stage wells, considering the standard is that the relative difference is less than 10%. The rate of success to apply the one-point model in this case is 90%.

Overall, the one-point model has a high accuracy to evaluate the gas productivity in the Xiagu formation of the Jingbian sector. **Eq. 17** can be a typical model to evaluate the gas production in the study area. The limitation of this model is not able to consider complex geological conditions such as shales or faults. It is suggested to combine with reservoir simulation if this model applies information of complex conditions.

CONCLUSION

This paper studies gas productivity based on the one-point model in the Jingbian sector. The following conclusions can be drawn:

1) When the pressure difference is big between different work modes, the absolute open flow from the binomial equation and that from the exponential equation are very similar. While the difference is small, a big relative difference will be observed between the two methods.
2) The one-point model is established based on a pseudo-steady binomial equation with the average characteristic coefficient of 0.9037 in the Jingbian sector. Compared with the empirical formula, the one-point model indicates a higher accuracy to match corrected absolute open flow. Besides, the one-point model also shows high accuracy for late-stage gas wells. The established model can be widely applied in the study area.

DATA AVAILABILITY STATEMENT

The original contributions presented in the study are included in the article/Supplementary Material. Further inquiries can be directed to the corresponding author.

AUTHOR CONTRIBUTIONS

LE-h, LY-y, and GL-j are responsible for the design of the model. ZD-s and LX are responsible for the writing of the manuscript. XJ-z is responsible for the improvement of the English language.

FUNDING

The authors would like to acknowledge the National Natural Science Foundation of China (No. 51804257, No. 52004220, No. 51934005, and No. 51874242) and Open Fund of State Key Laboratory of Oil and Gas Reservoir Geology and Exploitation (Chengdu University of Technology) (PLC20210316).

REFERENCES

Al Rbeawi, S. (2020). Analysing and Characterising Horizontal Well Performance in Rectangular Closed Gas Reservoirs Considering Non-darcy Flow Conditions. *Ijogct* 24 (3), 345–376. doi:10.1504/ijogct.2020.10028649

Bin, Q., Li, X., and Cheng, S. (2005). Oil/gas Percolation Performance of Condensate Reservoirs under Effect of High Velocity Flow [J]. *Nat. Gas Industry* 2, 136–139+19. doi:10.3321/j.issn:1000-0976.2005.02.044

Chen, Y., Guo, E., Peng, Z., Wang, M., and Zhou, Y. (2017). Derivation of Productivity Formulas for Horizontal wells in Anisotropic Fault-Block Reservoirs. *Acta Petrolei Sinica* 38 (12), 1420. doi:10.7623/syxb201712009

Chen, Y. (1990). Standardization on the Curves of Permeability and Capillary Pressure. *Exp. Pet. Geology.* 12 (1), 64–70.

Du, X., Zhang, Y., Zhou, C., Su, Y., Li, Q., Li, P., et al. (2022). A Novel Method for Determining the Binomial Deliverability Equation of Fractured Caved Carbonate Reservoirs. *J. Pet. Sci. Eng.* 208, 109496. doi:10.1016/j.petrol.2021.109496

Fu, J., Su, Y., Li, L., Wang, W., Wang, C., and Li, D. (2021). Productivity Model with Mechanisms of Multiple Seepage in Tight Gas Reservoir. *J. Pet. Sci. Eng.*, 109825. doi:10.1016/j.petrol.2021.109825

Huang, Q., Sun, L., Li, S., Yang, S., and Yang, H. (2005). Correct Prediction of Gas Well Productivity for Condensate Gas Reservoirs with Low Permeability. *Nat. Gas Industry* (11).

Li, J., and Chen, C. (2020). Numerical Simulation of the Non-darcy Flow Based on Random Fractal Micronetwork Model for Low Permeability sandstone Gas Reservoirs. *Geofluids* 2020, 1–9. doi:10.1155/2020/8884885

Li, X., Huang, B., and Hu, Y. (2001). The Establishment and Application of Binomial Deliverability Equation for Horizontal Gas Well. *J. Can. Pet. Technology* 42 (10). doi:10.2118/2001-081

Liang, B., Tan, X., Jiao, S., Peng, S., Zhang, L., and Duan., Y. (2018). "single-point"productivity Equation for Fractured Gas wells in Low-Porosity and Low-Permeability Reservoirs,east china Sea. *Well Test.* 27 (2), 73–78. doi:10.19680/j.cnki.1004-4388.2018.02.012

Nowrouzi, I., Mohammadi, A. H., and Manshad, A. K. (2020). Effect of a Synthesized Anionic Fluorinated Surfactant on Wettability Alteration for Chemical Treatment of Near-Wellbore Zone in Carbonate Gas Condensate Reservoirs. *Pet. Sci.* 17 (6), 1655–1668. doi:10.1007/s12182-020-00446-w

O'dell, H. G. (1967). Successfully Cycling a Low-Permeability, High-Yield Gas Condensate Reservoir. *J. Pet. Technology* 19 (01), 41–47.

Shah, M. S., Khan, M. H. R., Rahman, A., and Butt, S. (2020). Production Optimization in Well-6 of Habiganj Gas Field, Bangladesh: a Prospective Application of Nodal Analysis Approach. *J. Petrol. Explor Prod. Technol.* 10, 3557–3568. doi:10.1007/s13202-020-00908-2

Sun, H., Meng, G., and Cao, W. (2020). Applicable Conditions of the Binomial Pressure Method and Pressure-Squared Method for Gas Well Deliverability Evaluation. *Tianranqi Gongye/Natural Gas Industry* 40 (1), 69–75. doi:10.1016/j.ngib.2020.01.007

Tang, J., Ma, X., Jiao, C., and Fan, L. (2004). A New Testing Method of Gas Well Potential:backpressure Isochronal Test. *Nat. Gas Geosci.* 15 (5), 540–544.

Wakabayashi, D., and McGouldrick, M. (2020). Innovative High Efficiency Oil Burner Proves to Solve Many Environmental Challenges in Well Test Applications. *OnePetro*. In International Petroleum Technology Conference. doi:10.2523/iptc-19734-ms

Yan, H., Jia, A., Meng, F., Xia, Q., Xu, W., Feng, Q., et al. (2021). Comparative Study on the Reservoir Characteristics and Development Technologies of Two Typical Karst Weathering-Crust Carbonate Gas Reservoirs in China. *Geofluids* 2021, 1–19. doi:10.1155/2021/6631006

Ying, L., Wang, J., and Li, A. (2021). Effect of Non-darcy Seepage on Productivity of Tight Gas reservoirIOP Conference Series: Earth and Environmental Science. *IOP Publishing* 859 (No. 1), 012067. doi:10.1088/1755-1315/859/1/012067

Yu, X., Lei, S., Liangtian, S., and Shilun, L. (1996). A New Method for Predicting the Law of Unsteady Flow through Porous Medium on Gas Condensate Well. *OnePetro*. In SPE Gas Technology Symposium. doi:10.2118/35649-ms

Zhang, J., Mu, X., and Qiu, L. (2011). Correction for Well Testing Formula of "one point" Production Testing in Chuanxi Deep Layer. *Well Test.* 20 (5), 19–20.

Zhao, X., Jiang, B., Zhang, S., Liu, J., and Xu, Q. (2017). Main Controlling Factors of Productivity and Development Strategy of Cbm wells in Block 3 on the Eastern Margin of Ordos basin. *Acta Petrol. Sinica* 38 (11), 1310–1319. doi:10.7623/syxb201711010

Zhao, X., Rui, Z., Liao, X., and Zhang, R. (2015). A Simulation Method for Modified Isochronal Well Testing to Determine Shale Gas Well Productivity. *J. Nat. Gas Sci. Eng.* 27, 479–485. doi:10.1016/j.jngse.2015.08.035

Zhao, Z., Li, Z., Lai, F., and Wu, W. (2015). Study of Single-point Testing Time for Tight Gas of Fractured Horizontal wells. *Well Test.* 24 (1), 1–3.

Zhong, J., Tang, H., Dongliang, L., Zhang, Z., and Donglin, L. (2013). Study on a Single point Deliverability Formula of Horizontal wells in Sulige Gas Field. *Lithologic Reservoirs* 25 (2), 107–111.

Conflict of Interest: Authors LE-h, LY-y, and GL-j were employed by company Shanxi Yanchang Petroleum (Group) Co., Ltd.

The remaining authors declare that the research was conducted in the absence of any commercial or financial relationships that could be construed as a potential conflict of interest.

frontiers in Earth Science

ORIGINAL RESEARCH
published: 23 December 2021
doi: 10.3389/feart.2021.745393

Numerical Simulation Research on Influencing Factors of Post-Fracturing Flowback of Shale Gas Wells in the Sichuan Basin

Jiangfa Wu[1], *Yunting Di*[1]*, *Jian Zhang*[1], *Peiyun Li*[1], *Deliang Zhang*[1], *Yan Wang*[2] and *Hong Zhou*[1]

[1]Petrochina Southwest Oil & Gasfield Company, Chengdu, China, [2]Sinopec Southwest Petroleum and Natural Gas Company, Chengdu, China

The horizontal well multistage hydraulic fracturing technology is the most effective way to exploit shale gas resources. Compared with conventional reservoir fracturing, the flowback rate of a fracturing fluid in a shale reservoir is extremely low, and a large amount of fracturing fluid remains in the formation. Therefore, the research on the mechanism of shale reservoir fracturing fluid flowback process will contribute to laying a theoretical foundation for improving the effect of the innovation for increasing output of shale gas wells. Based on the shale in the Sichuan Basin, this study first describes basic experiments on physical properties such as the porosity, permeability, mineral composition, wettability, and microstructure. The physical properties of shale reservoirs were also analyzed, which laid the foundation for subsequent modeling. Second, CMG software is used to establish a numerical model that fits the characteristics of the flowback process. The effect of reservoir properties, fracturing parameters, drainage–production system, chemical permeability on gas and water production in the flowback process and their mechanisms are also analyzed. According to most numerical simulation results, the lower cumulative gas production will be with the higher cumulative water production which means the higher flowback rate. The pursuit of only a high flowback rate is not advisable, and the development of the drainage–production system requires reasonable control of the fracturing fluid flowback rate. This study provides a theoretical basis for the optimization of shale gas drainage–production system after hydraulic fracturing.

Keywords: shale, properties analysis, numerical simulation, chemical osmotic pressure, flowback pattern

OPEN ACCESS

Edited by:
Yulong Zhao,
Southwest Petroleum University, China

Reviewed by:
Lingfu Liu,
University of Wyoming, United States
Ruihan Zhang,
Southwest Petroleum University, China

***Correspondence:**
Yunting Di
dyt87797@petrochina.com.cn

Specialty section:
This article was submitted to Economic Geology, a section of the journal Frontiers in Earth Science

Received: *22 July 2021*
Accepted: *24 November 2021*
Published: *23 December 2021*

Citation:
Wu J, Di Y, Zhang J, Li P, Zhang D, Wang Y and Zhou H (2021) Numerical Simulation Research on Influencing Factors of Post-Fracturing Flowback of Shale Gas Wells in the Sichuan Basin. Front. Earth Sci. 9:745393. doi: 10.3389/feart.2021.745393

INTRODUCTION

As a clean, efficient, and unconventional resource with great potential, shale gas has been commercially developed in many countries around the world. Large-scale volume fracturing of a shale gas reservoir is required for realizing the value of industrial exploitation. During the hydraulic fracturing process of a shale gas reservoir, 2×10^4–5×10^4 m^3 of fracturing fluid will be injected into the reservoir. According to the statistical data of shale gas fields, the flowback rate of fracturing fluids in most shale reservoirs is lower than 50%, even less than 5% in some reservoirs. After fracturing, a large amount of fracturing fluid will be retained in fractures and matrix (Zhang, Li, Yang), which directly affects the damage degree of fracturing fluid to the formation and the fracture conductivity,

and then affects the development effect of the reservoir. Therefore, it is of great significance to study the distribution characteristics, flowback mechanism, and influencing factors of fracturing fluid in the reservoir after fracturing.

The research on the self-suction process of shale gas well mainly adopts the laboratory experiment method. The study on the self-absorption mechanism of the filtration process is helpful to deepen the understanding of flowback mechanism. Some scholars have studied the role of clay minerals in the shale self-absorption process by laboratory experiments. They believe that the clay minerals in shale have strong self-absorption ability and a semipermeable membrane effect, and water absorption volume can be larger than the measured pore volume. The water absorption expansion of clay minerals can induce a large number of microfractures in the shale reservoir (Dehghanpour et al., 2013; Fakcharoenphol et al., 2014; Zhou et al., 2014). Other scholars have studied the influence of physical properties such as wettability of shale on the self-absorption process. The main driving forces of spontaneous imbibition of fracturing fluid in the shale are capillary pressure and clay osmotic pressure. Adding a surfactant to fracturing fluid can change the wettability of shale surface and then affect the capillary pressure, spontaneous imbibition rate, and self-imbibition ability of shale (Engelder et al., 2014; Roychaudhuri et al., 2011). Understanding the physical properties of the shale reservoir, such as mineral composition and wettability, is the basis of studying the flowback mechanism of fracturing fluid in shale gas wells. However, the composition, content, and physical properties of clay minerals are different in different regions. There is a lack of measurement and analysis on the content of clay minerals and physical properties of shale, such as permeability, porosity, TOC content, and wettability at present.

The study of the large-scale flowback stage after fracturing is completed by numerical simulation, rather than a laboratory experiment. Most scholars used single-phase flow simulation to study the fracturing fluid flowback process after fracturing (Wu et al., 2003; Crafton and Gunderson, 2006). However, according to the analysis of production data of shale gas field, the early flowback process is mainly gas–aqueous two-phase flow. Therefore, a gas–aqueous two-phase flow model is needed for the analysis of fracturing fluid flowback after fracturing. In the study of the pressure of gas–aqueous two-phase flowback, some scholars only consider the influence of capillary pressure. When a gas–aqueous two-phase fluid exists, capillary force will be produced due to the difference of interfacial tension between the two phases in the pore. The matrix pores of shale are mainly nanoscale pore, and the capillary can even exceed 50 MPa. The capillary pressure produced by secondary fractures of shale is between 10 and 20 MPa. Therefore, it is difficult to return fracturing fluid in the matrix and secondary fractures due to capillary pressure (Guo et al., 2016; Wang and Rahman, 2015; Chen et al., 2016). Recently, some scholars have begun to study the role of chemical potential difference in the flowback process. The scholars believe that there is a semipermeable membrane effect on the contact surface between the injected fluid and the shale. The salinity of the fracturing fluid is about 1–5 kppm, while the salinity of the shale reservoir can be as high as 280 kppm, and the chemical potential difference will inhibit the flowback (Wang et al., 2016; Singh, 2016; Yang et al., 2016). Capillary pressure and chemical osmotic pressure are important factors affecting the flowback process of fracturing fluid after fracturing. At present, there is no study on these two factors together.

The obvious feature of fracturing fluid flowback is that most of the remaining fracturing fluid cannot be discharged, which leads to the fact that the flowback rate of the fracturing fluid is not high. It is necessary to study the factors affecting the flowback flow of fracturing fluid and clarify the rules of fracturing fluid flowback. The sensitivity analysis of shale gas well factors by various scholars shows that the factors influencing the flowback mainly include reservoir properties such as water saturation and wettability of reservoir (Zhang et al., 2017); fracture parameters such as fracture half-length, shape, conductivity, and cluster number (Liu et al., 2015; Bian et al., 2016; Guo et al., 2016); and the drainage–production system such as shut-in time and production pressure difference (Jiang et al., 2013; Zhang et al., 2017). The results of the present research show that the study on the factors affecting the flowback is lack of combination with the physical properties of shale reservoir. The laboratory experiment of describing the physical characteristics of the shale reservoir should be carried out before numerical simulation. At present, most scholars study the influence of single property on the flowback process, and there is a lack of sensitivity analysis that comprehensively considers the factors involved in the flowback process, including reservoir properties, fracturing parameters, production system, and chemical permeability.

Therefore, the overburden pressure porosity measurement and the SEM scanning experiment are used to analyze the pore permeability parameters, mineral composition, wettability, TOC content, and microstructure of shale in the Sichuan Basin and evaluate the physical properties of shale reservoir. On the basis of the aforementioned research, the gas–aqueous two-phase flow mechanism model of the early flowback process of shale gas wells is established by using commercial numerical simulation software and then initialized the formation pressure and water saturation after fracturing. According to the model, the effects of shale reservoir properties, fracturing parameters, and flowback system on the flowback rate and productivity can be studied quantitatively.

TESTS OF PHYSICAL PROPERTIES FOR THE SHALE RESERVOIR

Compared with conventional reservoirs, the shale reservoir is characterized by low porosity and low permeability, which leads to different laws of oil and gas flow in the reservoir. The physical properties such as pore throat structure and mineral composition of the shale reservoir are very different from those of conventional reservoirs. Therefore, it is necessary to conduct laboratory experiments on the physical properties of shale reservoirs, which will be helpful to understand the shale reservoir from a microscopic perspective and lay a foundation for the subsequent numerical simulation. The core samples of the shale reservoirs in the Sichuan Basin are taken for the study of this article. A total of

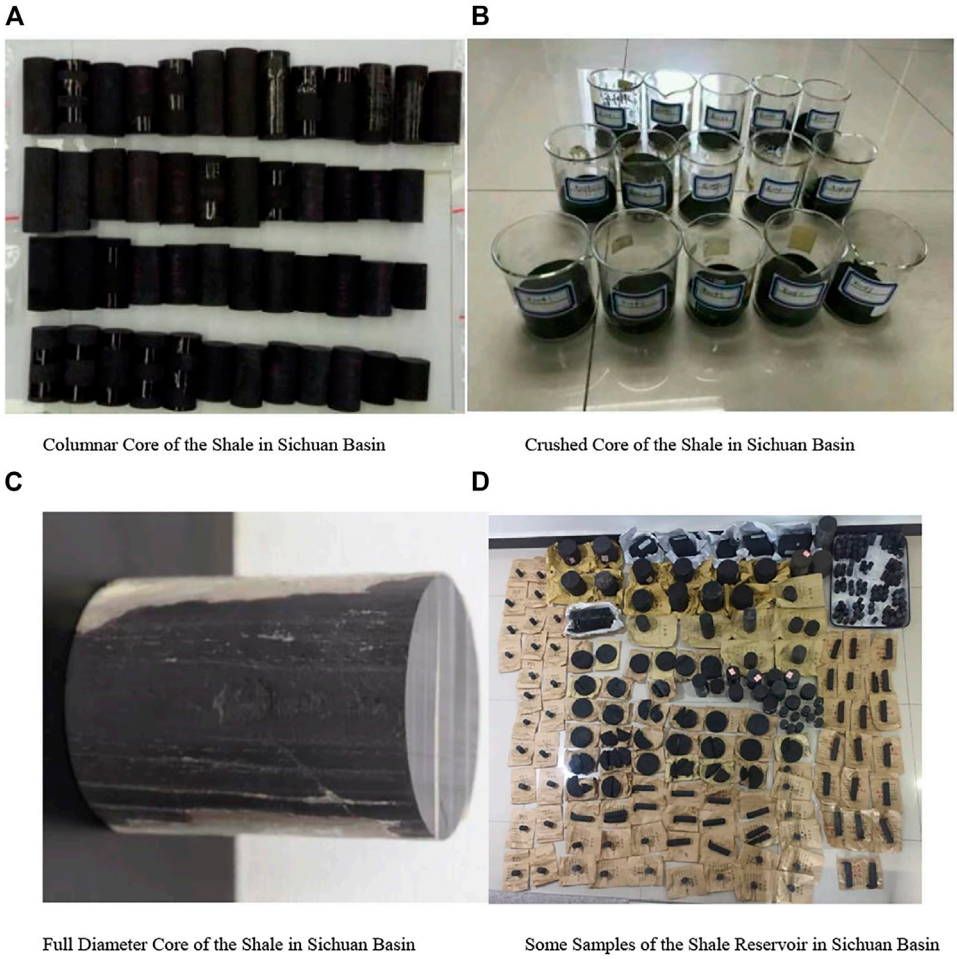

FIGURE 1 | Core samples of the shale reservoir in the Sichuan Basin.

214 columnar samples and 109 crushed samples are taken from 16 wells, which lays the foundation for clarifying the differences between each layer (**Figure 1**).

Porosity Measurement

According to the measurement results, it is found that the porosity of the 179 rock samples ranges from 0.39 to 9.729%, with an average of 3.834%. The shale porosity is measured with Poropem-200 type porosimeter at overburden pressure. Nitrogen with a purity of 99.99% is used as the medium, and a high-precision pressure sensor is used. The samples are prepared as cylinders with a diameter of 1.5 cm and a length of 2–3 cm. The particle volume is measured through pressurizing nitrogen from a pre-pressurization chamber of known volume into a sample chamber with rock samples on the basis of the helium expansion principle.

Permeability Measurement

The measurement results show that the shale core permeability is extremely low, and the shale permeability is about 10^{-4}~10^{-3} μm^2. A variety of permeability testing methods are used in this study, including pulse permeability testing and steady-state permeability testing. The permeability of a total of 147 rock samples is measured by pulse tests. Their permeability ranges from 0.00008 to 0.011 mD, with an average of 0.0691 mD. The permeability of a total of 114 rock samples is measured by steady-state tests, and the average of different horizons ranges from 0.00016 to 0.002 mD.

Mineral Composition and TOC Content Measurement

The mineral composition of the shale is one of the important indicators for understanding the reservoir, and the analysis on the mineral composition is helpful for studying the flow characteristics and retention reasons of fracturing fluid in the reservoir. In this study, Xan -ray diffractometer is used to conduct the full-mineral analysis of the target core. According to the X-ray diffraction analysis data of the core, the main mineral components of shale include quartz, feldspar, calcite, dolomite, clay, and pyrite; the clay minerals include mainly illite, illite/smectite formation, and chlorite.

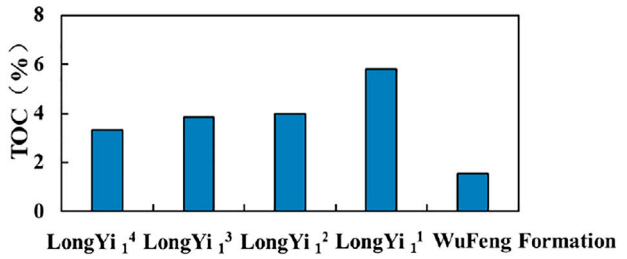

FIGURE 2 | Average TOC content of each layer.

It can be seen from the core analysis data that the rock minerals are mainly quartz, feldspar, carbonate rock, clay, and pyrite; the content of brittle minerals (quartz, feldspar, carbonate rock) is generally greater than 65%, while the content of expansive minerals is small. The clay minerals such as illite, chlorite, and illite/smectite formation are developed mainly, while illite is the most important mineral component with the content (mass fraction) of 77–83%, followed by kaolinite with the content of 4–17%, and the chlorite content is small.

The illite/smectite formation has a relatively large specific surface area and can absorb a large amount of water, which will cause easily spontaneous imbibition and retention of fracturing fluid. Since illite is a speed-sensitive mineral which will easily cause particle migration and reservoir choke, attention shall be paid to controlling the flowback speed during the flowback process. The low chlorite content indicates that the shale in this block is not an acid-sensitive mineral. When there are a large number of natural fractures filled with brittle minerals in the shale, volume fracturing will be easier for the shale reservoir; on the contrary, when the clay content in the shale reservoir is higher, the development of fractures will be difficult in the reservoir. The content of brittle minerals and clay largely determines whether shale reservoirs are compressible.

According to the TOC content analysis results (**Figure 2**), it can be seen that the TOC content of the LongYi $_1^1$ layer and LongYi $_1^2$ layer is distributed between 6.32 and 4.32%, which are much higher than the values of other layers; the Wufeng Formation has the lowest TOC content (1.53%).

Wettability Measurement

The rock wettability is the result of the interaction between rock minerals and fluid. It has significant influence on capillary pressure and relative permeability. In the shale wettability experiment, the core of ChangNing Block is used to measure the wetting angle and analyze the changing rule of wettability at different soaking times. On-site fracturing fluid is used to measure the two-phase wetting angle of the tested core after soaking for 0, 1, 5, 10, 15, 20, and 30 days. The results (**Figure 3**) show that as the soaking time increases, the measured wetting angle gradually decreases and the rock hydrophilicity increases. The changing degrees of the measured wetting angle are different for the same batch of rock samples soaked in different fracturing fluids, but the influence of different fracturing fluids on the wettability of rocks is small (**Figure 3**).

Scanning Electron Microscope Experiments

In this study, the environmental scanning electron microscope (ESEM) is used to characterize the micropore structure and micromorphology of shale under high- or low-vacuum conditions. The ESEM has a magnification of 6x-100000x and is equipped with accessories such as X-ray energy-dispersive spectroscopy (EDS) and cryogenic freezing table. It can be used for qualitative and quantitative analyses of micro-area elementary composition from points, lines, and planes based on morphology or observing samples directly.

The outcrop of the ChangNing Block is selected and soaked in the slick water fracturing fluid system (slick water fracturing fluid formula: 0.1% resistance reducing agent, 0.1% anti-swelling

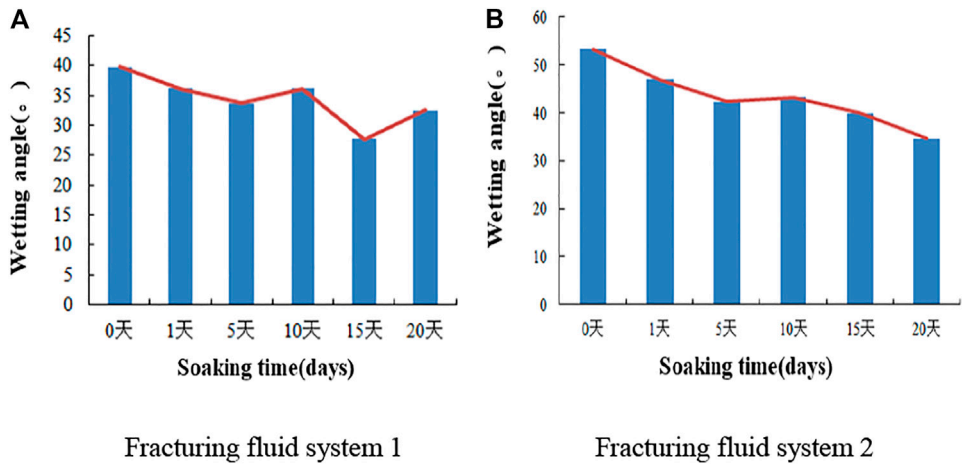

FIGURE 3 | Changes of the wetting angle with the soaking time.

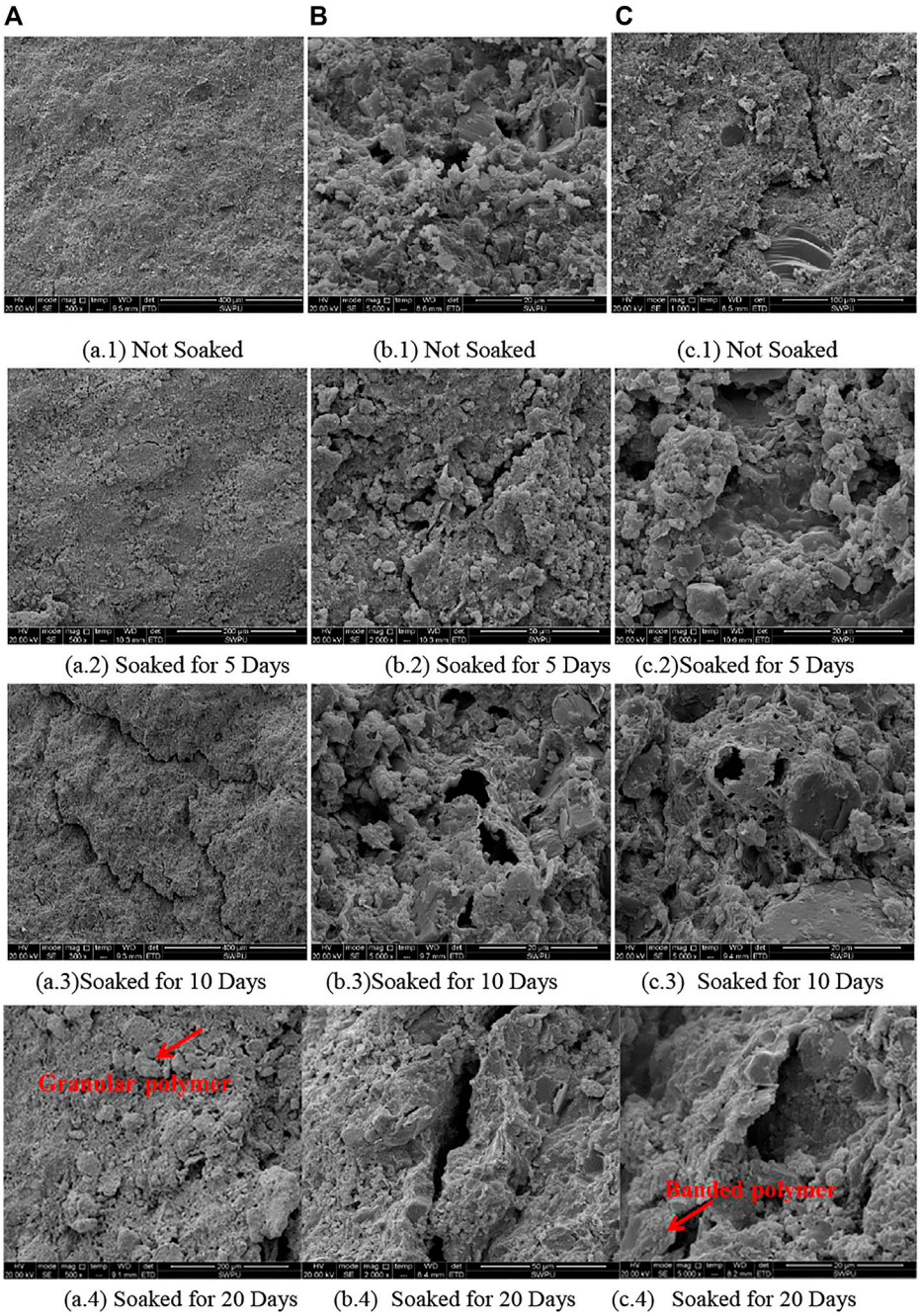

FIGURE 4 | The outcrop of the ChangNing Block soaked in the slick water fracturing fluid system for 0, 1, 5, 10, 15, and 20 days, respectively, for SEM experiments; **(A–C)** show how the three outcrop change after soaked.

agent, 1% discharge aiding agent) for 0, 1, 5, 10, 15, and 20 days, respectively, for SEM experiments (**Figure 4**). The properties of the pore structure, the microfracture development, and the change of shale micropore structure after soaking are observed in the experiments.

According to the experimental results, the shale outcrop in the ChangNing Block has a dense rock structure, and some of the rocks have microfractures and corrosion pores, with locally distributed calcite and a few intergranular pores filled with clay minerals; cracks and karst caves are developed; after soaking, a large number of granular or stripped polymers adhere to the rock surface as the number of soaking days increases possibly because clay in the rock expands and then migrates to the rock surface through microfractures as the number of soaking days increases. This shows that the intrusion of fracturing fluid will change the pore structure of

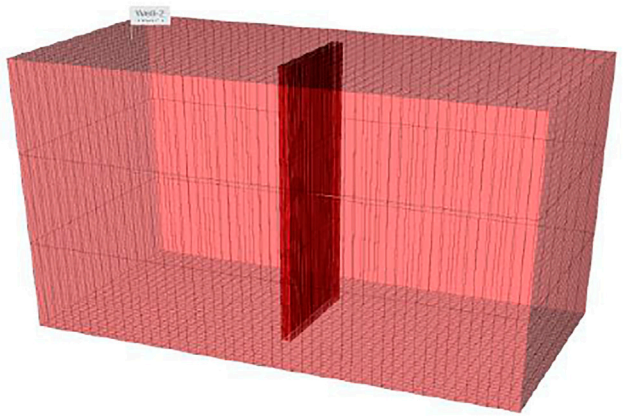

FIGURE 5 | Diagram of the shale gas reservoir mechanism model.

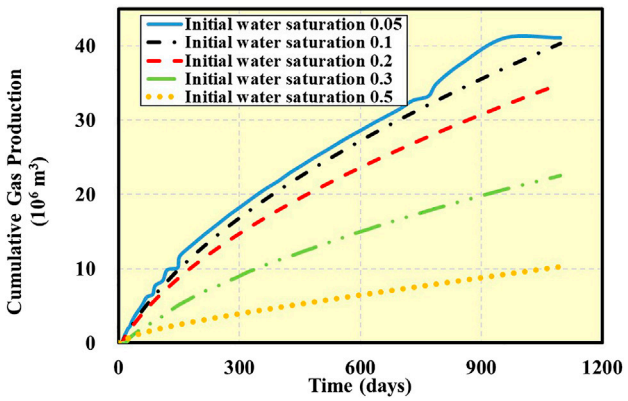

FIGURE 6 | Changing curves of the cumulative gas production after 10-day shut-in and 3-year production for different initial water saturation degrees.

TABLE 1 | Full-scale simulation model description.

Shale reservoir property	
Top height of shale reservoir (m)	3,000
Thickness of shale reservoir (m)	45
Porosity of shale matrix (fraction)	0.038
Permeability of shale matrix (md)	0.0001
Average temperature of shale reservoir (°C)	110
Initial pressure of shale reservoir (kPa)	78,000
Formation compressibility coefficient (1/kPa)	6.90E-06
Langmuir volume (cm^3/g)	3.
Langmuir pressure (kpa)	4,500
Fluid properties	
Hydrocarbon composition	CH_4
Relative gas specific gravity (fraction)	0.65
Formation water volume coefficient (rb/stb)	1
Water compressibility coefficient (1/kPa)	4.35E-07
Water viscosity (cp)	1
Fracture properties	
Main fracture width (m)	0.005
Effective permeability of the fracture (md·m)	65.62
Half-length of the fracture (m)	150
Fracture height (m)	45

shale, which lays a theoretical foundation for the subsequent mechanism analysis of factors influencing the flowback process.

SIMULATION OF FACTORS INFLUENCING THE FLOWBACK PROCESS AFTER SHALE GAS WELL FRACTURING

A dual-porosity/dual-permeability model is used in the research of this study: The matrix is the gas storage space, and the fractures are the main gas seepage channels. The Langmuir isothermal adsorption model is used to describe the desorption process of the gas in the matrix pores. The desorbed gas enters the fractures by diffusion; there is flow between matrixes and between the matrix and the fracture; the gas flow in the fracture system follows Darcy's law.

CMG numerical simulation software is used to establish a shale gas reservoir mechanism model (**Figure 5**), with the dimensions of 1200 m (length) × 600 m (width) × 45 m (height). This gas reservoir model includes a production well with a length of 1000 m, an injection well with a length of 1000 m, and a main fracture through the thickness of the gas reservoir along the horizontal well. The injection well is used to simulate the invasion process of fracturing fluid and assign a value to the initial saturation field in the flowback process after fracturing. The parameters of the reservoir properties are obtained through experiments, and the details are listed in **Table 1**.

Reservoir Properties

(1) Ultralow water saturation

During the reservoir-forming process, there are two ways to form water saturation (Roychaudhuri et al., 2011): displacement of liquid-phase water by the gas phase and liquid-phase water evaporation. In shale gas reservoirs, a phenomenon of "ultralow water saturation" exists; the main reason is that initial water saturation is lower than bound water saturation formed by displacement (Fakcharoenphol et al., 2014). Relevant studies have shown that the evaporation of liquid water during the reservoir-forming process and the natural gas's carrying effect on water vapor (gas-carrying liquid) are the main reasons for this phenomenon (Singh, 2016). The water saturation of the shale in the Sichuan Basin ranges from 30 to 60%; the bound water saturation is approximately 70%; ultralow water saturation exists. However, since the gas–aqueous two-phase relative permeability curve of the shale with a bound water saturation of 70% is difficult to obtain at present, actual values are not used in this article to study the effect of "ultralow water saturation" on the flowback rate and productivity. This study simulates five schemes with the initial reservoir water saturation of 5, 10, 20, 30, and 50% under the condition that the bound water saturation is 40%. The following production system is developed for

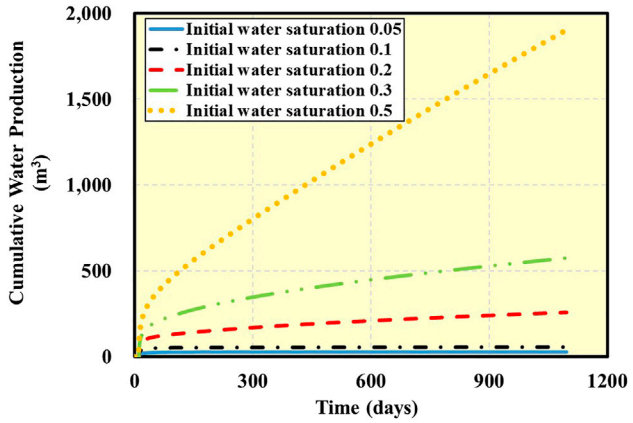

FIGURE 7 | Changing curves of the cumulative water production after 10-day shut-in and 3-year production for different initial water saturation degrees.

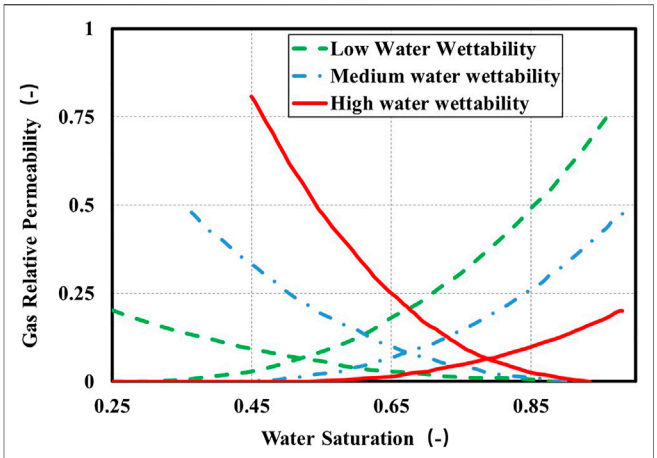

FIGURE 8 | Relative permeability curves for different wettability degrees.

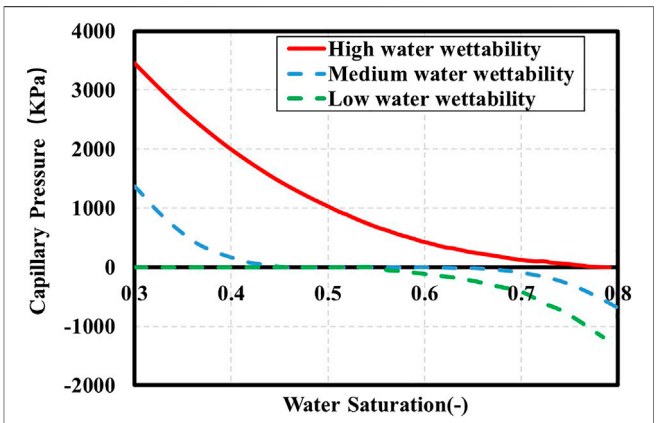

FIGURE 9 | Capillary pressure curves for different wettability degrees.

simulation: 10 days of well shut-in after injection of fracturing fluid and production for 3 years.

It can be seen from the simulation results that as the initial water saturation of the reservoir decreases, that is, the "ultralow water saturation" phenomenon becomes more serious; the higher the cumulative gas production is, the lower the cumulative water production will be. The reason is that the more severe the ultralow water saturation phenomenon is, the larger the fracturing fluid imbibition volume will be, which results in a higher increment of water saturation in the reservoir, larger amount of gas displacement into fractures during imbibition, and higher cumulative gas production (**Figure 6**). For example, for the reservoir with the most severe ultralow water saturation phenomenon (the initial water saturation is 5%), the daily gas production is around 50000 m^3/d; however, for the reservoir without ultralow water saturation (the initial water saturation is 50%), the daily gas production is about 10000 m^3/d. After the reservoir with high initial water saturation is shut in for 10 days, the average water saturation will be higher. The fracturing fluid will hinder the deep gas seepage from the reservoir to the wellbore, reducing long-term gas production. Therefore, the lower the initial water saturation is, that is, the more severe the ultralow water saturation phenomenon is, the higher the cumulative gas production of the reservoir will be. However, since the more severe the ultralow water saturation phenomenon is, the larger the imbibition volume of the reservoir will be, and the flowback of the fracturing fluid entering the matrix with extremely low conductivity through imbibition will be very difficult, and the flowback rate (cumulative water production) will be even lower (**Figure 7**).

(2) Influence of Wettability

There are many different views on the wettability of shale reservoirs. It is generally believed that shale wettability is closely related to TOC and clay content. Organic matters in kerogen are lipophilic, while inorganic matters such as clay, quartz, feldspar, and other minerals are hydrophilic. Most scholars studied the wettability of shale through imbibition experiments and wetting angle tests and believed that the wettability of the shale matrix is oily wettability or mixed wettability. The unclear understanding of wettability will directly affect the construction of capillary pressure and relative permeability curves that can represent real condition, which will further affect the prediction on the fracturing fluid flowback rate and productivity of the shale gas reservoir.

In order to study the influence of wettability, Fakcharonphol (Wang et al., 2016) constructed the relative permeability curves and capillary pressure curves of the reservoirs with high wettability, medium wettability, and low wettability (**Figure 8** and **Figure 9**).

It can be seen from the simulation results that as the degree of wettability decreases, the cumulative gas production decreases, and the cumulative water production gradually increases. The gas production for 3 years under high wettability is much larger than that under low wettability. On the contrary, for cumulative water production, the higher the wettability is, the lower the water

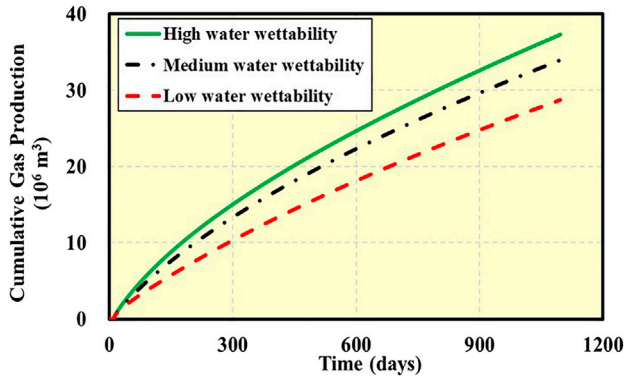

FIGURE 10 | Changing curves of the cumulative gas production after 10-day shut-in and 3-year production for different reservoir wettability degrees.

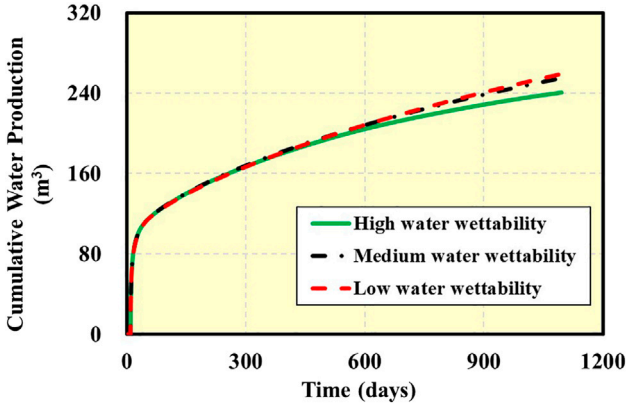

FIGURE 11 | Changing curves of the cumulative water production after 10-day shut-in and 3-year production for different reservoir wettability degrees.

production will be. It is generally believed that if the wettability of the reservoir is high, the liquid phase will form capillary water in the small wet pores after entering the reservoir, blocking the small pores, making it difficult for the gas to break through the high capillary pressure of the pores, which causes serious water blocking (Bimal and Sharma, 2004). However, the simulation results in this study show that the higher the wettability is, the better the gas production will be. According to the analysis, for reservoirs with high wettability, the fracturing fluid near the fracture wall will be quickly adsorbed into the reservoir under the action of strong capillary pressure after the well is shut in (Cheng, 2012), so that the water saturation near the fracture surface decreases, and the damage of water blocking can be reduced. At the same time, the effect of imbibition and displacement is also increased in this process, which improves the gas saturation in the fracture and leads to higher gas production and lower flowback rate (**Figure 10** and **Figure 11**). For reservoirs with low wettability, although the fracturing fluid can enter the reservoir under the pressure

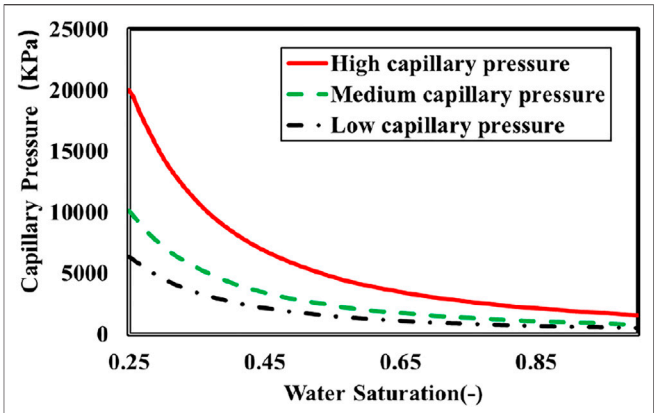

FIGURE 12 | Capillary pressure curves of the matrix.

difference between the well bottom and the reservoir after high-pressure fracturing, the reservoir will show oil-wet after its saturation is increased to be higher than 50%. The resistance of capillary pressure will be reflected: the water intrusion ability will be reduced; the displaced gas will be decreased; the flowback of the fracturing fluid will be increased. For the reservoir with medium wet, the gas and water production changing curves are between those of reservoirs with high and low wettability.

(3) Influence of Capillary Pressure of Reservoir Matrix

The pore throat radius of shale reservoirs is on the micro/nano scale, the capillary pressure generated by the gas–water contact is huge, and some of them even exceed 50 Mpa. The capillary pressure of the shale matrix determines the capability of fracturing fluid imbibition deep into the reservoir during the shut-in process and also determines the resistance of the same matrix water saturation to gas flow during the production process. In order to study the influence of matrix capillary pressure on the flowback rate and productivity, on the premise that all matrix capillary pressure is positive, three different capillary pressure curves (**Figure 12**) are constructed using the formula behind.

$$P_{cD} = 6.895 \times 10^{-3} \frac{\sigma}{a_2 (S_w)^{a_1}} \left(\frac{\varphi}{k}\right)^{a_3}, \quad (1)$$

where P_{cD} is the displacement capillary pressure (MPa); σ is the tension of gas–water contact, taken as 72 dynes/cm; S_w is the water saturation; φ is the porosity; k is the absolute permeability, $\times 10^{-3}$ μm^2; and a_1, a_2, and a_3 are constants, with values of 1.86, 6.42, and 0.5.

The simulation results show that as the matrix capillary pressure increases, the cumulative gas production increases, but the cumulative water production decreases. This is because the reservoirs with high capillary pressure have a strong imbibition effect; more free gas is displaced and enters the fractures, resulting in a high cumulative gas production in the reservoirs with high capillary pressure. Because of the strong imbibition effect of reservoirs with high capillary pressure, the flowback of the fracturing fluid entering the matrix through

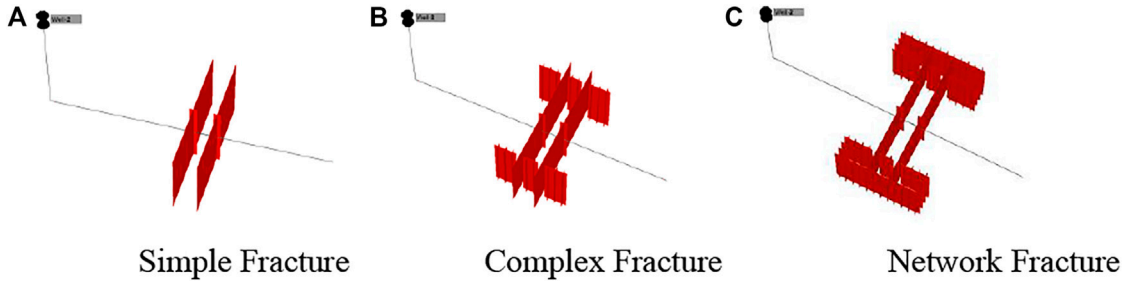

FIGURE 13 | Simulated diagrams of different fracture shapes. (Red areas in the figure **(A–C)** denote for the fracture systems.)

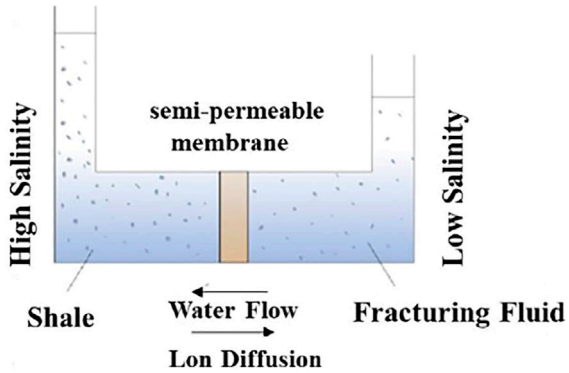

FIGURE 14 | Diagram of the osmosis process.

imbibition will be very difficult, and the flowback rate of the fracturing fluid will inevitably be lower. The pattern in reservoirs with low capillary pressure is completely opposite. For its weak imbibition effect, phenomena of low cumulative gas production and high flowback rate will occur in reservoirs with low capillary pressure .

Fracturing Parameters

(1) Influence of Fracture Half-Length

The cumulative gas production and cumulative water production curves after 3 years when the half-length of the simulated fractures ranges from 100 to 400 m are shown in the following figure. From the simulation results, the higher the cumulative gas production, the lower the cumulative water production will be if the fracture half-length is longer. The fracture half-length of 200 m is the inflection point of the changes of cumulative gas production and cumulative water production. The cumulative gas production increases with the increase in the fracture half-length, but its growth rate gradually slows down. This indicates that the half-length of the fracture network area will be larger than 200 m, and the larger the half-length is, the more beneficial it will be to production.

(2) Influence of Fracture Shape

The influence of three different fracture shapes (including simple, complex, and network fracture shapes) on the production is simulated. In the complex fracture system, two primary fractures are connected by a secondary fracture; in the network fracture system, all primary and secondary fractures are connected with each other (**Figure 13**).

The cumulative gas production and cumulative water production curves for 3 years corresponding to three fracture shapes are as shown in the following figures. It can be seen that the more complex the fracture shape is, the higher the cumulative gas production will be, but with the lower the flowback rate. In the network fracture system, for example, due to the low flow conductivity of the secondary fractures, a large amount of fracturing fluid will be retained in these fractures, resulting in a low flowback rate. Second, the more complicated the fracture network is, the more the fracturing fluid entering into the matrix through filtration will be and the more the liquid that is difficult to return; however, in this case, more gas will be replaced and the flow connectivity of fractures will become higher, which can improve the gas production significantly but make flowback more difficult.

(3) Influence of the Fracture Conductivity

When the fracture conductivity is 40 μm^2 cm during fracturing, it will be beneficial to production. It can be seen from the simulation results that when the fracture conductivity is lower than 40 μm^2 cm, with the increase in the fracture conductivity, the cumulative gas production gradually increases, and the water production increases first and then decreases. However, when the fracture conductivity is higher than 40μm^2 cm, with the increase in the fracture conductivity, the cumulative gas production does not change much and the water production gradually decreases. The reason is that when the conductivity is less than 40 μm^2 cm, with the increase in the fracture conductivity, the flowing capacity of the gas and liquid phases increases, and the water production and gas production become higher; with the further increase in the fracture conductivity, the fracturing fluid entering the formation through filtration increases, more gas is displaced, and the cumulative gas production increases. The effect of fracture

conductivity becomes weak after the fracturing fluid enters the matrix through filtration, which makes flowback difficult. Therefore, the cumulative water production is reduced. When the fracture conductivity is higher than 40 μm^2 cm, the fracturing fluid which enters the matrix through filtration is difficult to flowback, and more gas can be displaced. However, since the fracturing fluid entering deep into the reservoir causes water blocking, the influence of the fracture conductivity on the change of gas production will be small.

(4) Influence of the Number of Fracture Clusters

It can be seen from the simulation results about the effect of the number of fracture clusters on the production that the larger the number of fracture clusters is, the higher the initial gas production and cumulative gas production will be and the lower the flowback rate will be. The reason is that the larger the number of fracture clusters is, the fracture network becomes more developed. The fracturing fluid entering the secondary fractures and the matrix with weak flowing capacity through filtration becomes easier. In this case, the flowback will be more difficult, the cumulative water production will decrease, but the amount of the displaced gas will increase and the gas production will become high.

Drainage–Production System

(1) Shut-In Duration

Simulated the flowback conditions under the difference production conditions immediately produce or shut in for 3, 6, 9, and 12 months after fracturing. The simulation results show that with the increase in the shut-in duration, the initial gas production gradually increases, the later gas production does not change much, and the cumulative water production gradually decreases. The reason is that the longer the shut-in duration is, the stronger the imbibition effect of the micropores will be. The fracturing fluid in the primary fractures will further enter the matrix and secondary fractures through filtration which cause the fluid return difficult, resulting in a lower cumulative water production. The fracturing fluid that enters deep into the matrix will change the pore structure of the reservoir through spontaneous imbibition and hydration to displace more gas, so the initial gas production will be larger. However, since the fracturing fluid deep into the reservoir will cause water blocking due to the increase in water saturation, and the gas production in the later period will not change much.

(2) Influence of the Differential Pressure of Production

It simulated the influence on the production under the differential pressure ranging from 4 to 20 MPa (with 4 MPa interval). It can be seen from the simulation results that the differential pressure of production is the driving force for fluid seepage. The higher the differential pressure is, the higher the cumulative gas production and the flowback rate will be. If the fractures are stable and do not cause the propane flowback, a higher differential pressure shall be adopted for drainage and production. It can be seen from the figure that when the differential pressure of production is higher than 12 MPa, the increase in 3-year cumulative gas production is slightly slowed down. Therefore, the optimal differential pressure of production in this block shall be higher than 12 MPa.

Influence of the Osmotic Pressure

The microscopic mechanism of semipermeable membrane effect of the shale is explained in this section. The shale has a semipermeable membrane effect. Only water molecules are allowed to pass, but saline ions or some saline ions are not allowed to pass. The semipermeable membrane effect is a key factor causing the osmotic pressure, and the microscopic mechanism of the semipermeable membrane effect can be explained by the theory of clay diffuse double layer (DDL). Clay particles are negatively charged, and in order to maintain electrical neutrality, a large amount of positive ions must be adsorbed on the surface. Since the adsorbed positive ions aggregate on the surface of the clay particles, the concentration of positive ions around the particles is higher than that of the bulk solution. Under the effect of concentration difference and thermal motion of molecules, the positive ions tend to diffuse into the solution (**Figure 14**). The clay DDL is the result of the combined action of surface adsorption and diffusion.

Osmosis refers to the phenomenon that water molecules pass through a semipermeable membrane from the low-salinity solution side to the high-salinity solution side to maintain the salinity balance. The pressure of the high-salinity solution is increased during the osmosis process. This pressure is called osmotic pressure. Kurtoglu (2013) believes that the contact surface between the fracturing fluid and shale has a semipermeable membrane effect. The salinity of the slick water fracturing fluid is about 1–5 kppm, while the salinity of the shale reservoir can be as high as 280 kppm. After a large amount of low-salinity slick water fracturing fluid is injected into the formation, under the action of the osmotic pressure, the water enters the reservoir matrix through the semipermeable membrane effect of the shale. Under the action of an ideal semipermeable membrane, only water molecules can pass through the semipermeable membrane, while the ions in the solution could not pass through the semipermeable membrane. Therefore, a high pressure difference will be generated between both sides of the semipermeable membrane. The shale has a nonideal semipermeable membrane effect, which means water molecules can freely pass through the semipermeable membrane, but the saline ions in the fracturing fluid could not pass through or could only partially pass through the semipermeable membrane.

The influence on the production is simulated in the following situations: the salinity of the formation water and injected fracturing fluid is not taken into consideration. The formation water salinity is 280,000 ppm, and the salinity of the injected fracturing fluid is 100,000 ppm, 10,000 ppm, and 1,000 ppm. It can be seen from the simulation results that the chemical potential difference has a significant influence on both gas production and water production. As the salinity of the injected fracturing fluid gradually decreases, that is, the chemical potential difference gradually increases, the

cumulative gas production increases, while the cumulative water production decreases. The reason is that as the chemical potential difference increases, more fracturing fluid enters the formation matrix through osmosis and the flowback will be difficult. After entering the matrix, the fracturing fluid will induce the formation of more microfractures under the effect of spontaneous imbibition and hydration, or make the originally closed natural fractures reopen, so as to displace more gas and improve production.

CONCLUSION

The physical properties of shale reservoirs in the Sichuan Basin are studied and analyzed through the combination of experiments method and numerical simulation method. On this basis, the factors influencing the gas production and water production in the fracturing fluid flowback process after hydraulic fracturing are studied, and the following conclusions are reached:

(1) The porosity of the core samples from the Sichuan Basin ranges from 0.39 to 9.729%, with an average of 3.834%; the permeability of the shale matrix is about $10^{-4} \times 10^{-3}$μm^2; main mineral components include quartz, feldspar, calcite, dolomite, clay, and pyrite. The results of the wettability test show that as the soaking time increases, the measured wetting angle gradually decreases and the rock hydrophilicity increases.
(2) The shale outcrop in the Sichuan Basin has a dense rock structure, and some of the rocks have microfractures and corrosion pores, with locally distributed calcite and a few intergranular pores filled with clay minerals; cracks and karst caves are developed. A large number of granular or stripped polymers adhere to the rock surface as the number of soaking days increases. This indicates that the intrusion of fracturing fluid will change the pore structure of shale, which lays a theoretical foundation for the subsequent mechanism analysis of factors influencing the flowback process.
(3) According to the numerical simulation based on the flowback process mechanism model established for the fractured shale gas well, factors such as reservoir properties, fracturing parameters, drainage–production system, and chemical osmosis all have an impact on water production and gas production in the flowback process. With the analysis of the influencing mechanism of various sensitive factors on water and gas production, it is concluded that if various influencing factors can contribute to the further filtration of the injected fracturing fluid into the shale reservoir, the flowback of the fracturing fluid in the matrix and secondary fractures will be difficult due to their weak conductivity, so the cumulative water production will also become lower. However, the fracturing fluid that enters the reservoir through filtration will change the pore structure of the shale through spontaneous imbibition and hydration or osmosis, which can provide more gas flow channels to displace more gas and increase the cumulative gas production. The influence of most influencing factors on gas and water production shows that the higher the cumulative water production of shale gas well is, the lower the corresponding cumulative gas production will be. The influencing mechanisms of various factors should be taken into comprehensive consideration in the development of a reasonable drainage–production system, to optimize various control parameters and achieve the purpose of improving gas well productivity. This study can lay a theoretical foundation for the development of the drainage–production system.

DATA AVAILABILITY STATEMENT

The original contributions presented in the study are included in the article/supplementary material; further inquiries can be directed to the corresponding author.

AUTHOR CONTRIBUTIONS

JW: Overall article structure planning and technical check YD: This paper mainly studies people and writers JZ: Geological content researcher PL: Article layout correction and translation DZ: Numerical simulation study YW: Experimental data processing HZ: Summary of current situation at home and abroad.

FUNDING

This work was financially supported by the Research on Improvements ff the Producing Degree in Shale (kt 2021-11-02), the Major Technical Field Test Project of PetroChina (2019F-31-02), the National Key Research and Development Program (2018YFF0213802-02), and the Science and Technology Cooperation Project of the CNPC-SWPU Innovation Alliance (2020CX020202).

REFERENCES

Bian, X., Jiang, T., and Ran, W. (2016). Optimization of the Controlling Parameters of the Post-frac Flowback and Production for Normal-Pressure Shale-Gas Horizontal Wells [J]. *Pet. Geology. Oilfield Dev. Daqing* 35 (5), 170–174. doi:10.3969/J.ISSN.1000-3754.2016.05.034

Bimal, P., and Sharma, M. (2004). "Cleanup of Water Blocks in Depleted Low Permeability Reservoirs[C," in SPE Annual Technical Conference and Exhibition (Houston, Texas, USA: Society of Petroleum Engineers).

Chen, Shouyu., Shuzhi, Xiu., and Song, Bo. (2016). Research on Dynamic Simulation of Fracturing Fluid Flowback in Shale Gas Wells [J]. *Sino-Global Energy* 21 (7), 43–50.

Cheng, Y. (2012). Impact of Water Dynamics in Fractures on the Performance of Hydraulically Fractured wells in Gas-Shale Reservoirs [J]. *J. Can. Pet. Tech.* 51 (2), 143–151. doi:10.2118/127863-pa

Crafton, J. W., and Gunderson, D. W. (2006). *Use of Extremely High Time-Resolution Production Data to Characterize Hydraulic Fracture Properties [J].*

Dehghanpour, H., Lan, Q., Saeed, Y., Fei, H., and Qi, Z. (2013). Spontaneous Imbibition of Brine and Oil in Gas Shales: Effect of Water Adsorption and

Resulting Microfractures. *Energy Fuels* 27 (6), 3039–3049. doi:10.1021/ef4002814

Engelder, T., Cathles, L. M., and Bryndzia, L. T. (2014). The Fate of Residual Treatment Water in Gas Shale. *J. Unconventional Oil Gas Resour.* 7, 33–48. doi:10.1016/j.juogr.2014.03.002

Fakcharoenphol, P., Kazemi, H., and Charoenwongsa, S. (2014). *The Effect of Osmotic Pressure on Improve Oil Recovery from Fractured Shale Formations [C]//Spe Unconventional Resource Conference*.

Guo, X., Wang, J., and Liu, X. (2016). Gas-Water Two Phase Porous Flow Model of Fractured Horizontal Well in Shale Gas Reservoir [J]. *Acta Petrolei Sinica* 37 (9), 1165–1170. doi:10.7623/syxb201609011

Jiang, T., Bian, X., and Wang, H. (2013). Flow Back Mechanism Study of Multi-Stage Fracturing of Shale Gas Horizontal Wells [J]. *Pet. Drilling Tech.* (5), 21–25. doi:10.3969/j.issn.1001-0890.2013.05.004

Kurtoglu, B. (2013). Integrated Reservoir Characterization and Modeling in Support of Enhanced Oil Recovery for Bakken [J]. *Dissertations & Theses - Gradworks* 8, 1505–1508.

Li, Y., Chen, X., and Jiang, Y. (2019). Gas-water Two-phase Productivity Analysis for the Fractured Horizontal Well in Shale Reservoirs [J]. *Pet. Geology. Recovery Efficiency* 026 (003), 117–122. doi:10.13673/j.cnki.cn37-1359/te.2019.03.016

Liu, N., Liu, M., and Zhang, S. (2015). Flowback Patterns of Fractured Shale Gas Wells [J]. *Nat. Gas Industry* 35 (3), 50–54. doi:10.3787/j.issn.1000-0976.2015.03.007

Ll, A., Yw, B., and Saaa, C. (2021). Insights into Scale Translation of Methane Transport in Nanopores[J]. *J. Nat. Gas Sci. Eng* 96, 104220. doi:10.1016/j.jngse.2021.104220

Roychaudhuri, B., Tsotsis, T., and Jessen, K. (2011). An Experimental and Numerical Investigation of Spontaneous Imbibition in Gas Shales [J]. *J. Pet. Sci. Eng.* 111 (11), 87–97. doi:10.2118/147652-ms

Singh, H. (2016). A Critical Review of Water Uptake by Shales. *J. Nat. Gas Sci. Eng.* 34, 751–766. doi:10.1016/j.jngse.2016.07.003

Wang, F., Pan, Z., and Zhang, S. (2016). Modeling Fracturing-Fluid Flowback Behavior in Hydraulically Fractured Shale Gas under Chemical Potential Dominated Conditions. *Appl. Geochem.* 74, 194–202. doi:10.1016/j.apgeochem.2016.10.008

Wang, J., and Rahman, S. S. (2015). *An Investigation of Fluid Leak-Off Due to Osmotic and Capillary Effects and its Impact on Micro-fracture Generation during Hydraulic Fracturing Stimulation of Gas Shale[C]//Europec*.

Williams-Kovacs, J. D., Clarkson, C. R., and Zanganeh, B. (2015). *Case Studies in Quantitative Flowback Analysis[C]//SPE/CSUR Unconventional Resources Conference*.

Wu, J. D., Huang, C. Y., and Liao, C. C. (2003). Fracture Strength Characterization and Failure Analysis of Silicon Dies. *Microelectronics Reliability* 43 (2), 269–277. doi:10.1016/s0026-2714(02)00314-1

Zhang, L., Kang, Q., and Yao, J. (2014). The Explanation of Low Recovery of Fracturing Fluid in Shale Hydraulic Fracturing by Pore-Scale Simulation [J]. *Chin. Sci. Bull.* (32), 3197–3203. doi:10.1360/N972014-00461

Zhang, T., Li, X., and Yang, L. 2017, Effects of Shut-In Timing on Flowback Rate and Productivity of Shale Gas Wells [J]. *Nat. Gas Industry* 037 (8), 48–60. doi:10.3787/j.issn.1000-0976.2017.08.006

Zhou, Z., Hoffman, B. T., Bearinger, D., and Li, X. (2014). "Experimental and Numerical Study on Spontaneous Imbibition of Fracturing Fluids in Shale Gas Formation," in [C]//Society of Petroleum Engineers - Spe Canadian Unconventional Resources Conference, 425–437. doi:10.2118/171600-ms

Conflict of Interest: All authors are employed by the company Petrochina Southwest Oil & Gasfield Company.

frontiers in Earth Science

ORIGINAL RESEARCH
published: 03 January 2022
doi: 10.3389/feart.2021.794534

CO_2 Mass Transfer and Oil Replacement Capacity in Fractured Shale Oil Reservoirs: From Laboratory to Field

Runwei Qiao[1], Fengxia Li[2], Shicheng Zhang[1], Haibo Wang[2], Fei Wang[1] and Tong Zhou[2]*

[1]State Key Laboratory of Petroleum Resources and Prospecting, China University of Petroleum, Beijing, China, [2]Petroleum Exploration and Production Research Institute, SINOPEC, Beijing, China

CO_2-based fracturing is widely introduced to stimulate shale oil reservoirs for its multiple advantages. However, the range of CO_2 entering the matrix around fractures and CO_2-oil replacement capacity between matrix and fractures cannot be fully explained. To address this issue, a radial constant volume diffusion experiment on shale cores was designed in this study, and the pressure drop curve history was matched through numerical model to determine the composition effective diffusion coefficient. A field-scale numerical model was established, in which a series of certain grids were used to explicitly characterize fracture and quantify the prosess of CO_2 mass transfer and oil replacement. Based on the field-scale numerical model, the process of shut-in, flow back, and oil production was simulated. The distribution of CO_2 in fractured shale oil formation and its impact on crude oil during shut-in stage and flow back stage were investigated. This study concludes that CO_2 gradually exchanges the oil in matrix into fractures and improve the fluidity of oil in matrix until the component concentrations of the whole reservoir reaches equilibrium during the shut-in process. Finally, about 30~35 mole % of CO_2 in fractures exchanges for oil in matrix. The range of CO_2 entering the matrix around fractures is only 1.5 m, and oil in matrix beyond this distance will not be affected by CO_2. During the process of flow back and production, the CO_2 in fracture flows back quickly, but the CO_2 in matrix is keeping dissolved in oil and will not be quickly produced. It is conclued that the longest possible shut-in time is conducive to making full use of the CO_2-EOR mechanism in fractured shale oil reservoirs. However, due to the pursuit of economic value, a shut-in time of 10 days is the more suitable choice. This work can provide a better understanding of CO_2 mass transfer mechanism in fractured shale oil reservoirs. It also provides a reference for the evaluation of the shut-in time and production management after CO_2 fracturing.

Keywords: fractured shale oil reservoirs, carbon dioxide, mass transfer, CO_2-oil replacement, reservoir simulation

OPEN ACCESS

Edited by:
Feng Yang,
China University of Geosciences Wuhan, China

Reviewed by:
Junjing Zhang,
ConocoPhillips, United States
Nie Xiangrong,
Xi'an Shiyou University, China

****Correspondence:***
Fei Wang
wangfei@cup.edu.cn

Specialty section:
This article was submitted to Economic Geology, a section of the journal Frontiers in Earth Science

Received: *13 October 2021*
Accepted: *24 November 2021*
Published: *03 January 2022*

Citation:
Qiao R, Li F, Zhang S, Wang H, Wang F and Zhou T (2022) CO_2 Mass Transfer and Oil Replacement Capacity in Fractured Shale Oil Reservoirs: From Laboratory to Field. Front. Earth Sci. 9:794534. doi: 10.3389/feart.2021.794534

INTRODUCTION

Horizontal drilling and Hydraulic fracturing technologies have substantially increased oil production from unconventional resources (Zou et al., 2013; Zhao et al., 2018). The slick water fracturing fluid system is widely used in the process of hydraulic fracturing due to its high efficiency and low cost. However, a series of problems have also been introduced such as easily causing clay swelling,

reducing formation permeability and consuming water resources (Myers, 2012; Vengosh et al., 2013). Introducing CO_2 as a fracturing fluid seems to have broad application prospects for its multiple advantages (Liu et al., 2014; Meng et al., 2016; Wang et al., 2016b; Jin et al., 2017). Extensive experimental studies (Zhou et al., 2016; Zou et al., 2018; Li et al., 2019; Li et al., 2020a; Li et al., 2020b) and numerical simulation studies (Li et al., 2018b; Li and Zhang, 2019; Meng et al., 2019; He et al., 2020) have shown that CO_2 fracturing fluid is beneficial to fracture morphology and fracture scale. Moreover, CO_2-water-rock reaction also plays a positive role in the realization of large-scale hydraulic fracturing (Fischer et al., 2010; Zhang et al., 2018; Tian et al., 2020; Zhou et al., 2020a). In addition to the benefits of CO_2 for fracture propagation and fracture morphology, another huge advantage of CO_2 fracturing is the CO_2-oil interactions.

The subject on CO_2 enhancing oil recovery (EOR) in conventional oil and gas reservoir has been widely investigated. CO_2 flooding and CO_2 huff-n-puff has become an important means of enhancing oil reservoir production due to the behaviors of CO_2 such solubility, miscibility, reducing viscosity, and suppling oil pressure after it contacts with crude oil (Habibi et al., 2017a; Habibi et al., 2017b). However, There is a big difference on the EOR mechanism of CO_2 between unconventional formation and conventional formation mainly caused by the difference of transport mechanisms (Sorensen et al., 2015; Lu et al., 2016; Wang et al., 2016a; Zhou et al., 2019; Song et al., 2020).

In conventional reservoirs, the injected CO_2 flows through the rock matrix and sweeps the oil out. However, in unconventional fractured reservoirs, CO_2 will flow most rapidly through the major and minor fractures, but not significantly through the unfractured rock matrix due to the characteristics of low permeability and low porosity of rock matrix (Hawthorne et al., 2013, Hawthorne et al., 2014; Alharthy et al., 2015; Alfarge et al., 2018). In the early socking stage, pressure gradient between the fracture and the matrix lead to CO_2 penetrating into limited rock matrix maily known as solution-gas drive. As the shut-in stage continues, advective mass transfer gradually weaken, and CO_2 penetrates further into the matrix maily through diffusive mass transfer (Wei et al., 2020). During the whole socking satge, the CO_2 transported into the matrix dissolve into oil and causes oil swelling, viscosity reduction. In addition, the pressure slightly increases in the matrix around fractures and this creates a local gradient where oil is extracted out of the matrix through fractures (Hawthorne et al., 2014).

It is concluded that diffusive mass transfer contributes CO_2 transported further into the matrix, which may become the dominating transfer mechanism as pressure approaches equilibrium, until CO_2 concentration equilibrium in oil phase is approached (Sorensen et al., 2015; Yu et al., 2015; Alfarge et al., 2018; Santiago and Kantzas, 2020). Thus, research on the diffusion of CO_2 in porous media has become a vital subject for investigating CO_2-EOR mechanisms in unconventional reservoirs. In previous experimental studies, indirect methods are mainly carried out to determinate the CO_2 effective diffusion coefficient in laboratory. The process of CO_2 diffusion in bulk liquid or in porous media is indirectly reflected by measuring and recording experimental data, including pressure decay, volume change, gas-liquid interface location (Trivedi and Babadagli, 2009; Ghasemi et al., 2018; Zhou et al., 2020b).

Among the different experimental methods, the pressure decay method is applied most commonly, such as the constant volume diffusion (CVD) method and radial constant volume diffusion (RCVD) method. Scholars usually dertermined the CO_2 effective diffusion coefficient through establishing diffusion mathematical models with different factors considered (Li et al., 2016; Li et al., 2018a; Zhou et al., 2020b) or using commercial reservoir simulators (Ghasemi et al., 2016; Ghasemi et al., 2017; Tsau and Barati, 2018) and then historymatching the pressure profile. It is widely believed that the CO_2 effective diffusion coefficient ranges from 10^{-10} to 10^{-9} m^2/s, and lower viscosity of crude oil, higher temperature, and higher pressure facilitate the diffusion of CO_2 into crude oil, under tight formation conditions (Li et al., 2018a; Fayazi; Amir and Apostolos, 2019; Zhou et al., 2020b).

Although the diffusion phenomenon in the laboratory is widely studied, there are few studies on the role of CO_2 diffusion in field-scale simulation. The phenomenon that the distance of CO_2 penetrating the matrix from fractures is usually several meters cannot be captured with the grids of several meters to tens of meters used in field-scale simulation (Alharthy et al., 2015; Ribeiro et al., 2015; Kanfar and Clarkson, 2017; Zuloaga et al., 2017; Zhang et al., 2019). Moreover, the dua-porosity model applied generally to simulate fractured reservoirs uses two independent sets of grids to simulate fractures and matrix respectively, which results that transient mass transfer process cannot be identified in the matrix adjacent to the fractures (Hoteit, 2011; Ghasemi and Suicmez, 2019).

In this study, a radial constant volume diffusion experiment on kerosene saturated shale cores was designed. and the pressure drop curve history was matched through numerical model to determine the composition effective diffusion coefficient. A field-scale numerical model based on data obtained in the laboratory was established, in which a series of certain grids were used to explicitly characterize fracture instead of a dual-porosity model to quantify the prosess of CO_2 mass transfer and oil replacement. Through local refined grid of matrix around fractures, the true mass transfer distance of CO_2 is obtained. In order to establish the initial shut-in conditions after CO_2 fracturing, the porosity-permeability-pressure correlation curve of the fracture grids based on the fracture propagation numerical simulation results was used. Based on the field-scale numerical model, the process of shut-in, flow back and oil production after CO_2-fracturing was simulated. The distribution of CO_2 in fractured shale oil formation and its impact on crude oil during shut-in stage and flow back stage were investigated.

EXPERIMENTAL SECTION

Physical Model

The Radial-Constant-Volume-Diffusion (RCVD) method is adopted for this study, which physical model is shown in **Figure 1** (Li S. et al., 2018). A core sample with two end faces

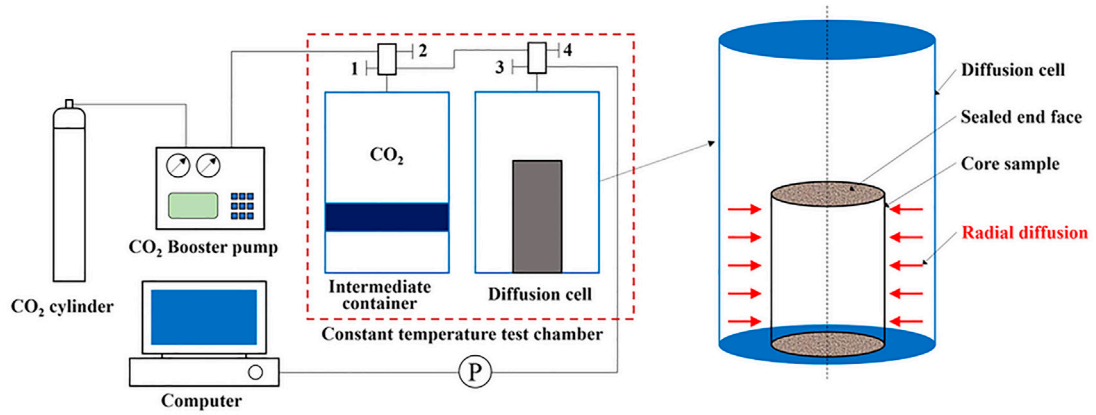

FIGURE 1 | Schematic diagram of experimental apparatus and the physical model for CO_2 diffusion.

TABLE 1 | Physical properties for the core samples with different test pressures at 46.4°C.

Test no.	Core diameter (mm)	Core length (mm)	Permeability (mD)	Porosity (%)	Test pressure (MPa)
1	25.39	56.39	0.311	10.83	14.1
2	25.35	63.54	0.192	9.26	20.8

TABLE 2 | Measured properties for the experimental oil sample and crude oil used in simulation.

Parameter	Kerosene	Live oil
Crude oil density (kg/m3) at 13.5 Mpa, 46.4°C	751.09	820.1
Crude oil viscosity (mPa·s) at 13.5 Mpa, 46.4°C	2.51	2.79
Solution gas-oil ratio (GOR) (Sm3/m3)	—	32.84
Saturation pressure (MPa)	—	7.39

sealed is positioned vertically in a diffusion cell. The gas diffusion occurs only along the radial direction as illustrated in **Figure 1**. The decrease of pressure in the diffusion cell is recorded as a function of time to generate a pressure decay curve which is used for determining the effective diffusion coefficient. The greater side surface area of the core sample provides a greater diffusion flux, and this advantage makes the measured pressure decay curve less sensitive to the environment than the constant volume diffusion (CVD) method (Li and Dong, 2009).

MATERIALS

Two core samples used in the experiments are collected from shale oil formation in the Ordos Basin, China, where its depth is 1,440 m at 46.4°C. After dring the core samples are dried at 105°C to constant weight, The permeabilities are determined with nitrogen gas flooding, and the porosities are determined using the Helium Porosimeter (**Table 1**). The core saturated with live oil cannot be put into the diffusion cell under high pressure in the experiment. As a compromise, kerosene withnot dissolved gas from the lab was used as experimental oil. As shown in **Table 2**, the viscosity and density of experimental oil are close to those of crude oil in the target formation characterized as a light oil. The CO_2 gas with purity of 99.99% were used.

Experimental Apparatus

The experimental apparatus is schematically shown in **Figure 1**. The core samples are placed vertically in the center of the diffusion cell with inner diameter of 37 mm and depth of 95 mm. The CO_2 in the container is supplied from a CO_2 cylinder, whose pressure can be controlled by a high-pressure booster pump. A constant temperature test chamber of accuracy 0.1°C is used to control the temperature of the CO_2 container and the diffusion cell (dotted area in **Figure 1**). The pressure transducer with full scale pressure of 40.0 MPa and full scale accuracy of 0.5% is used to measure the pressure of the diffusion cell.

Experimental Procedures

The procedure for conducting the diffusion experiments is briefly described as follows:

1) The core sample is cleaned and dried at 105°C to constant weight. Then, the permeability is determined with nitrogen gas flooding, and the porosity is determined using the Helium Porosimeter.
2) The core sample is placed in a container, and evacuated for more than 10.0 h. The experimental oil is pumped into the

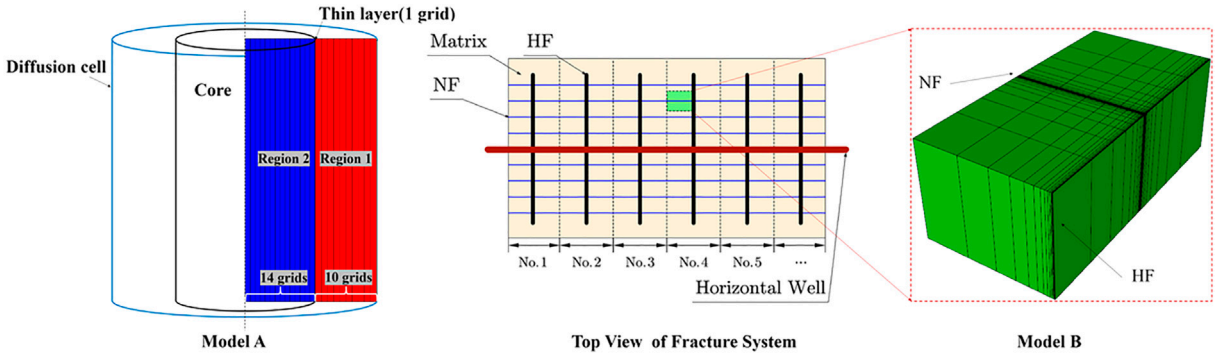

FIGURE 2 | Grid settings of model **(A)** and model **(B)**.

container under indoor temperature until the pressure reaches the test pressure. It is laid aside for 48.0 h for oil saturating.

3) After oil saturating, epoxy, and aluminum foil are used to seal the two end faces of the cylindrical core sample to establish an environment for radial diffusion.
4) The equipment required for the diffusion experiments is connected and the air tightness of the equipment is tested. Then, the core sample is placed into the diffusion cell. Low pressure CO_2 is injected into it to replace air.
5) Intermediate container and the diffusion cell are placed into the constant temperature test chamber. When the required temperature of test chamber is stable, open valve 2, pump CO_2 into intermediate container from the CO_2 cylinder, adjust the booster pump to ensure the pressure in the intermediate container reach the required test pressure. Then, the intermediate container and diffusion cell are kept in test chamber for 2.0 h at the constant test temperature and pressure to make CO_2 reach stabilization.
6) Open valve 3 to measure the pressure of the diffusion cell with the pressure transducer. Then, open valves 1 and 4 to connect the intermediate container full of high pressure CO_2 with the diffusion cell. After the pressure of the diffusion cell reaches a relative stable value within 1–2 min, close valves 1 and 4 quickly. Record the pressure data of the pressure transducer.
7) When the pressure of the diffusion cell no longer changes, the experiment can be stopped. Open all the valves of the diffusion cell slowly, discharge the remained CO_2, take out the used core sample, and clean the equipment.

NUMERICAL SIMULATION

Model Description

In this paper, two base numerical models are established. Model A is a 2-D laboratory-scale model with a cylindrical (radial-angular) grid type used to determine the CO_2 effective diffusion coefficient by historymatching the pressure decay curve of the diffusion experiments. Model B is a 2-D field-scale model used to investigate the distribution of CO_2 in the fractured shale oil reservoir after CO_2-fracturing during the process of shut-in, flow back and oil production.

Gridding and Model Set up

The commercial reservoir simulator GEM™ from CMG is used to construct numerical models in this study. The model A is represented by two regions with distinct properties. We refer the void space of the diffusion cell excluding the core as Region 1, and the core sample as Region 2. Although the height of the diffusion cell is not equal to the length of the core, according to the assumption that only Radial diffusion happens the RCVD experiment, we scale the height of the diffusion cell to be consistent with the length of the core in the model, keeping the void space volume constant.

A series of grids are set in the radial direction to capture the process of CO_2 diffusion, butonly one grid is set in both the axial direction and the circumferential direction (**Figure 2**), as the effect of gravity is ignored and the diffusion process is hypothetically symmetric in the circumferential direction. In addition, a thin layer (0.1 mm) is set at the interface between Region 1 and Region 2; it acts as a contact zone connecting the oil and gas phase to capture the diffusion transfer mechanism (Tsau and Barati, 2018). Therefore, the number of grids in model A is $25 \times 1 \times 1 = 25$, which are found to be sufficient to eliminate numerical effects.

Model B as a 2-D field-scale model includes three systems: matrix (M), hydraulic fracture (HF), and natural fracture (NF) drawing on (Zhang et al., 2017)' study (see **Figure 2**). It is assumed that the fracture system after fracturing is composed of HFs and NFs, where HFs are evenly distributed in the horizontal well and symmetrically distributed on both sides of the horizontal well. NFs are orthogonal to HFs with the same spacing and length. Only a segment of SRV region is simulated and then the results can be scaled back to the full lateral. In addition, the method of fracture permeability stress sensitivity is also used for approximately simulating the process of fracturing, which needs injecting a large amount of CO_2 into the formation in a short time (Zhang et al., 2017).

The scale of grid system is $16 \times 31 \times 1$ cells with 0.008 m width of HFs and 0.004 m width of NFs. Due to the drastically pressure and saturation changing in the regions near the fracture face, the size of grids increases logarithmically along planes of HFs and NFs to the reservoir matrix perpendicularly. The fracture width of HFs and NFs in this model is wider than reality to ensure

TABLE 3 | Grid properties for model B.

Reservoir thickness, m	16	Matrix porosity	0.1
Reservoir depth, m	1,440	Matrix permeability, mD	0.25
Reservoir temperature, °C	46.4	Matrix water saturaion	0
Reservoir pressure, MPa	13.5	Matrix compressibility, kPa-1	0.000004
HF half-length, m	100	NF half-length, m	12.5
HF height, m	16	NF height, m	16
HF spacing, m	25	NF spacing, m	25
HF aperture, m	0.008	NF aperture, m	0.004
HF porosity	0.6	NF porosity	0.6
HF permeability, D	2,500	NF permeability, D	100
HF conductivity, D·cm	2	NF conductivity, D·cm	0.04

numerical stability however still honors real dimensionless fracture conductivities. In other words, to be consistent with the real fracture conductivity, any widening of the fracture width in the model is compensated for by reduced fracture permeability.

Fluid Flow Mechanism

Advective flow and molecular diffusion are considered in this study. Advection is a transport mechanism that is based on pressure and gravity gradients. Gravity drainage is ignored in this study because it is a minor force in a liquid-rich shale reservoirs with low permeable matrix (Alharthy et al., 2015). The contribution from the pressure gradient can be through changes of pressure during fracturing and producion stages and also as a result of oil swelling. The oil swelling during CO_2 exposure causes reduction in hydrocarbon density, viscosity and interfacial tension. This in turn promotes CO_2-hydrocarbon interaction, miscibility, and oil mobility. Molecular diffusion mass transport is driven by chemical potential gradient of the molecular species and is rather slow as an oil recovery mechanism; however, miscibility of CO_2 and oil in a narrow region near the fracture-matrix surface interface is the main mechanism of oil extraction from the tight oil matrix. Thus, in this short distance, the role of molecular diffusion cannot be ignored.

Input Parameters

Parameters of core properties and fluid properties inputted in the laboratory-scale model (Model A) remain consistent with the diffusion experiments. According to (Tsau and Barati, 2018)'s research, the value of entry capillary pressure (Pe) is set to 0.69 kPa, the purpose of which is to keep the oil phase (wetting phase) held in the center of core cell.

The parameters of reservoir properties (**Table 3**) and fluid properties (**Table 2**) inputted in the field-scale model is from shale oil formation in the Ordos Basin, China. The target reservoir has low pressure and temperature, in which the crude oil is undersaturated, of low gas-oil ratio and of low viscosity. Considering that the solubility of CO_2 in oil phase is far greater than that in the water phase, the reaction between formation water and CO_2 is ignored this simulation. The parameters of the fracture system used in model B is from the research of (Zhang et al., 2017).

To simulating the process of fracturing, 28.8 m^3 of supercritical CO_2 (46.4°C, 13 MPa) is designed to be injected into model B within 1 h, equivalent to 230.4 m^3 of supercritical CO_2 fracturing fluid to create a SRV region of 25 m width in the formation of 16 m height.

Considering that in the process of fracturing fluid injection, the fractures with high conductivity will only form when the fluid pressure is greater than the breakdown pressure of the formation, while matrix permeability will increase, stress-dependent permeability of fracture grids is necessary. The following exponential empirical formula **Eq. 1** can be used to describe the permeability changing with the pressure.

$$\frac{K}{K_0} = 10^{mP_{net}} \tag{1}$$

Where K is current permeability, mD; K_0 is original permeability, mD; m is the permeability changing factor (exponent determined empirically), kPa^{-1}; P_{net} is net pressure (difference between original reservoir pressure and current gird cell pressure), kPa. The values of permeability changing factor m during the injection process are 0.197, 0.0943, and 0.116, respectively, and the production process are 0.197, 0.0276, and 0.131, respectively (Zhang et al., 2017). The result can be seen in the **Figure 3**.

Compositional Modeling

Considering the interaction between CO_2 and crude oil, compositional modeling is needed. The component compositions of kerosene used in model A and crude oil used in Model B are measured in the laboratory; the component critical properties (**Table 4**, **5**) are correctted by fitting a series of PVT experiments (such as CCEs, Swelling Tests) based on PR-EOS. For the crude oil components of the reservoir, proper combination of components is carried out to improve the calculation efficiency. The jobs of compositional modeling mentioned above are completed by the equation of state multiphase equilibrium property simulator Winprop™ from CMG.

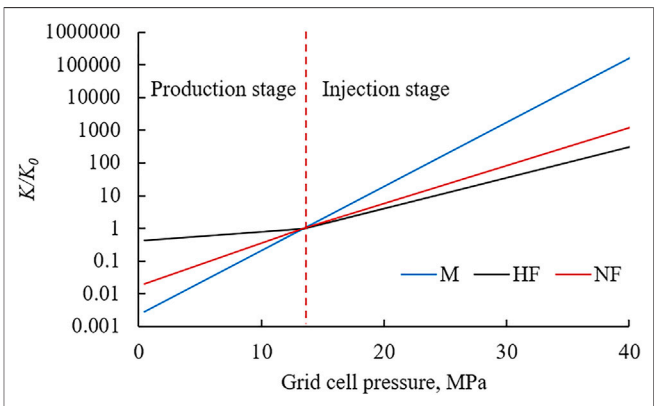

FIGURE 3 | Stress-dependent permeability during injection and production stage.

TABLE 4 | Composition and properties of experimental oil components.

Component	Mole frac (%)	Critical pressure (atm)	Critical temperature (K)	Acentric factor	Molecular weight (g/mol)
CO_2	—	72.8	304.2	0.225	44.01
C_8	4.867763	29.12	570.5	0.351327	107
C_9	19.55248	26.94	598.5	0.390781	121
C_{10}	24.60757	25.01	622.1	0.443774	134
C_{11}	19.82943	23.17	643.6	0.477482	147
C_{12}	13.58134	21.63	663.9	0.522263	161
C_{13}	11.53576	20.43	682.4	0.559558	175
C_{14}	2.99962	19.33	700.7	0.604823	190
C_{15}	2.794072	18.25	718.6	0.651235	206
C_{16}	0.231965	17.15	734.5	0.683728	222

TABLE 5 | Composition and properties of live oil pseudo-component.

Component	Mole frac (%)	Critical pressure (atm)	Critical temperature (K)	Acentric factor	Molecular weight (g/mol)
CO_2	—	72.8	304.2	0.225	44.01
C_1	19.78552	45.4	190.6	0.008	16.043
C_2-C_3	5.613936	45.00811	339.36685	0.125	37.0835
C_4-C_6	6.770647	33.390805	480.55144	0.24959292	77.12715
C_7-C_{12}	33.58425	26.947594	596.0906	0.3915828	120.42275
C_{13}-C_{34+}	34.24564	14.419591	776.46775	0.84967219	335.75825

DETERMINATION OF CO_2 EFFECTIVE DIFFUSION COEFFICIENT IN LAB-SCALE

The Principle of Fitting Experimental Data

For multicomponent mixtures, fick classical model assumes that diffusion of each component is independent of other components and diffusion flux is proportional to the component concentration gradient, and the physical quantity that characterizes the molecular diffusion ability of a substance is called the molecular diffusion coefficient. The effective diffusion coefficient mentioned in this paper is used to describe total dispersion phenomenon caused by diffusion, local velocity gradients, locally heterogeneous streamline lengths, and mechanical mixing (Lake, 1989). Dispersion phenomenon is a kind of strengthening effect on molecular diffusion caused by fluid flowing due to uneven velocity, which is called mechanical dispersion. It is impossible to separate mechanical dispersion from molecular diffusion in the diffusion experiment. Therefore, the diffusion coefficient obtained by the experiment is called the effective diffusion coefficient rather than the molecular diffusion coefficient to some extent.

The effective diffusion coefficient is related to the porous medium, temperature and pressure, and also the concentration at its location, which means that the effective diffusion coefficient changes at any time. For all that, we can still use a constant coefficient to characterize the diffusion process. Similar to fick's law of diffusion, that dispersion of each component is proportional to the component concentration gradient is assumed. The dispersion flux J_i is given by:

$$J_i = -\sum_k \tau^{-1}\rho_k D_{eff,ik}\nabla_{yik,}\ \ i = 1,....n_c; k = o, g \tag{2}$$

Where, τ is tortuosity of core sample, calculated by the Archie's law $\tau = \varphi^{-b}$, in which b is constant value of 0.25 (Matyka and Koza, 2012); ρ_k is the density of phase k; $D_{eff,ik}$ is effective diffusion coefficient of component i in phase k; y_{ik} is concentration of component i in phase k.

Due to the lack of experimental data support, The sigmund method is used to determinate the molecular diffusion coefficient of crude oil components in oil and gas phase (da Silva and Belery, 1989). In other words, mechanical dispersion was not considered for the crude oil components. Moreover, the CO_2 effective diffusion coefficient in the gas phase is also calculated. In short, only the CO_2 effective diffusion coefficient in oil phase is used as the target of fitting the experimental data.

In the early stage of diffusion, the pressure drop process is unstable due to the fast diffusion rate (Li et al., 2018a). Therefore, fitting the full curve of the experiment data does not yield perfect matching results. The stage of stable diffusion, whose pressure drop is proportional to $t^{1/2}$ explained by the analytical solution (Li et al., 2016), is selected as the target of numerical simulation fitting. Average absolute relative deviation (AARD) is used to check the fitness between experimental and simulated pressure curves with data recorded every five minutes:

$$AARD = \frac{1}{N}\sum_1^N \frac{\left|p_{\exp} - p_{\sin}\right|}{p_{\exp}} \tag{3}$$

Where P_{exp} is the experiment pressure and P_{sim} is the simulated pressure, and N is the number of data points.

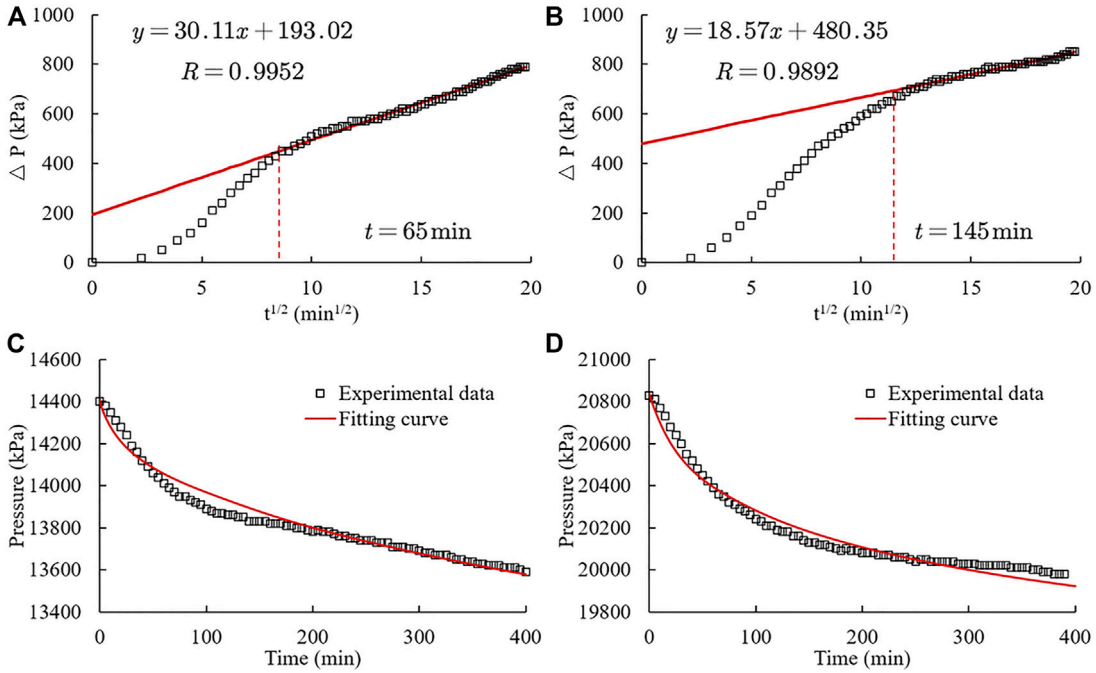

FIGURE 4 | Linear fitting result of pressure drop and $t^{1/2}$ of Test 1 **(A)** and Test 2 **(B)**; Best history fitting curves of Test 1 **(C)** and Test 2 **(D)**.

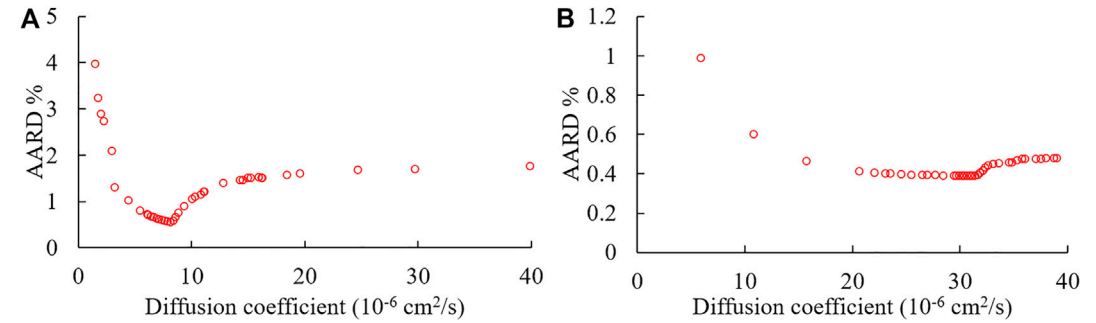

FIGURE 5 | Estimation of diffusion coefficients of Test 1 **(A)** and Test 2 **(B)**.

Best Fit Result

Figures 4A,B presents linear fitting result of pressure drop and $t^{1/2}$ for the two diffusion experiments respectively. For test 1, the pressure drop data after 65 min is used for history matching, and for test 2, 145 min.

Figures 4C,D presents the best history fitting curves of Test 1 and Test 2, and the fitting results show that the effective CO_2 diffusion coefficients are 8.105×10^{-6} cm^2/s and 3.138×10^{-5} cm2/s, respectively.

Figure 5 shows the average absolute relative deviation (AARD) of historymatching for different values of CO_2 effective diffusion coefficient. The AARDs of the best-fitting values are 0.56 and 0.39%, respectively.

The CO_2 effective diffusion coefficient fitting from test 1 is less than that of test 2. This result reflects that higher pressure facilitate the diffusion of CO_2 into crude oil, under tight formation conditions. Also, it is noticed that although there is an optimal fitting result, the average standard deviation of experimental and simulated data is less than 5% with the value of CO_2 effective diffusion coefficient ranging from 1×10^{-6} cm2/s to 4×10^{-5} cm2/s. Generally, field-scale numerical simulations with historical fitting errors less than 5% are accepted. This shows that for the field-scale model (model B), the selection of the CO_2 effective diffusion coefficient can be appropriately adjusted within a certain range. As a result, in model B, as a field-scale mechanism model, a typical value of 10^{-5} cm2/s is selected for the CO_2 effective diffusion coefficient.

CO_2 EOR Mechanisms in Field-Scale

During the shut-in process after the fracturing process is completed, CO_2 will continue to penetrate into the matrix

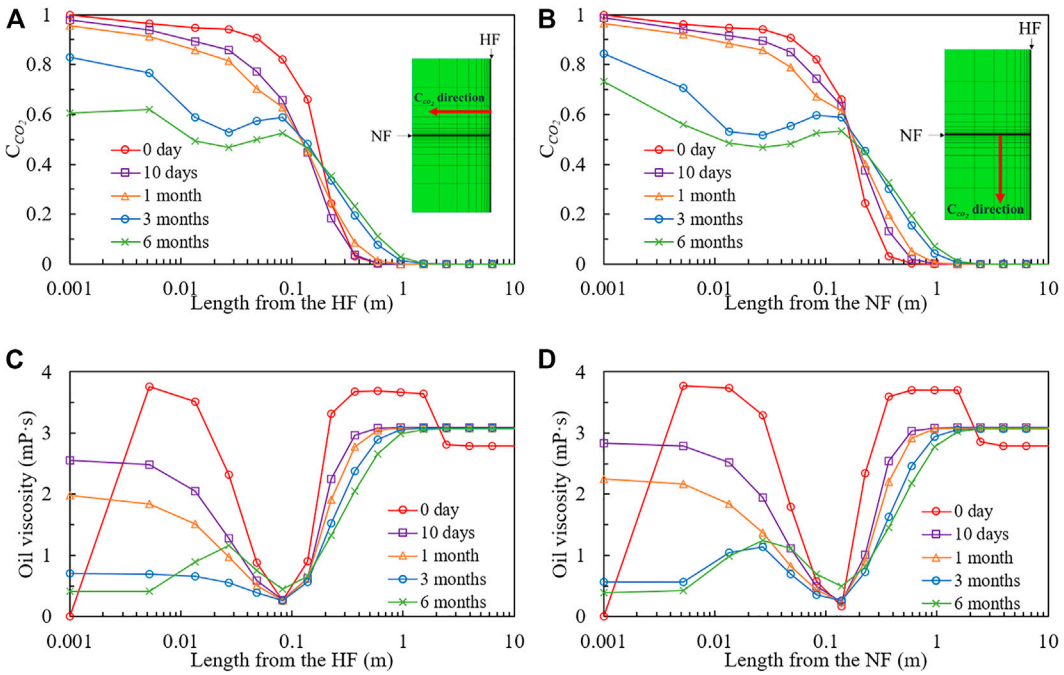

FIGURE 6 | Mole concentration distribution of CO_2 in from HF**(A)** and NF **(B)** and viscosity distribution of oil in from HF **(C)** and NF **(D)**.

along the fracture system. During the flow back and production stage, part of CO_2 is prodcucted with the crude oil, and some of CO_2 may still be dissolved in the crude oil left in the formation. Therefore, we investigated the distribution of CO_2 and the viscosity of crude oil during the long-term shut-in stage and during production stage after shutting in for a period of time, individually.

During Shut-in Stage

Figures 6A,B reports the concentration distribution of CO_2 in from HF and NF surface to deeper matrix under different shut-in time, respectively. At the moment when the CO_2 fracturing fluid injection is completed, the concentration of CO_2 in the matrix within 0.1 m of the fracture has reached 0.8, which means that CO_2 drives the crude oil to a deeper matrix in a short distance. As shown in **Figure 6**, with the increase of the shut-in period, the whole body of the curves move to the right direction. After shutting in for 6 months, the front edge of CO_2 concentration where concentration is greater than to 1% reached a distance of 1 m from the fractures.

Figures 6C,D reports the viscosity distribution of oil in from the surface of HF and NF to deeper matrix under different shut-in time. As the fracturing fluid increases the formation pressure, the viscosity of the crude oil in the matrix after fracturing is generally higher than the original viscosity. It can still be observed that the viscosity of the crude oil is greatly reduced in the matrix within 1 m of the fracture, where the lowest viscosity of crude oil reaches 0.26 mPa·s (one-tenth of the original crude oil viscosity). It is noticed that the viscosity of crude oil does not always increase with the increase of distance. The abnormal phenomenon of viscosity increasing appears in the position between the position of the lowest crude oil viscosity and the fracture, which is caused by CO_2 driving light components of crude oil deeper into matrix and leaving heavy components in this position. In the CO_2-EOR process of conventional reservoirs, this process is called CO_2 extraction. Long-term shut-in can eliminate the phenomenon of viscosity increase due to the redistribution of fluid components dominated by molecular diffusion mechanism.

Figure 7 reports the variation of average oil saturation and global CO_2 concentration in fracture system in the injecting stage (**Figure 7A**) and shut-in stage (**Figure 7B**).

During the 1-h injecting process, the fracture system was quickly filled with CO_2, and rate of CO_2 filling the NF was slightly slower than that of HF. At the end of fracturing, the HF contains the gas phase only constituted of CO_2, while 10% oil phase exists in NF. This oil phase in NF is composed of a small amount of heavy components and a large amount of CO_2, caused by the CO_2 extraction mechanism mentioned above.

During the long-term shut-in stage, the components of the crude oil return to the fracture system through advective flow and molecular diffusion, which is a long process. 360 and 546 days are the time when HF and NF are completely filled with oil phase, respectively. It is noted that the oil phase returning into the fracture system is dissolved with CO_2 with the molar concentration greater than 0.2. This part of the crude oil has better fluidity due to the viscosity reduction effect of CO_2.

During Flow Back (Produciton) Stage

To investigate the production performance after CO_2 fracturing, a basic production model was designed, in which the well is shut in for 10 days, and then producted at the bottom hole pressure of 5 MPa.

Figures 8A,B reports the concentration distribution of CO_2 in from HF and NF surface to deeper matrix under different

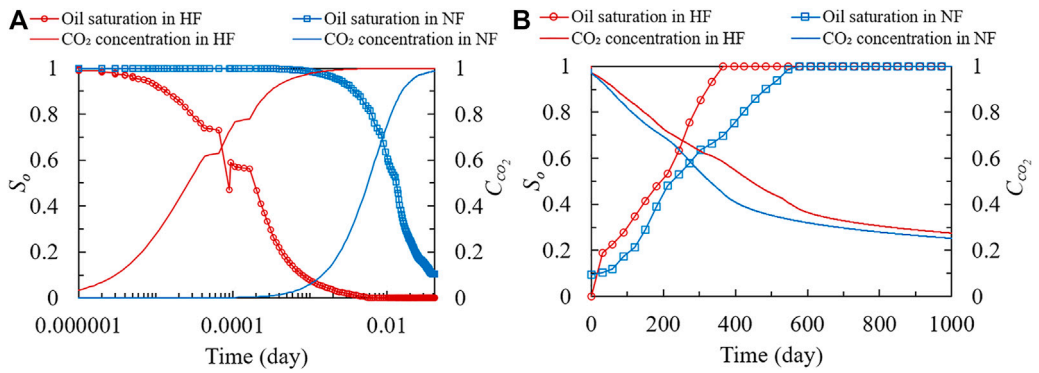

FIGURE 7 | Variations of average oil saturation and global CO_2 mole concentration in fracture system with the time of injecting stage **(A)** and shut-in stage **(B)**.

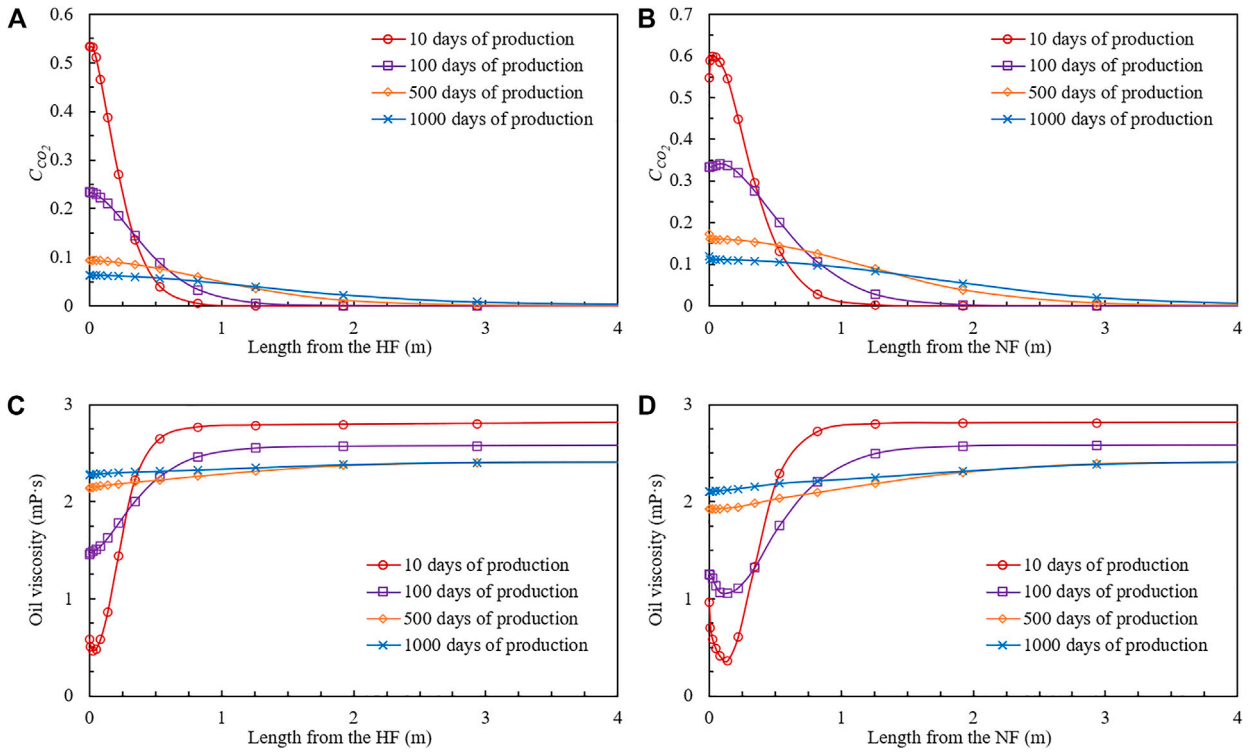

FIGURE 8 | Mole concentration distribution of CO_2 in from HF**(A)** and NF**(B)**and viscosity distribution of oil in from HF **(C)** and NF **(D)**.

production time, respectively. It is noted that the front edge of the CO_2 concentration continues to advance to the deeper matrix during production stage, for example, the front edge is located at a distance of about 3 m from the fracture system to matrix after 1,000 days of production. this phenomenon can be explained by the following two reasons: First, the existence of a concentration gradient provides a continuous driving force for the diffusion of CO_2; besides, the crude oil in the deep matrix is gradually migrated into the fractures and is recovered from the formation along the fracture system, which increases the concentration gradient of CO_2 and promotes the diffusion mechanism. In addition, it is also found that the concentration of CO_2 seems to be higher in the matrix near NF than near HF. This is because the conductivity of NF is less than that of HF, and the crude oil recovery and CO_2 recovery efficiency in the matrix near NF is lower than that near NF, making the apparent CO_2 concentration higher.

Figures 8C,D reports the viscosity distribution of oil in from HF (a) and NF (b) surface to deeper matrix under different production time. As the crude oil that has dissolved CO_2 is recovered from the reservoir, the viscosity-reducing effect of CO_2 on the remaining crude oil gradually weakens. Also due to the difference in the conductivity of HF and NF, CO_2 seems to have a stronger viscosity-reducing effect in the matrix near NF, where, in fact, the oil recovery is lower.

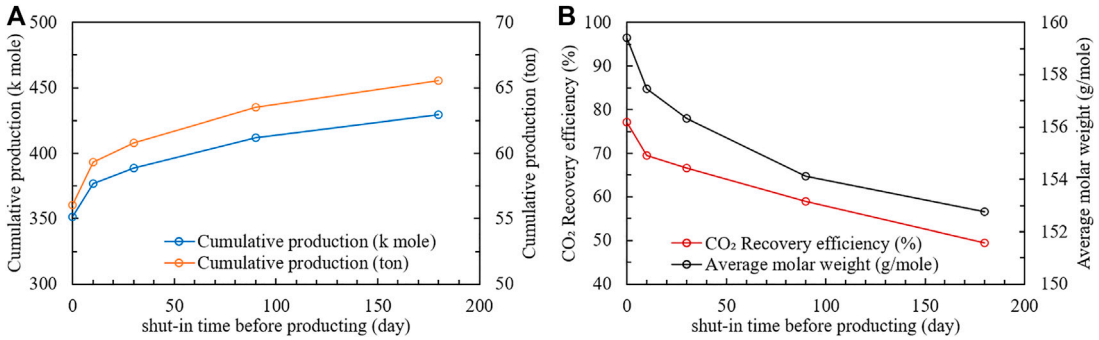

FIGURE 9 | Cumulative production **(A)**, average molar mass of oil producted and CO_2 recovery efficiency **(B)** at different shut-in times before producting.

Optimal Shut-in Time

Through the analysis of the CO_2 concentration distribution in the shut-in stage, we believe that the increase of shut-in time will facilitate CO_2 entering deeper matrix and thereby further exerting its EOR mechanism. In order to investigate the impact of shut-in time on production performance, based on the basic production model, a series of simulations is carried out at different shut-in times.

Figure 9 reports the production performance and CO_2 recovery efficiency at different shut-in times. Figure 9 visually shows that the increase in shut-in time helps to improve the oil recovery. The decrease of CO_2 recovery efficiency (Figure 9) also reflects that more CO_2 keeped in the formation is beneficial to oil recovery. Moreover, it is found that the increase of shut-in time makes the produced oil lighter through the calculation of the average molar mass of produced oil components (including produced oil and gas). In other words, the residual oil becomes heavier because more heavy components remain in the reservoir. For the target reservoirs saturated with low-viscosity oil, this phenomenon has no effect. However, for high-viscosity oil reservoirs rich in heavy components, a large amount of crude oil may not be recovered as a result.

Theoretically, unlimited shut-in time is the best choice to increase oil recovery for this reservoir in this study. However, due to the pursuit of economic value, short shut-in time is a popular choice. Therefore, according to the production curve in Figure 9, we tend to shut in the well for 10 days because the relative increase of production is the largest at this time.

DISCUSSION

In this paper, a radial constant volume diffusion (RCVD) experiment on kerosene saturated shale cores was designed, and the CO_2 effective diffusion coefficient is determined through historymatching the experimental pressure drop curve with simulated data based a lab-scale numerical model constructed by using the commercial simulator. The advancement of the process of determining the CO_2 effective diffusion coefficient is that it takes into account the molecular diffusion of the oil components, and it selects the stable diffusion stage as the target of historymatching, based on the conclusion of a typical analytical solution (pressure drop is proportional to $t^{1/2}$).

In this paper, based on the typical data of fractured shale oil reservoir, the field-scale numerical simulation model of shut-in and production stages after CO_2 fracuting is established by using the commercial simulator. The distribution of CO_2 in fractured shale oil formation and its impact on crude oil during shut-in stage and flow back stage are investigated. The novelties of this model is that: 1) a series of certain grids were used to explicitly characterize fracture instead of a dual-porosity model to capture the exchange of CO_2 between the matrix and the fracture system. 2) through the logarithmic distribution grid of the matrix near the fracture, the diffusion mechanism of CO_2 is described and the true mass transfer distance of CO_2 is obtained. 3) the process of injecting huge amount of CO_2 into formation within a short time during fracturing operation is described by taking into account stress-dependent permeability. 4) through compositional modeling, the interaction between CO_2 and crude oil is described.

This paper provides some explanation for the difference of the CO_2 EOR mechanism in field-scale and that in lab by comparing the lab-scale model and the field-scale model. When measuring the diffusion coefficient experimentally, the volume of CO_2 is in the same order of magnitude as the volume of crude oil or saturated crude oil porous media, and CO_2 can achieve sufficient dissolution and diffusion. Until the pressure balances, there is still a large amount of single phase contained with CO_2 only; however, in the formation, CO_2 gradually diffuses into the matrix along the fracture system, which volume is very small relative to the matrix, that is, the initial volume of CO_2 is limited in field-scale. Moreover, whether it is a full-diameter core or a small core column (2.5 cm or 3.8 cm in diameter) in lab, the scale of core samples remains at the centimeter level, which is still too small relative to the scale of the reservoir in meters. The distance that CO_2 enters the matrix through diffusion mechanism is relatively short in lab, causing the entire core easily swept by CO_2. That is, the actual mass transfer distance of CO_2 in the reservoir cannot be captured in the lab.

The CO_2 mass transfer distance obtained in this paper is basically agreed with previous reports. However, this paper further distinguishes the different performance of CO_2 in the shut-in stage and the production stage, which provide a better understanding of CO_2 EOR mechanism in fractured shale oil

reservoirs. CO_2-EOR performance during shut-in stage exhibits the characteristics of short effect distance and high viscosity-reducting effect. These characteristics indicate that, the CO_2 diffusion mechanism has limited effect, although it is more important in shale oil reservoir than in conventional reservoir. At the same time, in this limited range, the viscosity reducting effect of CO_2 on crude oil is very encouraging, mainly due to the undersaturation of the target crude oil. It is believed that the high solubility of CO_2 in undersaturated oil reservoirs promote the EOR effect of CO_2. During production stage, although more than half of the injected CO_2 will flow back to the surface, the remained CO_2 still plays a positive role in the reservoir. The viscosity of crude oil in the matrix within 1 m near the fracture system is still relatively low.

The relationship between shut-in time after fracturing operation and production performance is still controversial as the phenomenon of fracturing fluid imbibition is a mixed blessing. However, if the water-based fracturing fluid is replaced with CO_2 fracturing fluid, that production increases as the shut-in time prolongs seems to be an inevitable conclusion. In this research, we got the conclusion that the increase of shut-in time helps to improve the oil recovery. At the same time, we also found that the increase of shut-in time makes the produced oil lighter. Although an unlimited shut-in time as the best choice to increase oil recovery is not realistic. This conclusion also provides a reference for the evaluation of the shut-in time and flowback measure after CO_2 fracturing.

The interaction characteristics of CO_2 and different crude oils are different. For saturated oil, it is difficult for CO_2 to dissolve into crude oil, and the extraction effect of CO_2 may become more obvious. In addition, during the production stage, the pressure drop may cause CO_2 to separate from the crude oil in the formation. In this process, CO_2 may extract the light components of the crude oil, resulting in an increase in the viscosity of the residual oil, which may be a negative effect. Therefore, in future study, we need to understand the applicability of CO_2 in different unconventional reservoirs further. In addition, this work did not take into account the reaction of CO_2 with formation water and rocks as a regret, which is also a key direction that needs to be tackled in the future.

CONCLUSION

The main conclusions are obtained in this study:

1) the effective CO_2 diffusion coefficients are 8.105×10^{-6} cm^2/s and 3.138×10^{-5} cm^2/s.
2) During fracturing operation, CO_2 drives the crude oil in a short distance of less than 0.1 m to a deeper matrix.
3) During shut-in stage, the range of CO_2 entering the matrix around fractures is less than 1 m, where the viscosity of the crude oil is greatly reduced (the lowest viscosity of crude oil reaches 0.26 mPa·s). The crude oil gradually return to the fracture system through advective flow and molecular diffusion. 360 and 546 days are the time when HF and NF are completely filled with oil phase, respectively.
4) During production stage, more than half of the injected CO_2 will flow back to the surface. CO_2 left in the formation continues to maintain the advantage of improving the fluidity of oil in matrix. the front edge of the CO_2 concentration keeping moving forward is located at a distance of about 3 m from the fracture system to matrix after 1,000 days of production.
5) The increase in shut-in time helps to improve the oil recovery and makes the produced oil lighter. Due to the pursuit of economic value and high-yield shut-in time, 10 days is the optimal shut-in time.

DATA AVAILABILITY STATEMENT

The raw data supporting the conclusion of this article will be made available by the authors, without undue reservation.

AUTHOR CONTRIBUTIONS

RQ conducted experiments, numerical simulations and drafts. SZ and FW conducted experimental guidance, theoretical guidance and inspection of the first draft. FL, HW, and TZ provided samples and reservoir data needed for the experiment, assisted in completing the experiment, and conducted numerical simulation guidance.

FUNDING

The authors would like to acknowledge the National Natural Science Foundation of China (No. 51974332) for the financial support.

REFERENCES

Alfarge, D., Wei, M., and Bai, B. (2018). CO2-EOR Mechanisms in Huff-N-Puff Operations in Shale Oil Reservoirs Based on History Matching Results. *Fuel* 226, 112–120. doi:10.1016/j.fuel.2018.04.012

Alharthy, N., Teklu, T., Kazemi, H., Graves, R., Hawthorne, S., Braunberger, J., et al. (2015). Enhanced Oil Recovery in Liquid-Rich Shale Reservoirs: Laboratory to Field. *SPE* 29, 15–16. doi:10.2118/175034-ms

Amir, F., and Apostolos, K. (2019). Determining Diffusivity, Solubility, and Swelling in Gaseous Solvent–Heavy Oil Systems. *Ind. Eng. Chem. Res.* 58, 10031–10043. doi:10.1021/acs.iecr.9b01510

da Silva, F. V., and Belery, P. (1989). *Molecular Diffusion in Naturally Fractured Reservoirs: A Decisive Recovery Mechanism*. Society of Petroleum Engineers.

Fischer, S., Liebscher, A., and Wandrey, M. (2010). CO2-brine-rock Interaction - First Results of Long-Term Exposure Experiments at *In Situ* P-T Conditions of the Ketzin CO2 Reservoir. *Geochemistry* 70, 155–164. doi:10.1016/j.chemer.2010.06.001

Ghasemi, M., Astutik, W., Alavian, S. A., Whitson, C. H., Sigalas, L., Olsen, D., et al. (2017). Determining Diffusion Coefficients for Carbon Dioxide Injection in Oil-Saturated Chalk by Use of a Constant-Volume-Diffusion Method. *SPE J.* 22, 505–520. doi:10.2118/179550-pa

Ghasemi, M., Astutik, W., Alavian, S. A., Whitson, C. H., Sigalas, L., Olsen, D., et al. (2016). "Determining Diffusion Coefficients for CO2 Injection in Oil Saturated

Chalk Using a Constant Volume Diffusion Method," in SPE Improved Oil Recovery Conference, May 30–June 2, 2016 (Tulsa, Oklahoma, USA: Society of Petroleum Engineers). doi:10.2118/179550-ms

Ghasemi, M., Astutik, W., Alavian, S., Whitson, C. H., Sigalas, L., Olsen, D., et al. (2018). Experimental and Numerical Investigation of tertiary-CO2 Flooding in a Fractured Chalk Reservoir. *J. Pet. Sci. Eng.* 164, 485–500. doi:10.1016/j.petrol.2018.01.058

Ghasemi, M., and Suicmez, V. S. (2019). Upscaling of CO2 Injection in a Fractured Oil Reservoir. *J. Nat. Gas Sci. Eng.* 63, 70–84. doi:10.1016/j.jngse.2019.01.009

Habibi, A., Yassin, M. R., Dehghanpour, H., and Bryan, D. (2017a). "CO2-Oil Interactions in Tight Rocks: An Experimental Study," in SPE Unconventional Resources Conference, February 15–16, 2017 (Calgary, Alberta: Canada: Society of Petroleum Engineers). doi:10.2118/185047-ms

Habibi, A., Yassin, M. R., Dehghanpour, H., and Bryan, D. (2017b). Experimental Investigation of CO2-oil Interactions in Tight Rocks: A Montney Case Study. *Fuel* 203, 853–867. doi:10.1016/j.fuel.2017.04.077

Hawthorne, S. B., Gorecki, C. D., Sorensen, J. A., Miller, D. J., Harju, J. A., and Melzer, L. S. (2014). Hydrocarbon Mobilization Mechanisms Using CO2 in an Unconventional Oil Play. *Energ. Proced.* 63, 7717–7723. doi:10.1016/j.egypro.2014.11.805

Hawthorne, S. B., Gorecki, C. D., Sorensen, J. A., Steadman, E. N., Harju, J. A., and Melzer, S. (2013). "Hydrocarbon Mobilization Mechanisms from Upper, Middle, and Lower Bakken Reservoir Rocks Exposed to CO," in SPE Unconventional Resources Conference Canada, November 5–7, 2013 (Calgary, Alberta: Canada: Society of Petroleum Engineers).

He, Y., Yang, Z., Jiang, Y., Li, X., Zhang, Y., and Song, R. (2020). A Full Three-dimensional Fracture Propagation Model for Supercritical Carbon Dioxide Fracturing. *Energy Sci Eng* 8, 2894–2906. doi:10.1002/ese3.709

Hoteit, H. (2011). "Proper Modeling of Diffusion in Fractured Reservoirs," in SPE Reservoir Simulation Symposium, February 21–23, 2011 (The Woodlands, Texas, USA: Society of Petroleum Engineers). doi:10.2118/141937-ms

Jin, F., Shunyuan, Z., Bingshan, L., Chen, C., and Kedi, M. (2017). "Green Fracturing Technology of Shale Gas: LPG Waterless Fracturing Technology and its Feasibility in China," in SPE Latin America and Caribbean Petroleum Engineering Conference, May 18–19, 2017 (Buenos Aires, Argentina: Society of Petroleum Engineers). doi:10.2118/185500-ms

Kanfar, M. S., and Clarkson, C. R. (2017). "Factors Affecting Huff-N-Puff Efficiency in Hydraulically-Fractured Tight Reservoirs," in SPE Unconventional Resources Conference, February 15–16, 2017 (Calgary, Alberta: Canada: Society of Petroleum Engineers). doi:10.2118/185062-ms

Lake, L. W. (1989). *Enhanced Oil Recovery*. Englewood Cliffs, New Jersey: Prentice-Hall.

Li, S., Li, Z., and Dong, Q. (2016). Diffusion Coefficients of Supercritical CO 2 in Oil-Saturated Cores under Low Permeability Reservoir Conditions. *J. CO2 Utilization* 14, 47–60. doi:10.1016/j.jcou.2016.02.002

Li, S., Qiao, C., Zhang, C., and Li, Z. (2018a). Determination of Diffusion Coefficients of Supercritical CO2 under Tight Oil Reservoir Conditions with Pressure-Decay Method. *J. CO2 Utilization* 24, 430–443. doi:10.1016/j.jcou.2018.02.002

Li, S., and Zhang, D. (2019). How Effective Is Carbon Dioxide as an Alternative Fracturing Fluid? *SPE J.* 24, 857–876. doi:10.2118/194198-pa

Li, S., Zhang, S., Ma, X., Zou, Y., Li, N., Chen, M., et al. (2019). Hydraulic Fractures Induced by Water-/Carbon Dioxide-Based Fluids in Tight Sandstones. *Rock Mech. Rock Eng.* 52, 3323–3340. doi:10.1007/s00603-019-01777-w

Li, S., Zhang, S., Ma, X., Zou, Y., Li, N., Wu, S., et al. (2020a). Coupled Physical-Chemical Effects of CO2 on Rock Properties and Breakdown during Intermittent CO2-Hybrid Fracturing. *Rock Mech. Rock Eng.* 53, 1665–1683. doi:10.1007/s00603-019-02000-6

Li, S., Zhang, S., Zou, Y., Zhang, X., Ma, X., Wu, S., et al. (2020b). Experimental Study on the Feasibility of Supercritical CO2-gel Fracturing for Stimulating Shale Oil Reservoirs. *Eng. Fracture Mech.* 238, 5–11. doi:10.1016/j.engfracmech.2020.107276

Li, X., Li, G., Yu, W., Wang, H., Sepehrnoori, K., Chen, Z., et al. (2018b). Thermal Effects of Liquid/Supercritical Carbon Dioxide Arising from Fluid Expansion in Fracturing. *Spe J.* 23, 2026–2040. doi:10.2118/191357-pa

Li, Z., and Dong, M. (2009). Experimental Study of Carbon Dioxide Diffusion in Oil-Saturated Porous Media under Reservoir Conditions. *Ind. Eng. Chem. Res.* 48, 9307–9317. doi:10.1021/ie900145c

Liu, H., Wang, F., Zhang, J., Meng, S., and Duan, Y. (2014). Fracturing with Carbon Dioxide: Application Status and Development Trend. *Pet. Exploration Dev.* 41, 513–519. doi:10.1016/s1876-3804(14)60060-4

Lu, J., Sorensen James, A., Hawthorne Steven, B., Smith Steven, A., Bosshart Nicholas, W., Burton-Kelly Matthew, E., et al. (2016). "Improving Oil Transportability Using CO2 in the Bakken System – A Laboratory Investigation," in SPE International Conference and Exhibition on Formation Damage Control, February 24–26, 2016 (Lafayette, Louisiana, USA: Society of Petroleum Engineers).

Matyka, M., and Koza, Z. (2012). *How to Calculate Tortuosity Easily?* Germany: Potsdam, 17–22.

Meng, S., Liu, He., and Yang, Q. (2019). Exploration and Practice of Carbon Sequestration Realized by CO2 Waterless Fracturing. *Energ. Proced.* 158, 4586–4591. doi:10.1016/j.egypro.2019.01.750

Meng, S., Liu, H., Xu, J., Duan, Y., Yang, Q., and Yao, Z. (2016). "Optimisation and Performance Evaluation of Liquid CO2 Fracturing Fluid Formulation System," in SPE Asia Pacific Oil & Gas Conference and Exhibition, October 25–27, 2016 (Perth, Australia: Society of Petroleum Engineers). doi:10.2118/182284-ms

Myers, T. (2012). Potential Contaminant Pathways from Hydraulically Fractured Shale to Aquifers. *Groundwater* 50, 872–882. doi:10.1111/j.1745-6584.2012.00933.x

Ribeiro, L. H., Li, H., and Bryant, J. E. (2015). "Use of a CO2-Hybrid Fracturing Design to Enhance Production from Unpropped Fracture Networks," in SPE Hydraulic Fracturing Technology Conference., February 3–5, 2015

Santiago, C. J. S., and Kantzas, A. (2020). "On the Role of Molecular Diffusion in Modelling Enhanced Recovery in Unconventional Condensate Reservoirs," in *SPE Europec* (Amsterdam, The Netherlands: Society of Petroleum Engineers). doi:10.2118/200596-ms

Song, Z., Song, Y., Li, Y., Bai, B., Song, K., and Hou, J. (2020). A Critical Review of CO2 Enhanced Oil Recovery in Tight Oil Reservoirs of North America and China. *Fuel* 276, 118006. doi:10.1016/j.fuel.2020.118006

Sorensen, J. A., Braunberger, J. R., Liu, G., Smith, S. A., Hawthorne, S. A., Steadman, E. N., et al. (2015). Characterization and Evaluation of the Bakken Petroleum System for CO2 Enhanced Oil Recovery. *SPE* 21, 2–3. doi:10.2118/167200-MS

Tian, S., Zhang, P., Sheng, M., Wang, T., Tang, J., and Xiao, L. (2020). Modification of Microscopic Properties of Shale by Carbonic Acid Treatment: Implications for CO2-Based Fracturing in Shale Formations. *Energy Fuels* 34, 3458–3466. doi:10.1021/acs.energyfuels.9b03772

Trivedi, J. J., and Babadagli, T. (2009). Experimental and Numerical Modeling of the Mass Transfer between Rock Matrix and Fracture. *Chem. Eng. J.* 146, 194–204. doi:10.1016/j.cej.2008.05.032

Tsau, J.-S., and Barati, R. (2018). "Measurement of CO2 Diffusion Coefficient in the Oil-Saturated Porous Media," in Abu Dhabi International Petroleum Exhibition & Conference., November 12–15, 2018

Vengosh, A., Warner, N., Jackson, R., and Darrah, T. (2013). The Effects of Shale Gas Exploration and Hydraulic Fracturing on the Quality of Water Resources in the United States. *Proced. Earth Planet. Sci.* 7, 863–866. doi:10.1016/j.proeps.2013.03.213

Wang, H., Lun, Z., Lv, C., Lang, D., Pan, W., Luo, M., et al. (2016a). "Nuclear Magnetic Resonance Study on Mechanisms of Oil Mobilization in Tight Reservoir Exposed to CO_2 in Pore Scale," in SPE Improved Oil Recovery Conference, April 11–13, 2016 (Tulsa, Oklahoma, USA: Society of Petroleum Engineers).

Wang, L., Yao, B., Cha, M., Alqahtani, N. B., Patterson, T. W., Kneafsey, T. J., et al. (2016b). Waterless Fracturing Technologies for Unconventional Reservoirs-Opportunities for Liquid Nitrogen. *J. Nat. Gas Sci. Eng.* 35, 160–174. doi:10.1016/j.jngse.2016.08.052

Wei, B., Zhong, M., Gao, K., Li, X., Zhang, X., Cao, J., et al. (2020). Oil Recovery and Compositional Change of CO2 Huff-N-Puff and Continuous Injection Modes in a Variety of Dual-Permeability Tight Matrix-Fracture Models. *Fuel* 276, 117939. doi:10.1016/j.fuel.2020.117939

Yu, W., Lashgari, H. R., Wu, K., and Sepehrnoori, K. (2015). CO2 Injection for Enhanced Oil Recovery in Bakken Tight Oil Reservoirs. *Fuel* 159, 354–363. doi:10.1016/j.fuel.2015.06.092

Zhang, T., Li, X., Li, J., Feng, D., Li, P., Zhang, Z., et al. (2017). Numerical Investigation of the Well Shut-In and Fracture Uncertainty on Fluid-Loss and Production Performance in Gas-Shale Reservoirs. *J. Nat. Gas Sci. Eng.* 46, 421–435. doi:10.1016/j.jngse.2017.08.024

Zhang, X., Wei, B., Shang, J., Gao, K., Pu, W., Xu, X., et al. (2018). Alterations of Geochemical Properties of a Tight sandstone Reservoir Caused by Supercritical CO2-brine-rock Interactions in CO2-EOR and Geosequestration. *J. CO2 Utilization* 28, 408–418. doi:10.1016/j.jcou.2018.11.002

Zhang, Y., Hu, J., and Zhang, Q. (2019). Simulation Study of CO2 Huff-N-Puff in Tight Oil Reservoirs Considering Molecular Diffusion and Adsorption. *Energies* 12, 2136. doi:10.3390/en12112136

Zhao, X., Zhou, L., Pu, X., Jin, F., Han, W., Xiao, D., et al. (2018). Geological Characteristics of Shale Rock System and Shale Oil Exploration Breakthrough in a Lacustrine basin: A Case Study from the Paleogene 1st Sub-member of Kong 2 Member in Cangdong Sag, Bohai Bay Basin, China. *Pet. Exploration Dev.* 45, 377–388. doi:10.1016/s1876-3804(18)30043-0

Zhou, J., Liu, G., Jiang, Y., Xian, X., Liu, Q., Zhang, D., et al. (2016). Supercritical Carbon Dioxide Fracturing in Shale and the Coupled Effects on the Permeability of Fractured Shale: An Experimental Study. *J. Nat. Gas Sci. Eng.* 36, 369–377. doi:10.1016/j.jngse.2016.10.005

Zhou, J., Yang, K., Tian, S., Zhou, L., Xian, X., Jiang, Y., et al. (2020a). CO2-water-shale Interaction Induced Shale Microstructural Alteration. *Fuel* 263, 116642. doi:10.1016/j.fuel.2019.116642

Zhou, X., Jiang, Q., Yuan, Q., Zhang, L., Feng, J., Chu, B., et al. (2020b). Determining CO2 Diffusion Coefficient in Heavy Oil in Bulk Phase and in Porous media Using Experimental and Mathematical Modeling Methods. *Fuel* 263, 116205. doi:10.1016/j.fuel.2019.116205

Zhou, X., Yuan, Q., Zhang, Y., Wang, H., Zeng, F., and Zhang, L. (2019). Performance Evaluation of CO2 Flooding Process in Tight Oil Reservoir via Experimental and Numerical Simulation Studies. *Fuel* 236, 730–746. doi:10.1016/j.fuel.2018.09.035

Zou, C., Yang, Z., Cui, J., Zhu, R., Hou, L., Tao, S., et al. (2013). Formation Mechanism, Geological Characteristics and Development Strategy of Nonmarine Shale Oil in China. *Pet. Exploration Dev.* 40, 15–27. doi:10.1016/s1876-3804(13)60002-6

Zou, Y., Li, N., Ma, X., Zhang, S., and Li, S. (2018). Experimental Study on the Growth Behavior of Supercritical CO 2 -induced Fractures in a Layered Tight sandstone Formation. *J. Nat. Gas Sci. Eng.* 49, 145–156. doi:10.1016/j.jngse.2017.11.005

Zuloaga, P., Yu, W., Miao, J., and Sepehrnoori, K. (2017). Performance Evaluation of CO2 Huff-N-Puff and Continuous CO2 Injection in Tight Oil Reservoirs. *Energy* 134, 181–192. doi:10.1016/j.energy.2017.06.028

Conflict of Interest: Authors FL, HW and TZ were employed by the company SINOPEC.

The remaining authors declare that the research was conducted in the absence of any commercial or financial relationships that could be construed as a potential conflict of interest.

Publisher's Note: All claims expressed in this article are solely those of the authors and do not necessarily represent those of their affiliated organizations, or those of the publisher, the editors and the reviewers. Any product that may be evaluated in this article, or claim that may be made by its manufacturer, is not guaranteed or endorsed by the publisher.

frontiers in Earth Science

ORIGINAL RESEARCH
published: 10 January 2022
doi: 10.3389/feart.2021.813585

A Model for the Apparent Gas Permeability of Shale Matrix Organic Nanopore Considering Multiple Physical Phenomena

Wei Guo, Xiaowei Zhang, Rongze Yu*, Lixia Kang, Jinliang Gao and Yuyang Liu*

PetroChina Research Institute of Petroleum Exploration and Development, Beijing, China

The flow of shale gas in nano scale pores is affected by multiple physical phenomena. At present, the influence of multiple physical phenomena on the transport mechanism of gas in nano-pores is not clear, and a unified mathematical model to describe these multiple physical phenomena is still not available. In this paper, an apparent permeability model was established, after comprehensively considering three gas flow mechanisms in shale matrix organic pores, including viscous slippage Flow, Knudsen diffusion and surface diffusion of adsorbed gas, and real gas effect and confinement effect, and at the same time considering the effects of matrix shrinkage, stress sensitivity, adsorption layer thinning, confinement effect and real gas effect on pore radius. The contribution of three flow mechanisms to apparent permeability under different pore pressure and pore size is analyzed. The effects of adsorption layer thinning, stress sensitivity, matrix shrinkage effect, real gas effect and confinement effect on apparent permeability were also systematically analyzed. The results show that the apparent permeability first decreases and then increases with the decrease of pore pressure. With the decrease of pore pressure, matrix shrinkage, Knudsen diffusion, slippage effect and surface diffusion effect increase gradually. These four effects will not only make up for the permeability loss caused by stress sensitivity and adsorption layer, but also significantly increase the permeability. With the decrease of pore radius, the contribution of slippage flow decreases, and the contributions of Knudsen diffusion and surface diffusion increase gradually. With the decrease of pore radius and the increase of pore pressure, the influence of real gas effect and confinement effect on permeability increases significantly. Considering real gas and confinement effect, the apparent permeability of pores with radius of 5 nm is increased by 13.2%, and the apparent permeability of pores with radius of 1 nm is increased by 61.3%. The apparent permeability model obtained in this paper can provide a theoretical basis for more accurate measurement of permeability of shale matrix and accurate evaluation of productivity of shale gas horizontal wells.

Keywords: apparent permeability, shale gas, adsorption layer, stress sensitivity, matrix shrinkage, multiple transport mechanisms

OPEN ACCESS

Edited by:
Xiaohu Dong,
China University of Petroleum, China

Reviewed by:
Bailu Teng,
China University of Geosciences, China
Luo Zuo,
Sinopec, China
Dong Feng,
China University of Petroleum, China

****Correspondence:***
Xiaowei Zhang
zhangxw69@petrochina.com.cn
Rongze Yu
yurz201169@petrochina.com.cn

Specialty section:
This article was submitted to Economic Geology, a section of the journal Frontiers in Earth Science

Received: *12 November 2021*
Accepted: *14 December 2021*
Published: *10 January 2022*

Citation:
Guo W, Zhang X, Yu R, Kang L, Gao J and Liu Y (2022) A Model for the Apparent Gas Permeability of Shale Matrix Organic Nanopore Considering Multiple Physical Phenomena. Front. Earth Sci. 9:813585. doi: 10.3389/feart.2021.813585

1 INTRODUCTION

Shale gas is an unconventional natural gas that is mainly stored in shale as adsorption gas and free gas. Scanning electron microscopy (SEM) shows the development of numerous connected nanoscale pores in shale matrix. The mechanism of gas flow in nanoscale pores differs significantly from that in conventional reservoirs, and the classical Darcy's law cannot be used to describe the flow pattern of shale gas. Therefore, elucidating the flow mechanism of shale gas in nanoscale pores and establishing a mathematical model to characterize the flow behavior of shale gas for numerical simulation and production prediction of shale gas reservoirs has considerable theoretical significance.

The special occurrence mechanism of shale gas and nano scale gas transmission space lead to the complexity of flow behavior. Currently, many scholars have used the apparent permeability as an important parameter to comprehensively characterize this complex gas flow behavior. Sakhaee-Pour and Bryant (2012) analyzed the effect of the methane adsorption layer and gas slip at the pore wall on the flow behavior of shale gas to determine the permeability of shale reservoirs. Swami et al. (2012) used an apparent permeability model for various nanopores of shale matrix to analyze the effect of the pore radius and formation pressure on the apparent permeability and Darcy permeability ratio. Song et al. (2016) developed a model of the apparent permeability of inorganic and organic matter considering stress-sensitivity effects. Cao et al. (2017) proposed a three-dimensional coupled model for inorganic and organic matter to calculate the permeability of shale. Singh et al. (2014) derived an analytical model for the apparent permeability that does not require empirical parameters to characterize the effects of the pore size, pore geometry, temperature, gas properties and average reservoir pressure on the apparent permeability. Akkutlu and Fathi, (2012) developed an apparent permeability model considering the stress sensitivity, mainly considering surface diffusion and Knudsen diffusion in the flow mechanism. Wang et al. (2015) developed an apparent permeability model considering stress-sensitivity effects and the pore gas adsorption layer. The evolution of the apparent permeability during production and the effects of the stress sensitivity and adsorption layer on the permeability were determined. Wu et al. (2016a) developed a model for the apparent permeability considering slip flow, Knudsen diffusion, surface diffusion, stress sensitivity and the adsorption layer. A bulk phase gas transport model was formulated by superposing the two transport mechanisms of slip flow and Knudsen diffusion with a weighting factor. Zhao et al. (2016) established mass flux equations for four shale gas flow regimes based on the Knudsen number and derived a unified apparent permeability calculation model for the different flow regimes. Jia et al. (2018) considered the comprehensive effects of effective stress increase and gas desorption on pore size, established an apparent permeability model considering slippage, Knudsen diffusion and surface diffusion and analyzed the permeability changes during shale gas production. Huang et al. (2018) considered the dense gas effect and introduced a surface diffusion correction factor to study the effect of the adsorption layer on the apparent permeability under different mass transfer mechanisms (slip flow, surface diffusion and Knudsen diffusion). Sheng et al. (2018) analyzed the effect of the microscale compressibility on the apparent permeability and porosity. Geng et al. (2016) proposed a viscous-diffusive model to simulate the transport of shale gas in nanopores. The extended Navier-Stokes equation was used to describe multiple flow mechanisms, including viscous flow, slip and transition flow. Sun et al. (2019) proposed a model for gas transport in elliptical nanotubes based on a weighted superposition of continuous flow and Knudsen diffusion. The contribution of Knudsen diffusion contribution to the apparent permeability was found to increase with the aspect ratio. Tian et al. (2018) proposed a model for shale gas transport in circular nanotubes with weighted contributions from slip flow, bulk phase diffusion and Knudsen diffusion. Yin et al. (2017) proposed an analytical model for gas transport in nanopores considering real gas effects and surface diffusion. Wang et al. (2019) derived a model for the apparent shale gas permeability based on fractal theory, considering gas slip flow, Knudsen diffusion and surface diffusion transport mechanisms. Chai et al. (2019) divided the gas flow in a circular tube into viscous, Knudsen diffusion and surface diffusion zones. Coefficients were introduced for the viscous slip flow and Knudsen diffusion contributions to establish a unified apparent gas permeability model. Shi et al. (2013) studied pore size and water phase distribution in shale matrix. Combined with the mechanism of gas transportation, a new diffusion and slip flow model is proposed. Zhang et al. (2017) established a gas-water two-phase permeability model. The model considers not only the gas slippage and water film thickness in the whole Knudsen diffusion range, but also the real gas effect and stress sensitivity. Zhang T. et al. (2018) proposed an apparent permeability model for shale considering the initial water content saturation distribution. Surface diffusion and Knudsen diffusion were found to be the key factors affecting the permeability. Nanopores smaller than 2 nm in organic matter were found to exhibit a higher permeability than macro-pores at pressures below 6 MPa. Wang et al. (2018) used a logarithmic normal distribution function to characterize the pore size distribution and derived a gas transport model for organic and inorganic matter. The effects of a real gas, the water film thickness and the stress sensitivity on the gas transport were considered in the model. The permeability was found to increase with the organic carbon content at pressures above 5 MPa. Sun et al. (2018a) modeled the apparent permeability of circular organic nanopores and inorganic matrix slit pores, considering the water distribution characteristics. The effects of the bulk phase gas slip flow, stress sensitivity and real gas effects on the apparent permeability were considered. In addition, the effect of the water film thickness on the apparent permeability was considered for the inorganic pore. Although water saturation was considered in the model, matrix shrinkage was neglected. Sheng et al. (2019) considered the effect of the adsorption layer, stress sensitivity and desorption-induced shrinkage on the pore radius and proposed an apparent permeability model for organic pore. The matrix porosity and

apparent permeability were found to decrease under the stress-sensitivity effect for pore pressures above 20 MPa, where matrix shrinkage and adsorption layer thinning compensated for the reduction in the permeability after the pore pressure decreased to 20 MPa. Zhang L. et al. (2020) developed a unified apparent permeability model for a shale matrix considering gas transport behavior in organic and inorganic pores. Zhang Q. et al. (2020) established a unified apparent permeability model for inorganic and organic matter by considering the effects of the adsorption layer, matrix shrinkage and stress sensitivity on the pore radius. The main innovation of this model was to consider the effect of surface diffusion on slip flow, whereas the effect of the gas flow patterns over the full range of Knudsen numbers was neglected.

A literature search shows that three flow mechanisms have mainly been considered in apparent permeability models of shale matrix: surface diffusion (Wasaki and Akkutlu, 2015; Wang and Marongiu-Porcu, 2015; Wang et al., 2015; Wu et al., 2016b; Wu et al. 2016c; Wu et al.2016d; Wu et al. 2017; Sun et al., 2017; Zhang L. et al., 2018; Jia et al., 2019), Knudsen diffusion and slip flow (Sakhaee-Pour and Bryant, 2012; Akkutlu and Fathi, 2012; Xiong et al., 2012; Sheng et al., 2015; Zhang et al., 2015; Song et al., 2016; Li et al., 2019). Stress sensitivity (Dong et al., 2010; Pang et al., 2017; Cui et al., 2018a; Cui et al., 2018b), the water film thickness (Li et al., 2016; Sun et al., 2017; Li et al., 2018; Peng et al., 2018) and adsorption layer thinning (Li et al., 2020) are the three main factors affecting the pore radius. A few scholars believe that the matrix shrinkage effect (An et al., 2017; Sheng et al., 2019) has a certain impact on the porosity and apparent permeability of shale matrix, but the influence degree of matrix shrinkage is not clear enough. The factors considered in these models are not comprehensive enough. In this paper, a apparent permeability model is established, after comprehensively considering three gas flow mechanisms in shale matrix organic pores, including viscous slippage flow, Knudsen diffusion and surface diffusion of adsorbed gas, and real gas effect and confinement effect, and at the same time considering the effects of matrix shrinkage, stress sensitivity, adsorption layer thinning, confinement effect and real gas effect on pore radius. The contribution of three flow mechanisms to apparent permeability under different pore pressure and pore size is analyzed. The effects of adsorption layer thinning, stress sensitivity, matrix shrinkage effect, real gas effect and confinement effect on apparent permeability are also systematically analyzed.

2 MODEL DESCRIPTION AND FORMULATION

2.1 Model Description

Gas transport in organic pores includes slip flow, Knudsen diffusion, and surface diffusion of the adsorption gas. The adsorption gas occupies a portion of the transport space of pores, which reduces the effective pore radius for gas transport. During production, adsorption layer thinning and matrix shrinkage expand the organic matrix pore radius because the adsorption gas desorbs from the matrix pore walls, whereas stress sensitivity decreases the pore radius. The pore radius and porosity of the shale organic matrix are in a dynamic change state under this triple effect (the stress sensitivity, adsorption layer thinning and matrix shrinkage), as shown in **Figure 1**. Considering the effects of dynamic pore radius, real gas effect and confinement effect on gas transport, in the next part, we will establish the mathematical models of slippage flow, Knudsen diffusion and surface diffusion respectively.

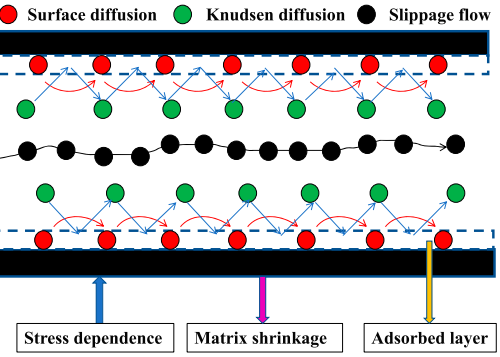

FIGURE 1 | Schematic of the gas transport mechanism in the organic pore.

2.2 Mathematical Model

2.2.1 Real Gas Effect and Confinement Effect

Shale gas is dense under high reservoir pressures. Intermolecular forces and the gas molecular size affect the gas transport capacity. This effect of real gas on the gas transport can be described by using a dimensionless gas deviation factor Z, the gas viscosity and the mean free path of the gas molecules (Sun et al., 2018a):

$$Z = 0.702e^{-2.5T_{pr}} \times P_{pr}^2 - 5.524e^{-2.5T_{pr}} \times P_{pr} + 0.044T_{pr}^2 - 0.164T_{pr} + 1.15 \quad (1)$$

where

$$P_r = P/P_{cb} \quad (2)$$

$$T_r = T/T_{cb} \quad (3)$$

and P denotes the reservoir pore pressure, MPa; T denotes the reservoir temperature, K; P_r is the dimensionless contrast pressure; T_r is the dimensionless gas contrast temperature; and P_{cb} and T_{cb} denote the critical pressure (MPa) and temperature (K) of the bulk phase gas, respectively.

The force between gas molecules and pore wall will have a certain impact on the gas transport mechanism and ability. This effect is called confinement effect. Due to the confinement effect, the critical pressure and temperature of gas will change. The critical parameters of the gas in the nanopores are related to the pore size as follows (Sun et al., 2018b):

$$\frac{T_{cc}}{T_{cb}} = 1 - 1.2\left(\frac{D}{\sigma} - \frac{d_a}{\sigma}\right)^{-1/0.88} \quad (4)$$

$$\frac{P_{cc}}{P_{cb}} = 1 - 1.5\left(\frac{D}{\sigma} - \frac{d_a}{\sigma}\right)^{-1/1.6} \quad (5)$$

TABLE 1 | Coefficients in eqation6.

Coefficient	Value
A_1	0.00850507486545010
A_2	–0.00104065426590739
A_3	–0.00217777225933512
A_4	–0.000510724061609292
A_5	0.00595154429253907
A_6	–0.000548942531453252

where D denotes the pore diameter, nm; σ denotes the Lennard-Jones parameter, which is taken as 0.28 nm in this study; d_a denotes the thickness of the adsorption layer, nm; and T_{cc} and P_{cc} denote the critical gas temperature (K) and pressure (MPa) considering the confinement effect, respectively.

The real gas viscosity μ_g, mPas, varies with the pressure and temperature as follows (Zhang L. et al., 2020):

$$\mu_g = A_1 \times T_{pr} + A_2 \times P_{pr} + A_3 \times \sqrt{P_{pr}} + A_4 \times T_{pr}^2 + A_5 \times \frac{P_{pr}}{T_{pr}} + A_6 \tag{6}$$

The coefficients in **Equation 6** are shown in **Table 1**:

$$\rho_g = \frac{pM_g}{ZRT} \tag{7}$$

where ρ_g denotes the gas density, kg/m^3; M_g denotes the gas molecular mass, kg/mol; and R denotes the universal gas constant, Pa/mol/K.

The mean free path λ_r, m of real gas molecules is defined as

$$\lambda_r = \frac{\mu_g}{p}\sqrt{\frac{\pi ZRT}{2M_g}} \tag{8}$$

The true Knudsen number Kn_r (dimensionless) of the real gas in the nanopores is defined as

$$Kn_r = \frac{\lambda_r}{2r} \tag{9}$$

where r denotes the pore radius, nm.

2.2.2 Variation in the Pore Radius of an Organic Matrix

1) Effect of the Stress Sensitivity on the Pore Radius

During shale gas production, the intrinsic permeability, porosity and nanopore radius of shale decrease as the effective stress increases, and the gas flow capacity decreases accordingly. Dong et al. (2010) used the results of shale core experiments to propose a power law for the variation in the shale porosity and permeability with the pressure:

$$K = K_o\left(\frac{p_e}{p_o}\right)^{-s} \tag{10}$$

$$\varphi_m = \varphi_{mo}\left(\frac{p_e}{p_o}\right)^{-q} \tag{11}$$

where P_o denotes the atmospheric pressure, MPa; and P_e denotes the overlying effective stress, MPa, which is defined as

$$P_e = \sigma_c - p \tag{12}$$

where σ_c denotes the overlying stress, MPa; K denotes the intrinsic permeability under the effective stress, μm^2; K_o denotes the intrinsic permeability under atmospheric pressure, μm^2; φ_m and φ_{mo} are dimensionless variables denoting the matrix porosity under the effective stress and atmospheric pressure, respectively; and s and q are dimensionless coefficients for the shale permeability and shale porosity, respectively, obtained by fitting experimental results.

The organic pore radius under effective stress, r_s, nm is related to K and φ_m as follows:

$$r_s = 2\sqrt{2\tau}\sqrt{\frac{K}{\varphi_m}} \tag{13}$$

where τ denotes the dimensionless pore tortuosity.

Equations 11, **12**, **14** can be used to express r_s as follows:

$$r_s = r_o\left(p_e/p_o\right)^{0.5(q-s)} \tag{14}$$

where r_o denotes the pore radius at atmospheric pressure, nm.

2) Effect of Gas Desorption on the Pore Radius

The large quantity of adsorption gas on the organic pore wall reduces the pore radius. However, gas desorption thins the adsorption layer and thus increases the pore radius. Therefore, during the production of shale gas wells, the effects of both the adsorption layer thinning and the stress sensitivity on the pore radius need to be considered.

$$r_{esd} = r_s - \theta d_m \tag{15}$$

In the equation above, r_{esd} denotes the pore radius, nm considering both stress sensitivity and the adsorption layer thinning; d_m denotes the methane molecular diameter, 0.4 nm; and θ denotes the dimensionless gas coverage, which is defined considering the real gas effect as:

$$\theta = \frac{p/Z}{p_L + p/Z} \tag{16}$$

where P_L denotes the Langmuir pressure, MPa.

3) Effect of matrix Shrinkage on the Pore Radius

Most gas has been shown to be stored as adsorbed state in the organic kerogen. During depressurization production, the pore pressure decreases, and the desorption of adsorption gas leads to the shrinkage of shale organic matrix. The dimensionless matrix volume strain ε_m caused by gas desorption can be expressed as

$$\varepsilon_m = \varepsilon_L\frac{p_L\left(p_{in} - p\right)}{\left(p_L + p\right)\left(p_{in} + p_L\right)} \tag{17}$$

where ε_L denotes the dimensionless Langmuir strain; and p_{in} denotes the initial pore pressure, MPa. The change in the matrix

volume from the shrinkage of the organic matrix ΔV_m, m^3, can be expressed as

$$\Delta V_m = V_{m\_in}\varepsilon_m \tag{18}$$

The initial dimensionless matrix porosity φ_{int} and pore volume V_{p_in} are defined as

$$\varphi_{\text{int}} = \frac{V_{p\_in}}{V_{p\_in} + V_{m\_in}} \tag{19}$$

$$V_{p\_in} = n_p \pi r_{in}^2 l_p \tag{20}$$

where n_p denotes the dimensionless number of pores; l_p denotes the pore length, m; and r_{in} denotes the initial pore radius, m.

The initial volume of the organic substrate is obtained by substituting **Equation 21** into **Equation 20**:

$$V_{m\_in} = n_p \pi r_{in}^2 l_p \frac{(1-\varphi_{int})}{\varphi_{int}} \tag{21}$$

Shrinkage of the organic matrix shrinkage increases the nanopore radius. The matrix pore volume V_p considering the matrix shrinkage can be expressed as

$$V_p = V_{p\_in} + \Delta V_m$$

Substituting **Equations 21**, **19** into **Equation 23** yields

$$V_p = n_p \pi r_{ds}^2 l_p = n_p \pi r_{in}^2 l_p \left(1 + \frac{(1-\varphi_{int})}{\varphi_{int}} \frac{\varepsilon_L p_L (p_{in}-p)}{(p_L+p)(p_{in}+p_L)}\right) \tag{22}$$

where r_{ds} denotes the pore radius considering the shrinkage of the organic matrix, nm:

$$r_{ds} = r_{in}\left(\sqrt{1 + \frac{(1-\phi_{\text{int}})}{\phi_{\text{int}}} \frac{\varepsilon_L p_L (p_{in}-p_p)}{(p_L+p_p)(p_{in}+p_L)}}\right) \tag{23}$$

4) Pore Radius under the Triple Effect

During the production of shale gas wells, an increase in the effective stress produces a decrease in pore radius, whereas matrix shrinkage increases the pore radius. In addition, adsorption layer thinning at the pore wall expands the pore radius. Thus, the dynamically changing nanopore radius of the shale organic matrix r_{ef}, nm, under these three effects is expressed as:

$$r_{ef} = \left(r_o (p_e/p_o)^{0.5(q-s)} - \theta d_m\right) \times \left(\sqrt{1 + \frac{(1-\varphi_m)}{\varphi_m} \frac{\varepsilon_L p_L (p_{in}-p)}{(p_L+p)(p_{in}+p_L)}}\right) \tag{24}$$

2.2.3 Viscous Slip Flow

Kn_r is an important indicator of the gas flow state. For $10^{-3} < Kn_r < 10^{-1}$, the gas in the nanopores is in slip flow. Using a slip flow correction factor for the viscous flow yields the real gas slip flow mass flux J_{vs}, kg/(m^2·s) (Wu et al., 2017):

$$J_{vs} = -\frac{\varphi_m}{\tau} \frac{r_{ef}^2 \rho_g}{8\mu_g} (1 + \alpha_r Kn_r)\left(1 + \frac{4Kn_r}{1 - bKn_r}\right)\nabla p \tag{25}$$

where

$$\alpha_r = \alpha_o \frac{2}{\pi} tan^{-1}\left(\alpha_1 Kn_r^{\beta}\right) \tag{26}$$

and α_o is the dimensionless coefficient for the rarefaction effect at infinite Kn_r; α_1 and β are dimensionless fitting constants; α_r is the dimensionless ideal gas rarefaction effect coefficient; and b is the dimensionless gas slip constant.

2.2.4 Knudsen Diffusion

For $Kn_r > 10$, Knudsen diffusion is the main contribution to the gas flow in the nanopores. The real gas mass flux under Knudsen diffusion J_{kn}, kg/(m^2·s) is obtained by considering the influence of the pore wall roughness on the gas flow:

$$J_{kn} = -\left(\frac{\varphi_m}{\tau} \frac{2r_{ef}}{3} \delta^{D_f-2}\right)\left(\frac{8ZRT}{\pi M_g}\right)^{1/2} \frac{pM_g C_g}{ZRT} \nabla p \tag{27}$$

$$C_g = \frac{1}{p} - \frac{1}{Z}\frac{dZ}{dp} \tag{28}$$

where δ denotes the dimensionless ratio of the molecular diameter to the local pore diameter; D_f denotes the dimensionless fractal dimension of the pore wall; and C_g is the gas compression factor, 1/MPa.

2.2.5 Surface Diffusion of Adsorption Gas

There is a large concentration gradient of adsorption gas in organic matter over a large specific surface area. In addition to desorption, surface diffusion will occur in shale organic matrix under concentration gradient. The surface diffusion mass flux J_{sa}, kg/(m^2·s), is expressed as

$$J_{sa} = -\frac{\varphi_m M_g D_s \rho_s V_L}{V_{std}\tau} \frac{p_L}{(p+p_L)^2} \nabla p \tag{29}$$

where ρ_s denotes the shale matrix density, kg/m^3; V_L denotes the Langmuir volume, m^3/kg; V_{std} denotes the gas molar volume in the standard state, m^3/mol; and D_s denotes the surface diffusion coefficient (m^2/s) considering the effect of coverage on surface diffusion and is expressed as (Huang et al., 2018):

$$D_s = D_s^0 \frac{(1-\theta) + \frac{\kappa}{2}\theta(2-\theta) + [H(1-\kappa)](1-\kappa)\frac{\kappa}{2}\theta^2}{\left(1 - \theta + \frac{\kappa}{2}\theta\right)^2} \tag{30}$$

where

$$H(1-\kappa) = \begin{cases} 0, \kappa \geq 1 \\ 1, 0 \leq \kappa \leq 1 \end{cases}$$

and D_s^0 denotes the surface diffusion coefficient at zero gas coverage, m^2/s; κ is a dimensionless molecular blockage coefficient for surface gas blockage.

2.2.6 Mass Flow Equation for Gas in Organic Matrix

The gas transport mechanism in the pores of the shale organic matrix consists of the slip flow of free gas and Knudsen and

surface diffusion of adsorption gas. The total mass flow is obtained by linear superposition, in which the slippage flow and Knudsen diffusion of bulk free gas are weighted by contribution coefficient. The total mass flow in the organic matrix pores is expressed as:

$$J_{or} = \omega_v J_v + \omega_k J_k + J_{sa} \tag{31}$$

Substituting **Equations 25**, **27**, **29** into **Equation 31** yields:

$$J_{or} = -\frac{\varphi_m}{\tau}\left[\begin{array}{l} f_s\frac{r_{ef}^2\rho_g}{8\mu_g}(1+\alpha_r Kn_r)\left(1+\frac{4Kn_r}{1-bKn_r}\right)+f_k\left(\frac{2r_{ef}\delta^{D_f-2}}{3}\right)\left(\frac{8ZRT}{\pi M_g}\right)^{1/2}\rho_g C_g \\ +\frac{M_g D_s \rho_s V_L}{V_{std}}\frac{p_L}{(p+p_L)^2}\end{array}\right]\nabla p \tag{32}$$

where φ_{mt} denotes the dimensionless total matrix porosity under the effective stress. The dimensionless coefficient for the slip flow contribution f_s is given as the ratio of the collision frequency between molecules to the total collision frequency, and the dimensionless coefficient for the Knudsen diffusion contribution f_{k} is given as the ratio of the collision frequency of molecules with the pore wall to the total collision frequency:

$$f_s = \frac{1}{(1+Kn_r)} \tag{33}$$

$$f_k = \frac{1}{(1+1/Kn_r)} \tag{34}$$

2.2.7 Apparent Permeability of the Shale Organic Matrix

The definition of the apparent permeability can be used to relate the total mass flow to the apparent permeability of the organic matric to gas K_{map}, expressed in the form of Darcy's equation as:

$$J_T = -\left(\frac{K_{map}\rho_g}{\mu_g}\right)\nabla p \tag{35}$$

Combining Equations 39, 44 yields K_{map}:

$$K_{map} = -\frac{\varphi_m}{\tau}\left[\begin{array}{l} f_s\frac{r_{ef}^2}{8}(1+\alpha_r Kn_r)\left(1+\frac{4Kn_r}{1-bKn_r}\right)+f_k\left(\frac{2r_{ef}\delta^{D_f-2}}{3}\right)\left(\frac{8ZRT}{\pi M_g}\right)^{1/2}\mu_g C_g \\ +\frac{D_s\mu_g ZRT\rho_s V_L}{V_{std}p}\frac{p_L}{(p_L+p)^2}\end{array}\right] \tag{36}$$

3 RESULTS AND DISCUSSION

Basic parameters presented in **Table 2** were used to analyze how the pore pressure, pore radius, stress sensitivity, adsorption layer and matrix shrinkage affect the apparent permeability of the shale organic matrix.

Figure 2 shows the ratio of the apparent permeability to the intrinsic permeability for different pore radii. This ratio increases as the pore pressure decreases, especially for pressures below 10 MPa. The ratio decreases as the pore radius increases. The apparent permeability differs from the intrinsic permeability in this study in accounting for three flow mechanisms: gas slip flow, Knudsen diffusion and surface diffusion. The variation in the permeability ratio with the pore pressure in **Figure 2** indicates that the pore pressure and especially the pore radius are the key factors affecting the gas flow mechanism.

Figure 3A and **Figure 3B** show the contribution of viscous slippage flow, Knudsen diffusion and surface diffusion to apparent permeability with the change of pore radius under low pressure (P = 3 Mpa) and high pressure (p = 30 MPa), respectively. With the decrease of pore radius, the contribution of viscous slippage flow gradually decreases, while the contributions of surface diffusion and Knudsen diffusion gradually increase. When the pore radius is less than 10 nm, this phenomenon becomes more significant. Under high pressure, when the pore radius is greater than 2 nm, the contribution of Knudsen diffusion and surface diffusion to the apparent permeability is almost negligible (<5%). Under low pressure, when the pore radius is greater than 20 nm, the contribution of Knudsen diffusion and surface diffusion to the apparent permeability can be ignored (<5%). Under both low pressure and high pressure, the slippage coefficient decreases to nearly 1 with the increase of pore radius, which indicates that the bulk fluid gradually changes from slippage to viscous flow with the increase of pore radius. Pore pressure and pore size are the key factors affecting surface diffusion, slippage effect and Knudsen diffusion. The smaller the pore pressure and pore radius, the greater the contribution of surface diffusion and Knudsen diffusion to the apparent permeability.

The deviation of apparent permeability Ψ, % is defined as:

$$\psi = \left(\frac{Kmat - Kma}{Kma}\right)\times 100\% \tag{37}$$

TABLE 2 | Basic parameters.

Parameters	Value	Parameters	Value
Organic pore radius (nm)	0.5	Initial stratigraphic pressure (MPa)	60
Tortuosity (dimensionless)	2	Methane molecular diameter (nm)	0.4
Total matrix porosity (dimensionless)	0.05	Overlying strata pressure (MPa)	61
Langmuir pressure (MPa)	5	Langmuir strain (dimensionless variable)	0.003
Langmuir volume (m^3/kg)	0.003	Fitting constant *b* (dimensionless variable)	0.4
Shale permeability coefficient (dimensionless)	0.08	Shale porosity coefficient (dimensionless)	0.04
Molecular mass of methane (kg/mol)	0.016	Universal gas constant J/(mol.K)	8.314
Shale core density (kg/m^3)	2,600	Molar volume at standard conditions (m^3/mol)	0.0224
Equivalent heat of adsorption at zero gas coverage (J/mol)	16,000	Reservoir temperature (K)	373
Gas wall diffusion obstruction coefficient κ (dimensionless)	0.5	Ratio of molecular diameter to local pore diameter δ (dimensionless)	0.5
Fractal dimension of the pore wall (dimensionless)	2.5	Gas slip constant (dimensionless)	−1
Rarefaction effect coefficient (dimensionless)	1.19	Fitting constant *a* (dimensionless)	4

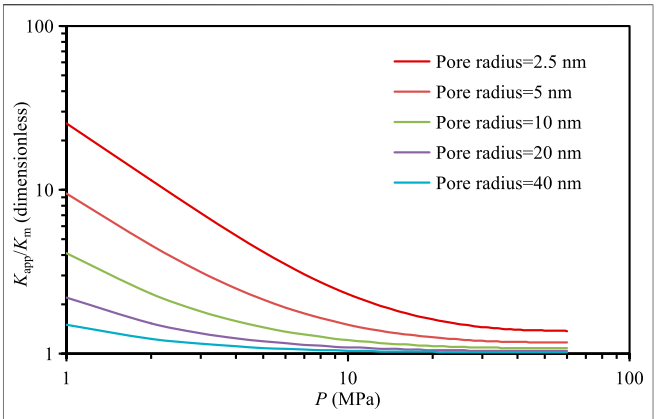

FIGURE 2 | Ratio of the apparent permeability to the intrinsic permeability for different pore radii.

where K_{mat} and K_{ma} denote the apparent permeability of shale matrix with and without the triple flow mechanisms, nD, respectively.

Figure 4 shows the variation of apparent permeability deviation with pore pressure under different pore radius with or without considering the influence of triple flow mechanism. The average deviation of apparent permeability in two cases is given in **Table 3**. When the pore radius is 2.5, 5, 10, and 20 nm, the corresponding apparent permeability decreases by 59.4, 57.6, 56.4 and 55.7% respectively. Generally speaking, with the decrease of pore pressure, the permeability deviation first decreases and then increases. When the pore pressure is greater than 8Mpa, the permeability deviation decreases with the increase of pore radius; When the pore pressure is less than 8Mpa, the permeability deviation increases with the increase of pore radius. This is because the smaller the pore radius, the more significant the influence of the adsorption layer on the apparent permeability. With the decrease of pore pressure, the nano scale effect will increase significantly, so as to improve the apparent permeability and weaken the negative impact of the triple flow mechanisms on the permeability.

Figure 5 and **Figure 6** show the effects of Langmuir strain (matrix shrinkage effect)on apparent permeability and permeability deviation respectively. The apparent

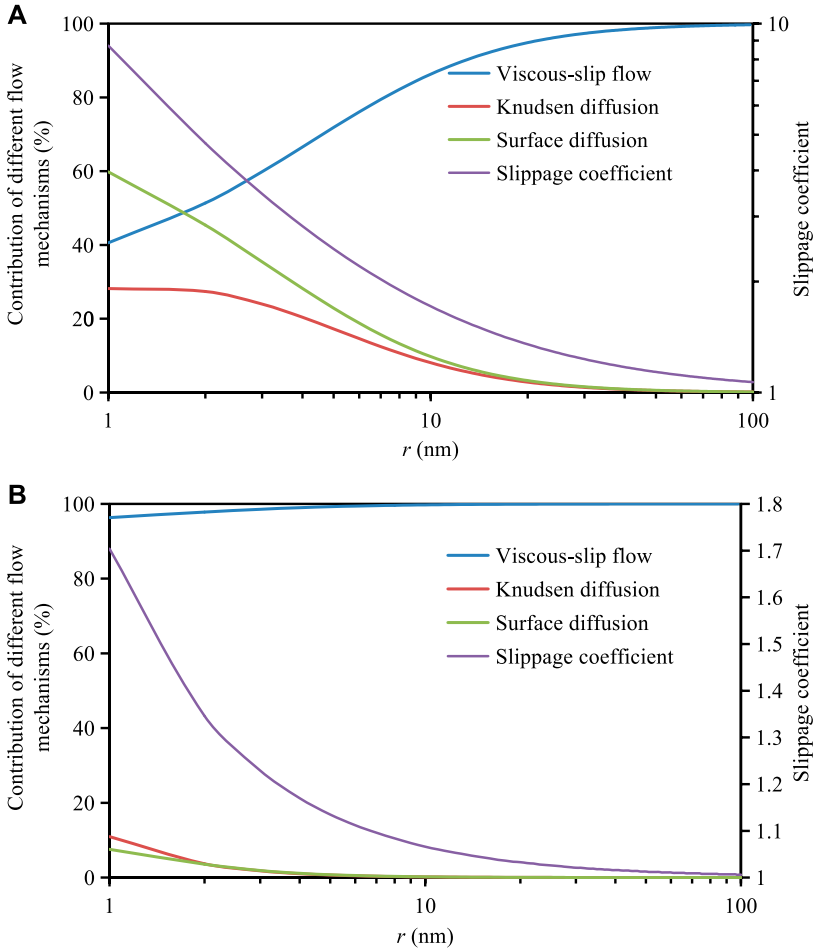

FIGURE 3 | (A) Percentage contribution of different flow mechanisms to the apparent permeability (p = 3 MPa). **(B)** Percentage contribution of different flow mechanisms to the apparent permeability (p = 30 MPa).

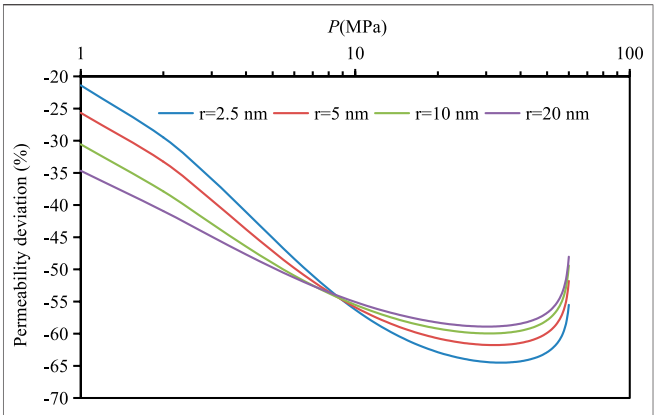

FIGURE 4 | Difference in apparent permeability deviation with and without the triple flow mechanisms for different pore radii.

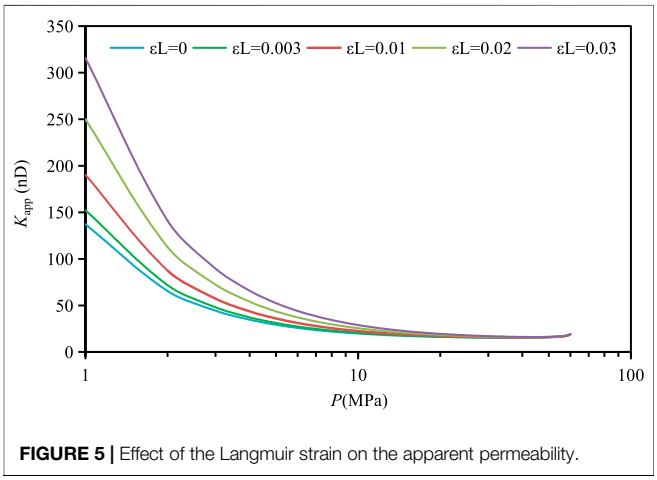

FIGURE 5 | Effect of the Langmuir strain on the apparent permeability.

TABLE 3 | Average apparent permeability deviation considering the triple flow mechanisms for different pore radius.

r (nm)	2.5	5	10	20
Ψ(%)	−59.4	−57.6	−56.4	−55.7

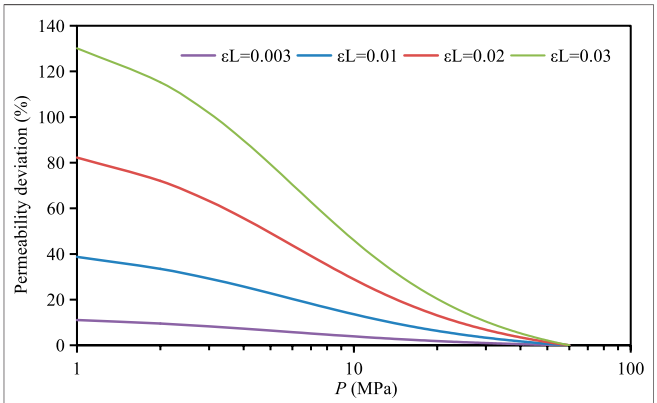

FIGURE 6 | Apparent permeability deviation versus the pore pressure at different Langmuir strains.

permeability increases with the increase of Langmuir strain. As shown in **Table 4**, when the Langmuir strain is 0.003, 0.01, 0.02 and 0.03, the permeability considering matrix shrinkage effect increases by 1.95, 6.76, 14.3, and 22.6% respectively. When the pore pressure drops to 10MPa, the effect of matrix shrinkage on permeability becomes more obvious with the decrease of pore pressure and the increase of Langmuir strain.

Figure 7 and **Figure 8** show the effect of different mechanisms on pore radius in organic pores (shown in **Table 5**). **Table 6** shows the percentage of influence of different mechanisms on pore radius. According to the results in the table, it can be seen that the matrix shrinkage effect increases the pore radius by 4% on average, and the existence of stress sensitive and adsorption layer reduces the pore radius by 10.3 and 6.4% on average. If the effects of stress sensitivity, adsorption layer thinning and matrix shrinkage are considered at the same time, the average pore radius decreases by 13%, and the maximum pore radius decreases by 17% to about 6%. This shows that with the decrease of pore pressure, the matrix shrinkage effect and the thinning of adsorption layer will make up for the loss of pore radius caused by stress sensitivity and increase the pore radius.

Figure 9 shows the variation of apparent permeability of ideal gas and real gas with pore pressure under different pore radius. **Table 7** shows the permeability deviation of ideal gas and real gas under different pore radius and pore pressure. It can be found from the figure that the apparent permeability of the real gas is higher than that of the ideal gas. With the decrease of pore pressure, the permeability deviation between ideal gas and real gas gradually decreases, which is due to the repulsion of gas molecules under high pressure and

TABLE 4 | Apparent permeability deviation at different Langmuir strains.

ε_L	0	0.003	0.01	0.02	0.03
Ψ(%)	0	1.95	6.76	14.3	22.6

attraction under low pressure. As shown in the data in **Table 7** and **Figure 10**, when the pore radius is 2.5, 5 and 10 nm respectively, the apparent permeability of the real gas is increased by 27.5, 16.5 and 9.3% on average compared with the ideal gas. Therefore, it can be found that with the decrease of pore radius, the influence of real gas effect on permeability increases, and the influence of real gas effect on permeability is more obvious under high pressure. At a pore pressure of 60MPa, the apparent permeability calculated based on real gas in pores with a pore radius of 2.5 nm is about 42% higher than that of ideal gas. Therefore, the influence of real gas effect on shale permeability can not be ignored.

Figure 11 shows the influence of confinement effect on permeability under different pore radius. **Figure 11** and **Table 8** show the variation of permeability deviation and

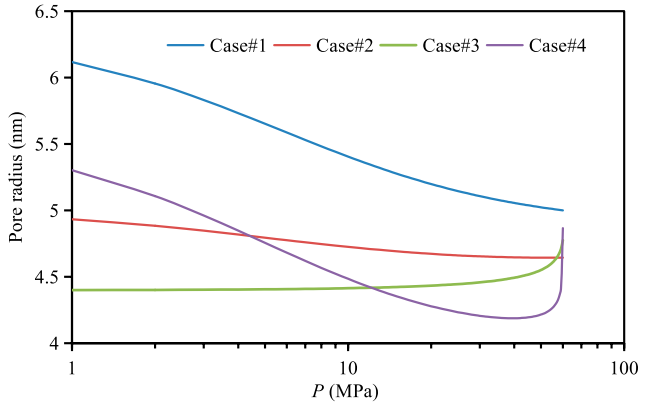

FIGURE 7 | Effects of different mechanisms on pore radius in organic pores.

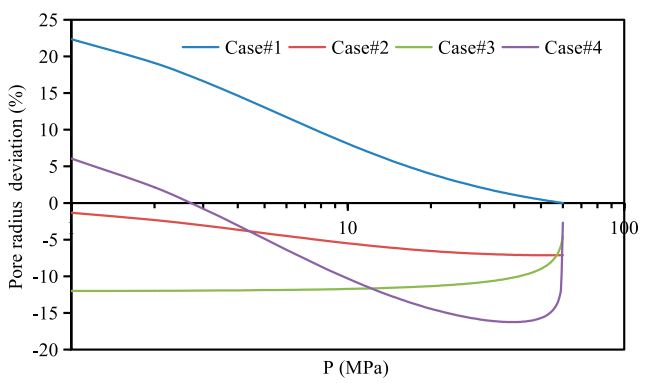

FIGURE 8 | Influence of different mechanisms on pore radius deviation in organic pores.

TABLE 5 | Different mechanisms in organic pores.

case #1	Considering substrate shrinkage only
Case #2	Considering adsorption layer thinning only
Case #3	Considering stress sensitivity only
Case #4	Considering stress sensitivity, adsorption layer and matrix shrinkage effects

average permeability deviation with pore pressure under different pore radius with and without confinement effect. **Figure 11** shows that the apparent permeability is improved after considering the influence of confinement effect compared with not considering confinement effect. According to the data in **Figure 12** and **Table 8**, when the pore radius is 1 nm, 2 nm, 4 nm and 8 nm, the apparent permeability considering the confinement effect is increased by 61.3, 22.4, 8.2, and 2.9% respectively. The permeability deviation decreases with the decrease of pore pressure and increases with the decrease of pore radius. Under the pore pressure of 60MPa, the influence of confinement effect on permeability in organic pores with pore radius of 1 nm can be increased by 88%. Therefore, the influence of confinement effect can not be ignored for small pore radius and high pressure.

TABLE 6 | Effect of different mechanisms on organic pore radius.

case #	1	2	3	4
Ψ (%)	4.0	−6.4	−10.3	−13.0

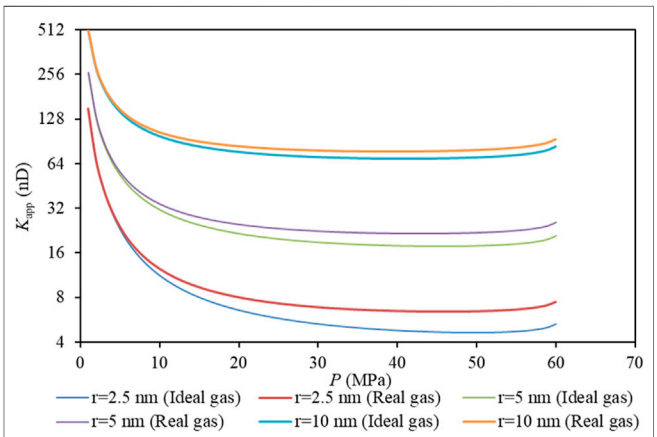

FIGURE 9 | Effect of ideal and real gas on the apparent permeability for different pore radii.

TABLE 7 | Average apparent permeability deviation for real and ideal gases for different pore radii.

r	2.5	5	10
Ψ(%)	27.5	16.5	9.3

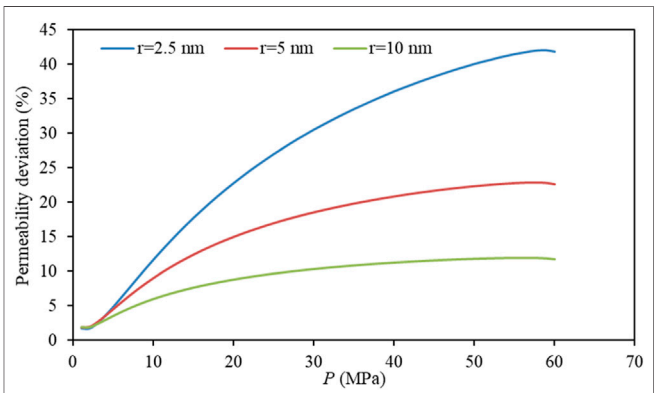

FIGURE 10 | Apparent permeability deviation for real and ideal gases for different pore radii.

TABLE 8 | Influence of confinement effect on apparent permeability deviation.

r (nm)	1	2	4	8
Ψ(%)	61.3	22.4	8.2	2.9

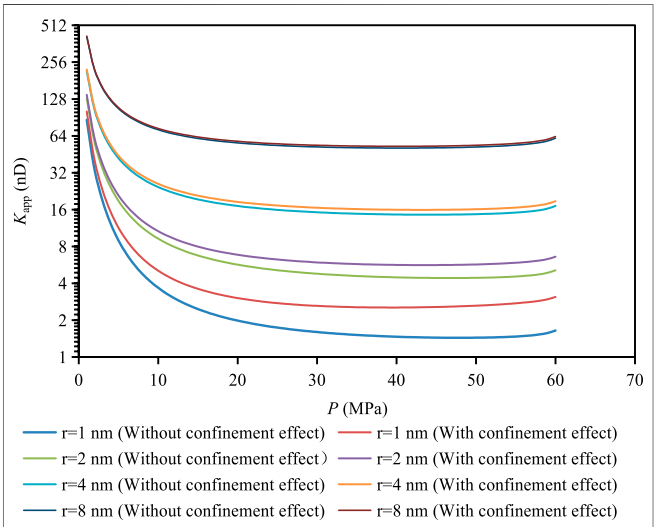

FIGURE 11 | Effect of confinement on the apparent permeability at different pore radii.

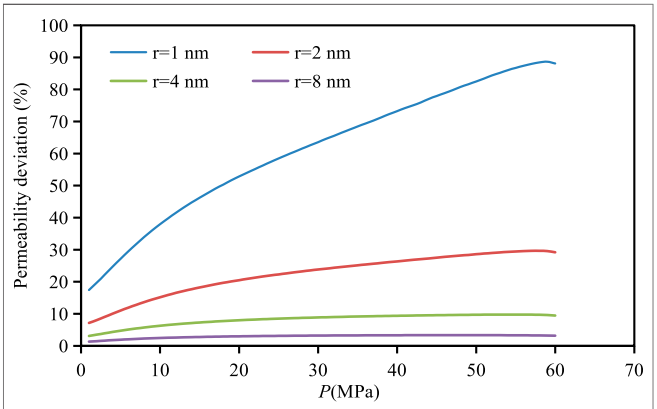

FIGURE 12 | The influence of confinement effect on apparent permeability for different pore radius.

4 CONCLUSION

A apparent permeability model is established, after comprehensively considering three gas flow mechanisms in shale matrix organic pores, including viscous slippage flow, Knudsen diffusion and surface diffusion of adsorbed gas, and real gas effect and confinement effect, and at the same time considering the effects of matrix shrinkage, stress sensitivity, adsorption layer thinning, confinement effect and real gas effect on pore radius. The contribution of three flow mechanisms to apparent permeability under different pore pressure and pore size is analyzed. At the same time, the effects of adsorption layer thinning, stress sensitivity, matrix shrinkage effect, real gas effect and confinement effect on apparent permeability are systematically analyzed. The results show that:

1) Pore pressure and pore radius are the key factors affecting the gas flow mechanism. With the decrease of pore radius, the contribution of viscous slippage flow decreases gradually, and the contributions of surface diffusion and Knudsen diffusion increase gradually. When the pore radius is less than 10 nm, this phenomenon becomes more significant; The apparent permeability decreases first and then increases with the decrease of pore pressure.
2) Adsorption layer and stress sensitivity will reduce the effective radius of pores. With the increase of Langmuir strain and the decrease of pore pressure, the matrix shrinkage effect increases, and the matrix shrinkage will increase the effective pore radius. When the pore pressure drops to 10 MPa, with the decrease of pore pressure and the increase of Langmuir strain, the influence of matrix shrinkage effect on permeability will become more obvious. The matrix shrinkage effect may make up for the loss of effective radius of organic pores caused by stress sensitivity and the existence of adsorption layer.
3) The real gas effect can improve the apparent permeability. With the increase of pore pressure and the decrease of pore radius, the effect of real gas effect on the apparent permeability increases. The influence of real gas effect on shale permeability can not be ignored.
4) The confinement effect can improve the apparent permeability. With the increase of pore pressure and the decrease of pore radius, the influence of confinement effect on apparent permeability increases rapidly. Under the conditions of nano pores and high pressure, the influence of confinement effect can not be ignored.

DATA AVAILABILITY STATEMENT

The raw data supporting the conclusions of this article will be made available by the authors, without undue reservation.

AUTHOR CONTRIBUTIONS

WG, XZ, and RY contributed to conception and design of the study. wrote the first draft of the manuscript. LK, JG, and YL wrote sections of the manuscript. All authors contributed to manuscript revision, read, and approved the submitted version.

REFERENCES

An, C., Fang, Y., Liu, S., Alfi, M., Yan, B., Wang, Y., et al. (2017). "Impacts of Matrix Shrinkage and Stress Changes on Permeability and Gas Production of Organic-Rich Shale Reservoirs," in [C] //Society of Petroleum Engineers-SPE Reservoir Characterisation and Simulation Conference and Exhibition, Abu Dhabi, UAE, 1–16. doi:10.2118/186029-ms

Cao, G., Lin, M., Jiang, W., Li, H., Yi, Z., and Wu, C. (2017). A 3D Coupled Model of Organic Matter and Inorganic Matrix for Calculating the Permeability of Shale. *Fuel* 204, 129–143. doi:10.1016/j.fuel.2017.05.052

Chai, D., Fan, Z., and Li, X. (2019). A New Unified Gas-Transport Model for Gas Flow in Nanoscale Porous Media. *SPE J.* 24 (02), 698–719. doi:10.2118/194208-pa

Cui, G., Liu, J., Wei, M., Feng, X., and Elsworth, D. (2018a). Evolution of Permeability during the Process of Shale Gas Extraction. *J. Nat. Gas Sci. Eng.* 49, 94–109. doi:10.1016/j.jngse.2017.10.018

Cui, G., Liu, J., Wei, M., Shi, R., and Elsworth, D. (2018b). Why Shale Permeability Changes under Variable Effective Stresses: New Insights. *Fuel* 213, 55–71. doi:10.1016/j.fuel.2017.10.068

Dong, J.-J., Hsu, J.-Y., Wu, W.-J., Shimamoto, T., Hung, J.-H., Yeh, E.-C., et al. (2010). Stress-dependence of the Permeability and Porosity of sandstone and Shale from TCDP Hole-A. *Int. J. Rock Mech. Mining Sci.* 47, 1141–1157. doi:10.1016/j.ijrmms.2010.06.019

Geng, L., Li, G., Zitha, P., Tian, S., Sheng, M., and Fan, X. (2016). A Diffusion-Viscous Flow Model for Simulating Shale Gas Transport in Nano-Pores. *Fuel* 181, 887–894. doi:10.1016/j.fuel.2016.05.036

Huang, S., Wu, Y., Cheng, L., Liu, H., Xue, Y., and Ding, G. (2018). Apparent Permeability Model for Shale Gas Reservoirs Considering Multiple Transport Mechanisms. *Geofluids*. doi:10.1155/2018/2186194

Jia, B., Tsau, J.-S., and Barati, R. (2018). A Workflow to Estimate Shale Gas Permeability Variations during the Production Process. *Fuel* 220, 879–889. doi:10.1016/j.fuel.2017.11.087

Jia, B., Tsau, J.-S., and Barati, R. (2019). Investigation of Shale-Gas-Production Behavior: Evaluation of the Effects of Multiple Physics on the Matrix. *SPE Reservoir Eval. Eng.* 23 (01), 068–080. doi:10.2118/197069-pa

Li, J., Chen, Z., Wu, K., Zhang, T., Zhang, R., Xu, J., et al. (2018). Effect of Water Saturation on Gas Slippage in Circular and Angular Pores. *Aiche J.* 64 (9), 3529–3541. doi:10.1002/aic.16196

Li, J., Li, X., Wang, X., Li, Y., Wu, K., Shi, J., et al. (2016). Water Distribution Characteristic and Effect on Methane Adsorption Capacity in Shale clay. *Int. J. Coal Geology.* 159, 135–154. doi:10.1016/j.coal.2016.03.012

Li, Z., Qi, Z., Yan, W., Xiang, Z. P., Ao, X., Huang, X. L., et al. (2020). Prediction of Production Performance of Refractured Shale Gas Well Considering Coupled Multiscale Gas Flow and Geomechanics. *Geofluids* 2020, 1–21. doi:10.1155/2020/9160346

Li, Z., Yan, W., Qi, Z., Dong, D., Huang, X., and Yu, R. (2019). Production Performance Model Based on Quadruple-Porosity Medium in Shale Gas Reservoirs Considering Multi-Transport Mechanisms. *Energy Sourc. A: Recovery, Utilization, Environ. Effects*, 1–19. doi:10.1080/15567036.2019.1662520

Pang, Y., Soliman, M. Y., Deng, H., and Emadi, H. (2017). Analysis of Effective Porosity and Effective Permeability in Shale-Gas Reservoirs with Consideration of Gas Adsorption and Stress Effects. *SPE J.* 22 (06), 1–739. doi:10.2118/180260-pa

Peng, Y., Liu, J., Pan, Z., Qu, H., and Connell, L. (2018). Evolution of Shale Apparent Permeability under Variable Boundary Conditions. *Fuel* 215, 46–56. doi:10.1016/j.fuel.2017.11.024

Sakhaee-Pour, A., and Bryant, S. L. (2012). Gas Permeability of Shale. *SPE Reservoir Eval. Eng.* 15 (04), 401–409. doi:10.2118/146944-pa

Sheng, G., Javadpour, F., and Su, Y. (2019). Dynamic Porosity and Apparent Permeability in Porous Organic Matter of Shale Gas Reservoirs. *Fuel* 251, 341–351. doi:10.1016/j.fuel.2019.04.044

Sheng, G., Javadpour, F., and Su, Y. (2018). Effect of Microscale Compressibility on Apparent Porosity and Permeability in Shale Gas Reservoirs. *Int. J. Heat Mass Transfer* 120, 56–65. doi:10.1016/j.ijheatmasstransfer.2017.12.014

Sheng, G., Su, Y., Wang, W., Liu, J., Lu, M., Zhang, Q., et al. (2015). A Multiple Porosity media Model for Multi-Fractured Horizontal wells in Shale Gas Reservoirs. *J. Nat. Gas Sci. Eng.* 27, 1562–1573. doi:10.1016/j.jngse.2015.10.026

Shi, J. T., Zhang, L., Li, Y. S., Yu, W., He, X., Liu, N., et al. (2013). "Diffusion and Flow Mechanisms of Shale Gas through Matrix Pores and Gas Production Forecasting," in Paper SPE 167226 Presented at the SPE Unconventional Resources Conference Canada, Calgary, Alberta, Canada, 1–14. doi:10.2118/167226-ms

Singh, H., Javadpour, F., Ettehadtavakkol, A., and Darabi, H. (2014). Nonempirical Apparent Permeability of Shale. *SPE Reservoir Eval. Eng.* 17 (03), 414–424. doi:10.2118/170243-pa

Song, W., Yao, J., Li, Y., Sun, H., Zhang, L., Yang, Y., et al. (2016). Apparent Gas Permeability in an Organic-Rich Shale Reservoir. *Fuel* 181, 973–984. doi:10.1016/j.fuel.2016.05.011

Sun, Z., Li, X., Shi, J., Zhang, T., and Sun, F. (2017). Apparent Permeability Model for Real Gas Transport through Shale Gas Reservoirs Considering Water Distribution Characteristic. *Int. J. Heat Mass Transfer* 115, 1008–1019. doi:10.1016/j.ijheatmasstransfer.2017.07.123

Sun, Z., Shi, J., Wu, K., and Li, X. (2018a). Gas Flow Behavior through Inorganic Nanopores in Shale Considering Confinement Effect and Moisture Content. *Ind. Eng. Chem. Res.* 57 (9), 3430–3440. doi:10.1021/acs.iecr.8b00271

Sun, Z., Shi, J., Wu, K., Xu, B., Zhang, T., Chang, Y., et al. (2018b). Transport Capacity of Gas Confined in Nanoporous Ultra-tight Gas Reservoirs with Real Gas Effect and Water Storage Mechanisms Coupling. *Int. J. Heat Mass Transfer* 126, 1007–1018. doi:10.1016/j.ijheatmasstransfer.2018.05.078

Sun, Z., Shi, J., Wu, K., Zhang, T., Feng, D., Huang, L., et al. (2019). An Analytical Model for Gas Transport through Elliptical Nanopores. *Chem. Eng. Sci.* 199, 199–209. doi:10.1016/j.ces.2019.01.013

Swami, V., Clarkson, C. R., and Settari, A. (2012). "Non Darcy Flow in Shale Nanopores: Do We Have a Final Answer?," in Paper SPE 162665 Presented at the SPE Canadian Unconventional Resources Conference, Calgary, Alberta, Canada, 1–15.

Tian, S., Wang, T., Li, G., Sheng, M., Liu, Q., and Zhang, S. (2018). An Analytical Model for Shale Gas Transport in Circular Tube Pores. *Int. J. Heat Mass Transfer* 127, 321–328. doi:10.1016/j.ijheatmasstransfer.2018.07.046

Wang, H. Y., and Marongiu-Porcu, M. (2015). "A Unified Model of Matrix Permeability in Shale Gas Formations," in Paper SPE 173196 Presented at the SPE Reservoir Simulation Symposium, Houston, Texas, USA, 1–10. doi:10.2118/173196-ms

Wang, J., Liu, H., Wang, L., Zhang, H., Luo, H., and Gao, Y. (2015). Apparent Permeability for Gas Transport in Nanopores of Organic Shale Reservoirs Including Multiple Effects. *Int. J. Coal Geology.* 152, 50–62. doi:10.1016/j.coal.2015.10.004

Wang, Q., Hu, Y., Zhao, J., Ren, L., Zhao, C., and Zhao, J. (2019). Multiscale Apparent Permeability Model of Shale Nanopores Based on Fractal Theory. *Energies* 12 (17), 3381. doi:10.3390/en12173381

Wang, S., Shi, J., Wang, K., Sun, Z., Miao, Y., and Hou, C. (2018). Apparent Permeability Model for Gas Transport in Shale Reservoirs with Nano-Scale Porous media. *J. Nat. Gas Sci. Eng.* 55, 508–519. doi:10.1016/j.jngse.2018.05.026

Wasaki, A., and Akkutlu, I. Y. (2015). Permeability of Organic-Rich Shale. *SPE J.* 20 (06), 1–384. doi:10.2118/170830-pa

Wu, K., Chen, Z., Li, X., and Dong, X. (2016c). Methane Storage in Nanoporous Material at Supercritical Temperature over a Wide Range of Pressures. *Sci. Rep.* 6, 33461. doi:10.1038/srep33461

Wu, K., Chen, Z., Li, X., Guo, C., and Wei, M. (2016d). A Model for Multiple Transport Mechanisms through Nanopores of Shale Gas Reservoirs with Real Gas Effect-Adsorption-Mechanic Coupling. *Int. J. Heat Mass Transfer* 93, 408–426. doi:10.1016/j.ijheatmasstransfer.2015.10.003

Wu, K., Chen, Z., Li, X., Xu, J., Li, J., Wang, K., et al. (2017). Flow Behavior of Gas Confined in Nanoporous Shale at High Pressure: Real Gas Effect. *Fuel* 205, 173–183. doi:10.1016/j.fuel.2017.05.055

Wu, K., Li, X., Guo, C., Wang, C., and Chen, Z. (2016a). A Unified Model for Gas Transfer in Nanopores of Shale-Gas Reservoirs: Coupling Pore Diffusion and Surface Diffusion. *SPE J.* 21 (05), 1–583. doi:10.2118/2014-1921039-pa

Wu, K., Li, X., Guo, C., Wang, C., and Chen, Z. (2016b). A Unified Model for Gas Transfer in Nanopores of Shale-Gas Reservoirs: Coupling Pore Diffusion and Surface Diffusion. *SPE J.* 21 (05), 1583–1611. doi:10.2118/2014-1921039-pa

Xiong, X. Y., Devegowda, D., Villazon, M., Sigal, R., and Civan, F. (2012). "A Fully-Coupled Free and Adsorptive Phase Transport Model for Shale Gas Reservoirs Including Non-darcy Flow Effects," in SPE annual technical conference and exhibition (SPE-159758-MS), San Antonio, Texas, USA, 1–16. doi:10.2118/159758-ms

Yin, Y., Qu, Z. G., and Zhang, J. F. (2017). An Analytical Model for Shale Gas Transport in Kerogen Nanopores Coupled with Real Gas Effect and Surface Diffusion. *Fuel* 210, 569–577. doi:10.1016/j.fuel.2017.09.018

Yucel Akkutlu, I., and Fathi, E. (2012). Multiscale Gas Transport in Shales with Local Kerogen Heterogeneities. *SPE J.* 17, 1002–1011. doi:10.2118/146422-pa

Zhang, L., Liang, H., Zhao, Y., Xie, J., Peng, X., and Li, Q. (2020). Gas Transport Characteristics in Shale Matrix Based on Multiple Mechanisms. *Chem. Eng. J.* 386, 124002. doi:10.1016/j.cej.2019.124002

Zhang, L., Shan, B., Zhao, Y., Du, J., Chen, J., and Tao, X. (2018). Gas Transport Model in Organic Shale Nanopores Considering Langmuir Slip Conditions and Diffusion: Pore Confinement, Real Gas, and Geomechanical Effects. *Energies* 11 (1), 223. doi:10.3390/en11010223

Zhang, M., Yao, J., Sun, H., Zhao, J.-l., Fan, D.-y., Huang, Z.-q., et al. (2015). Triple-continuum Modeling of Shale Gas Reservoirs Considering the Effect of Kerogen. *J. Nat. Gas Sci. Eng.* 24, 252–263. doi:10.1016/j.jngse.2015.03.032

Zhang, Q., Wang, W.-D., Kade, Y., Wang, B.-T., and Xiong, L. (2020). Analysis of Gas Transport Behavior in Organic and Inorganic Nanopores Based on a Unified Apparent Gas Permeability Model. *Pet. Sci.* 17 (1), 168–181. doi:10.1007/s12182-019-00358-4

Zhang, T., Li, X., Sun, Z., Feng, D., Miao, Y., Li, P., et al. (2017). An Analytical Model for Relative Permeability in Water-Wet Nanoporous media. *Chem. Eng. Sci.* 174, 1–12. doi:10.1016/j.ces.2017.08.023

Zhang, T., Li, X., Wang, X., Li, J., Sun, Z., Feng, D., et al. (2018). A Discrete Model for Apparent Gas Permeability in Nanoporous Shale Coupling Initial Water Distribution. *J. Nat. Gas Sci. Eng.* 59, 80–96. doi:10.1016/j.jngse.2018.08.024

Zhao, J., Li, Z., Hu, Y., Ren, L., and Tao, Z. (2016). The Impacts of Microcosmic Flow in Nanoscale Shale Matrix Pores on the Gas Production of a Hydraulically Fractured Shale-Gas Well. *J. Nat. Gas Sci. Eng.* 29, 431–439. doi:10.1016/j.jngse.2016.01.025

Conflict of Interest: Authors WG, XZ, RY, LK, JG and YL were employed by PetroChina.

frontiers in Earth Science

ORIGINAL RESEARCH
published: 20 January 2022
doi: 10.3389/feart.2021.823764

Two-phase Flow Model and Productivity Evaluation of Gas and Water for Dual-Medium Carbonate Gas Reservoirs

Lixia Kang[1], Wei Guo[1], Xiaowei Zhang[1]*, Yuyang Liu[1]*, Jinliang Gao[1], Zhaoyuan Shao[1], Min Li[2] and Yue Sun[3]*

[1]*Research Institute of Petroleum Exploration and Development (RIPED), Beijing, China,* [2]*Beijing Gas Group Co., Ltd., Beijing, China,* [3]*Institute of Safety, Environment Protection and Technical Supervision, PetroChina Southwest Oil and Gasfield Company, Chengdu, China*

Fluid flow in the dual-medium carbonate gas reservoir is characterized by stress sensitivity and non-Darcy flow effect. In order to accurately describe the unsteady flow of gas and water in the dual-medium gas reservoir, a two-phase flow model of gas and water is built. First, reservoir space and fluid flow characteristics of carbonate gas reservoirs are investigated, and the flow model that considers both the stress sensitivity and non-Darcy flow is built based on the fundamental flow theory, after fully investigating the reservoir space and fluid flow characteristics of carbonate gas reservoirs. Then, the perturbation theory is introduced, and the model is solved in the Laplace space, after which the obtained Laplace space analytical solution is converted into the real-space solution. Finally, the productivity evaluation model for the dual-medium gas reservoir with the gas-water two-phase flow is built, based on the flowing material balance method and Newton iteration. The presented productivity evaluation model is applied to analyze the effects of stress sensitivity and non-Darcy flow on the two-phase flow model of gas and water for the dual-medium gas reservoir and the reservoir productivity. The results indicate that a higher stress sensitivity coefficient is demonstrated to indicate higher stress sensitivity and accelerated production decline of the reservoir, while a lower non-Darcy flow effect coefficient represents a stronger non-Darcy effect and boosted drop of initial production of the reservoir. Hence, it is not reasonable to neglect the effects of stress sensitivity and non-Darcy flow during the evaluation of the productivity of a dual-medium carbonate gas reservoir. The model presented in this research provides important references for improving the recovery performance of dual-medium gas reservoirs.

Keywords: stress sensitivity, non-darcy flow effect, dual-medium, two-phase flow of gas and water, flow model, productivity evaluation

OPEN ACCESS

Edited by:
Xiaohu Dong,
China University of Petroleum, China

Reviewed by:
Pin Jia,
China University of Petroleum, China
Bl Liu,
Yangtze University, China

****Correspondence:***
Wei Guo
guowei69@petrochina.com.cn
Xiaowei Zhang
zhangxw69@petrochina.com.cn
Yuyang Liu
yuyangliu@petrochina.com.cn

Specialty section:
This article was submitted to Economic Geology, a section of the journal Frontiers in Earth Science

Received: *28 November 2021*
Accepted: *20 December 2021*
Published: *20 January 2022*

Citation:
Kang L, Guo W, Zhang X, Liu Y, Gao J, Shao Z, Li M and Sun Y (2022) Two-phase Flow Model and Productivity Evaluation of Gas and Water for Dual-Medium Carbonate Gas Reservoirs. Front. Earth Sci. 9:823764. doi: 10.3389/feart.2021.823764

INTRODUCTION

Carbonate reservoirs are important targets for hydrocarbon exploration and exploitation, because they contain abundant oil and gas resources (Xu et al., 2007). Compared with conventional gas reservoirs, the dual-medium carbonate gas reservoir is associated with greatly different reservoir characteristics that may result from the relatively developed pores and fractures. Its flow is typically

characterized by stress sensitivity, non-Darcy effect, and unique relative gas-water permeability relationship.

In terms of stress sensitivity, Fan et al. (2011) develop a flow model incorporating the stress-sensitive permeability of fracture systems via analyzing the medium deformation of the dual-medium gas reservoir. Zhao et al. (2013) carry out stress sensitivity experiments using four types of cores, namely the matrix type, the fully-filled-fracture type, the semi-filled-fracture type, and the non-filled-fracture type. They rank the stress sensitivity of these four types of cores in the increasing order of matrix, fully-filled-fracture, semi-filled-fracture, and non-filled-fracture types. Moreover, they identify a power-law relationship between permeability and stress. Peng et al. (2015) experimentally analyzed the stress sensitivity of cores under the constant confining pressure and varied pressure and its effects on the reservoir productivity. Zhang R et al. (2016) compare five frequently-used formulas for stress sensitivity via an experimental-theoretical-integrated approach and conclude that the stress sensitivity of fractured reservoirs can be characterized using the power-law formula. Luo et al. (2021) considered the stress-sensitive effects of natural fractures based on the dual-medium flow theory model.

Also, studies on the characteristics of non-Darcy flow have been reported. Cheng and Chen (1998) probe the characteristics of low-speed non-Darcy flow in the case of two-phase flow of oil and gas and point out that non-Darcy flow to some extent impacts (reduces) oil production. Moreover, with the same water content, the productivity index of non-Darcy flow is smaller than that of Darcy flow. Lu (2010) experimentally investigates the fluid flow characteristics under the varied fracture and fracture-vug conditions and identifies the critical parameter values for non-Dary flow, and builds the flow model by introducing Forchheimer number to characterize non-Darcy flow. Zhang F et al. (2016) study the effects of high-speed non-Darcy flow on the productivity of gas wells with certain water cut, *via* theoretical derivation. Furthermore, the analysis based on the derived productivity equation and actual data of production wells demonstrates that the productivity of gas wells with a certain water cut is considerably lower than that of gas wells with no water production; the non-Darcy effect of productivity of gas wells declines after water production starts. Javadpour et al. (2021) considered the non- Darcy flow of shale gas, and reviewed the dominant gas-flow processes in a single nanopore based on theoretical models and molecular dynamics simulations, and Lattice Boltzmann modeling.

As for the relative permeability of gas and water, Esmaeili et al. (2020) use a newmethodology and conduct limited steady-state relative permeability measurements at different temperatures to confirm the validity of displacement-based relative permeability. Fang et al. (2015) study the pattern of the relative permeability curves of gas and water in high-temperature, high-pressure tight gas reservoirs. Their research identifies that gas permeability under high temperature and high pressure is found to be higher than that under conventional conditions, which means high temperature and high pressure are in favor of gas flow. Liao (2016) investigates the characteristics of the two-phase flow of gas and water in the fractured gas reservoir using numerical models. In his research, he discussed the effects of numerous factors on the production characteristics of the gas reservoir based on the mechanism model, including geological parameters, aquifer parameters, production schemes, water intrusion patterns, and heterogeneity.

At last, for the flow model and productivity evaluation model of gas reservoirs, Zhang et al. (2017a) combine the material balance equation and stress-dependent production equation in the case of over-pressurization to analyze the stress sensitivity of formations and derive the productivity prediction model. The result indicate the critical role of stress sensitivity in reducing the production of gas wells and shortening the duration of stable production. Brown et al. (2009) analyze the pressure and productivity characteristics of stage-fractured horizontal wells of shale gas reservoirs using an analytical tri-linear flow model. Deng et al. (2011), based on their analysis of the gas-water relative permeability regularity, modify the productivity prediction model of water-producing gas wells and the production decline analysis method for water-involved gas reservoirs with the non-Darcy flow. Chen (2016) probes the fluid flow patterns of low-permeability gas reservoirs and develops the productivity calculation formulas for fractured horizontal wells and those with inclined fractures and gas-water two-phase flow, respectively. The presented models are validated by the good application performance of the models to the production data of actual production wells. In 2017, a productivity evaluation method for abnormally over-pressurized gas reservoirs, incorporating both the reservoir rock deformation and gas-water relative permeability, is developed by Zhang et al. (2017b), which is then applied to investigating the factors affecting the production performance of gas wells via actual production data. Based on the material balance theory, Zhang W et al. (2017) derive the pressure calculation formula and production prediction equation for gas wells featuring two-phase flow, which provide theoretical support to production forecasting of gas wells with coexisting gas and water.

The above review demonstrates substantial progress in studying the flow regularity and productivity prediction of carbonate gas reservoirs. Nonetheless, most research only considers the effects of a single factor, and rare studies have been reported to investigate the joint impacts of stress sensitivity, non-Darcy flow, and two-phase relative permeability of gas and water on carbonate gas reservoirs. Moreover, complete, systematic productivity evaluation methods for carbonate gas reservoirs haven't been presented yet. Given these, this study aims and manages to build a gas-water two-phase flow model of carbonate gas reservoirs, incorporating both stress sensitivity and non-Darcy flow. Results of this study are expected to provide references for improving the recovery performance of dual-medium carbonate gas reservoirs.

FLUID FLOW PATTERNS FOR CARBONATE GAS RESERVOIRS

Dual-medium carbonate gas reservoirs are different from conventional reservoirs, and they are composed of matrix and fracture systems (Li et al., 2017)—the low-porosity,

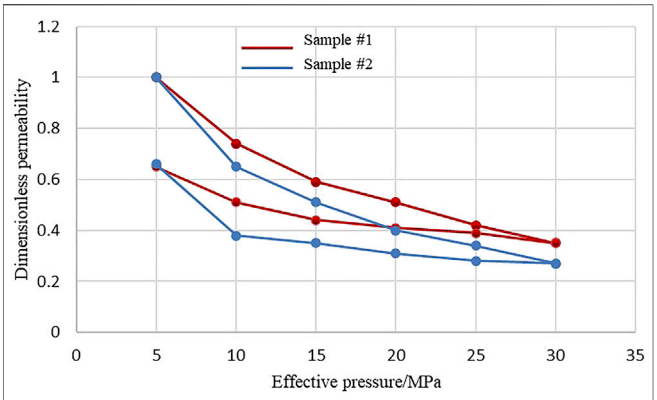

FIGURE 1 | Relationship between core permeability and overburden pressure.

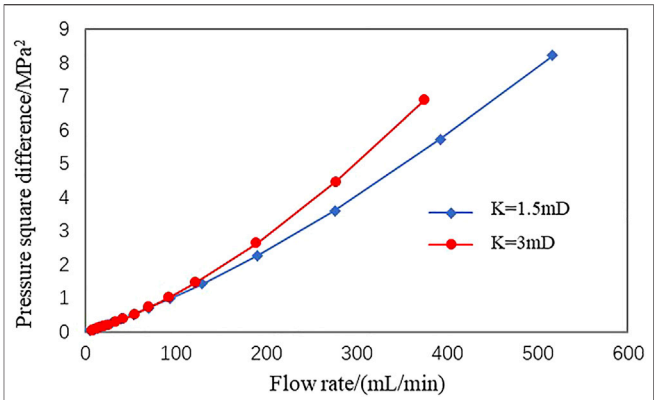

FIGURE 2 | Non-Darcy feature of the fracture-pore type reservoir rock.

high-permeability fracture system is the main flow channel for fluids, while the high-porosity, low-permeability matrix system is the main storage space for gas. Such dual-medium carbonate reservoirs have greatly different pore-throat structures and more complicated fluid flow than conventional pore-dominated gas reservoirs (Jia et al., 2013).

Stress Sensitivity of Reservoirs

During the recovery process of carbonate gas reservoirs, the reservoir rock framework deforms, as the effective stress grows (e.g., the overburden stress) owing to the sustained production of natural gas and consequent pore pressure decline (Li et al., 2011). The ultimate resultant variation of the reservoir physical parameters such as permeability and porosity is referred to as stress sensitivity (Peng et al., 2015). It is known that with the progress in hydrocarbon recovery, the reservoir permeability and productivity are both degraded.

The core porosity and permeability measurements under the overburden pressure of the L carbonate gas reservoir of the A gas field (**Figure 1**) shows that the tendencies of permeability to decline with increasing overburden pressure are generally consistent; as the overburden pressure reaches 30 MPa, the core permeability declines by 60%; as the overburden pressure restores to the initial value, the permeability recovers to about 60% of the initial permeability (in other words, a permanent permeability loss of 40% is caused). The dimensionless permeability in **Figure 1** is the ratio of permeability under certain pressure conditions to initial permeability (k_i/k_0).

The stress sensitivity can be characterized using the power-law function (Petrosa, 1986):

$$k_f = k_{fi} e^{-\gamma_f (\psi_i - \psi_f)} \tag{1}$$

where k_f is the permeability of the fracture system, mD; k_{fi} is the fracture system permeability corresponding to the original formation conditions, mD; γ_f is the permeability modulus, MPa^{-1}; ψ_i is the initial pseudo-pressure of formations, $MPa^2/(mPa{\cdot}s)$; ψ_f is the pseudo-pressure of the fracture system, $MPa^2/(mPa{\cdot}s)$.

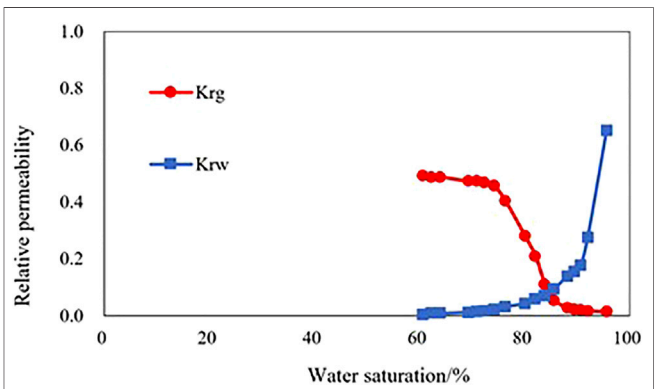

FIGURE 3 | Two-phase relative permeability of gas and water for the dual-medium.

The pseudo-permeability modulus is defined as:

$$\gamma_f = \frac{1}{k_f} \frac{\partial k_f}{\partial \psi_f} \tag{2}$$

Effects of High-Speed Non-Darcy Flow

Due to the reservoir rock property, the dual-medium carbonate reservoir is subjected to considerable gas turbulence and thus the intensive non-Darcy effect (Chen et al., 2015). The non-Darcy flow regularity of the fracture-pore type reservoir rock of the L gas reservoir in the A gas field is illustrated in **Figure 2**. When the flow rate grows, the non-linearity between the pressure square difference and the gas flow rate gradually climbs up. Gas wells, subjected to the non-Darcy effect, are expected to present a certain degree of production decline.

The non-Darcy effect can be characterized by introducing a correction factor dependent on fluid flow rates (Huang et al., 2004).

$$-\frac{dP}{dr} = \frac{\mu_g u_g}{K} + \delta \rho u_g^2 \tag{3}$$

where μ_g is the fluid viscosity, mPa·s; u_g is the flow rate, cm/s; δ is the non-Darcy coefficient, cm^{-1}; ρ is the fluid density, kg/m^3.

Two-phase Relative Permeability Pattern of Gas and Water

Because of the presence of dual media composed of pores and fractures and the substantial difference of fluid flow space between them, the fracture-pore type carbonate reservoir presents highly complex flow characteristics. Accordingly, the two-phase relative permeability pattern of gas and water is also greatly different from that in the conventional gas reservoir (**Figure 3**). Cores in the study area are proven to be highly hydrophilic, with the relative permeability intersection point occurring at the water saturation of above 70%. This is caused by the micropore structure of the gas reservoir—some tiny throats in the pore structure are too small to allow water to form a continuous flowing phase after penetrating such space.

TWO-PHASE PRODUCTIVITY EVALUATION MODEL FOR GAS AND WATER IN DUAL-MEDIUM GAS RESERVOIRS

Flow Model

The fracture-pore type dual-medium has been demonstrated to primarily consist of two types of pore structures, namely primary inter-granular pores and secondary pores. Primary pores are largely affected by deposition and diagenesis processes, dimensions, distributions, and shapes of reservoir rock grains, thereby presenting heterogeneous features of permeability and porosity. As for secondary pores, they are composed of fractures, joints, and dissolved pores. In other words, the dual-medium consists of two systems, namely pore and fracture systems. In most cases, the fracture system serves as the main fluid flow channel, while the rock matrix provides the main storage space.

The fractured reservoir has the following characteristics:

1) Dual structural characteristics. The reservoir rock is associated with the extensive development of both primary and secondary pores (in other words, it consists of dual media of pores and fractures, respectively). Both the pore and fracture media have their own porosity and permeability features and the two media are connected.
2) The compressibility of the fracture system is considerably higher than that of the pore system. Therefore, as the fluid (pore) pressure decreases, the fracture may close under the overburden pressure; moreover, such fracture closure is irreversible. Ultimately, the fracture permeability is reduced.
3) Anisotropy. The reservoir permeability is highly anisotropic. For productivity evaluation, if the goal is only to investigate the formation characteristics in a vertical well, the medium can be considered isotropic.

The fracture-pore medium model assumes that the reservoir is a dual-medium for fluid storage and flow composed of the matrix and fracture systems. The assumptions of the physical model for production decline of wells in the fracture-pore type reservoir are summarized below:

1) The vertical well is producing at a constant production rate from a reservoir with the closed outer boundary.
2) The payzone is producing across its whole thickness and the fluid flows into the wellbore via the radial flow regime.
3) The rock compressibility is neglected, while the gas compressibility and stress-dependency of the fracture system permeability are considered.
4) Fluids have two components, namely gas and water.
5) The effects of capillary pressure and gravity are ignored.
6) Fractures are the only channel for fluids to flow into the wellbore. Fluids in the matrix system flow into fractures via the pseudo-steady cross flow and then enter the wellbore through fractures.

The mathematic model of the fracture system is described below:

The continuity equation:

$$\frac{1}{r}\frac{\partial}{\partial r}\left[r\left(\rho_g v_g + \rho_w v_w\right)\right] = \frac{\partial\left(\rho_g S_g + \rho_w S_w\right)}{\partial t} - q_{mf} \tag{4}$$

where ρ_g is the gas density, kg/m^3; v_g is the gas flow rate, cm/s; ρ_w is the water density, kg/m^3; v_w is the water flow rate cm/s; S_g is the gas saturation, decimals; S_w is the water saturation, decimals.

Equations of motion:

$$v_g = -\delta\frac{kk_{rg}}{\mu_g B_g}\frac{\partial p}{\partial r} \tag{5}$$

where k_{rg} is the relative permeability of gas, decimals; μ_g is the gas viscosity, mPas; B_g is the formation volume coefficient of gas, decimals.

$$v_w = -\delta\frac{kk_{rw}}{\mu_w B_w}\frac{\partial p}{\partial r} \tag{6}$$

where k_{rw} is the relative permeability of water, decimals; μ_w is the water viscosity, mPa·s; B_w is the formation volume coefficient of water, decimals.

The cross-flow rate between the matrix and fracture systems can be determined by:

$$q_{jmf} = \frac{\alpha_m k_m k_{rjm} S_j}{B_j}\left(p_m - p_f\right), j = w, g \tag{7}$$

By combing the above equations, basic control equations of flow for the fracture system can be obtained:

$$\frac{\lambda_g k_f}{r}\frac{\partial p_f}{\partial r} + \lambda_g\frac{\partial k_f}{\partial p_f}\left(\frac{\partial p_f}{\partial r}\right)^2 + \lambda_g k_f\frac{\partial^2 p_f}{\partial r^2} + \frac{\alpha_m k_m k_{rgm} S_g}{\delta k_{rgf} B_g}\left(p_m - p_f\right) = \frac{\phi_f}{0.0864\delta k_{rgf}}\frac{\partial}{\partial t}\left(\frac{S_g}{B_g}\right) \tag{8}$$

where k_{rgm} is the relative permeability of gas for the matrix system, decimals; k_{rgf} is that for the fracture system, decimals.

$$\frac{\lambda_w k_{\mathrm{f}}}{r}\frac{\partial p_{\mathrm{f}}}{\partial r}+\lambda_w\frac{\partial k_f}{\partial p_{\mathrm{f}}}\left(\frac{\partial p_{\mathrm{f}}}{\partial r}\right)^2+\lambda_w k_{\mathrm{f}}\frac{\partial^2 p_{\mathrm{f}}}{\partial r^2}+\frac{\alpha_m k_m k_{\mathrm{rwm}} S_w}{\delta k_{\mathrm{rwf}} B_w}\left(p_m-p_f\right)=\frac{\phi_{\mathrm{f}}}{0.0864\delta k_{\mathrm{rwf}}}\frac{\partial}{\partial t}\left(\frac{S_w}{B_w}\right) \tag{9}$$

where k_{rwm} is the relative permeability of water for the matrix system, decimals; k_{rwf} is that for the fracture system, decimals.

Similarly, the basic control equations of flow for the matrix system can be obtained:

$$\frac{\alpha_m k_m k_{\mathrm{rgm}} S_{\mathrm{g}}}{B_{\mathrm{g}}}\left(p_m-p_f\right)=\frac{\phi_{\mathrm{m}}}{0.0864k_{\mathrm{m}}}\frac{\partial}{\partial t}\left(\frac{S_{\mathrm{g}}}{B_{\mathrm{g}}}\right) \tag{10}$$

$$\frac{\alpha_m k_m k_{\mathrm{rgm}} S_{\mathrm{g}}}{B_{\mathrm{g}}}\left(p_m-p_f\right)=\frac{\phi_{\mathrm{m}}}{0.0864k_{\mathrm{m}}}\frac{\partial}{\partial t}\left(\frac{S_{\mathrm{w}}}{B_{\mathrm{w}}}\right) \tag{11}$$

The pseudo-pressure is defined as:

$$\psi_{\mathrm{g}}=\int_0^p\lambda_{\mathrm{g}}\mathrm{d}p,\ j=f,m \tag{12}$$

where $\lambda_{\mathrm{g}}=\frac{1}{\mu_{\mathrm{g}}B_{\mathrm{g}}}$.

Thus, the basic control equation for gas flow in the fracture system is

$$\frac{1}{r}\frac{\partial\psi_{\mathrm{f}}}{\partial r}+\gamma_{\mathrm{f}}\left(\frac{\partial\psi_{\mathrm{f}}}{\partial r}\right)^2+\frac{\partial^2\psi_{\mathrm{f}}}{\partial r^2}+\frac{\alpha_m k_m k_{\mathrm{rgm}} S_{\mathrm{g}}}{k_{\mathrm{f}}\lambda_g^2\delta k_{\mathrm{rgf}} B_{\mathrm{g}}}\left(\psi_m-\psi_f\right)=\frac{1}{k_{\mathrm{f}}\theta_{\mathrm{f}}}\frac{\partial\psi_{\mathrm{f}}}{\partial t} \tag{13}$$

where

$$\frac{1}{\theta_{\mathrm{f}}}=\frac{\phi_{\mathrm{f}}}{0.0864\delta k_{\mathrm{rgf}}}\frac{1}{\lambda_{\mathrm{g}}^2}\left(-\frac{S_{\mathrm{g}}}{B_g^2}\frac{\mathrm{d}B_{\mathrm{g}}}{\mathrm{d}p_{\mathrm{f}}}\right) \tag{14}$$

The basic control equation for gas flow in the matrix system is

$$\frac{\alpha_m k_m k_{\mathrm{rgm}} S_{\mathrm{g}}}{\lambda_g B_{\mathrm{g}}}\left(\psi_m-\psi_f\right)=\frac{1}{\theta_m}\frac{\partial\psi_m}{\partial t} \tag{15}$$

where

$$\frac{1}{\theta_{\mathrm{m}}}=\frac{\phi_{\mathrm{m}}}{0.0864k_{\mathrm{m}}k_{\mathrm{rgm}}}\frac{1}{\lambda_{\mathrm{g}}}\left(-\frac{S_{\mathrm{g}}}{B_{\mathrm{g}}^2}\frac{\mathrm{d}B_{\mathrm{g}}}{\mathrm{d}p_{\mathrm{m}}}\right) \tag{16}$$

The initial condition is:

$$\psi_{\mathrm{f}}(r,t)\big|_{t=0}=\psi_{\mathrm{m}}(r,t)\big|_{t=0}=\psi_{\mathrm{i}} \tag{17}$$

The inner boundary condition is:

$$\delta\frac{\partial\psi_{\mathrm{f}}}{\partial r}\bigg|_{r=r_w}=\frac{Tq_{\mathrm{sc}}}{78.489K_{\mathrm{fi}}h} \tag{18}$$

The outer boundary condition is:

$$\frac{\partial\psi_{\mathrm{f}}}{\partial r}\bigg|_{r=r_e}=0 \tag{19}$$

Solving the Model

The duration for productivity prediction is divided into numerous time intervals. The parameters dependent on saturations are calculated explicitly, which means that within a time step, the saturation remains the same. In contrast, parameters dependent on pressure are determined implicitly. The gas production is determined by solving our model, and meanwhile, the water production is predicted using the gas/water ratio. In other words, the model solving involves only the gas equation. After the gas production is determined, the average pressure and saturation across the production-affected (pressure drawdown) zone of the gas reservoir are computed via the flowing material balance method, according to which the model parameters are updated. Finally, the semi-analytical solutions of the model are obtained after numerous iterations. The solving workflow is summarized below:

1) Parameter normalization and equation linearization

The parameter normalization is shown below:

The dimensionless stress sensitivity coefficient is defined as:

$$\gamma_{\mathrm{fD}}=\frac{Tq_{\mathrm{sc}}}{78.489K_{\mathrm{fi}}h}\gamma_f \tag{20}$$

The dimensionless time:

$$t_{\mathrm{D}}=\frac{3.6k_{\mathrm{fi}}}{\mu_i r_{\mathrm{w}}^2\left(\phi_{\mathrm{m}}C_{\mathrm{m}}+\phi_{\mathrm{f}}C_{\mathrm{f}}\right)_i}t \tag{21}$$

The dimensionless radius:

$$r_{\mathrm{D}}=\frac{r}{r_{\mathrm{wa}}}=\frac{r}{r_{\mathrm{w}}\mathrm{e}^{-S}} \tag{22}$$

The dimensionless pseudo-pressure:

$$\psi_{\mathrm{fD}}=\frac{78.489K_{\mathrm{fi}}h}{Tq_{\mathrm{sc}}}\left(\psi_{\mathrm{i}}-\psi_{\mathrm{f}}\right) \tag{23}$$

$$\psi_{\mathrm{mD}}=\frac{78.489K_{\mathrm{fi}}h}{Tq_{\mathrm{sc}}}\left(\psi_{\mathrm{i}}-\psi_{\mathrm{m}}\right) \tag{24}$$

Accordingly, the fracture control equation can be rewritten as:

$$\frac{1}{r_D}\frac{\partial\psi_{fD}}{\partial r_D}-\gamma_{fD}\left(\frac{\partial\psi_{fD}}{\partial r_D}\right)^2+\frac{\partial^2\psi_{fD}}{\partial r_D^2}=e^{\gamma_{fD}\psi_{fD}}\left[\frac{3.6k_{fi}e^{-2S}}{\theta_f\mu_i\left(\phi_m C_m+\phi_f C_f\right)_i}\frac{\partial\psi_{fD}}{\partial t_D}-\frac{r_w^2e^{-2S}\alpha_m k_m k_{rgm}S_g}{\lambda_g^2\delta k_{rgf}B_g}\left(\psi_{fD}-\psi_{mD}\right)\right] \tag{25}$$

The matrix control equation can be rewritten as:

$$\frac{\alpha_m k_m k_{\mathrm{rgm}} S_{\mathrm{g}}}{\lambda_g B_{\mathrm{g}}}\left(\psi_{fD}-\psi_{mD}\right)=\frac{1}{\theta_m}\frac{3.6k_{\mathrm{fi}}}{\mu_i r_w^2\left(\phi_{\mathrm{m}}C_{\mathrm{m}}+\phi_{\mathrm{f}}C_{\mathrm{f}}\right)_i}\frac{\partial\psi_{mD}}{\partial t_D} \tag{26}$$

The rewritten expression of the initial condition:

$$\psi_{\mathrm{fD}}(r_{\mathrm{D}},t_{\mathrm{D}})\big|_{t_{\mathrm{D}}=0}=\psi_{\mathrm{mD}}(r_{\mathrm{D}},t_{\mathrm{D}})\big|_{t_{\mathrm{D}}=0}=0 \tag{27}$$

The inner boundary condition:

$$\left(e^{-\gamma_{\mathrm{mD}}\psi_{\mathrm{fD}}}\delta\frac{\partial\psi_{\mathrm{fD}}}{\partial r_{\mathrm{D}}}\right)\Big|_{rD=1}=-1 \tag{28}$$

The outer boundary condition:

$$\frac{\partial\psi_{\mathrm{fD}}}{\partial r_{\mathrm{D}}}\Big|_{r_{\mathrm{D}}=r_{\mathrm{eD}}}=0 \tag{29}$$

The perturbation theory is introduced:

$$\psi_{\mathrm{fD}}(r_{\mathrm{D}},t_{\mathrm{D}})=-\frac{1}{\gamma_{\mathrm{fD}}}\ln\left[1-\gamma_{\mathrm{fD}}\eta_{\mathrm{fD}}(r_{\mathrm{D}},t_{\mathrm{D}})\right] \tag{30}$$

$$\psi_{\mathrm{mD}}(r_{\mathrm{D}},t_{\mathrm{D}})=-\frac{1}{\gamma_{\mathrm{fD}}}\ln\left[1-\gamma_{\mathrm{fD}}\eta_{\mathrm{mD}}(r_{\mathrm{D}},t_{\mathrm{D}})\right] \tag{31}$$

The zeroth-order solution for perturbation is adopted and simplified as:

$$\frac{1}{r_D}\frac{\partial\eta_{0\mathrm{fD}}}{\partial r_D}+\frac{\partial^2\eta_{0\mathrm{fD}}}{\partial r_D^2}=\frac{3.6k_{\mathrm{fi}}\mathrm{e}^{-2S}}{\theta_{\mathrm{f}}\mu_i\left(\phi_{\mathrm{m}}C_{\mathrm{m}}+\phi_{\mathrm{f}}C_{\mathrm{f}}\right)_i}\frac{\partial\eta_{0\mathrm{fD}}}{\partial t_D}-\frac{r_w^2\mathrm{e}^{-2S}\alpha_m k_m k_{\mathrm{rgm}}S_{\mathrm{g}}}{\lambda_{\mathrm{g}}^2\delta k_{\mathrm{rgf}}B_{\mathrm{g}}}\left(\eta_{0fD}-\eta_{0mD}\right) \tag{32}$$

$$\frac{\alpha_m k_m k_{\mathrm{rgm}}S_{\mathrm{g}}}{\lambda_g B_{\mathrm{g}}}\left(\eta_{0fD}-\eta_{0mD}\right)=\frac{3.6k_{\mathrm{fi}}}{\theta_m\mu_i r_{\mathrm{w}}^2\left(\phi_{\mathrm{m}}C_{\mathrm{m}}+\phi_{\mathrm{f}}C_{\mathrm{f}}\right)_i}\frac{\partial\eta_{0mD}}{\partial t_D} \tag{33}$$

Correspondingly, the initial condition:

$$\eta_{\mathrm{fD}}(r_{\mathrm{D}},t_{\mathrm{D}})\big|_{t_{\mathrm{D}}=0}=\eta_{\mathrm{mD}}(r_{\mathrm{D}},t_{\mathrm{D}})\big|_{t_{\mathrm{D}}=0}=0 \tag{34}$$

The inner boundary condition:

$$\left(\delta\frac{\partial\eta_{0\mathrm{fD}}}{\partial r_{\mathrm{D}}}\right)\Big|_{r_{\mathrm{D}}=1}=-1 \tag{35}$$

The outer boundary condition:

$$\frac{\partial\eta_{0\mathrm{fD}}}{\partial r_{\mathrm{D}}}\Big|_{r_{\mathrm{D}}=r_{\mathrm{eD}}}=0 \tag{36}$$

2) Laplace transform and solutions of the mathematic model

For the convenience of derivation, we perform the Laplace transform to solve the model in the Laplace space. Subsequently, the Stehfest numerical inversion method is applied to obtain the solutions of the real space of the model.

The equation group is re-arranged using the Laplace transform of t_{D}:

$$\frac{1}{r_D}\frac{\partial\bar{\eta}_{0\mathrm{fD}}}{\partial r_D}+\frac{\partial^2\bar{\eta}_{0\mathrm{fD}}}{\partial r_D^2}=\frac{3.6k_{\mathrm{fi}}\mathrm{e}^{-2S}}{\theta_{\mathrm{f}}\mu_i\left(\phi_{\mathrm{m}}C_{\mathrm{m}}+\phi_{\mathrm{f}}C_{\mathrm{f}}\right)_i}\bar{\eta}_{0\mathrm{fD}}-\frac{r_{\mathrm{w}}^2\mathrm{e}^{-2S}\alpha_m k_m k_{\mathrm{rgm}}S_{\mathrm{g}}}{\lambda_{\mathrm{g}}^2\delta k_{\mathrm{rgf}}B_{\mathrm{g}}}\left(\bar{\eta}_{0fD}-\bar{\eta}_{0mD}\right) \tag{37}$$

$$\frac{\alpha_m k_m k_{\mathrm{rgm}}S_{\mathrm{g}}}{\lambda_g B_{\mathrm{g}}}\left(\bar{\eta}_{0fD}-\bar{\eta}_{0mD}\right)=\frac{3.6k_{\mathrm{fi}}}{\theta_m\mu_i r_{\mathrm{w}}^2\left(\phi_{\mathrm{m}}C_{\mathrm{m}}+\phi_{\mathrm{f}}C_{\mathrm{f}}\right)_i}\bar{\eta}_{0\mathrm{mD}} \tag{38}$$

The initial condition:

$$\bar{\eta}_{\mathrm{fD}}(r_{\mathrm{D}},t_{\mathrm{D}})\big|_{t_{\mathrm{D}}=0}=\bar{\eta}_{\mathrm{mD}}(r_{\mathrm{D}},t_{\mathrm{D}})|_{t_{\mathrm{D}}=0}=0 \tag{39}$$

The inner boundary condition:

$$\left(\delta\frac{\partial\bar{\eta}_{0\mathrm{fD}}}{\partial r_{\mathrm{D}}}\right)\Big|_{r_{\mathrm{D}}=1}=-1 \tag{40}$$

The outer boundary condition:

$$\frac{\partial\bar{\eta}_{0\mathrm{fD}}}{\partial r_{\mathrm{D}}}\Big|_{r_{\mathrm{D}}=r_{\mathrm{eD}}}=0 \tag{41}$$

Combining **Eqs 37**, **38** yields:

$$\frac{1}{r_D}\frac{\partial\bar{\eta}_{0\mathrm{fD}}}{\partial r_D}+\frac{\partial^2\bar{\eta}_{0\mathrm{fD}}}{\partial r_D^2}-f(\xi)\bar{\eta}_{0\mathrm{fD}}=0 \tag{42}$$

where

$$f(\xi)=\frac{\mathrm{e}^{-2S}3.6k_{\mathrm{fi}}}{\theta_{\mathrm{f}}\mu_i\left(\phi_{\mathrm{m}}C_{\mathrm{m}}+\phi_{\mathrm{f}}C_{\mathrm{f}}\right)_i}-\frac{\mathrm{e}^{-2S}\lambda_g B_{\mathrm{g}}3.6k_{\mathrm{fi}}}{\theta_m\mu_i r_{\mathrm{w}}^2\alpha_m k_m k_{\mathrm{rgm}}S_{\mathrm{g}}\left(\phi_{\mathrm{m}}C_{\mathrm{m}}+\phi_{\mathrm{f}}C_{\mathrm{f}}\right)_i+\lambda_g B_{\mathrm{g}}3.6k_{\mathrm{fi}}} \tag{43}$$

Substituting the inner and outer boundary conditions into **Eq. 42**, the solution is obtained:

$$\bar{\eta}_{0\mathrm{fD}}=\frac{1}{\delta D}I_0\left(r_D\sqrt{f(\xi)}\right)K_1\left(r_{eD}\sqrt{f(\xi)}\right)+\frac{1}{\delta D}I_1\left(r_{eD}\sqrt{f(\xi)}\right)K_0\left(r_D\sqrt{f(\xi)}\right) \tag{44}$$

where

$$D=\sqrt{f(\xi)}\left[I_1\left(r_{eD}\sqrt{f(\xi)}\right)K_1\left(\sqrt{f(\xi)}\right)-I_1\left(\sqrt{f(\xi)}\right)K_1\left(r_{eD}\sqrt{f(\xi)}\right)\right] \tag{45}$$

The production is expressed as below:

$$\bar{q}_{\mathrm{gf}}=-2\pi k_{\mathrm{f}}k_{\mathrm{rgf}}hr_{\mathrm{w}}\frac{\partial\Delta\bar{\eta}_{\mathrm{f}}}{\partial r}\Big|_{r\to r_{\mathrm{w}}} \tag{46}$$

3) Calculating the average formation pressure using the material balance method

We manage to linearize the two-phase equation by introducing the pseudo- time and pressure. However, the obtained general solution is a function of the pseudo-time, while the pseudo-time is a function of pressure. Hence, the iterative calculation is required to compute the productivity corresponding to the real time and its composition (gas and water production). In iteration, the average gas reservoir pressure needs to be computed at each time step.

The overall material balance equation of the gas system is presented below:

$$IGIP-RGIP=G_{\mathrm{p}} \tag{47}$$

where $IGIP$ is the initial gas in place, m^3; $RGIP$ is the remaining gas in place, m^3; G_{p} is the cumulative gas production, m^3.

Moreover, the IGIP can be calculated using the following equation:

$$IGIP = \pi r_{\text{ginv}^2} h\phi \left(\frac{S_{\text{gi}}}{B_{\text{gi}}}\right) \tag{48}$$

where r_{ginv} is the drainage radius of gas, m; S_{gi} is the initial gas saturation, decimals; B_{gi} is the initial formation volume coefficient of gas, decimals.

The RGIP is determined as below:

$$RGIP = \pi r_{\text{ginv}^2} h\phi \left(\frac{\bar{S}_{\text{g}}}{\bar{B}_{\text{g}}}\right) \tag{49}$$

where $\bar{S}_{\text{g}}$ is the average gas saturation, decimals; $\bar{B}_{\text{g}}$ 为is the average formation volume coefficient of gas, decimals.

The cumulative gas production:

$$G_{\text{p}} = \int_0^t q_{\text{g}} \text{d}t \tag{50}$$

where q_g is the daily gas production, m^3/d.

By substituting **Eqs 48–50** into **Eq. 47**, we have:

$$\frac{\bar{S}_g}{\bar{B}_g} = \frac{S_{\text{gi}}}{B_{\text{gi}}} - \frac{G_{\text{p}}}{\pi r_{\text{ginv}^2} h\phi} \tag{51}$$

The overall material balance equation of water is:

$$IWIP - RWIP = N_{\text{w}} \tag{52}$$

where $IWIP$ is the initial water in place, m^3; $RWIP$ is the remaining water in place, m^3; N_{w} is the cumulative water production, m^3.

The IWIP can be calculated using the following equation:

$$IWIP = \pi r_{\text{winv}^2} h\phi \left(\frac{S_{\text{wi}}}{B_{\text{wi}}}\right) \tag{53}$$

where r_{winv} is the drainage radius of water, m; S_{wi} is the initial water saturation, decimals; B_{wi} is the initial formation volume coefficient of water, decimals.

The RWIP can be calculated as below:

$$RWIP = \pi r_{\text{winv}^2} h\phi \left(\frac{\bar{S}_{\text{w}}}{\bar{B}_{\text{w}}}\right) \tag{54}$$

where $\bar{S}_w$ is the average water saturation, decimals; $\bar{B}_w$ is the average formation volume coefficient of water, decimals.

The cumulative water production:

$$N_{\text{w}} = \int_0^t q_{\text{w}} \text{d}t \tag{55}$$

where q_{w} is the daily water production, m^3/d.

Substituting **Eqs 53–55** into **Eq. 50** yields:

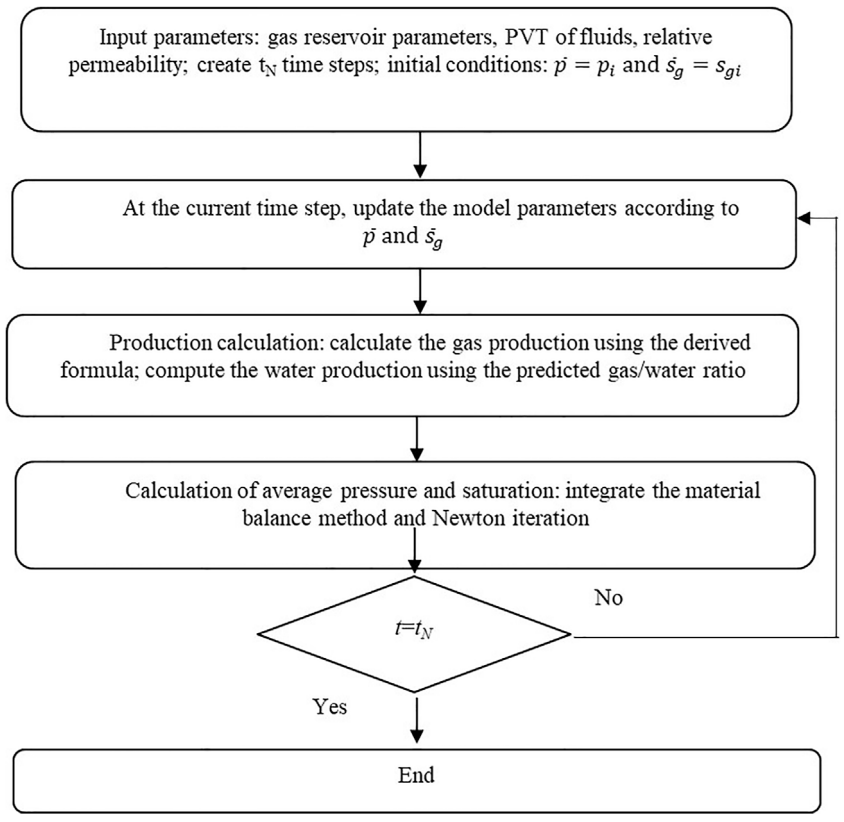

FIGURE 4 | Productivity prediction workflow based on the semi-analytic model for two-phase flow of gas and water.

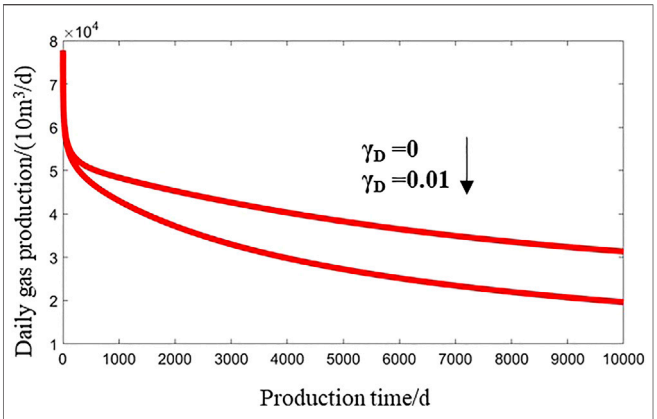

FIGURE 5 | The effect of stress sensitivity on the productivity of gas wells with the two-phase flow of gas and water.

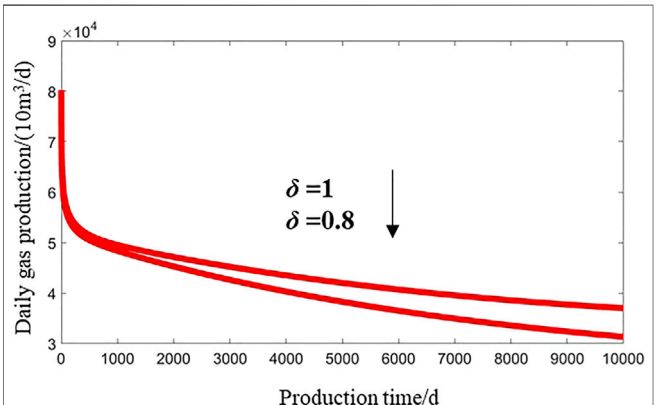

FIGURE 6 | The effect of non-Darcy flow on gas wells with two-phase flow of gas and water.

$$\frac{\bar{S}_w}{\bar{B}_w} = \frac{S_{wi}}{B_{wi}} - \frac{N_w}{\pi r_{winv^2} h\phi} \tag{56}$$

The correlation between the water and gas saturation is shown below:

$$\bar{S}_g + \bar{S}_w = 1 \tag{57}$$

By combining **Eqs 51**, **56**, **57**, we have:

$$f(\bar{p}) = \frac{1}{\bar{B}_g} + \left(\frac{\bar{B}_w}{\bar{B}_g}\right) m_1 - m_2 \tag{58}$$

where

$$m_1 = \left(\frac{S_{wi}}{B_{wi}}\right) - \frac{N_w}{\pi r_{inv^2} h\phi} \tag{59}$$

$$m_2 = \left(\frac{S_{gi}}{B_{gi}}\right) - \frac{G_p}{\pi r_{inv^2} h\phi} \tag{60}$$

The derivative of **Eq. 58** is:

$$f'(\bar{p}) = -\frac{1}{\bar{B}_g^2}\frac{dB_g}{dp} + m_1\left(-\frac{1}{\bar{B}_w}\frac{dB_w}{dp} + \frac{B_w}{\bar{B}_g^2}\frac{dB_g}{dp}\right) \tag{61}$$

Then the Newton iteration equation can be written as **Eq. 62**:

$$\bar{p}_{k+1} = \bar{p}_k - \omega\frac{f\left(\overline{p_k}\right)}{f'\left(\overline{p_k}\right)} \tag{62}$$

The two-phase flow model of gas and water is solved in a semi-analytical approach. The productivity prediction workflow for the two-phase flow of gas and water is illustrated in **Figure 4**. The duration for productivity prediction is divided into numerous time steps. The saturation-dependent parameters are calculated explicitly, while the pressure-dependent ones are computed implicitly. Specifically, within one time step, the saturation is defined as a constant, and the pressure-dependent parameter is calculated using the pseudo-pressure. After obtaining the gas production, the average reservoir pressure and saturation across the pressure drawdown-affected zone are determined using the flowing material balance method. Subsequently, the model parameters are updated according to the new average reservoir pressure and saturation and the production is calculated again. The semi-analytical solutions of the model are finally obtained after multiple iterations.

ANALYSIS OF FACTORS AFFECTING PRODUCTIVITY OF CARBONATE GAS RESERVOIRS

The value of the permeability modulus γ represents how much the production performance of gas wells is affected by stress sensitivity (**Figure 5**). A higher permeability modulus indicates higher stress sensitivity of the reservoir, which is associated with lowering down of the type curve and faster production decline. The dual-medium carbonate reservoir is found with extensive development of fractures. During the recovery process, the increase of the effective overburden pressure results in deformation of the rock framework and decline of

TABLE 1 | Basic parameters of Well M2.

Porosity Φ (%)	Effective thickness h (m)	Gas viscosity μ_g (mPa·s)	Formation volume coefficient of gas B_g
5	**49.6**	**0.025**	**0.00269**
Comprehensive Compressibility C_t (1/MPa)	Middle Depth of Gas Reservoir (m)	Wellbore Radius (m)	q_i (10^4 m^3/d)
6.1×10^{-3}	4,620	0.061	17

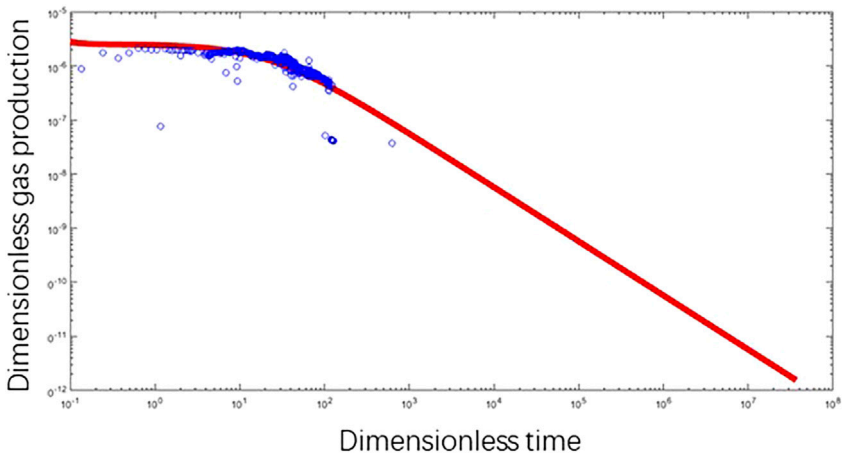

FIGURE 7 | The fitting interpretation curve of production decline of Well M2.

TABLE 2 | Fitting interpretation results for production decline of Well M2.

	Interpretation reults						
Interpretation method	***K*** **(10^{-3} μm^2)**	***S***	ω	λ	r_{eD}	γ_D	δ
Our model	0.171	2.8	0.0193	3.4×10^{-3}	8.91×10^3	0.015	0.606

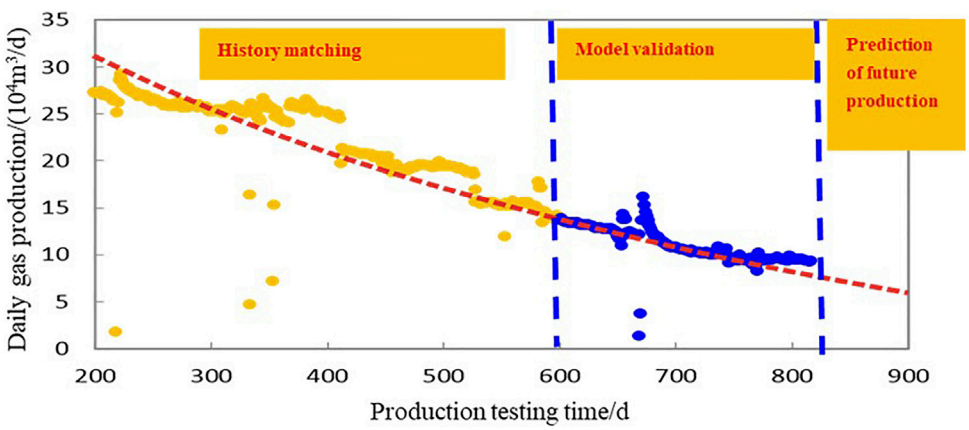

FIGURE 8 | Production prediction of Well M2.

TABLE 3 | Production prediction of Well M2.

Time (d)	Flowing bottomhole pressure (MPa)	Predicted daily production (10^4 m^3/d)	Predicted cumulative produciton (10^8m^3)
200	53.57	—	—
400	51.59	—	—
600	51.31	13.58	1.42
800	48.81	9.47	1.65

permeability, accelerating production decline. Moreover, with the elapsed time of recovery, the effect of stress sensitivity grows. Hence, the recovery of carbonate gas reservoirs shall adopt a proper recovery rate and drawdown pressure to minimize the impact of stress sensitivity and improve recovery performance.

The high-speed non-Darcy coefficient δ represents the effect of the high-speed non-Darcy flow on the type curve (**Figure 6**). With a smaller value of the high-speed non-Darcy coefficient, the non-Darcy effect grows, the type curve is lowered, and the initial production is reduced. Therefore, the productivity evaluation of the dual-medium carbonate gas reservoir cannot neglect the non-Darcy effect.

CASE STUDY

Here the L carbonate gas reservoir of the A gas field is taken as an example and the developed two-phase flow model of gas and water based on the dual-medium is applied to productivity prediction of the production well, Well M2. This well presents an initial gas production of $17 \times 104\ m^3/d$ during the production testing, and after 1 month of production, the production is raised to $28 \times 104\ m^3/d$. After 3 years of production, the daily gas production of this well is $9.6 \times 104\ m^3/d$, the daily water is $9.8\ m^3/d$, and the water/gas ratio is $0.98\ m^3/10^4m^3$. The basic parameters of this well are summarized in **Table 1**.

The developed productivity evaluation model is used for fitting the interpretation of the reservoir drilled by this well, based on its production performance. The fitting interpretation results are concluded in **Figure 7**; **Table 2**.

The future production of Well M2 at a constant flowing bottomhole pressure is forecasted, based on the model parameters interpreted from its actual production performance. The results are summarized in **Figure 8**; **Table 3**.

The error analysis of the predicted production shows that on Day 800, the predicted daily production of Well M2 is $9.47 \times 104\ m^3/d$, while the actual production rate is $9.61 \times 104\ m^3/d$. The error of the calculation is 1.5%, which is within the allowed error range and thus means that the productivity prediction results meet the engineering criterion.

CONCLUSION

1) The dual-medium carbonate gas reservoir is greatly different from the conventional gas reservoir, in terms of the storage space and fluid flow characteristics. Therefore, the flow model shall consider both the stress sensitivity and high-speed non-Darcy flow effect.
2) The stress sensitivity and non-Darcy effect coefficients are introduced into the flow model of the dual-medium gas reservoir, which results in the nonlinearity of the flow equations. Then, the perturbation theory is applied to eliminate the nonlinearity and the flow equations are transformed into the Laplace space for solutions. The solution of fluid production is obtained via the Stehfest numerical inversion, and the semi-analytical solutions of the model are calculated via the flowing material balance method and Newton iteration.
3) The analysis of the production decline type curve of the dual-medium carbonate gas reservoir shows that the dual-medium gas reservoir with higher stress sensitivity is associated with accelerated production decline; that with a more intensive non-Darcy flow effect is found with lower initial production.
4) The developed model is used for the case study of an actual production well. The analysis results show that the error of the predicted production of the analyzed well is within the engineering-permissible range, which validates the high applicability and practicability of our model.

DATA AVAILABILITY STATEMENT

The original contributions presented in the study are included in the article/Supplementary Material, further inquiries can be directed to the corresponding authors.

AUTHOR CONTRIBUTIONS

LK, WG, XZ, and YL contributed to design of the study and method establishment, wrote the first draft of the manuscript. JG, ZS, ML, and YS wrote sections of the manuscript. All authors contributed to manuscript revision, read, and approved the submitted version.

FUNDING

The work was funded by R&D Department of Petrochina (No. 2021DJ2 005). The APC was funded by R&D Department of Petrochina (No. 2021DJ2 005). The funders had no role in the design, execution, interpretation, or writing of the study.

REFERENCES

Brown, M. L., Ozkan, E., Raghavan, R. S., and Kazemi, H. (2009). Practical Solutions for Pressure-Transient Responses of Fractured Horizontal wells in Unconventional Shale Reservoirs. *SPE Reservoir Eval. Eng.* 14 (6), 663–676. doi:10.1016/s1876-3804(17)30031-9

Chen, C. (2016). *Research on Productivity of Fractured Horizontal wells with Steady-State Two-phase Flow of Gas and Water in the YD Gas Reservoir*. Chengdu: Southwest Petroleum University.

Chen, Y.-F., Zhou, J.-Q., Hu, S.-H., Hu, R., and Zhou, C.-B. (2015). Evaluation of Forchheimer Equation Coefficients for Non-darcy Flow in Deformable Rough-Walled Fractures. *J. Hydrol.* 529, 993–1006. doi:10.1016/j.jhydrol.2015.09.021

Cheng, S., and Chen, M. (1998). Numerical Simulation of Two-Dimensional Two-phase Non-Darcy Slow Flow. *Pet. Exploration Develop.* 25 (1), 41–43.

Deng, Q., Tang, H., Lv, Z., Wang, Q., Lv, D., and Liu, Q. (2011). The Study of Productivity Forecast in Water-Producing Gas Well. *Pet. Geology. Eng.* 25 (3), 68–69. doi:10.3969/j.issn.1673-8217.2011.03.020

Esmaeili, S., Sarma, H., Harding, T., and Maini, B. (2020). Effect of Temperature on Bitumen/water Relative Permeability in Oil Sands. *Energy Fuels* 34 (10), 12314–12329. doi:10.1021/acs.energyfuels.0c02180

Fan, H., Li, X., Dou, T., Chen, J., and Yuan, F. (2011). Study on the Flowing Performance of Gas Wells in Dual-Porosity Deformable Fractal Reservoirs.

J. Southwest Pet. Univ. (Science Technol. Edition) 33 (2), 115–120. doi:10.3863/j.issn.1674-5086.2011.02.019

Fang, J., Guo, P., Xiao, X., Du, J., Dong, C., Xiong, Y., et al. (2015). Gas-Water Relative Permeability Measurement of High Temperature and High Pressure Tight Gas Reservoirs. *Pet. Exploration Develop.* 42 (1), 84–87. doi:10.1016/s1876-3804(15)60010-6

Huang, B., Ran, X., and Li, X. (2004). *Analysis Method of Gas Reservoir Engineering*. Beijing: Petroleum industry Press, 87–90.

Javadpour, F., Singh, H., Rabbani, A., Babaei, M., and Enayati, S. (2021). Gas Flow Models of Shale: A Review. *Energy & Fuels* 35 (4), 2999–3010. doi:10.1021/acs.energyfuels.0c04381

Jia, A. L., Yan, H. J., Guo, J. L., He, D. B., Cheng, L. H., and Jia, C. Y. (2013). Development Characteristics for Different Types of Carbonate Gas Reservoirs. *Acta Petrolei Sinica* 34 (5), 914–923. doi:10.7623/syxb201305012

Li, D., Kang, Y., and You, L. (2011). "Experimental Study on Permeability Stress Sensitivity of Carbonate Rocks," in The Chinese Conference on Theoretical and Applied Mechanics 2011 in Memorial of Tsien Hsue-Shen's 100th Anniversary, Harbin, China, August 22–24, 2011.

Li, X., Guo, Z., Wan, Y., Liu, X., Zhang, M., Xie, W., et al. (2017). Geological Characteristics and Development Strategies for Cambrian Longwangmiao Formation Gas Reservoir in Anyue Gas Field, Sichuan Basin, SW China. *Pet. Exploration Develop.* 44 (3), 398–406. doi:10.1016/s1876-3804(17)30049-6

Liao, Z. (2016). *Research on the Water Production Pattern and Production Performance of Water Flooding in Fractured Gas Reservoirs*. Chengdu: Southwest Petroleum University.

Lu, Z. (2010). *Fluid Flow Law in Fractured Vuggy media*. Qingdao: China University of Petroleum.

Luo, A., Li, Y., Wu, L., Peng, Y., and Tang, W. (2021). Fractured Horizontal Well Productivity Model for Shale Gas Considering Stress Sensitivity, Hydraulic Fracture Azimuth, and Interference between Fractures. *Nat. Gas Industry B* 8 (3), 278–286. doi:10.1016/j.ngib.2021.04.008

Peng, X., Lu, Y., Liu, X., Duan, C., Li, Z., Liu, S., et al. (2015). Rock Stress Sensitivity and its Influence on Productivity of Overpressured Gas Reservoir: A Case Study in Yinggehai Basin, China. *Int. J. Oil Gas Coal Eng.* 3 (3), 33. doi:10.11648/j.ogce.20150303.11

Petrosa, O. A., Jr. (1986). "Pressure Transient Response in Stress-Sensitive Formation," in SPE California Regional Meeting, SPE15115, Oakland, CA, April 2–4, 1986. doi:10.2118/15115-ms

Xu, J. L., Cheng, X. B., Pan, X. H., and Fei, H. Y. (2007). Fracture and Cavity Prediction Method in Carbonate Reservoirs and its Application. *Nat. Gas Industry* 11 (11), 56–63. doi:10.3321/j.issn:1000-0976.2007.11.011

Zhang, F., Wu, Y., and Wang, X. (2016). Effect of High-Speed Non-Darcy Flow on Productivity for Gas-Well with Producing Water. *Petrochemical Industry Appl.* 35 (1), 34–36. doi:10.3969/j.issn.1673-5285.2016.01.010

Zhang, H., Wang, J., Jin, S., Chen, H., and Wang, L. (2017a). Rational Production of Water Producing Gas wells in the South Area of Sulige Gasfield, Ordos Basin. *Nat. Gas Exploration Develop.* 40 (3), 72–77. doi:10.12055/gaskk.issn.1673-3177.2017.03.011

Zhang, H., Wang, L., Wang, X., Zhou, W., Zeng, X., Liu, C., et al. (2017b). Productivity Analysis Method for Gas-Water wells in Abnormal Overpressure Gas Reservoirs. *Pet. Exploration Develop.* 44 (2), 258–262. doi:10.1016/s1876-3804(17)30031-9

Zhang, R., Ning, Z., Zhang, H., and Xie, Q. (2016). New Insights and Discussions on Stress Sensitivity of Fractured Tight Reservoir. *Nat. Gas Geosci.* 27 (5), 918–923. doi:10.11764/j.issn.1672-1926.2016.05.0918

Zhang, W., Meng, Z., and Li, H. (2017). Study on Development Performance Pattern Prediction of Gas Reservoirs with Abnormal Overpressure. *China Pet. Chem. Stand. Qual.* 37 (17), 94–95. doi:10.3969/j.issn.1673-4076.2017.17.045

Zhao, L., Chen, Y., Ning, Z., Wu, X., Liu, L., and Chen, X. (2013). Stress Sensitive Experiments for Abnormal Overpressure Carbonate Reservoirs: A Case from the Kenkiyak Fractured-Porous Oil Field in the Littoral Caspian Basin. *Pet. Exploration Develop.* 40 (2), 208–215. doi:10.1016/s1876-3804(13)60024-5

Conflict of Interest: Author ML was employed by Beijing Gas Group Co., Ltd. Author YS was employed by PetroChina Southwest Oil and Gasfield Company.

The remaining authors declare that the research was conducted in the absence of any commercial or financial relationships that could be construed as a potential conflict of interest.

frontiers in Earth Science

ORIGINAL RESEARCH
published: 16 February 2022
doi: 10.3389/feart.2021.782279

Investigation of Shut-In Effect on Production Performance in Shale Oil Reservoirs With Key Mechanisms

Pin Jia[1,2], *Xianzhe Ke*[1,2]*, *Langyu Niu*[1,2], *Yang Li*[1,2] *and Linsong Cheng*[1,2]

[1]State Key Laboratory of Petroleum Resources and Prospecting, China University of Petroleum (Beijing), Beijing, China, [2]College of Petroleum Engineering, China University of Petroleum (Beijing), Beijing, China

With the continuous development of the petroleum resources, unconventional oil reservoirs such as shale oil and tight oil have gradually become a main development direction of oil reservoirs in various countries. The reserves of shale oil in China are huge, reaching 1.42×10^{11} t; therefore, China has a great development potential and prospects for exploitation. However, in the process of developing shale oil reservoirs, we encountered many problems, such as un-replenishment of formation pressure and low flowback rate. At this stage, the development technology of shale oil reservoirs cannot effectively solve these problems. The proposition of shut-in technology can effectively improve these problems in theory, but the current shut-in technology of shale reservoirs after fracturing in China is still in its infancy. There is no in-depth understanding of the mechanism of shut-in wells. In addition, the factors affecting the change of oil-water distribution during shut-in after fracturing are complex, mainly including reservoir permeability, capillary force, fracture stress sensitivity, and reservoir damage. This paper investigates the mechanism of shut-in in shale reservoirs after fracturing and summarizes the mechanism of the shut-in process. Then, a single well shut-in numerical simulation model is established for the three complex characteristics of spontaneous imbibition, fracture stress sensitivity, and reservoir damage, and the oil-water distribution and change laws of shut-in shale reservoirs after fracturing are analyzed. Finally, the numerical model is used to study the influence of reservoir permeability, capillary force, fracture stress sensitivity, and reservoir damage on oil-water replacement, pressure increase, and daily fluid production during shut-in. The research results show that the influence of reservoir permeability and capillary force is more obvious, and the influence of fracture stress sensitivity and reservoir damage is relatively small.

Keywords: numerical simulation, shut-in, spontaneous imbibition, oil-water replacement, shale oil reservoirs

OPEN ACCESS

Edited by:
Feng Yang,
China University of Geosciences, China

Reviewed by:
Youwei He,
Southwest Petroleum University, China
Suran Wang,
CNOOC Research Institute Co. Ltd., China

***Correspondence:**
Xianzhe Ke
2020210329@student.cup.edu.cn

Specialty section:
This article was submitted to Economic Geology, a section of the journal Frontiers in Earth Science

Received: *24 September 2021*
Accepted: *22 November 2021*
Published: *16 February 2022*

Citation:
Jia P, Ke X, Niu L, Li Y and Cheng L (2022) Investigation of Shut-In Effect on Production Performance in Shale Oil Reservoirs With Key Mechanisms. Front. Earth Sci. 9:782279. doi: 10.3389/feart.2021.782279

INTRODUCTION

The effective development of shale oil usually relies on horizontal wells and multi-stage hydraulic fracturing technology, which usually requires the injection of a large amount of fracturing fluid into the reservoir to form a complex fracture network, so that the oil and gas production of shale reservoirs can achieve economic benefits. After the fracturing measures are over, the shut-in measures will be carried out first, and the duration varies from a few weeks to a few months (Wust et al., 2018). The shut-in process is usually accompanied by the imbibition effect of fracturing

fluid from the fracture to the matrix, which plays three roles: The first is that the fracturing fluid enters the matrix through the fracture under the action of imbibition to raise the formation pressure of the near-fracture matrix, which plays a role in increasing the formation energy. The second is that the fracturing fluid enters the matrix through the fractures to replace the oil phase into the fractures under the action of imbibition, making it easier to produce oil during the development process. The third is that the fracturing fluid penetrates deeper into the matrix, so that the water saturation curve of the invasion zone is lower and flatter, and the relative permeability of the oil phase during flowback is higher. The effects of these three aspects are reflected in the higher initial production of flowback after shut-in (Bertoncello et al., 2014; Yaich et al., 2015; Wang and Leung, 2016). Therefore, shut-in is conducive to early flowback and production, but the interaction between fracturing fluid and reservoir fluid in the shut-in phase will bring many problems. Among them, the most difficult one is that it will increase the fracturing fluid absorption, which will lead to the effects of water sensitivity and water blocking in the reservoir. At the same time, the fracture may close after the fracture pressure is reduced, which will eventually lead to a decrease in shale oil production. Therefore, the influence of shut-in on production has gradually gained attention and related research has been carried out.

Odumabo (Odumabo et al., 2014) found that the water saturation distribution of the near-fracture surface during shut-in is closely related to the shut-in time and the fracturing fluid imbibition of the reservoir. And there are differences in the mode of action between the two. At the same time, Odumabo also found that the important factors affecting gas seepage after fracturing are the water saturation distribution and permeability changes of fracturing fluid intruding near the fracture surface. Wang (Wang et al., 2012) discovered the change of fluid seepage phenomenon under the action of osmotic pressure and capillary force, and studied the relationship between microfractures caused by hydraulic fracturing and imbibition in shale oil reservoirs. It is found that clay minerals are equivalent to a semi-permeable membrane and have a stronger ability to absorb water. Le (Le et al., 2009) used numerical simulation to analyze the changes in gas phase permeability of the fracturing fluid invaded area during the shut-in process. At the same time, he also noticed the deep fracturing fluid imbibition and gas phase evaporation phenomena in the matrix. Furthermore, he got a more reasonable conclusion: it takes time to recover the permeability, which shows that the imbibition of capillary force can promote the recovery of permeability during the flowback process of shut-in. He (He et al., 2020) presents a PTA model of an MFHW which considers the nonuniform properties of fractures, including unequal fracture conductivity, nonuniform production distribution, asymmetric fractures, and arbitrary locations. He found when the distance between fractures with high production (FHP) increases or number of FHP decreases, the early-radial flow can be obviously observed, and the duration of this regime depends on the interference among fractures. Jia (Jia et al., 2021a) proposed a fully coupled flow and geomechanics model to capture the dynamic behavior of key fracture parameters for flowback and early-time production. In this coupled model, the controlled volume method is used to numerically simulate the fracture flow, which can consider the geometry and conductivity distribution of the propped and unpropped fractures. For the fracture geomechanics, the joint-closure relationship is introduced to describe the fracture aperture of unpropped fracture. Fakcharoenphol (Fakcharoenphol et al., 2014) believed that the composition of the fracturing fluid and the physical characteristics of the reservoir itself have an effect on the fracturing fluid imbibition, and he discovered that micro-fractures may be formed after shale imbibition. Yan (Yan et al., 2015) studied the relationship between the change in gas volume attracted by spontaneous imbibition and shut-in time, and found that the important factor affecting the relationship between shut-in time and permeability recovery is the lithology of the reservoir. Jia (Jia et al., 2021b) built a transient model for multistage fractured horizontal wells, based on point-source method and superposition principle, which considers the couple of fracture flow and reservoir seepage, and solved with the Laplace transformation. The transient pressure behavior in multistage fractured horizontal wells is discussed, and effects of influence factors are analyzed. The result of this article can be used to identify the response characteristic of fracture conductivity to pressure and pressure differential and provide theoretical basis for effective development of tight oil reservoirs. He (He et al., 2022) provided a novel approach to enhance oil recovery from unconventional oil reservoirs through synchronous inter-fracture injection and production (SiFIP) and asynchronous inter-fracture injection and production (AiFIP). He demonstrated the feasibility of SiFIP and AiFIP to improve oil recovery. The proposed methods improved flooding performance by transforming fluid injection among wells to among hydraulic fractures from the same Multi-fractured horizontal well (MFHW). Liu (Liu, 2017) used nuclear magnetic resonance to discover the fluid flow law during the spontaneous imbibition process, and summarized the microscopic imbibition law during shut-in, that is, under the action of capillary force, the liquid imbibition rate in small pores is the fastest. Therefore, the water saturation in the small pores is the highest, while the large pores are the opposite. He divided the fracturing fluid imbibition into two main stages: one is the imbibition saturation of the fracture surface, and the other is the diffusion of the fracturing fluid in the deep part of the matrix. It not only analyzes the mechanism of shut-in measures to increase productivity at the microscopic level, but also summarizes the applicable conditions for shut-in.

Still, there is a lack of detailed and comprehensive numerical simulation studies on shut-in in shale reservoirs after fracturing, and the research on the change law of the oil-water distribution state of shut-in after fracturing is not comprehensive enough, and there is a lack of research on its influencing factors. As a result, the rules and applicable conditions of shut-in on productivity are unclear. In this paper, by constructing a complex fracture network of volume fracturing, a numerical simulation model of shut-in considering imbibition, near-fracture matrix damage, and stress sensitivity is established to clarify the change law of oil-

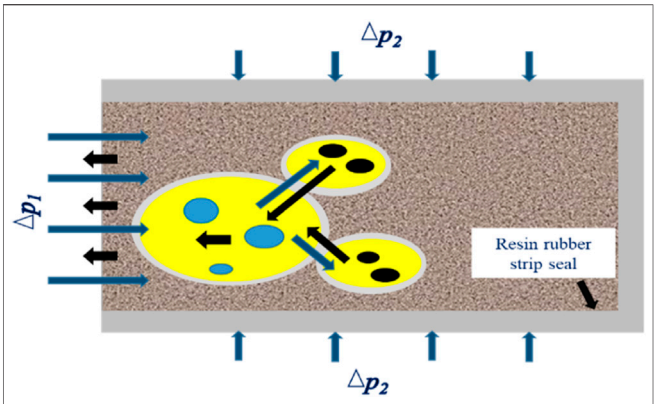

FIGURE 1 | Imbibition in a fractured stuffy well (Li et al., 2017).

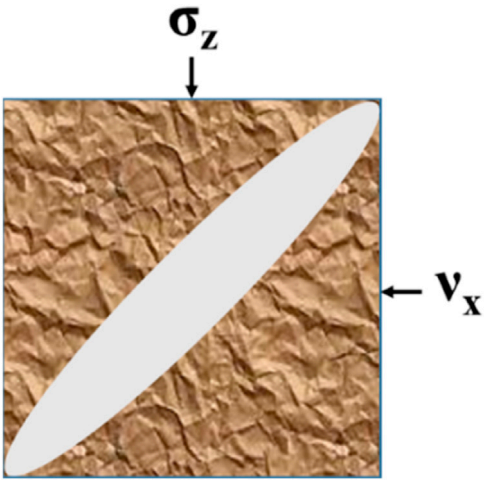

FIGURE 2 | Schematic diagram of the stress state of the crack (Wang, 2018).

water distribution state at different shut-in times, and explore the influence rules of different capillary forces, different fracture stress sensitivity coefficients, and different reservoir damage levels on productivity, and determine the hidden laws and main control factors of the shut-in effect.

KEY MECHANISMS IN SHUT-IN PERIOD

In the process of shut-in in shale reservoirs after fracturing, under the action of higher bottom hole pressure, fracturing fluid with a large amount of energy enters the near-fracture shale matrix, and the formation energy is improved through imbibition and oil-water replacement is carried out. At the same time, as the internal pressure of the crack decreases, the crack may close. After fracturing fluid intrudes into the formation, it also causes near-fractured reservoir damage, such as solid damage, some hydration caused by liquid incompatibility, etc., which are all important mechanisms for shut-in in shale reservoirs after fracturing. Each mechanism is explained in turn.

The Imbibition Mechanism of Fracturing Fluid-Shale Matrix

Under the action of capillary force, the fracturing fluid and the shale matrix are imbibed, that is, the wetting phase (fracturing fluid) displaces the non-wetting phase (oil phase) in the reservoir. In shale reservoirs, the capillary force in the matrix is higher due to the nano-scale pore structure, so the imbibition effect becomes more obvious. The imbibition phenomenon in the shut-in after fracturing is shown in **Figure 1**.

A key quantity in the process of imbibition is the amount of imbibition and the rate of imbibition. The amount of imbibition is not only related to time, but also closely related to space and imbibition capacity. The amount of imbibition directly affects the increase in formation pressure, and the amount of imbibition is usually proportional to the increase in pore pressure. The more the amount of imbibition, the better the effect of supplementing the formation energy. In the process of imbibition, the main body of fracturing fluid is slippery water that creates fractures, which can not only supplement energy, but also effectively replace the oil phase of the matrix.

In the process of imbibition, the imbibition rate of liquid in small pores is much higher than that in large pores. Fracturing fluid first enters the small pores to fill them, but the large pores are not filled. The fracturing fluid continuously displaces the crude oil in the small pores into the large pores. When the oil phase pressure exceeds the pore pressure, the oil phase will migrate to larger pores. During the entire imbibition process, the pore oil phase will be displaced into the fractures by a large amount of fracturing fluid, which realizes the oil-water replacement during the shut-in process (Liu, 2017).

Crack Closure Mechanism

During the shut-in process of a shale reservoir, because the fractures are subjected to external ground stress and internal fracturing fluid pressure in the reservoir, the mechanical balance of the fractures is maintained by the vertical stress, horizontal stress, and pressure in the fracture (Wang, 2018). As shown in **Figure 2**. During the shut-in process of a shale reservoir, due to imbibition, the pressure in the fracture continuously spreads to the deep part of the shale matrix, and the pressure in the fracture is continuously reduced.

The phenomenon of fracture closure is due to the decrease of internal pore pressure caused by the outflow of fluid in the fracture, and the previous balance system is broken. During the shut-in process, the pressure in the fractures is continuously reduced, and the fractures near the wellbore will close earlier. After the fractures are closed, it is difficult for the reservoir to return to its original seepage capacity. Therefore, the residual crude oil in the matrix cannot be recovered, which will affect the oil and gas production capacity.

Damage to Near-Fracture Matrix

For the fracturing process of shale reservoirs, on the one hand, the fracturing fluid entering the reservoir can form fractures with

high conductivity and improve the oil-water flow channel of the reservoir; on the other hand, the fracturing fluid will also bring damage to the reservoir. Some damages result in reduced permeability and reduced output.

The damage of fracturing fluid is to reduce the permeability of the formation through physical or chemical actions, which is mainly reflected in two aspects: First, the blockage of the pores caused by the expansion of clay minerals and the dispersion and migration of particles has serious damage to the reservoir. In particular, the incompatibility of foreign fluids causes various physical or chemical reactions with clay minerals. These reactions can cause many serious problems, such as wettability reversal, permeability reduction, hydration, pore structure changes, etc., which can damage the reservoir. Second, after the fracturing fluid enters the throat, due to the presence of capillary force, a water lock phenomenon may be formed, which has a serious impact on the reservoir. The higher the capillary resistance, the more clogged or even permanent clogging of the pores, causing serious damage.

NUMERICAL SIMULATION USING A FULLY NUMERICAL MODEL

Characterization of Key Parameters of Shut-In Mechanism

Characterization of imbibition parameters: The Handy model (Cai and Yu, 2012), the theoretical model of imbibition, refers to imagining the core as a bundle of closely arranged parallel capillaries. Under the action of capillary force, fluid is imbibed into the interior of the rock matrix. This process can be regarded as a displacement process. Without considering the influence of gravity and gas pressure gradient, the relationship between core imbibition quality and time can be obtained, as shown in **Equation 1**.

$$V_{imb}^2 = \left(\frac{2P_c \varnothing k_w S_w A_c^2}{u_w}\right) t \tag{1}$$

where V_{imb} is the imbibition volume of the fluid, mL ; P_c is the capillary force, P_a; φ is the porosity; K_w is the permeability, md; S_w is the water saturation; A_c is the cross-sectional area of water absorption, c_m^2; u is the viscosity of the liquid, $mPa \cdot s$; t is the soaking time, min.

It can be seen from the above relationship that in the process of spontaneous imbibition in the Handy model (Cai and Yu, 2012)' the square of the imbibed volume has a linear relationship with the imbibition time.

Dynamic changes of cracks: In this paper, for the characteristic parameters of crack dynamic change, it is necessary to obtain the crack stress sensitivity coefficient, the crack stress sensitivity coefficient and use the power method. To obtain the basic form of the power formula, the fracture permeability and the effective stress of the rock need to be processed without dimension. After processing, the following form is obtained:

$$K/K_0 = \alpha\left(\frac{\sigma}{\sigma_0}\right)^{-S} \tag{2}$$

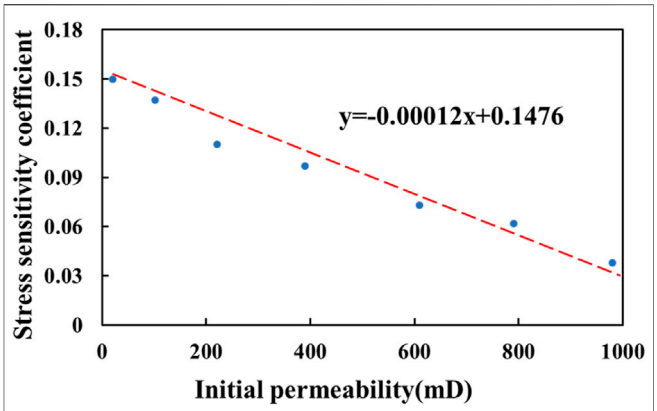

FIGURE 3 | Relationship between stress sensitivity coefficient and initial fracture permeability.

In the above formula, σ is the effective stress of the crack, MPa; σ_0 is the initial effective stress of the crack, MPa; K is the crack permeability when the effective stress of the crack is σ_{eff}, mD; K_0 is the initial crack permeability, mD; α is the effective stress coefficient; S is the stress sensitivity coefficient. Substituting $K = K_0$ and $\sigma = \sigma_0$ into the formula, $\alpha = 1$. The original formula becomes:

$$K/K_0 = \left(\frac{\sigma}{\sigma_0}\right)^{-S} \tag{3}$$

Substituting the initial data of fracture permeability and the corresponding fracture stress sensitivity coefficient under this permeability into the rectangular coordinate system, and fitting it to obtain:

$$S = aK_0 + b \tag{4}$$

Among them, the fitting constants of a and b can be obtained as follows: $a = -0.0003$, $b = 0.1437$. Substituting into **Eq. 3**, the characteristic parameters of fracture dynamic change can be obtained (Jia et al., 2021b):

$$K = K_0\left(\frac{\sigma}{\sigma_0}\right)^{-0.0003K_0+0.1437} \tag{5}$$

In the formula: σ is the effective stress of the crack, MPa; σ_0 is the initial effective stress of the crack; K is the crack permeability at which the effective stress of the crack is σ, mD; K_0 is the initial permeability of the crack, mD.

The relationship curve between fracture stress sensitivity coefficient and initial fracture permeability is shown in **Figure 3**. It can be seen from the figure that the fracture stress sensitivity coefficient has a good linear relationship with the initial fracture permeability.

Damage to the reservoir matrix: The numerical simulation model in this paper believes that the main judgment basis for reservoir damage in the near-fracture area is the permeability of the reservoir, that is, the permeability of the reformed area and the unreformed area in the model are different, as shown in

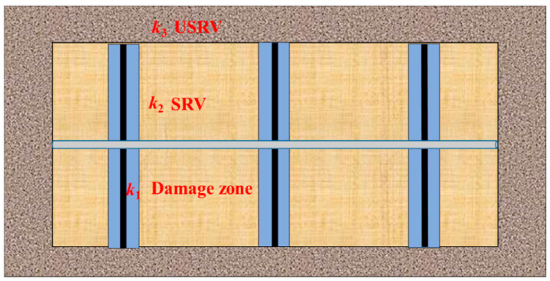

FIGURE 4 | Diagram of reservoir damage permeability.

Figure 4. The blue area is the unreformed area of the reservoir, with a permeability of k_3; the three small rectangular areas are the fracturing area, the yellow area on the left half is the reservoir damage area, and the green area on the right half is the undamaged area. The permeability is k_1, k_2, respectively. Where $k_1<k_2$, $k_3<k_2$.

Numerical Simulation Model of Shut-In Well

Based on the shut-in mechanism of shale reservoirs after fracturing, a numerical simulation model for shut-in wells for shale reservoirs with low permeability and low porosity characteristics is established using tNavigator software. The establishment of the numerical model for the shut-in of the single well after fracturing considered the three factors of spontaneous matrix imbibition, dynamic changes of fractures (expansion and closure), and reservoir matrix damage. The grid model of the numerical simulation model is shown in **Figure 5**. The basic parameters and relative permeability curves are shown in **Figure 6**.

For the imbibition effect, we use different capillary force curve in key word SWFN to model the imbibition strength, and represent the wettability between the fracturing, oil, and matrix essentially. And for the dynamic behavior of fracture (crack), we use the permeability-pressure table to update the fracture permeability in each simulation step for capturing fracture dynamic behavior. For the damage to the reservoir matrix, a lower permeability zone with different width surrounding fracture is assigned.

The basic parameters of the numerical simulation model are shown in **Tables 1**, **2**.

WATER AND OIL DISTRIBUTION IN SHUT-IN PERIODS

Using the shut-in numerical simulation model established above, first analyze the oil-water and pressure distribution characteristics during the shut-in process. The selection of

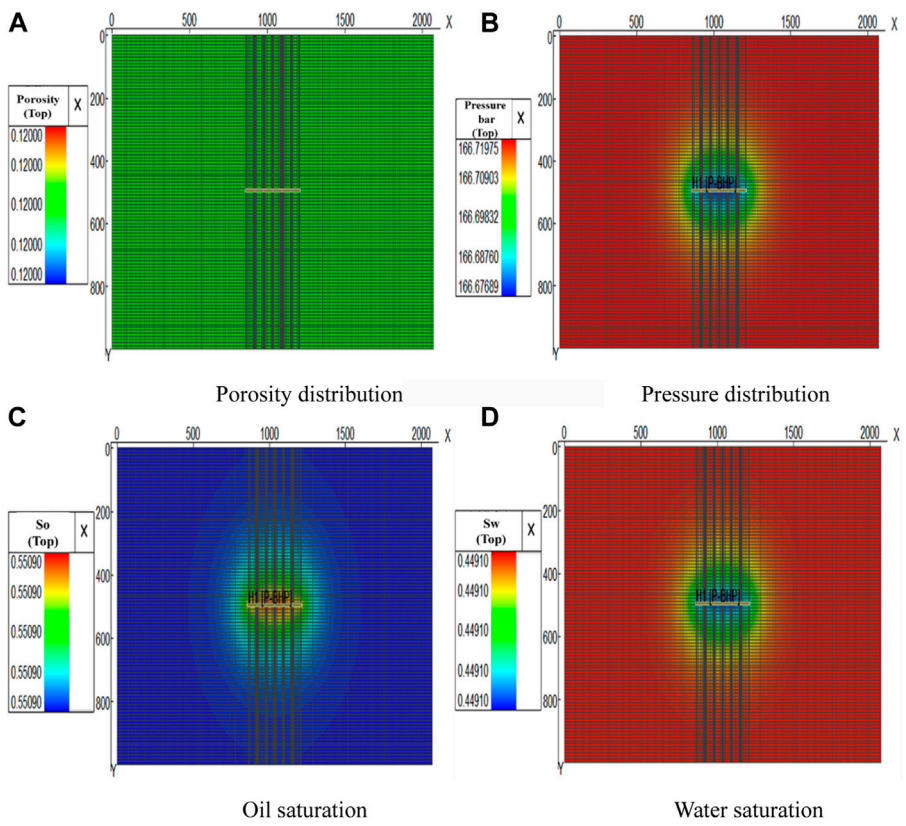

FIGURE 5 | The grid model of the numerical simulation model. **(A)** Porosity distribution. **(B)** Pressure distribution. **(C)** Oil saturation. **(D)** Water saturation.

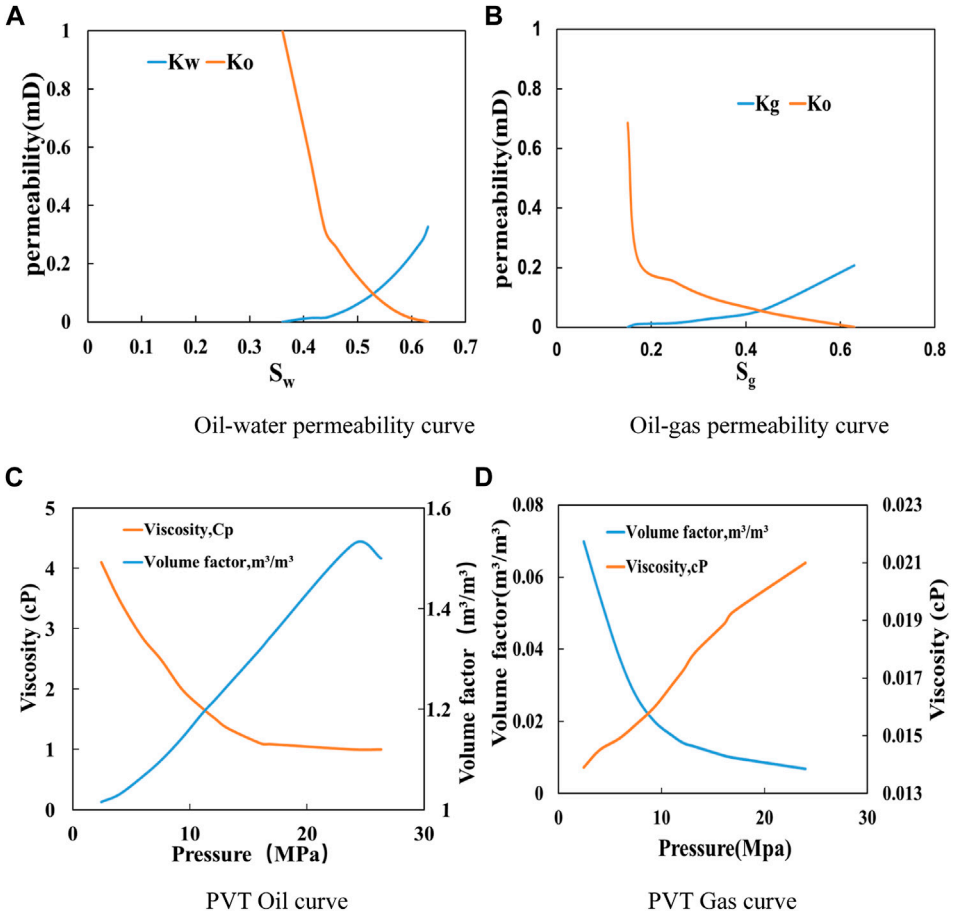

FIGURE 6 | The basic parameters and relative permeability curves. **(A)** Oil-water permeability curve. **(B)** Oil-gas permeability curve. **(C)** PVT Oil curve. **(D)** PVT Gas curve.

TABLE 1 | Basic parameters of the model.

Basic parameters of the model	Numerical value
Number of grids	269 × 100×5
Grid size, m^3	10 × 10×1
Model size, m^3	2,690 × 1,000×5
Porosity, %	12
Permeability of inner zone, mD	0.0001
Permeability of outer zone, mD	0.00001
Original formation pressure, MPa	16.73
Mode of production	Constant pressure
S_o, %	55
S_w, %	45

TABLE 2 | Table of basic parameters of single well numerical simulation model.

P_m/MPa	k_f/mD	k_m/mD
16.73	450	0.11
S_{oi}	L_f/m	P_c/MPa
0.55	60	0

model parameters for shut-in of this single well after fracturing is shown in the table below.

The oil-water distribution characteristics of shut-in in shale reservoirs after fracturing are described by the distribution of oil saturation and near-fracture formation pressure distribution, and the oil-water distribution characteristics of shut-in in shale reservoirs after fracturing are analyzed through these two aspects.

1) Oil-water distribution: take the 30, 60, 90, 120 days fractures and the oil saturation distribution in the near-fracture area after the shut-in measures are taken. The schematic diagram is shown in **Figure 7A**.

From the schematic diagram of the distribution of oil saturation, there were obvious changes in the oil saturation in the fractures. By the time the well was shut in for 120 days, the average oil saturation in the fracture had increased to 0.43, but the change in oil saturation in the near-fracture area was not obvious.

2) Near-fracture formation pressure distribution: For the near-fracture formation pressure distribution, we take the pressure

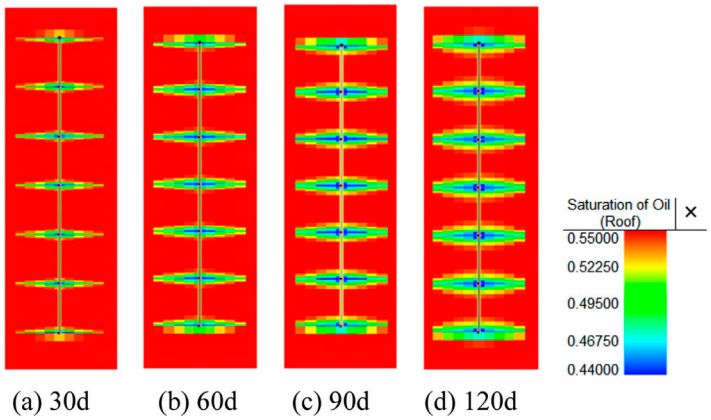

(1) Schematic diagram of oil saturation change during closing

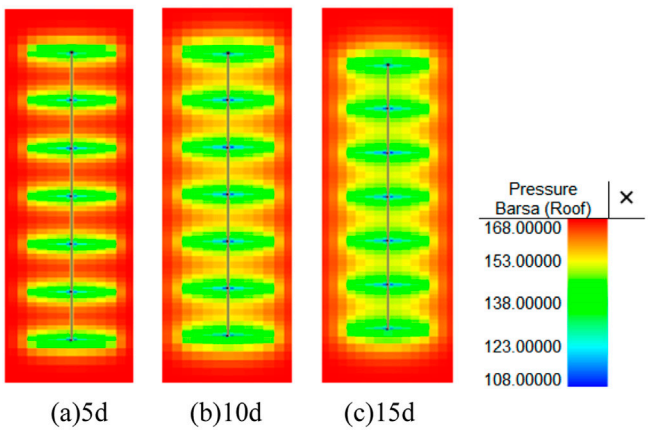

(2) Schematic diagram of pressure change of near fracture formation during well boring

FIGURE 7 | The schematic diagram. **(A)** Schematic diagram of oil saturation change during closing **(i)** 30d, **(ii)** 60d, **(iii)** 90d, **(iv)** 120d. **(B)** Schematic diagram of pressure change of near fracture formation during well boring **(i)** 5d, **(ii)** 10d, **(iii)** 15d.

distribution in the near-fracture area for 5, 10, and 15 days of shut-in. The schematic diagram is shown in **Figure 7B**.

It can be seen from the figure above that the propagation speed of the pressure wave is far greater than the oil-water replacement rate. And on the 15th day of the shut-in measures, formation pressure increase effect in the near-fracture area is very obvious, and the range of pressure spread is also rapidly expanding. From the above figure, it can be found that after the shut-in measures are taken, the formation pressure has increased significantly, and the maximum value can reach 16.69 MPa. It can be clearly seen that the shut-in measures influence the formation pressure increase in shale oil reservoir production.

EFFECT OF KEY PARAMETERS ON PRODUCTION PERFORMANCE

Effect of Different Capillary

Take the capillary force as 1 MPa (low capillary force) and 5 MPa (high capillary force), and observe the distribution of oil saturation in the near fracture area after shut-in at low and high capillary forces for 30, 60, 90, and 120 days. The schematic diagram is shown in **Figure 8**.

It can be obtained from the figure that the capillary force has a very important influence on the imbibition of the matrix. In the above figure, it can be seen that the oil-water replacement effect of a 60-days shut-in under 5 MPa (high capillary force) is roughly the same as that of a 120-days shut-in under 1 MPa (low capillary force). It can be obtained that the higher the capillary force, the better the oil-water replacement effect.

Similarly, numerical simulation can be used to obtain the pressure distribution in the near fracture area after shut-in at low and high capillary force levels for 5, 10, and 15 days. The schematic diagram is shown in **Figure 9**.

It can be seen from the figure that under the capillary force level of 1 and 5 MPa, the pressure propagation range is roughly the same, and there is not much difference. The pressure in the near-slit area under the capillary force of 5 MPa is slightly higher than the pressure in the near-slit area under the capillary force of 1 MPa, but it is not very obvious.

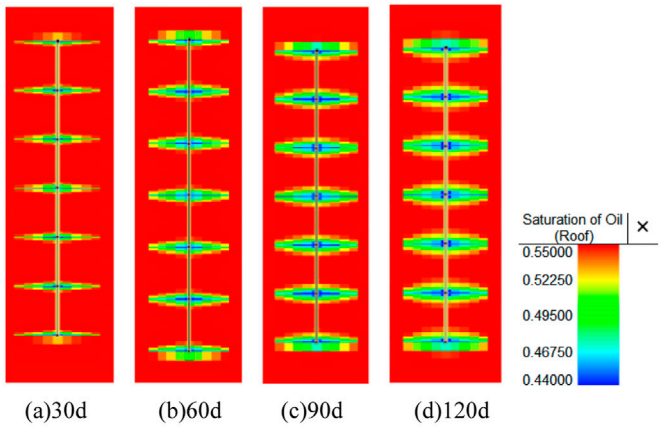

(1) Diagram of oil saturation variation in the process of shut in under low capillary force

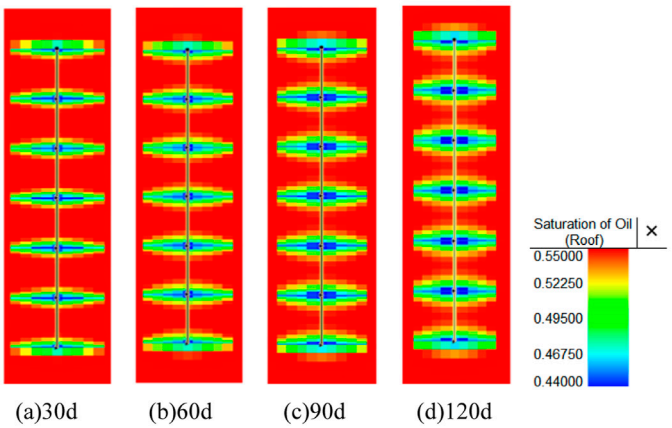

(2) Diagram of oil saturation variation in the process of shut in under high capillary

FIGURE 8 | Diagram of oil saturation variation in the process of shut in under different capillary. **(A)** Diagram of oil saturation variation in the process of shut in under low capillary force **(i)** 30d, **(ii)** 60d, **(iii)** 90d, **(iv)** 120d. (**B**) Diagram of oil saturation variation in the process of shut in under high capillary **(i)** 30d, **(ii)** 60d, **(iii)** 90d, **(iv)** 120d.

It is also possible to obtain the change rule of daily liquid production under different capillary forces with the number of production days. As shown in **Figure 10**.

It can be seen from the figure that the change trend of daily liquid production under different capillary force levels with the number of production days is basically the same. That is, it increases first and then decreases, increases rapidly after shutting in, and then stabilizes. However, the peak value is different. The peak value of daily fluid production after shut-in under high capillary force is relatively larger. Therefore, the daily fluid output increases with the increase of capillary force.

The capillary force level has a great influence on the oil-water replacement effect during the development of shale reservoirs. The greater the capillary force, the more obvious the effect of oil-water replacement. In terms of daily fluid production, capillary force also has a positive effect on it. But for the pressure distribution, the pressure under different capillary forces tends to be basically the same, so the capillary force does not have much influence on the pressure distribution.

Effect of Different Stress-Sensitive of Fracture Permeability

Take the fracture stress sensitivity coefficients as 0.14, 0.098, and 0.056 respectively, and observe the distribution changes of oil saturation in the near fracture area after shut-in 30, 60, 90, and 120 days under different fracture stress sensitivity conditions. It can be seen that the distribution of oil saturation during shut-in of shale reservoirs is basically the same under the three fracture stress sensitive conditions. The oil saturation under 0.098 and 0.056 stress-sensitive conditions has a slight increase, only a 10^{-3} level increase, and the oil-water replacement effect is roughly the same. It shows that the crack stress sensitivity has little or no effect on the oil-water replacement effect.

The same numerical simulation method can also be used to obtain the pressure distribution in the near fracture area after shut-in for 5, 10, and 15 days under different fracture stress sensitivity. It can be seen from the figure that under different fracture stress-sensitive conditions, the pressure distribution in the near-fracture area during the shut-in process of a shale

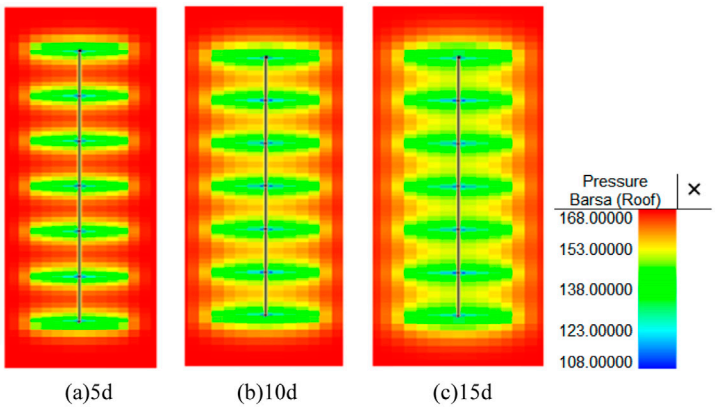

(1) Schematic diagram of pressure change in near fracture area during well shut down under low capillary force

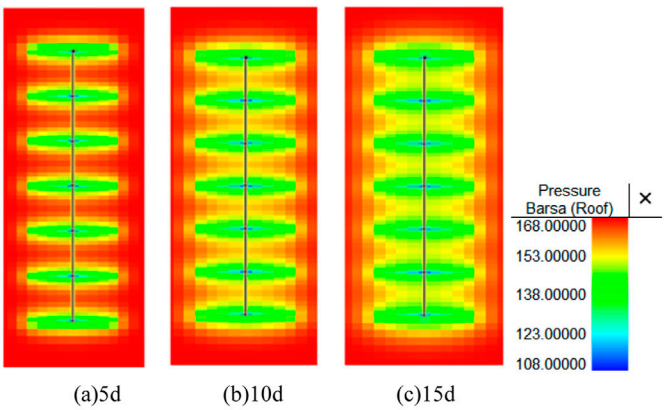

(2) Schematic diagram of pressure change in near fracture area during well shut down under high capillary force

FIGURE 9 | Schematic diagram of pressure change in near fracture area during well shut down under different capillary force. **(A)** Schematic diagram of pressure change in near fracture area during well shut down under low capillary force **(i)** 5d, **(ii)** 10d, **(iii)** 15d. **(B)** Schematic diagram of pressure change in near fracture area during well shut down under high capillary force **(i)** 5d, **(ii)** 10d, **(iii)** 15d.

reservoir is basically the same, with almost no change. Therefore, it shows that the stress sensitivity of different fractures has no obvious influence on the pressure distribution in the near-fracture area during shut-in.

It can be seen that the stress sensitivity of different fractures has little effect on the oil saturation and pressure distribution in the near-fracture area during the shut-in process of shale oil reservoirs. For the daily fluid production, the smaller fracture stress sensitivity corresponds to a little more daily fluid production.

Effect of Formation Damage

By changing the thickness of the reservoir damage to 0.1, 0.2, 0.4 m, the influence of the reservoir damage on the oil saturation distribution in the near fracture area during the shut-in process is studied. Observe the distribution changes of oil saturation in the near fracture area after shut-in 30, 60, 90, and 120 days under the three thickness of the reservoir damage. It can be seen from the figure that the pressure distribution changes in the near fracture area under different reservoir thicknesses are basically the same. The larger the width, the higher the pressure, but it is also very small. Therefore, it is concluded that the influence of different reservoir damage thickness on the pressure increase effect in shale oil reservoir development is minimal.

Similarly, we can also obtain the change rule of daily fluid production with the number of production days under the condition of different reservoir damage thickness. It can be seen from the figure that the greater the thickness of the reservoir damage, the higher the peak of the daily fluid production will be correspondingly, but the increase is not very large.

It can be seen that in the development process of shale oil reservoirs, the influence of reservoir damage caused by different reservoir damage thickness on the oil-water replacement effect and pressure increase effect during the shut-in process is not very

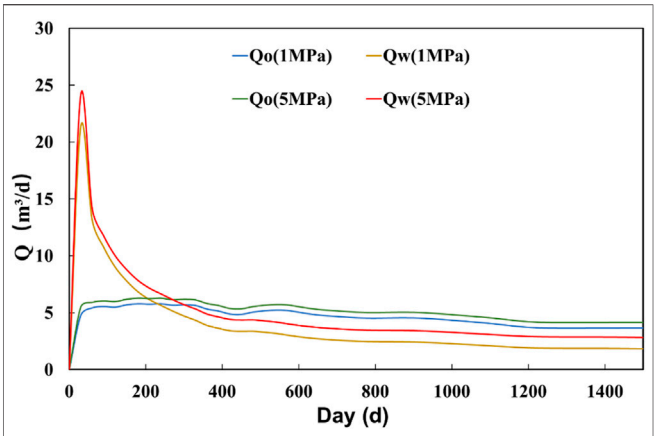

FIGURE 10 | Variation rule of daily liquid production with days of development and production under1MPa capillary force and 5 MPa capillary force.

obvious. But in comparison, the smaller the thickness, the better the effect. The same is true for daily fluid production.

CONCLUSION

This paper first summarized the shut-in mechanism of shale oil reservoirs, including three aspects: shut-in imbibition, dynamic changes of fractures, and reservoir damage. And the mechanism was characterized. Finally, based on the reservoir numerical simulation method, the distribution of oil and water in shale reservoirs and the law of their influence on productivity are analyzed. The main conclusions drawn are as follows:

1) Most of the energy in the fracturing fluid in the reservoir is used for matrix imbibition, increasing the pressure of the formation. Under the action of the fracturing fluid, the natural fractures are expanded and the hydraulic fractures pass through the natural fractures to form a complex fracture grid, increasing the permeability of the reservoir. There is also reservoir damage caused by factors such as the incompatibility of foreign fluids, which leads to a decrease in reservoir permeability.
2) Considering the three aspects of matrix spontaneous imbibition, a numerical simulation model for shut-in of a single well after fracturing is established.
3) The higher the reservoir permeability and capillary force, the better the oil-water replacement effect during shut-in. Fracture stress sensitivity and reservoir damage have little impact on the oil-water replacement effect.
4) The greater the reservoir permeability, the greater the pressure range, and the better the effect of the increase. The influence of capillary force is second, and the influence of fracture stress sensitivity and reservoir damage on pressure increase is even smaller.
5) The higher the reservoir permeability and capillary force, the higher the peak daily fluid production. The smaller the fracture stress sensitivity, the higher the daily fluid production. The greater the thickness of the reservoir damage, the lower the daily fluid production.

In general, among the four influencing factors, reservoir permeability and capillary force have the most obvious effects, while fracture stress sensitivity and reservoir damage are less obvious than the former two.

DATA AVAILABILITY STATEMENT

The original contributions presented in the study are included in the article/supplementary material. Further inquiries can be directed to the corresponding author.

AUTHOR CONTRIBUTIONS

PJ: the idea; XK: the numerical simulation; YL: figures and tables; LC: revision; LN: the mechanism.

ACKNOWLEDGMENTS

We acknowledge that this study was partially supported by the National Natural Science Foundation of China (No. 52004307), Beijing Municipal Natural Science Foundation (No. 3204053), and Science Foundation of China University of Petroleum, Beijing (No. 2462018YJRC015). We would further like to thank financial support of the National Natural Science Foundation of China (No. 51774297 and No. U1762210).

REFERENCES

Bertoncello, A., Wallace, J., Blyton, C., Honarpour, M., and Kabir, C. S. S. (2014). Imbibition and Water Blockage in Unconventional Reservoirs: Well-Management Implications during Flowback and Early Production. *SPE Res. Eval. Eng.* 17, 497–506. doi:10.2118/167698-pa

Cai, J., and Yu, B. (2012). Research Progress of Spontaneous Imbibition in Porous media. *progress mechanics[J]* 42 (06), 735–754.

Fakcharoenphol, P., Kurtoglu, B., Kazemi, H., Charoenwongsa, S., and Wu, Y-S. (2014). "The Effect of Osmotic Pressure on Improve Oil Recovery from Fractured Shale Formations[C]," in SPE Unconventional Resources Conference.

He, Y., Qiao, Y., Qin, J., Tang, Y., Wang, Y., and Chai, Z. (2022). A Novel Method to Enhance Oil Recovery by Inter-fracture Injection and Production through the Same Multi-Fractured Horizontal Well. *J. Energ. Resour. Technol.* 144 (4), 043005. doi:10.1115/1.4051623

He, Y., Qin, J., Cheng, S., and Chen, J. (2020). Estimation of Fracture Production and Water Breakthrough Locations of Multi-Stage Fractured Horizontal wells Combining Pressure-Transient Analysis and Electrical Resistance Tomography. *J. Pet. Sci. Eng.* 194, 74–79. doi:10.1016/j.petrol.2020.107479

Jia, P., Zhuang, L., Cheng, L., and Hengfei, Y. *Study on Stress Sensitivity Characteristics and Quantitative Characterization of highland Saturated Differential Pressure Reservoirs, Special Oil and Gas Reservoirs*.

Jia, P., Ma, M., Cao, C., Chengab, L., Yine, H., and Lid, Z. Capturing Dynamic Behavior of Propped and Unpropped Fractures during Flowback and Early-Time Production of Shale Gas wells Using a Novel Flow-Geomechanics Coupled Model. *J. Pet. Sci. Eng.* 208, 2021. doi:10.1016/j.petrol.2021.109412

Jia, P., Wu, D., Yin, H., Li, Z., Cheng, L., and Ke, X. (2021). A Practical Solution Model for Transient Pressure Behavior of Multistage Fractured Horizontal Wells with Finite Conductivity in Tight Oil Reservoirs. *Geofluids* 2021, 9948505. doi:10.1155/2021/9948505

Le, D. H., Hoang, H. N., and Mahadevan, J. (2009). "Impact of Capillary Suction on Fracture Face Skin Evolution in Waterblocked Wells[C]," in SPE Hydraulic Fracturing Technology Conference.

Li, S., Ding, Y., and Yang, Y. (2017). Simulation Study on Forced Imbibition of Tight Rock Samples and Multi-Scale Modeling. *J. Oil Gas Technology[J]* 39 (2), 66. doi:10.12677/jogt.2017.392019

Liu, D. (2017). *Fracturing Fluid Microscopic Imbibition and "stuffy Well" Stimulation mechanism[D]*. Beijing: China University of Petroleum.

Odumabo, S. M., Karpyn, Z. T., and Ayala H., L. F. (2014). Investigation of Gas Flow Hindrance Due to Fracturing Fluid Leakoff in Low Permeability Sandstones. *J. Nat. Gas Sci. Eng.* 17, 1–12. doi:10.1016/j.jngse.2013.12.002

Wang, M., and Leung, J. Y. (2016). Numerical Investigation of Coupling Multiphase Flow and Geomechanical Effects on Water Loss during Hydraulic-Fracturing Flowback Operation. *SPE Res. Eval. Eng.* 19, 520–537. doi:10.2118/178618-pa

Wang, Q., Guo, B., and Gao, D. (2012). "Is Formation Damage an Issue in Shale Gas Development? [C]," in SPE International Symposium and Exhibition on Formation Damage Control.

Wang, Y. (2018). *Research on the Fracture Closure Mechanism of Tight sandstone reservoirs[D]*. Beijing: China University of Petroleum.

Wust, R. A., Mattucci, M., Hawkes, R., Quintero, H., and Sebastian, S. (2018). "Early Insights from Various Load Fluid Recoveries after Hydraulic Fracturing Treatments: A Case History of a Developing Unconventional Oil Shale Play in Alberta," in Paper presented at the SPE International Hydraulic Fracturing Technology Conference and Exhibition, Muscat, Oman, October 2018. doi:10.2118/191421-18ihft-ms

Yaich, E., Williams, S., Bowser, A., Goddard, P., SouzaDiaz, O. C. de., and Foster, R. A. (2015). "A Case Study: The Impact of Soaking on Well Performance in the Marcellus," in Paper presented at the SPE/AAPG/SEG Unconventional Resources Technology Conference, San Antonio, Texas, USA, July 2015. doi:10.15530/urtec-2015-2154766

Yan, Q., Lemanski, C., Karpyn, Z. T., and Ayala, L. F. (2015). Experimental Investigation of Shale Gas Production Impairment Due to Fracturing Fluid Migration during Shut-In Time. *J. Nat. Gas Sci. Eng.* 24, 99–105. doi:10.1016/j.jngse.2015.03.017

Conflict of Interest: The authors declare that the research was conducted in the absence of any commercial or financial relationships that could be construed as a potential conflict of interest.

Publisher's Note: All claims expressed in this article are solely those of the authors and do not necessarily represent those of their affiliated organizations, or those of the publisher, the editors, and the reviewers. Any product that may be evaluated in this article, or claim that may be made by its manufacturer, is not guaranteed or endorsed by the publisher.

frontiers in Earth Science

ORIGINAL RESEARCH
published: 03 March 2022
doi: 10.3389/feart.2021.825253

Feasibility Investigation on the N_2 Injection Process to Control Water Coning in Edge Water Heavy Oil Reservoirs

Wei Zheng[1,2], *Yabin Feng*[3], *Xianhong Tan*[1,2], *Renfeng Yang*[1,2], *Huiqing Liu*[3]*, *Haojun Xie*[1,2] *and Taichao Wang*[1,2]

[1]State Key Laboratory of Offshore Oil Exploitation, Beijing, China, [2]CNOOC Research Institute Co., Ltd., Beijing, China, [3]State Key Laboratory of Petroleum Resources and Prospecting, China University of Petroleum, Beijing, China

N_2 injection process is a potential technique to control the water coning behavior in heavy oil reservoirs. In this paper, by using the methods of experiment and numerical simulation, the N_2 injection process for controlling the edge water coning behavior is investigated. First, through a visual fluid flow experimental device, the flow behavior of N_2-water in porous media is discussed. Also, the effects of temperature, pressure, and injection rate were studied. Then, based on the experimental results, aiming at an actual edge water heavy oil reservoir, a reservoir simulation model is developed. Thus, the water coning behavior of edge aquifer is systematically studied. Also, two novel indicators are proposed to evaluate the water coning behavior. Then, a series of numerical models are developed to investigate the performance of N_2 injection process in edge water heavy oil reservoirs after water coning, and the adaptability and the optimal operation parameters are analyzed. Results indicate that under the effect of porous media, N_2 can cut into a series of small gas bubbles. It is a typical dispersed phase and can effectively plug the water coning path. Compared with pressure and injection rate, temperature is a more sensitive factor to affect the plugging performance of N_2. From the simulation results, it is observed that the permeability, water/oil ratio, and distance between well and aquifer can significantly affect the performance of water coning behavior. N_2 injection process can effectively control the edge water coning and improve the CSS performance. Furthermore, from the simulation results, it is found that the optimal operation parameters for a N_2 injection process is that the total N_2 injection volume should be higher than 6,000 m^3 within one operation cycle and the optimal N_2 injection rate should be lower than 700 m^3/day. This investigation further clarifies the mechanisms of N_2 injection process to control the water coning behavior in heavy oil reservoirs. It can provide a useful reference for the EOR process of the heavy oil reservoirs with edge water.

Keywords: heavy oil, water coning, N_2 injection process, edge water, numerical simulation

OPEN ACCESS

Edited by:
Yulong Zhao,
Southwest Petroleum University, China

Reviewed by:
Hong-Bin Liang,
Southwest Petroleum University, China
Lingfu Liu,
University of Wyoming, United States

***Correspondence:**
Huiqing Liu
liuhq110@126.com

Specialty section:
This article was submitted to Economic Geology, a section of the journal Frontiers in Earth Science

Received: *30 November 2021*
Accepted: *20 December 2021*
Published: *03 March 2022*

Citation:
Zheng W, Feng Y, Tan X, Yang R, Liu H, Xie H and Wang T (2022) Feasibility Investigation on the N_2 Injection Process to Control Water Coning in Edge Water Heavy Oil Reservoirs. Front. Earth Sci. 9:825253. doi: 10.3389/feart.2021.825253

1 INTRODUCTION

Heavy oil reservoir is an important type of petroleum resources (Meyer et al., 2007; Liu et al., 2019). It refers to the petroleum reservoir whose oil viscosity is higher than about 50 mPa·s at reservoir condition. The world proven heavy oil resources is about 9,911.8 × 10^8 t, and the recoverable heavy oil resources is about 1,267.4 × 10^8 t. The heavy oil resources in the regions of America and Middle East can account for about 72% in the world (Liu et al., 2019). Because of the high viscosity of heavy oil, how to effectively reduce the oil viscosity is usually the top concern for all the heavy oil corporations. Different with the recovery method of light oil reservoirs (e.g., natural depletion, water flooding, polymer flooding, etc.), thermal recovery process is always the first option of heavy oil reservoirs. Currently, steam-based recovery process is the main development method of heavy oil reservoirs, including CSS (cyclic steam stimulation), steam flooding, and SAGD (steam-assisted gravity drainage) (Farouq Ali, 2007; Speight James, 2013; Dong et al., 2019). However, considering the diversity of the type of heavy oil reservoirs, the three classic thermal recovery processes usually have the optimal screening criterion. It indicates that for some special or complicated heavy oil reservoirs, the conventional steam injection process is usually not effective (Dong et al., 2019).

Among the so many heavy oil reservoirs, the heavy oil reservoir with an edge water zone is a typical heavy oil reservoir (Liu, 2013; Liu et al., 2013; Delamaide and Moreno, 2015). Because of the effect of aquifer energy, once the conventional steam injection process, CSS, is performed, a serious problem of water coning can be observed, especially in the initial stage of recovery process. Then, as the recovery process continues, the water coning behavior is aggravated, and thus the normal development process is affected (Liu et al., 2013; Pang et al., 2020). Specifically, the following three characteristics can be observed. First, CSS process is a pressure-declining recovery process. For an actual heavy oil reservoir, with the CSS cycle increasing, the reservoir pressure is gradually reduced. Thus, the coning behavior of edge water can be observed (Pang et al., 2020; Dong et al., 2021). On the other hand, because of the injection of high-temperature steam, the oil viscosity is reduced and oil mobility is improved. It can benefit the declining process of formation pressure, and thus the coning process of edge water is induced. Third, as the CSS process continues, the coning behavior of edge water will change the distribution of reservoir temperature. Under the effect of edge water, the reservoir section around the edge water can have a lower temperature and a higher water saturation. It indicates that a water coning path will be developed (Liu, 2013; Dong et al., 2019). After the formation of a water coning path, an obvious water coning behavior can be observed in the thermal wells.

To effectively control the water coning behavior and improve the heavy oil recovery process, many different methods of preventing water coning are proposed. Specifically, they include the methods of adjusting operation parameters, N_2 injection process and NCG (non-condensable gas) foam injection process (Lai and Wardlaw, 1999; Wang et al., 2018; Dong et al., 2021). First, for the process of adjusting operation parameters, e.g., reducing steam injection rate, increasing flow wellbore pressure, and reducing liquid production rate, it is usually valid in the early stage of water coning. Compared with the other two methods, this process is the most economic one. However, once a serious water coning behavior is observed, it will be no longer effective. Second, for NCG foam injection process, it is more effective than the process of adjusting operation parameters (Lu et al., 2013; Pang et al., 2018; Liu et al., 2020; Wang et al., 2020; Dong et al., 2021). By using the high resistance capability of NCG foam, the water coning path can be effectively plugged, and correspondingly the recovery performance can be improved. However, because of the high cost of chemical agent, the operation cost of this process can usually hinder the expansion of this process. Comparatively, N_2 injection process is the most attractive one among the three commonly used processes. Compared with the process of adjusting operation parameters, this process is more effective. Compared with the process of NCG foam system, it is more economic. The detailed mechanisms to control the water coning behavior are as follows (Pang et al., 2008; Pang et al., 2015; Wang et al., 2018; Chen et al., 2021; Kirmani et al., 2021): 1) N_2 has a low solubility in heavy oil and water. Once N_2 is injected into heavy oil reservoir, the dispersed nitrogen gas bubbles can plug the water thief zone and improve the recovery process. 2) On account of the effect of small gas bubbles, N_2 can effectively reduce the relative permeability of water phase. 3) Under the effect of gravitational differentiation, N_2 will rise up and develop a secondary gas cap. It will benefit the recovery process in upper pay zone. 4) N_2 has a higher expansibility. Therefore, after the injection of N_2, the reservoir pressure can be recovered. This high-pressure reservoir zone can prevent the early breakthrough of aquifer. Although some investigations about the performance of N_2 injection in heavy oil reservoirs have been performed, most of them are based on the simulation process. There is still lack of a systematical study for the dynamic characteristics of N_2 injection process to control the water coning behavior in heavy oil reservoirs.

In this paper, combining the methods of visualized micro-model and numerical simulation, the anti-water coning process by N_2 injection process will be discussed. First, in **section 2**, by using a visualized micro-model, the N_2–water two-phase flow behavior at different conditions is investigated. Specifically, the effects of pressure, temperature, and injection rate on the two-phase flow behavior are all discussed. Thus, the reasonability and mechanism of N_2 injection for controlling water coning can be addressed. Then, in **section 3**, through the method of numerical simulation, the water coning behavior in an actual edge water heavy oil reservoir will be discussed. Thereafter, the adaptability of N_2 injection process is studied, and the operation parameters are also optimized. The concluding remarks will be given in **section 4**.

2 EXPERIMENT

2.1 Experimental Setup and Procedure

(1) Experimental Setup

Figure 1 shows a schematic of the visualized experiments. As shown, it is consisted by the injection system, sand pack model, constant temperature oven, camera recording system, back pressure regulator, and liquid acquisition system. In this

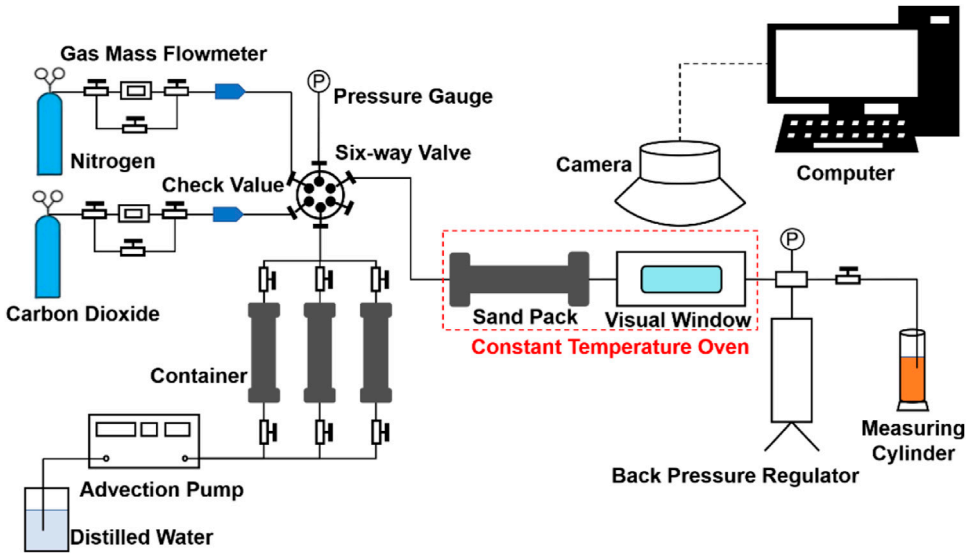

FIGURE 1 | A schematic of the visualized micromodel for the multiphase fluid flow behavior.

TABLE 1 | Experimental design for the flow behavior of N_2 and water in porous media

No	Quartz sand (mesh)	Porosity (%)	Permeability (10^{-3} μm^2)	Temperature (°C)	Operation pressure (MPa)	Injection rate (ml/min)	Fluids
1	80–120	36.5	4.3	25	1	150	N_2-water
2	80–120	35.9	4.1	50	1	150	N_2-water
3	80–120	36.1	4.4	25	2	150	N_2-water
4	80–120	36.2	4.0	50	3	150	N_2-water
5	80–120	36.2	4.0	100	3	150	N_2-water
6	80–120	35.2	4.0	100	5	150	N_2-water
7	80–120	36.7	4.3	50	5	150	N_2-water
8	80–120	36.7	4.3	50	5	200	N_2-water

visualized experiment, a sand pack model is used to simulate the porous medium environment. By injecting the multicomponent fluids (i.e., N_2, formation water, and heavy oil) into the sand pack model, the actual multiple phase fluid flow process in a heavy oil reservoir can be simulated. Then, through a connected micromodel, the multiple phases fluid flow behavior in porous medium can be visually observed.

Using the aforementioned experimental device, eight groups of visualized experiments for the flow behavior of N_2 and water were carried out, as shown in **Table 1**. By observing the phenomenon of nitrogen separation into bubbles and gas–liquid flow in water, the effect of temperature and pressure conditions on the anti-water behavior by N_2 can be discussed. Cases no. 1–7 can be applied to study the characteristics of N_2 separation into bubbles and the law of gas–liquid flow under different temperature and pressure conditions. Cases no. 7 and 8 can be used to compare and analyze the effects of different injection rates on the separation of nitrogen into bubbles and gas–liquid flow.

(2) Experimental Procedures

1) Fill the model pipe. Wash the required quart sand, and dry it in the constant temperature oven. Then, fill it into the sand pack. The sand is fully compacted to avoid the migration of quartz sand during the experiment, blocking the pipeline and causing the experiment to fail;
2) Gas tightness test. Connect an intermediate container with nitrogen gas and a pressure gauge at one end of the sand pack. Inject nitrogen gas into the sand pack until the pressure reaches 12 MPa, then close the valve and stabilize the pressure for 30 min and control the pressure drop within 0.2 MPa;
3) Measure the porosity and permeability. Use saturated water to measure porosity and permeability;
4) Connect the equipment and instruments. Put the sand pack in the constant temperature oven, so that the sand pack is at a constant experimental temperature during the whole experiment, and the high-temperature and high-pressure visual window is placed on top of the constant temperature oven;
5) Experiment. According to the experimental scheme, set the model temperature, pressure, and injected gas composition, and inject N_2 into the sand pack to simulate the N_2 seepage in porous medium under different conditions;
6) Data collection. Observe the high-temperature and high-pressure visual window and the computer terminal

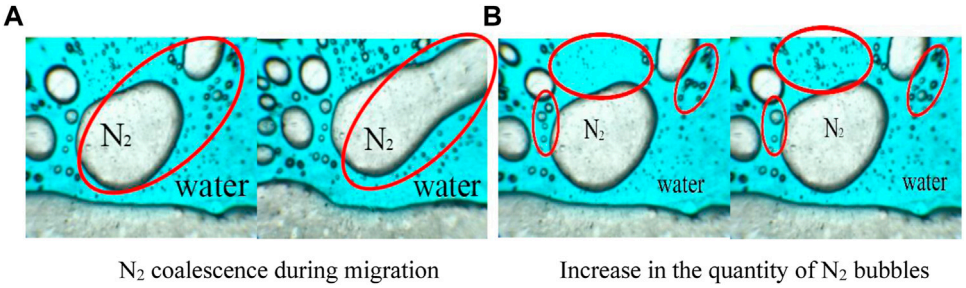

FIGURE 2 | N_2 bubble volume and quantity variation diagram. **(A)** N_2 coalescence during migration **(B)** Increase in the quantity of N_2 bubbles.

acquisition software. After the fluid flows in the visual window, start to record the fluid flow state under different experimental conditions, and collect high-definition images every 3 min until gas channeling appears in the visual window;

7) Cleaning device. After the experiment, close each gas cylinder, and pour kerosene into the high-temperature and high-pressure visual window to clean the glass, and then inject active water. When there is no obvious stain on the glass, dry the visual window for subsequent experiments.

2.2 Experimental Results

From the experimental results of cases no. 1–3, it can be observed that under a low-pressure condition, N_2 is injected into the continuous phase water as a dispersed phase, which is an approximate gas drive water process, as shown in **Figure 2**. In the process of simulating actual N_2 water suppression, the injected N_2 is separated into bubbles of different shapes and sizes, occupying the water space and inhibiting the flow of water. N_2 bubbles have a certain blocking effect when they do not form a gas channel. On the one hand, from **Figure 2A**, when the injection rate is constant, the nitrogen gas will coalesce during the migration process in the water, and small bubbles will merge into large bubbles. On the other hand, from **Figure 2B**, at the same nitrogen injection rate, with the continuous injection of nitrogen, the number of nitrogen bubbles in water is increasing. During migration, small bubbles coalesce and gradually merge into large bubbles. Therefore, the quantity of N_2 bubbles is increasing and the volume of nitrogen bubbles becomes larger.

Temperature and pressure are the main factors affecting the performance of nitrogen bubbles in water. As the temperature increases, the thermal expansion of gas leads to the increase of the proportion of large bubbles. And with the pressure increasing, the gas is compressed and the size of N_2 bubbles in water becomes smaller. The experimental results are shown in **Figure 3**. Through the comparison between the first group of experiments and the second group of experiments, it is found that the bubbles in the left picture is smaller than that in the right picture from **Figure 3A**. The temperature of the right picture is higher than that in the left picture. When the large bubbles increase to a certain extent, the large bubbles are easy to burst. Therefore, the front stability of large bubbles becomes poor due to the increase of its shape. On the contrary, when large bubbles coalesce in water and form gas channeling, the resistance effect of separation into bubbles will become worse. Through the comparison between the second group of experiments and the third group of experiments, it is found that when the temperature is the same, the solubility of N_2 in water becomes larger with the increase of pressure, and the quantity of small N_2 bubbles in water also increases. As shown in **Figure 3B**, the picture on the left has lower pressure than the picture on the right.

By comparing the fourth group of experiments and the fifth group of experiments, the number of N_2 bubbles in water increases as a result of the nitrogen injection volume increase at the same time. With the continuous migration of nitrogen bubbles in water, N_2 bubbles continue to coalesce and form large bubbles, resulting in an increase in the proportion of large bubbles. Due to the increase of injection rate, the migration speed of N_2 in water is accelerated and the proportion of large bubbles increases, resulting in poor stability of large bubbles and poor resistance effect of separation into small bubbles. Also, large bubbles are easy to gather and form a steam channel. Therefore, the blocking effect of large bubbles is lower than that of small bubbles. In the process of nitrogen water suppression, the injection rate of nitrogen should be reduced. As shown in **Figure 4**, the large bubbles grow larger and larger from left to right, causing a negative effect.

3 NUMERICAL SIMULATION

3.1 Simulation Model Development

From the aforementioned experimental results, it can be observed that the method of N_2 injection process can significantly prevent the water coning and improve the recovery performance. Nitrogen mainly plays the purpose of water suppression for edge water heavy oil reservoirs. Therefore, by using the average reservoir and fluid properties of a typical edge water heavy oil reservoir, the numerical simulation method is applied to discuss the water coning behavior of edge water and the adaptability of N_2 injection operation. On the other hand, the operation parameters are also optimized. The basic properties are shown in **Table 2**. The numerical simulation model has 50 grids in direction I. Each grid step length is 5 m, and the length in direction I is 250 m. In direction J, there are 21 grids. Each grid step length is 5 m, and the length in direction J is 105 m. **Figure 5** shows the oil–water and gas–liquid relative

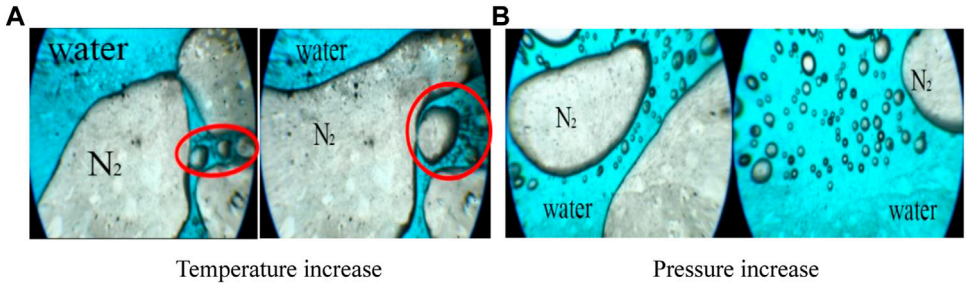

FIGURE 3 | N_2 bubble diagram at different temperatures and pressures. **(A)** Temperature increase. **(B)** Pressure increase.

permeability curves. **Figure 6** provides a schematic of the simulation model.

3.2 Simulation Results and Discussion

3.2.1 Water Coning Behavior

For the heavy oil reservoirs with an aquifer, how to accurately evaluate the water coning behavior is always the top concern. In this paper, two evaluation indicators will be proposed, the ratio of cumulative-water to cumulative-oil (RWO) and the ratio of cumulative-edge-water to cumulative-water (REWW). The slope for the curve of RWO versus time will be used to effectively evaluate the speed of water coning. Also, the slope for the curve of REWW versus time will used to evaluate the strength of water coning and thus to design the suitable injection volume of plugging agent. Therefore, from the two new indicators, the water coning behavior of edge water heavy oil reservoirs after CSS process will be discussed in this section.

(1) Effect of Permeability

Permeability is one of the most important factors to affect the water coning performance. As the permeability increases, the water coning strength will be enhanced, and the water invasion volume will be also increased. Therefore, to study the effect of permeability on the water coning behavior of edge water, based on the basic properties in **Table 2**, a series of simulation models with different horizontal permeabilities are developed. The other properties were kept unchanged. Also, the RWO and REWW will be used as the evaluation indicators. The simulation results are shown in **Figure 7**. From **Figure 7A**, it can be observed that as the permeability increases, the time of water coning is advanced. As shown, the water coning time for the case of 2,500 md is advanced by about 7 days than that of 1,500 md. Simultaneously, with the permeability increasing, the slope of RWO versus time is also increased. It indicates that a higher water coning speed can be observed for the heavy oil reservoir with a higher permeability. On the other hand, from **Figure 7B**, it can be found that with the permeability increasing, the edge water invasion volume will increase. Especially, for the simulation model of 1,000 md, a low REWW can be observed. It indicates that a serious water coning behavior is not observed.

(2) Effect of Water/Oil Ratio

Similarly, on the basis of the basic properties in **Table 2**, the ratio of edge water zone and pure reservoir zone is changed, and thus the effect of water/oil ratio on the edge water coning behavior can be discussed. The simulation results are shown in **Figure 8**. As shown, with the water/oil ratio increasing, the time of water coning is advanced. Also, the slopes of RWO versus time and REWW versus time are also increased. However, compared with reservoir permeability, the effect of water/oil ratio on water coning behavior is more significant. On the other hand, from **Figure 8**, it can be also observed that once the water/oil ratio reaches to a certain value, the changing tendency between water coning speed and water/oil ratio is reduced. When the water/oil ratio is increased from 1 to 5, the changes of curve slope are significant. However, as it is increased from 5 to 20, the changing tendency is less significant. Therefore, for the CSS process in edge water heavy oil reservoirs, it can be recommended that the optimal water/oil ratio should be lower than 5.

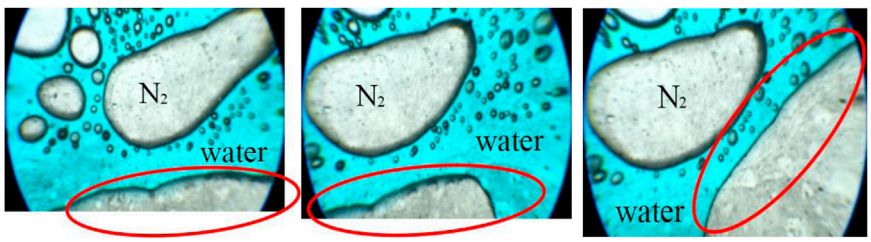

FIGURE 4 | N_2 bubble diagram at injection rate increasing.

TABLE 2 | The basic reservoir and fluid properties

Parameter	Value	Parameter	Value
Model scale (m)	250 × 105 × 10	Initial reservoir pressure (MPa)	5.1
Grid system	50 × 21 × 10	Reservoir temperature (°C)	42
Well spacing (m)	100	Water–oil contact (m)	517
Grid top (m)	500	Water/oil ratio	1
Reservoir thickness (m)	10	Initial oil saturation/decimal	0.75
Porosity (decimal)	0.35	Oil viscosity @RC (mPa·s)	3,000
Horizontal permeability (10^{-3} μm^2)	3,000	Rock compressibility (kPa^{-1})	7.7 × 10^{-6}
K_v/K_h	0.3		

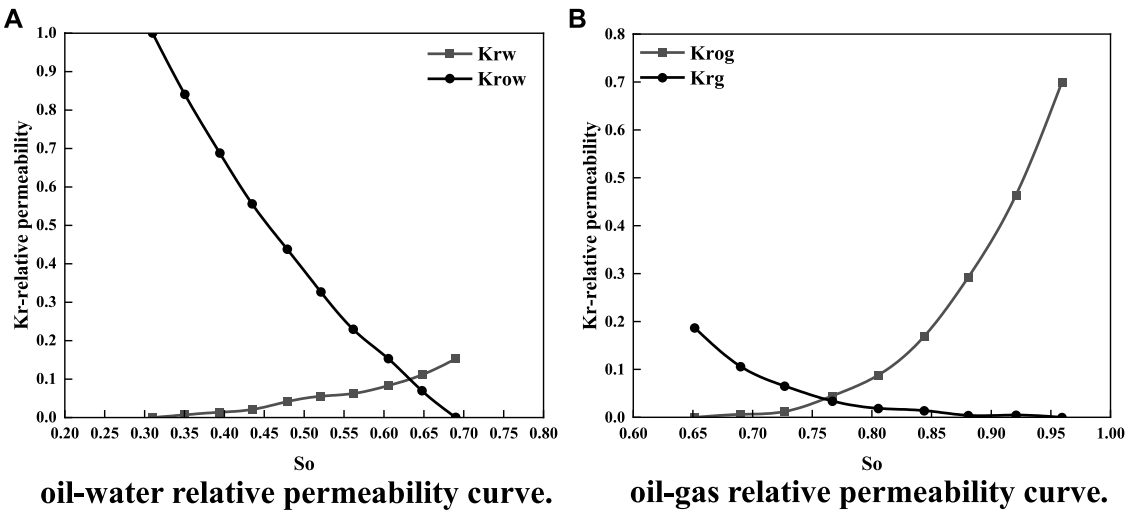

FIGURE 5 | Relative permeability curves. **(A)** Oil–water relative permeability curve. **(B)** Oil–gas relative permeability curve.

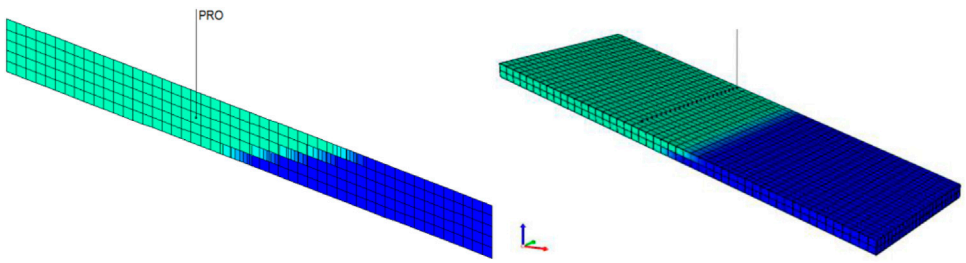

FIGURE 6 | A schematic for the simulation model of edge water heavy oil reservoir.

(3) Effect of the Distance Between Well and Edge Water

In this section, the effect of the distance between well and edge water will be discussed. For the thermal recovery processes in edge water heavy oil reservoirs, it is a very important parameter. With the distance reducing, the edge water can invade the thermal wells early. The simulation results are shown in **Figure 9**. As shown, as the distance reduces, an obvious water coning phenomenon can be observed. Simultaneously, the slopes of RWO versus time and REWW versus time are also increased. It indicates that the water coning strength and water intrusion volume are increased. From the results in **Figure 9**, we can find that as the distance is increased to about 50 m, the water coning phenomenon does not occur. It indicates that the safe distance is 50 m.

3.2.2 Adaptability Evaluation of N_2 Injection Process

Based on the aforementioned discussion, it can be found that the occurrence of water coning will significantly affect the normal development of heavy oil reservoirs, and N_2 injection process will be the potential technology to effectively prevent the water coning

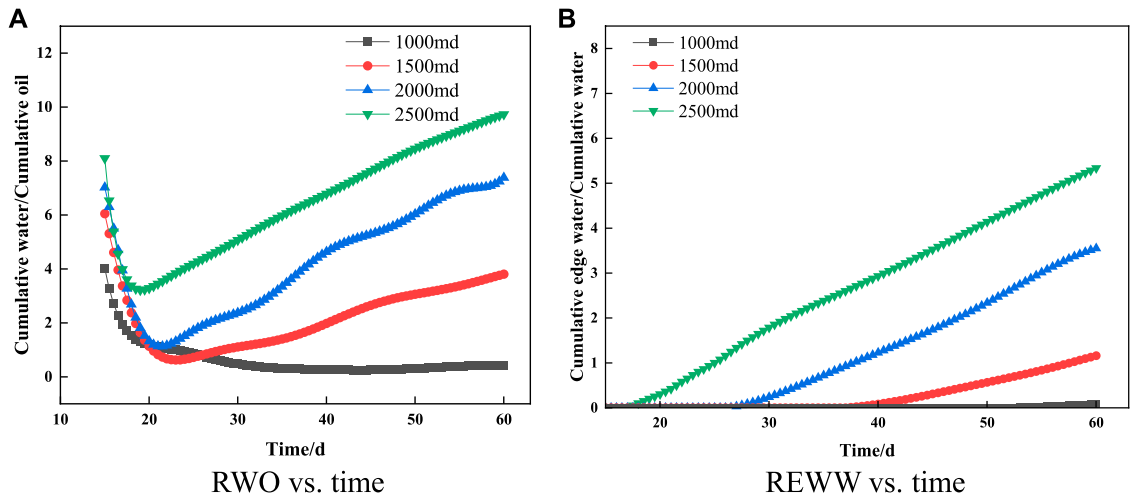

FIGURE 7 | Simulation results for the effect of permeability. **(A)** RWO vs. time. **(B)** REWW vs. time.

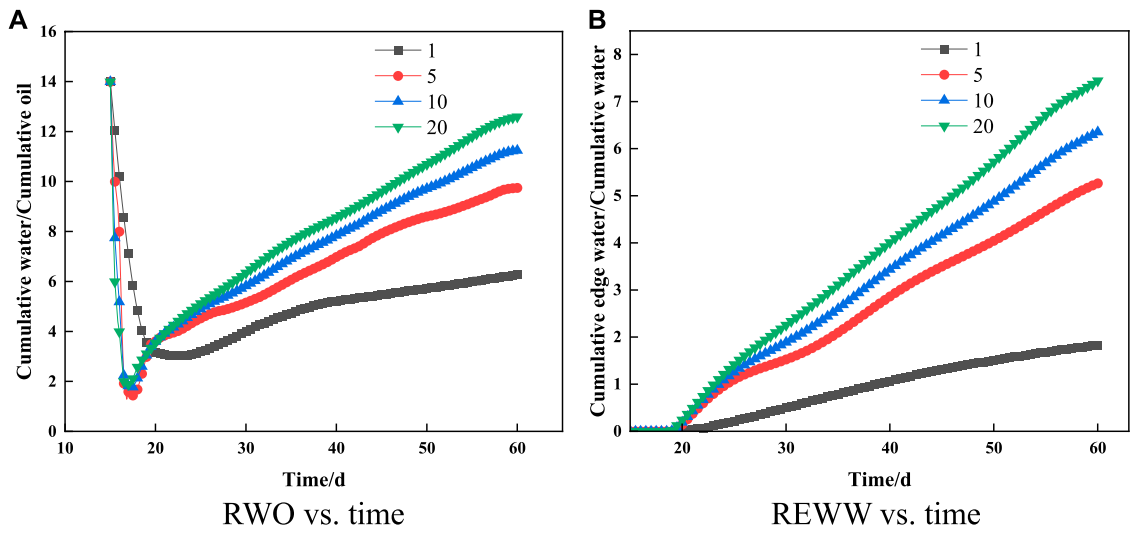

FIGURE 8 | Simulation results for the effect of water/oil ratio. **(A)** RWO vs. time. **(B)** REWW vs. time.

phenomenon. Therefore, in this section, using the same reservoir simulation model, the adaptability of N_2 injection process in edge water heavy oil reservoirs will be numerically discussed, including reservoir thickness, water/oil ratio, and the distance between well and edge water. Using the same numerical simulation model in the previous section, two CSS cycles is first simulated. Then, after the second CSS cycle, considering the serious water coning behavior, the N_2 injection process is first performed, and then the steam injection process is activated to simulate the third CSS cycle. The incremental oil production and the three pure CSS cycles process will be used as the evaluation indicators.

(1) Effect of Reservoir Thickness

Using the aforementioned simulation model, we respectively adjust the reservoir thickness as 2, 4, 6, 8, 10, and 12 m, and the other properties remain unchanged. Thus, by comparing the simulation results of different cases, the effect of reservoir thickness on the N_2 injection performance can be evaluated. The simulation results are shown in **Figure 10**. As shown, with the reservoir thickness increasing, the incremental oil production is increased. The thicker the reservoir thickness, the more obvious the preventing performance of water coning. It can be observed that as the reservoir thickness is higher than about 6 m, the increasing tendency is more significant. It indicates that for the N_2 injection operation in field, the reservoir thickness should be higher than 6 m.

(2) Effect of Water/Oil Ratio

Similarly, the effect of water/oil ratio on the performance of N_2 injection process can be also evaluated. As discussed in the previous section, water/oil ratio represents the aquifer energy.

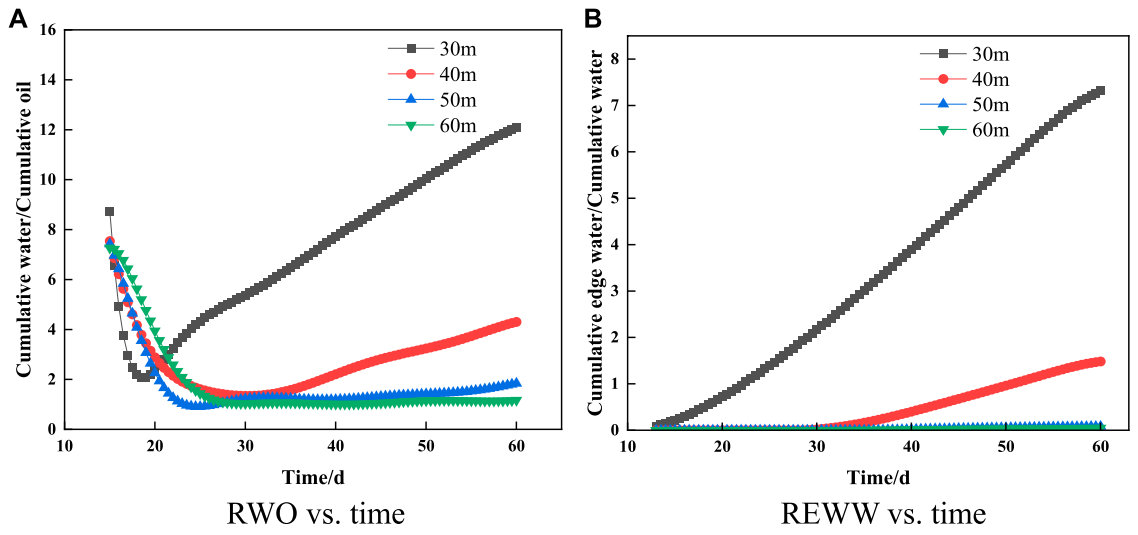

FIGURE 9 | Simulation results for the effect of the distance between well and edge water. **(A)** RWO vs. time. **(B)** REWW vs. time.

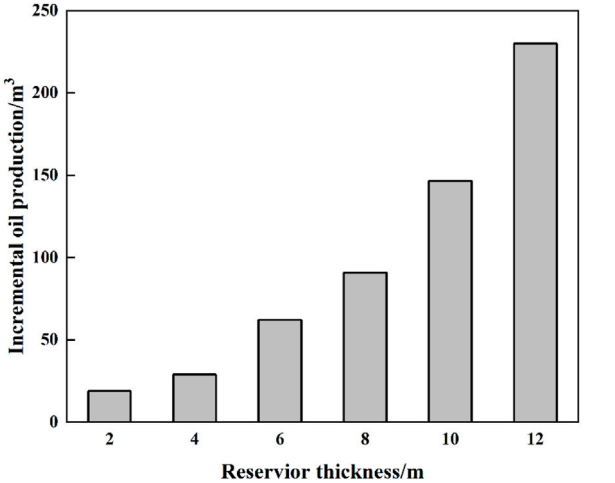

FIGURE 10 | Incremental oil production vs. reservoir thickness.

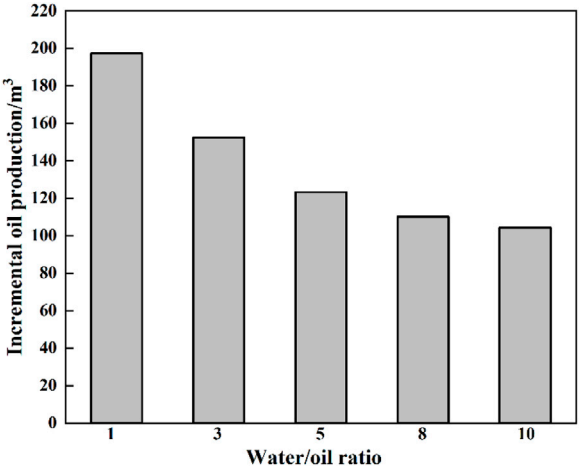

FIGURE 11 | Incremental oil production vs. water/oil ratio.

As the water/oil ratio increases, the aquifer energy is increased, and the water coning strength will be enhanced. The simulation results of different water/oil ratios are shown in **Figure 11**. With the water/oil ratio increasing, the incremental oil production is significantly reduced. It indicates that a serious water coning phenomenon can be observed for the heavy oil reservoirs with a higher water/oil ratio. From **Figure 11**, we can see that as the water/oil ratio is higher than 5, the changing tendency is smoothed. Thus, for the N_2 injection operation in field, the water/oil ratio should be less than 5.

(3) Effect of the Distance Between Well and Edge Water

In this section, the effect of the distance between well and edge water is discussed. The simulation results are shown in **Figure 12**. As shown, with the distance increasing, the incremental oil production is increased, and an "S"-shaped relationship can be observed. Therefore, the appropriate distance between thermal well and edge water should be higher than 80 m, and N_2 injection process can have a better anti-water performance.

3.2.3 Optimization on the Operation Parameters

In this section, the operation parameters of a N_2 injection process to prevent edge water coning will be optimized, including total N_2 injection volume and daily N_2 injection rate. The incremental oil production and then the three pure CSS cycles process and the cumulative edge water production will be used as the evaluation indicators.

(1) Optimization of the Total N_2 Injection Volume

Under the conditions of the other operation parameters that were unchanged, we respectively developed a series of simulation models

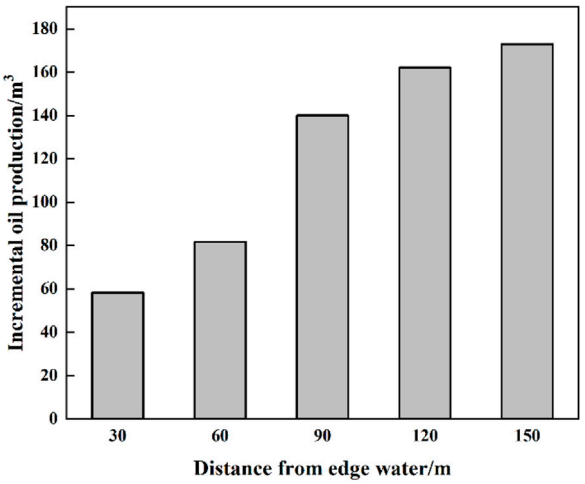

FIGURE 12 | Incremental oil production vs. the distance between well and edge water.

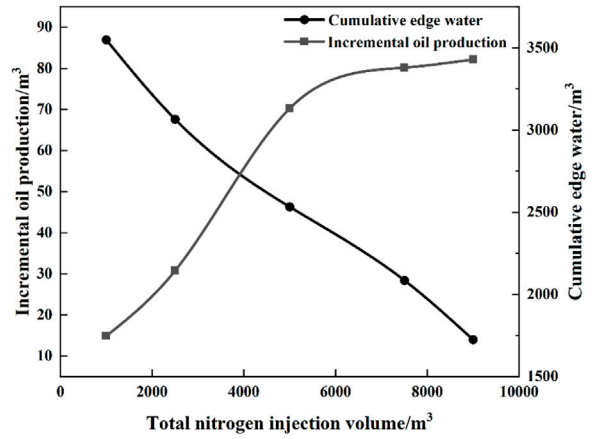

FIGURE 13 | Simulation results of different N_2 injection volumes.

to discuss the effect of N_2 injection volume on the performance of anti-water process. The simulation results are shown in **Figure 13**. As shown, with the N_2 injection volume increasing, the incremental oil production increases and the cumulative edge water production decreases. Under the condition of the other operation parameters that were unchanged, the higher the nitrogen injection volume is, the better the inhibition effect on edge water is. From **Figure 13**, we can see that once the N_2 injection volume reaches above 6,000 m^3, the changing tendency is smoothed. It indicates that an optimal N_2 injection volume has been reached. If the N_2 injection volume is higher than the optimal N_2 injection volume, the incremental oil production basically remains unchanged. Thus, the optimal N_2 injection volume is 6,000 m^3.

(2) Optimization of the N_2 Injection Rate

Similarly, using the same numerical simulation model, the N_2 injection rate can be also optimized. The simulation results are shown in **Figure 14**. As shown, with the N_2 injection rate increasing, the cumulative oil production gradually decreases and the cumulative edge water production gradually increases. It is because that for a higher N_2 injection rate, the distribution of nitrogen in formation becomes uneven, so that the nitrogen cannot achieve a good performance to prevent the edge water coning. Therefore, the water intrusion volume is increased. From **Figure 14**, it can be found that the optimal N_2 injection rate should be lower than 700 m^3/day.

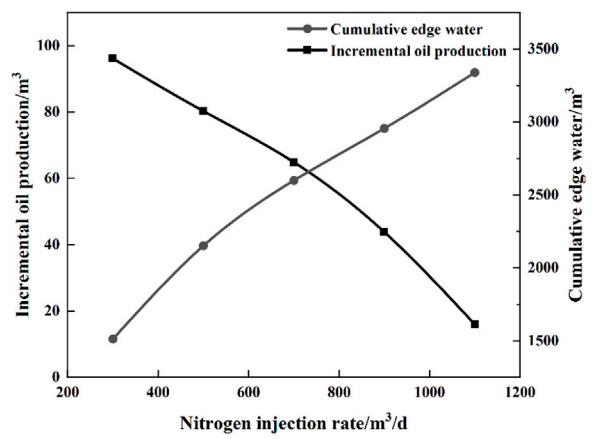

FIGURE 14 | Simulation results of different N_2 injection rates.

4 CONCLUSION

In this paper, combining the methods of visualized experiment and numerical simulation, the performance of N_2 injection process to control the water coning in edge water heavy oil reservoirs is discussed. The anti-water coning mechanisms of N_2 are investigated. Two indicators are proposed to evaluate the water coning behavior of edge water. Simultaneously, the adaptability and optimal operation parameters of N_2 injection process are also studied. The main conclusions are drawn as follows:

1) From the visualized fluid flow experiment, it is observed that in the porous media environment, N_2 can cut into a series of small gas bubbles. It is a typical dispersed phase and can effectively plug the water coning path. Temperature can have an important influence on the plugging performance of N_2 in porous media. With the temperature and N_2 injection rate increasing, the N_2 gas bubble can merge and form a large size gas bubble. It is not beneficial for the water coning controlling process.
2) The ratio of cumulative-water to cumulative-oil (RWO) and the ratio of cumulative-edge-water to cumulative-water (REWW) are proposed to evaluate the water coning behavior of edge aquifer. From the simulation results, it is found that the permeability and distance between the thermal well and aquifer have an important influence on the water coning process. With the permeability increasing and the distance reducing, a serious water coning can be observed.

3) For the adaptability of N_2 injection process, from the numerical simulation results, it is found that a better anti-water coning performance can be observed in the edge water heavy oil reservoirs whose thickness is higher than 6 m, water/oil ratio is less than 5, and distance between the thermal well and edge aquifer is higher than 80 m. For the optimal operation parameters, numerical simulation results show that the optimal N_2 injection volume should be higher than 6,000 m^3, and the optimal N_2 injection rate should be lower than 700 m^3/day.

DATA AVAILABILITY STATEMENT

The original contributions presented in the study are included in the article/Supplementary Material; further inquiries can be directed to the corresponding author.

AUTHOR CONTRIBUTIONS

WZ, YF, XT, and RY contributed to conception and design of the study. WZ and YF wrote the first draft of the article. HL supervised this investigation. HX and TW wrote sections of the article. All authors contributed to article revision, read, and approved the submitted version.

FUNDING

This work was financially supported by the Science Foundation of China University of Petroleum, Beijing (2462020YXZZ032) and the National Natural Science Foundation of China (U20B6003). The financial support of a project from CNOOC Research Institute Co. (CCL2021RCP0361RSN) is also acknowledged.

REFERENCES

Chen, D., Zhao, H., Liu, K., Huang, Y., and Li, B. (2021). The Effect of Emulsion and Foam on Anti-water Coning during Nitrogen Foam Injection in Bottom-Water Reservoirs. *J. Pet. Sci. Eng.* 196, 107766. doi:10.1016/j.petrol.2020.107766

Delamaide, E., and Moreno, W. P. (2015). "Enhanced Oil Recovery of Heavy Oil in Reservoirs with Bottom Aquifer," in SPE 174050 presented at the SPE Western Regional Meeting, Garden Grove, California, USA, 27-30 April.

Dong, X., Liu, H., and Chen, Z. (2021). *Hybrid Enhanced Oil Recovery Processes for Heavy Oil Reservoirs. Developments in Petroleum Science*. 1st Edn. Amsterdam: Elsevier.

Dong, X., Liu, H., Chen, Z., Wu, K., Lu, N., and Zhang, Q. (2019). Enhanced Oil Recovery Techniques for Heavy Oil and Oilsands Reservoirs after Steam Injection. *Appl. Energ.* 239, 1190–1211. doi:10.1016/j.apenergy.2019.01.244

Farouq Ali, S. M. (2007). *Practical Heavy Oil Recovery*. Calgary: Lecture Notes, University of Calgary.

Kirmani, F. U. D., Raza, A., Gholami, R., Haidar, M. Z., and Fareed, C. S. (2021). Analyzing the Effect of Steam Quality and Injection Temperature on the Performance of Steam Flooding. *Energ. Geosci.* 2 (1), 83–86. doi:10.1016/j.engeos.2020.11.002

Lai, S. Z., and Wardlaw, N. C. (1999). Factors Affecting the Application of Anti-water Coning Technology (AWACT) at the South Jenner Oil Field, Southeast Alberta. *J. Can. Pet. Technol.* 38 (03), 25–37. doi:10.2118/99-03-02

Liu, H. Q. (2013). *Principle and Design of thermal Oil Recovery Processes*. Beijing: Petroleum Industry Press. (in Chinese).

Liu, H., Wang, Y., Zheng, A., Sun, X., Dong, X., Li, D., et al. (2020). Experimental Investigation on Improving Steam Sweep Efficiency by Novel Particles in Heavy Oil Reservoirs. *J. Pet. Sci. Eng.* 193, 107429. doi:10.1016/j.petrol.2020.107429

Liu, Y., Li, Y., Jiang, S., Li, S., Zhang, L., Zhang, C., et al. (2013). An Application of Hall Curve to thermal Recovery wells in Bohai Oilfields. *China Offshore Oil and Gas* 25 (5), 43–45.

Liu, Z., Wang, H., Blackbourn, G., Ma, F., He, Z., Wen, Z., et al. (2019). Heavy Oils and Oil Sands: Global Distribution and Resource Assessment. *Acta Geologica Sinica - English Edition* 93 (1), 199–212. doi:10.1111/1755-6724.13778

Lu, C., Liu, H., Lu, K., Liu, Y., and Dong, X. (2013). "The Adaptability Research of Steam Flooding Assisted by Nitrogen Foam in Henan Oilfield," in IPTC 16678 presented at the International Petroleum Technology Conference, Beijing, China, 26-28 March. doi:10.2523/16678-ms

Meyer, R. F., Attanasi, E. D., and Freeman, P. A. (2007). *Heavy Oil and Natural Bitumen Resources in Geological Basins of the World*. Open File-Report 2007-1084. U.S. Geological Survey.

Pang, Z.-x., Cheng, L.-s., Xu, J.-f., and Feng, R.-y. (2008). Application of Material Balance Method to Nitrogen Anti-water-coning Technology. *Pet. Exploration Develop.* 35 (2), 234–238. doi:10.1016/s1876-3804(08)60033-6

Pang, Z., Jiang, Y., Wang, B., Cheng, G., and Yu, X. (2020). Experiments and Analysis on Development Methods for Horizontal Well Cyclic Steam Stimulation in Heavy Oil Reservoir with Edge Water. *J. Pet. Sci. Eng.* 188, 106948. doi:10.1016/j.petrol.2020.106948

Pang, Z., Liu, H., and Zhu, L. (2015). A Laboratory Study of Enhancing Heavy Oil Recovery with Steam Flooding by Adding Nitrogen Foams. *J. Pet. Sci. Eng.* 128, 184–193. doi:10.1016/j.petrol.2015.02.020

Pang, Z., Lyu, X., Zhang, F., Wu, T., Gao, Z., Geng, Z., et al. (2018). The Macroscopic and Microscopic Analysis on the Performance of Steam Foams during thermal Recovery in Heavy Oil Reservoirs. *Fuel* 233, 166–176. doi:10.1016/j.fuel.2018.06.048

Speight James, G. (2013). *Heavy Oil Production Processes*. Houston: Gulf Publishing Company.

Wang, Y., Liu, H., Chen, Z., Wu, Z., Pang, Z., Dong, X., et al. (2018). A Visualized Investigation on the Mechanisms of Anti-water Coning Process Using Nitrogen Injection in Horizontal wells. *J. Pet. Sci. Eng.* 166, 636–649. doi:10.1016/j.petrol.2018.03.083

Wang, Y., Liu, H., Zhang, Q., Chen, Z., Wang, J., Dong, X., et al. (2020). Pore-scale Experimental Study on EOR Mechanisms of Combining thermal and Chemical Flooding in Heavy Oil Reservoirs. *J. Pet. Sci. Eng.* 185, 106649. doi:10.1016/j.petrol.2019.106649

Conflict of Interest: Authors WZ, XT, RY, HX, and TW were employed by the company CNOOC Research Institute Co., Ltd.

The remaining authors declare that the research was conducted in the absence of any commercial or financial relationships that could be construed as a potential conflict of interest.

Publisher's Note: All claims expressed in this article are solely those of the authors and do not necessarily represent those of their affiliated organizations, or those of the publisher, the editors, and the reviewers. Any product that may be evaluated in this article, or claim that may be made by its manufacturer, is not guaranteed or endorsed by the publisher.

Advantages of publishing in Frontiers

OPEN ACCESS
Articles are free to read for greatest visibility and readership

FAST PUBLICATION
Around 90 days from submission to decision

HIGH QUALITY PEER-REVIEW
Rigorous, collaborative, and constructive peer-review

TRANSPARENT PEER-REVIEW
Editors and reviewers acknowledged by name on published articles

Frontiers
Avenue du Tribunal-Fédéral 34
1005 Lausanne | Switzerland

Visit us: www.frontiersin.org
Contact us: frontiersin.org/about/contact

REPRODUCIBILITY OF RESEARCH
Support open data and methods to enhance research reproducibility

DIGITAL PUBLISHING
Articles designed for optimal readership across devices

FOLLOW US
@frontiersin

IMPACT METRICS
Advanced article metrics track visibility across digital media

EXTENSIVE PROMOTION
Marketing and promotion of impactful research

LOOP RESEARCH NETWORK
Our network increases your article's readership